**UNIVERSITÀ DEGLI STUDI DI PADOVA**
**Dipartimento di Fisica ed Astronomia**

CORSO DI DOTTORATO DI RICERCA IN ASTRONOMIA
CICLO XXX

# GROUPS AND CLUSTERS OF GALAXIES IN THE XXL SURVEY

**Tesi redatta con il contributo finanziario dell'Istituto Nazionale di Astrofisica**

**Coordinatore:** Ch.mo Prof. Giampaolo Piotto
**Supervisore:** Dr. Bianca Maria Poggianti
**Co-supervisori:** Dr. Christophe Adami, Dr. Benedetta Vulcani

Dottoranda: Valentina Guglielmo

*Alle tutte le stelle che, nelle notti della vita,*
*hanno illuminato questo mio cammino.*

*"Per aspera ad astra"*
*"Light thinks it travels faster than anything but it is wrong. No matter how fast light travels, it finds the darkness has always got there first, and is waiting for it."*
*Terry Pratchett, Reaper Man.*

# Acknowledgements

*Alla fine di questo lungo percorso, i miei ringraziamenti sono volti alle persone che vi hanno preso parte, nel lavoro e nella vita di ogni giorno.*
*Il primo grande grazie va alla mia relatrice, Bianca. Dopo quasi sei anni di lavoro insieme, queste frasi sicuramente non bastano ad esprimere la mia profonda stima e riconoscenza nei suoi confronti. La sua passione per la scienza, la sua dedizione nel lavoro e la sua positivitá ed unica capacitá di affrontare i problemi e le situazioni dalle quali tante volte mi sono sentita sommersa, sono solo alcune delle cose che mi ha trasmesso ed insegnato. Non avrei potuto avere una guida migliore, e mi auguro di portare con me questa esperienza sempre nel mio futuro, qualunque direzione esso prenda.*
*Desidero ringraziare anche la mia co-relatrice, Benedetta. La nostra collaborazione si è fatta sempre più fitta nel corso del mio dottorato, e le sono infinitamente grata per la sua pazienza, per la sua instancabile voglia di analizzare le questioni ed affrontare le problematiche insieme, per i suoi consigli ed insegnamenti e per la sua disponibilità in qualunque momento.*
*Questo lavoro di tesi non sarebbe stato possibile senza le numerose persone di XXL con le quali ho potuto collaborare e dalle quali ho imparato molto. Ringrazio innanzitutto il mio co-relatore Christophe Adami, per avermi permesso di passare sei mesi a Marsiglia molto importanti, dal punto di vista professionale e personale, e per essere sempre stato molto disponibile nei miei confronti. Un doveroso grazie va anche a Marguerite Pierre, la PI della collaborazione, a Fabio Gastaldello, Stefano Ettori, Lucio Chiappetti, Angela Iovino, e tutto il consorzio.*
*Ringrazio inoltre i miei referee di tesi, David Wilman, Paola Popesso, Florence Durret e Melville Ulman, per gli importanti commenti che hanno permesso di migliorare questo lavoro e renderlo davvero soddisfacente. Ringrazio anche Meghan Gray, per aver letto la mia tesi ed aver appoggiato la mia candidatura al titolo di Doctor Europaeus.*
*Ringrazio tutti i miei amici per aver sempre creduto in me e per avermi sempre ascoltata negli innumerevoli momenti negativi degli ultimi mesi e non solo, per avermi sempre incoraggiata a credere in me stessa e perseguire quello in cui credevo. Un grazie particolare*

*a Camilla, Carlo, Caterina, Elisa, Erica, Federica, Fiore, Gighen, Giulia, Ilaria, Marta, Miriam, Sissi, e tutte le squadre ed i compagni di ore di gioco che si sono susseguiti negli anni e che hanno riempito le mie serate, migliorato le mie giornate ed alleviato ogni fatica.*
*Un importantissimo grazie va alla mia famiglia. Ai miei genitori che mi hanno sempre appoggiato nelle mie scelte di vita e hanno sempre creduto nella strada che ho deciso di intraprendere per il mio futuro, e senza il cui amore non sarei sicuramente mai arrivata fin qui. Alle mie sorelle, alle mie nonne, ai miei zii e cugini per essere parte della nostra meravigliosa famiglia e aver sempre riempito il mio cuore.*
*Ringrazio infine Gabriele, per il suo appoggio costante, per gli anni trascorsi insieme e per l'amore ed il supporto che mi da ogni giorno. L'esito di questo percorso non sarebbe stato ugualmente appagante, positivo e soprattutto promettente senza la sua presenza.*
*Mi sento fortunata a poter ringraziare così tante persone al termine di questa avventura, soprattutto sapendo che il raggiungimento di questo importantissimo traguardo è stato contribuito in parte da ognuna di esse, e che la forza, la tenacia e la passione con la quale sono riuscita ad affrontarlo sono derivate anche dal loro supporto.*

# Contents

# Abstract

This thesis presents one of the first census of the properties of galaxies in X-ray selected groups and clusters at intermediate redshift, with the aim of assessing the role of environment on the galaxy stellar mass assembly, star formation activity and observed stellar population properties.

My project is framed in the XXL Survey (Pierre et al. 2016), the largest XMM-Newton programme approved to date, covering two extragalactic regions in the sky of 25 $deg^2$ each one. Extended X-ray sources identified as groups and clusters are spectroscopically confirmed and their main properties are characterised either via direct measurements or by means of scaling relations. Among them, inferred X-ray luminosities and temperatures, virial masses and radii are of fundamental importance for the development of this thesis. The great advantage of XXL is that the XXL-North field (XXL-N) is fully covered by photometric and spectroscopic observations coming from the most recent extragalactic surveys of galaxies.

The availability of such a treasure trove of information motivates the development of my research on galaxy populations at $0.1 \leq z \leq 0.6$ in XXL-N, exploring the most diverse environments ranging from the field, to groups, clusters and superclusters.

The first task of my work consists in the creation of a homogeneous spectrophotometric sample of galaxies, released in Guglielmo et al. (2017), suitable for scientific purposes. The catalogue contains spectroscopic redshifts, membership information on groups and clusters, spectroscopic completeness weights as a function of position in the sky and observed magnitude, stellar masses and absolute magnitudes computed by means of a spectral energy distribution (SED) technique. The catalogue is fundamental for all XXL studies that aims at relating optical properties derived from galaxies with X-ray information and is widely used in the whole XXL collaboration.

The released spectrophotometric catalogue enables the first scientific achievement of this thesis regarding the study of the galaxy stellar mass function (GSMF). The goal of this analysis is to unveil whether the mass assembly of galaxies depends on global environment, i.e. field vs groups and clusters and, among groups and clusters, on X-ray luminosity, used

as a proxy for the halo mass. I performed the analysis in four redshift bins in the range $0.1 \leq z \leq 0.6$, finding overall that environment does not affect the GSMF, at least in the mass range probed. The result is further confirmed by the invariance of the mean mass of member galaxies on X-ray luminosity. I also looked into the evolution of the mass assembly from z=0.6 down to z=0.1, finding that the high mass end is already in place at the oldest epoch and does not evolve and detecting an increase in the low-mass galaxy population in the same redshift range. This study is one of the first systematic studies on the GSMF conducted for X-ray extended sources ranging from the group to the cluster environment, and is published in the second part of Guglielmo et al. (2017).

Having assessed the independence of the mass distributions on the global environment, I proceed investigating whether and to what extent the environment affects the star formation activity and the observed properties of the galaxy stellar populations.

I started this analysis from the richest supercluster identified in XXL-N, XLSSsC N01, located at redshift $z \sim 0.3$ and composed of 14 groups and clusters. This work has been submitted in Guglielmo et al. (2018a). With focus on the region surrounding XLSSsC N01, I divided galaxies in different environments, ranging from the virial regions of groups and clusters to the field, using a combination of *global* and *local* environment parametrisations. The main results of this study are that, in the supercluster environment, while the star forming fractions and quenching efficiency strongly depend on environment, the SFR-mass relation does not. The star forming fraction progressively declines from the field to filaments to the virialised regions of groups and clusters, with an interesting enhancement in the outer regions of the X-ray structures. Moreover, while the average luminosity weighted (LW)-age-mass relation is independent of the environment, a clear signature for recent star formation quenching is found in the stellar ages of passive galaxies in the virialised regions of X-ray structures.

Finally, I extend the analysis of this peculiar supercluster to the whole XXL-N field. This work will be enclosed in two articles in preparation (Guglielmo et al. 2018 b,c in prep.). Thanks to the higher statistics of the entire sample, I investigated the properties of galaxies and their evolution at $0.1 \leq z \leq 0.5$ in different environments, with the goal of characterising the changing in the stellar population properties and the build up of the passive population via environmental quenching. Besides distinguishing among galaxies in the field, and in groups and clusters (virial regions and outskirts), I also focused on galaxies located in structures of different X-ray luminosity and in galaxies located within superclusters. Simultaneously, I also investigated the properties of galaxies located at different projected local densities (LD).

In particular, I characterised the fraction of star forming/blue galaxies and of the SFR-mass relation, as a function of both *global* and *local* environment. The fraction of star forming and blue galaxies is strictly related to the environment, having the lowest value in the virial regions of groups and clusters, and the highest in the field. In outer members, the same fraction is similar to that in the field at $z \geq 0.2$, and assumes intermediate values with respect to virial members and the field at $0.1 \leq z < 0.2$.

The SFR-mass relation is also environment dependent, and in particular the number of virial member galaxies having reduced SFR (galaxies in transition) nearly doubles that of

field galaxies. Again, outer members show intermediate properties: the fraction of galaxies in transition is similar to the virial population at $z>0.3$, when it is found to be associated to the supercluster environment, and then reduces to values typical of field galaxies at $0.1\leq z<0.3$. The star forming and blue fractions also decrease with increasing LD at all redshifts. On the contrary, the fraction of galaxies in transition does not vary in the same LD range. These significant differences emerging among the *global* and *local* environments are intrinsically related to the different physical meaning of the two parametrisations, thus to the different physical mechanisms acting on galaxies when bound in the potential well of a dark matter halo (according to the *global* definition) or when exposed to interactions with other galaxies in over dense and highly populated regions (according to the *local* definition).

During the first stages of my PhD, I also completed the analysis of my master thesis, and I report the full text of the published paper in the Appendix (Guglielmo et al. 2015). The results are closely related to the scientific questions tackled in my PhD project, addressed through a complementary approach that reconstructed the star formation history of low-redshift galaxies in clusters and in the field to study the dependence on *global* environment, stellar mass and observed morphology.

# Résumé de thèse

Cette thèse présente l'un des premiers recensements des propriétés des galaxies dans un échantillon de groupes et d'amas sélectionnés en rayons X et avec un décalage spectroscopique intermédiaire. Le but de cette étude est d'évaluer le rôle de l'environnement dans la croissance de la masse stellaire des galaxies, dans l'activité de formation stellaire et dans les propriétés des populations stellaires que l'on observe.

Mon projet prend place dans le cadre du sondage XXL (Pierre et al. 2016), le plus grand programme d'observation de XMM-Newton approuvé jusqu'à présent, couvrant deux régions extragalactiques de 25 $\mathrm{deg}^2$ chacune. Les sources diffuses identifiées comme groupes et amas ont été confirmées spectroscopiquement au cours d'un processus itératif décrit dans Adami et al. (2018). Ce processus fait appel à des données spectroscopiques collectées au moyen de divers télescopes de la classe des 4 et 8-10m. Les propriétés principales des amas considérés ont été caractérisées soit par des mesures directes basées sur des spectres X soit au moyen de lois d'échelle. Parmi ces quantités, les plus importantes pour le développement de cette thèse sont les luminosités et les températures provenants de comptages en rayons X, d'où les masses et les rayons Viriels ont été derivés. Ces structures couvrent une vaste gamme de masses de halos ($1.24 \times 10^{13} \leq \mathrm{M}_{500}(\mathrm{M}_{\odot}) \leq 6.63 \times 10^{14}$) et de luminosités measurées en rayons X ($2.27 \times 10^{41} \leq \mathrm{L}_{500}^{\mathrm{XXL}}(\mathrm{erg\,s^{-1}}) \leq 2.15 \times 10^{44}$).

D'un point de vue général, un des grands avantages de XXL est que le champ nord (XXL-N) est entièrement couvert par des observations photométriques du CFHT Legacy Survey (Veillet 2007) CFHTLS Wide 1 (W1) T0007 et spectroscopiques provenant des sondages extragalactiques les plus récents, principalement GAMA, SDSS, VIPERS et des programmes d'observations dédiés à XXL.

Malgré la combinaison sans précédent d'informations en plusieurs longueurs d'onde reliants les propriétés des amas de galaxies en rayons X à la population de galaxies à l'intérieur et autour de leur potentiel gravitationnel, les catalogues spectroscopiques et photométriques étaient encore bruts et inexplorés.

La disponibilité d'une telle mine d'information a motivé le développement de ma recherche sur les populations de galaxies à décalage spectroscopique $0.1 \leq z \leq 0.6$, en explorant les

environnements les plus divers s'étendant du champ, aux groupes, aux amas et aux superamas.
*La première tâche de mon travail consiste en la création d'un échantillon spectrophotométrique homogène de galaxies, adapté aux buts scientifiques. Le catalogue est publié dans Guglielmo et al. (2017).*
Ma première tâche a été induite par l'effet suivant: la superposition de différents sondages spectroscopiques a parfois conduit à la présence d'observations multiples des mêmes galaxies. J'ai identifié et supprimé ces doublons en sélectionnant ceux avec la meilleure qualité spectroscopique et donc la meilleure fiabilité de mesure du décalage spectroscopique vers le rouge.
J'ai ensuite associé ce catalogue spectroscopique "propre" avec des informations photométriques et de décalage photométrique vers le rouge provenant principalement du catalogue CFHTLS et complétées par d'autres données photométriques afin de maximiser le nombre de spectres finalement utilisés.
L'élaboration du catalogue spectrophotométrique final a été poursuivie avec l'attribution de l'appartenance aux groupes et aux amas, en dérivant les dispersions de vitesse à partir des masses Viriels, et en utilisant les rayons du Viriel.
J'ai calculé les complétudes en fonction de la position dans le ciel et de la magnitude observée dans la bande $r$ (la bande photométrique la plus homogène dans le sondage CFHTLS), afin de tenir compte de la variation de complétude découlant de la contribution de différents sondages.
Cette analyse m'a permis de définir la limite de complétude de l'analyse à r=20.0, et de calculer la limite de complétude de masse stellaire de l'échantillon en fonction du décalage spectroscopique vers le rouge (de $log(M/M_{\odot})$=9.6 à z=0.1 jusqu'à $log(M/M_{\odot})$=11.0 à z=0.6).
Le catalogue spectrophotométrique a ensuite été utilisé pour dériver les masses stellaires et les magnitudes absolues calculées au moyen d'une technique d'ajustement de la distribution d'énergie spectrale (SED) au moyen de l'outils LePhare (Arnouts et al. 1999; Ilbert et al. 2006). Cet outil utilise des distributions d'énergie spectrale théoriques qu'il ajuste sur les observations (magnitude observée et décalage spectroscopique vers le rouge) avec, entres autres, comme paramètre libre la masse stellaire.
Le catalogue résultant est fondamental pour toutes les études XXL qui visent à relier les propriétés optiques des galaxies avec les informations sur les groupes et les amas en rayons X. Il est maintenant très utilisé au sein de la collaboration XXL.
*Le catalogue spectrophotométrique qui a été publié permet la première réalisation scientifique de cette thèse concernant l'étude de la fonction de masse stellaire des galaxies (GSMF ci-aprés).*
Le but de cette analyse est de dévoiler si la croissance de la masse des galaxies dépend de l'environnement global, c.-à-d. champ versus groupes et amas et, parmi les groupes et les amas, de la luminosité en rayons X, utilisée comme mesure de la masse des halos. La masse des halos est en effet un paramètre difficilement accessible et l'usage de la luminosité X est un bon moyen d'approximer ce paramètre.
Cette étude est l'une des premières études systématiques de la GSMF conduite dans un

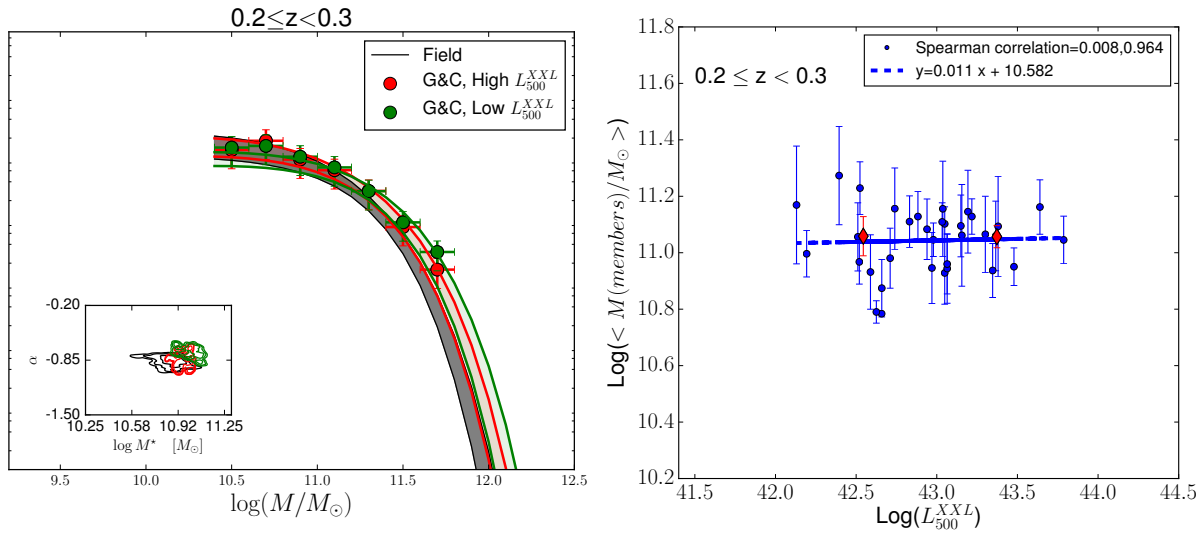


Figure 1: *Gauche.* Exemple de GSMF à décalages vers le rouge dans l'intervalle 0.2≤z<0.3, comme indiqué dans le panneau, pour les galaxies dans des amas de galaxies avec différentes luminosités en rayons X et dans le champ. Les membres des amas de galaxies avec une luminosité élevée en rayons X ($L_{500,scal}^{XXL} > 10^{43}\mathrm{erg\,s^{-1}}$) sont représentés par des symboles rouges, les membres des amas de galaxies avec faibles luminosités en rayons X sont représentés par des symboles verts. Seul les points au-dessus de la limite de complètude en masse stellaire sont affichés. Les paramètres provenants des fonctions de Schechter sont également représentées en zones ombrées, en suivant la même couleur que les points. Dans les encarts, des courbes de contour 1, 2, 3 $\sigma$ sur les paramètres de Schechter $\alpha$ et $M^*$ sont également affichées. *Droite.* Corrélation entre la masse moyenne des galaxies membres des amas de galaxies et la luminosité en rayons X de l'amas hôte (points bleus) dans le même intervalle de décalage spectroscopique. La valeur moyenne de la quantité sur l'axe $y$ a été calculée dans des intervalles de luminosité en rayons X également peuplées et est représentée avec des losanges rouges. L'ajustement des moindres carrés est représenté par des pointillés dans la figure et les paramètres d'ajustement des moindres carrés sont indiqués dans la légende. L'analyse complète se trouve dans le Chapitre 5.

échantillon de groupes et amas observés en rayons X et couvrant un tel domaine de masse de halos. En effet, jusqu'à présent, les amas très massifs étaient employés en priorité dans la littérature, eu égard à leur flux X plus important et donc à la plus grande facilité qu'ils offraient quant à l'estimation de leurs paramètres caractéristiques. Les résultats ont été publiés dans la deuxième partie de l'article Guglielmo et al. (2017).

Après avoir validé la méthode utilisée pour calculer les GSMF en comparant avec les résultats de la littérature, j'ai divisé mon échantillon en quatre intervalles de décalage vers le rouge dans la gamme 0.1≤z≤0.6, et j'ai comparé quantitativement la forme des GSMF dans différents environnements en analysant les paramètres de Schechter résultants. Les résultats indiquent que l'environnement n'affecte pas la GSMF au moins dans la gamme

de masse sondée, même lorsque des régimes de luminosité en rayons X élevés et faibles ont été mis en contraste. Ce résultat est confirmé par l'invariance de la masse moyenne des membres des groupes et des amas en fonction de la luminosité en rayons X. Un exemple de l'analyse complete qui a été conduite dans le Chapitre 5 est représenté dans la Figure 1, pour un seul intervalle parmi les quatre considerés ($0.2 \leq z < 0.3$).

J'ai également examiné l'évolution de la fonction de masse stellaire dans le domaine $0.1 \leq z \leq 0.6$, et j'ai constaté que l'extrèmité supérieure de la fonction de masse est déjà en place à l'époque la plus ancienne et n'évolue pas, ce qui est entièrement en accord avec les résultats disponibles dans la littérature. J'ai détecté en revanche une augmentation de la population de galaxies de faible masse de $z=0.6$ jusqu'à $z=0.1$.

Ces résultats ont conduit à la conclusion que les galaxies ayant des masses supérieures à la limite de complétude de la masse stellaire avaient déjà assemblé la plupart de leur masse stellaire avant que les influences de l'environnement ne deviennent efficaces.

Après avoir évalué l'indépendance des distributions de masse par rapport à l'environnement *global*, j'ai investigué dans quelle mesure l'environnement peut affecter l'activité de formation stellaire et les propriétés observées des populations stellaires des galaxies.

*La complexité de ce sujet motive la choix de se concentrer sur l'étude d'un superamas récemment découvert dans XXL situé à $z \sim 0.3$.*

Il s'agit du superamas le plus riche identifié dans XXL-N, XLSSsC N01, composé de 14 groupes et amas. Il est à noter que c'est l'une des premières études sur les propriétés des populations stellaires et l'activité de la formation d'étoiles dans un superamas entièrement composé d'amas de galaxies détectés en rayons X et avec un décalage vers le rouge intermédiaire. Ce superamas a été détecté sur la base d'une analyse Friend-of-Friend et sa richesse et son degré de robustesse ont été caractérisés au moyen d'une analyse en cellules de Voronoi (voir Adami et al. 2018). Le présent travail à été soumis à la revue A&A dans Guglielmo et al. (2018a).

En se concentrant sur la région entourant XLSSsC N01, j'ai discriminé les galaxies en divers environnements, s'étendant des régions Viriels des groupes et des amas jusqu'au champ, en utilisant une combinaison des paramétrisations d'environnement *global* et *local* afin de sonder toute la gamme des conditions environnementales qu'une galaxie pourrait rencontrer dans la région. La Figure 2 représente la région dans le ciel où se trouve le superamas XLSSsC N01, et montre la distribution de groupe et amas dans le superamas ainsi que les galaxies divisées dans des différents environnement (indiqués dans la légende).

L'analyse des propriétés des galaxies a suivi deux canaux différents: les propriétés de formation d'étoiles et la couleur des galaxies dans leur référentiel local.

Dans le Chapitre 6 j'ai utilisé le code de spectral fitting SINOPSIS (SImulatiNg OPtical Spectra wIth Stellar population models, Fritz et al. 2007, 2011, 2017) pour dériver le taux de formation stellaire (SFR ci-après suivant l'acronyme anglais) actuel, l'histoire de formation stellaire et l'histoire de l'assemblage de la masse stellaire dans quatre époques passées, et le luminosity-weighted(LW)-age.

Les résultats principaux de cette étude sont que, dans ce superamas la fraction de galaxies actives dans le processus de formation stellaire et le paramètre d'efficacité de quenching dépendent fortement de l'environnement, alors que ce n'est pas le cas de la relation SFR-

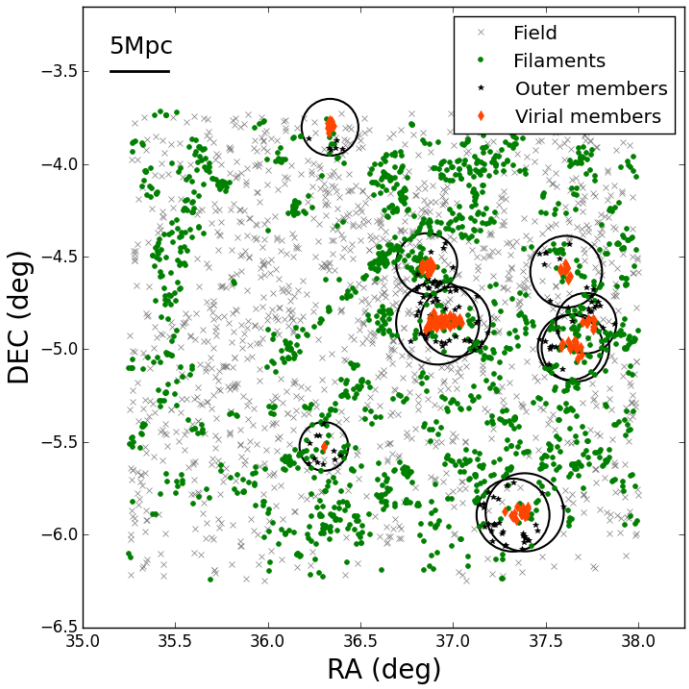


Figure 2: Distribution des galaxies dans la région du superamas XLSSsC N01, codées par couleur en fonction de leur environnement, tel que défini dans la Section 6.2. Les croix grises représentent les galaxies de champ, les points verts sont les galaxies en filaments, les losanges orange foncé représentent les membres dans les régions Viriels des amas de galaxies et les étoiles noires montrent les membres dans les régions externes des amas de galaxies. Les cercles noirs montrent l'extension projetée dans le ciel de $3r_{200}$ (le rayon Viriel) pour chaque groupe et amas de galaxies dans la superstructure.

masse.

En effet, l'environnement des superamas influence les galaxies lorsque l'on regarde la fraction de galaxies actives dans la formation stellaire et les galaxies bleues. Comme montré dans la Figure 3, dans les régions Viriels des amas de galaxies (points oranges), la fraction de galaxies actives dans la formation stellaire et celle des galaxies bleues est plus faible que dans tous les autres environnements. Par contre, les galaxies dans les régions externes des structures en rayons X (entre 1 et 3 $r_{200}$, points noirs) ont une activité de formation d'étoiles augmentée par rapport aux membres dans les zones Viriels, conduisant à une fraction de galaxies formant des étoiles qui est même plus élevée que les filaments (points verts) et les galaxies de champ (points gris). Dans le régime complet de masse stellaire, qui ne sélectionne que les galaxies de masse élevée ($\log(M/M_\odot) > 10.78$), le nombre de galaxies actives dans la formation stellaire et de galaxies bleues diminue dans tous les environnements et les dépendences environnementales sont moins evidentes. Ce résultat confirme le scénario nommé *downsizing* dans la littérature de l'évolution des galaxies massives.

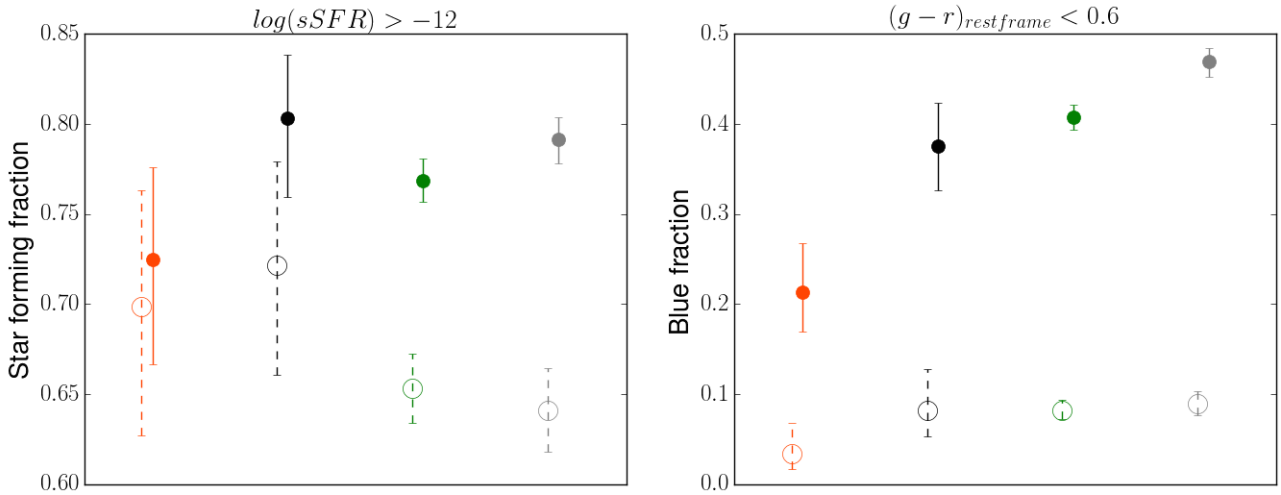


Figure 3: Fraction de galaxies avec formation stellaire active dans les différents environnements identifiés, calculée à travers le specific-SFR (sSFR, le SFR divisé par la masse stellaire observée) (panneau de gauche) et la couleur rest-frame (panneau de droite). Les membres dans les zones Viriels sont montrés en orange, les membres dans les regions externes des amas de galaxies sont répresentés en noir, les filaments en vert et le champ en gris. Les fractions obtenues en utilisant l'échantillon limité en magnitude observée sont représentées avec des symboles pleins, celles obtenues en utilisant une échantillon limité en masse sont représentées par des symboles vides.

J'ai également étudié la relation specific SFR (sSFR, le SFR divisé par la masse stellaire observée)-masse dans le régime de masse complet, ne trouvant aucune différence entre les galaxies dans le champ, dans les filaments et dans les amas de galaxies. Le fait que la relation sSFR-masse ne montre aucune dépendence de l'environnement contrairement à la fraction des galaxies active dans la formation stellaire pointe vers la direction d'un mécanisme d'extinction rapide agissant dans ce superamas riche et conduisant à la formation d'une population passive, preuve d'un phénomène de transition.
Egalement, alors que la relation moyenne entre la luminosity weighted (LW)-age et la masse stellaire est indépendante de l'environnement, une signature claire d'un récent arrêt de la formation d'étoiles est evident dans les âges des populations stellaires des galaxies passives dans les régions Viriels des structures en rayons X.
*Enfin, la dernière étape de cette thèse est de prolonger l'analyse de ce superamas particulier au champ entier XXL-N dans le domaine de décalage spectroscopique vers le rouge de $0.1 \leq z \leq 0.5$.*
Cet objectif est traité dans le Chapitre 7 et sera présenté dans deux articles scientifiques en préparation.
En prenant avantage d'une statistique plus élevée dans l'échantillon entier, j'ai étudié les propriétés des galaxies et leur évolution dans différents environnements, avec le but de caractériser le changement dans les propriétés stellaires des populations de galaxies et la

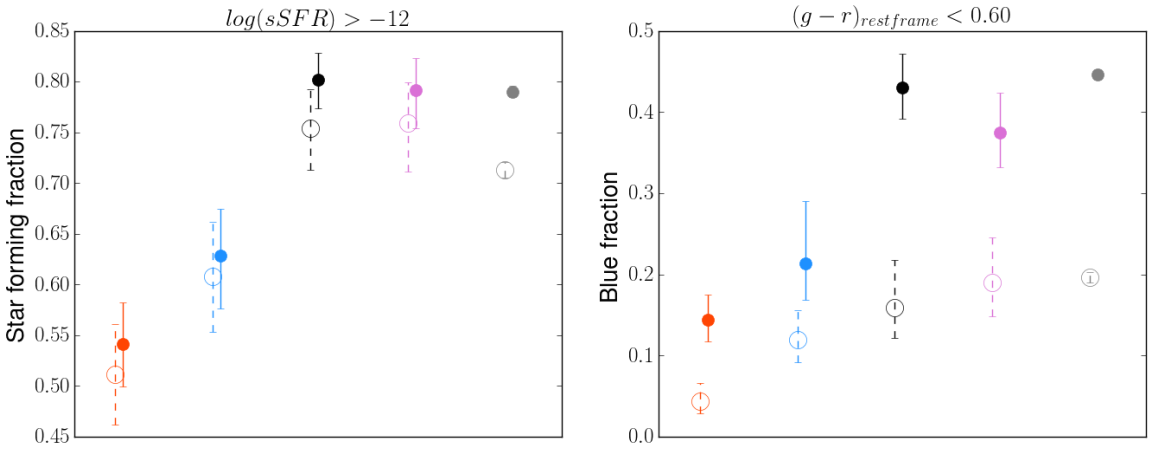


Figure 4: Fraction de galaxies avec formation stellaire active dans des environnements différents, calculés avec le sSFR (panneau de gauche) et la couleur rest-frame (panneau de droite) dans le domaine de décalage spectroscopique $0.2 \leq z < 0.3$, montré comme exemple. Les membres dans les zones Viriels sont montrés en orange si non-appartenants à un superamas (NS) et en bleu si appartenants à un superamas (S), les membres dans les regions externes des amas de galaxies sont représentés en noir (NS) et violet (S), le champ en gris. Les fractions obtenues en utilisant l'échantillon limité en magnitude observée sont représentées avec des symboles pleins, celles obtenues en utilisant une échantillon limité en masse sont représentées par des symboles vides.

naissance de la population passive à cause des conditions environnementales.

Dans la première partie, j'ai considéré l'environnement *global*, et outre la distinction parmi les galaxies de champ, et de groupes et d'amas (à l'intérieur des régions Viriels et à la périphérie), j'ai également considéré les galaxies situées dans des structures avec une luminosité X différente et les galaxies situées dans des superamas.

L'empreinte de l'environnement global sur les galaxies est double.

En premier lieu, la fraction de galaxies qui forment des étoiles et celle des galaxies bleues sont strictement liées à l'environnement, ayant la valeur la plus basse dans les régions Viriels des groupes et des amas, et la plus haute dans le champ. Dans les membres externes, la même fraction est semblable à celle dans les membres des zones Viriels à z>0.2, et est augmentée par rapport aux membres Viriels dans le domaine $0.1 \leq z \leq 0.2$. Ni la luminosité en rayons X des amas de galaxies, ni leur appartenance éventuelle aux superamas, ne semblent conduire à la suppression des fractions enregistrées dans le composant Viriel ou à l'augmentation de la population des membres externes.

Dans la Figure 4 je reporte un exemple de l'analyse qui vient d'être décrite dans le domaine de décalage spectroscopique $0.2 \leq z < 0.3$; les differents environnements sont représentés dans la figure avec des couleurs differentes reportées dans la description ci dessus.

La relation entre la masse stellaire et le SFR est également dépendante de l'environnement. En particulier, le nombre de membres des zones Viriels ayant un SFR réduit par rapport

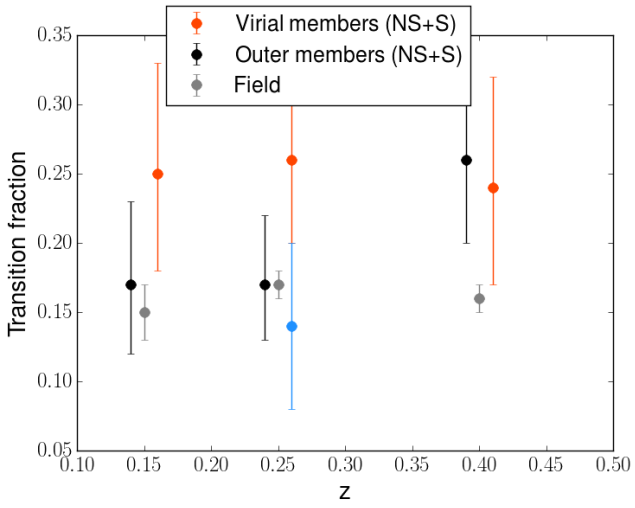


Figure 5: Fraction de galaxies en transition dans l'échantillon complet en masse, dans des environnements différents en fonction du décalage spectroscopique vers le rouge dans le domaine $0.1 \leq z \leq 0.5$. Les environnements correspondants aux points montrés dans la figure sont décrits dans la légende. En bleu, les galaxies en transition dans les membres Viriels des superamas à $0.2 \leq z < 0.3$ sont représentés pour mettre en évidence leur particularité.

à la valeur typique dans la séquence principale (galaxies en transition) est le double du nombre calculé dans le champ. De plus, les membres externes montrent des propriétés intermédiaires: la fraction des galaxies en transition est semblable à la population Viriel à $z > 0.3$, où l'on trouve qu'elle est associée aux superamas, puis réduite aux valeurs typiques des galaxies de champ à $0.1 \leq z < 0.3$.
La particularité des superamas à $0.2 \leq z < 0.3$, où se trouve également le superamas XLSSsC N01, émerge. En effet, à ces décalages spectroscopiques vers le rouge, la fraction des galaxies en transition dans les superamas est la plus faible et représente moins de la moitié des valeurs trouvées dans les autres groupes et dans les périphéries. Dans la Figure 5 les fractions de galaxies en transition sont reportées dans les membres Viriels et externes des amas de galaxies (S+NS) et dans le champs, selon la couleur indiquée dans la légende. En bleu, les galaxies en transition dans les membres Viriels des superamas à $0.2 \leq z < 0.3$ sont représentées pour mettre en évidence leur particularité par rapport aux autres membres Viriels.
J'ai également étudié les propriétés des galaxies situées dans des environnements à différentes densités locales (LD). Des différences substantielles apparaissent.
La fraction de galaxies actives dans le processus de formation stellaire aussi bien que la fraction de galaxies bleues diminuent avec l'augmentation de la LD à tous les décalages vers le rouge. La Figure 6 montre un exemple de l'évolution de la fraction de galaxies actives dans le processus de formation stellaire (panneau de gauche) et bleues (panneau de droite) dans le domaine de décalage spectroscopique $0.2 \leq z < 0.3$. La LD augmente d'un facteur 2 dex dans l'intervalle consideré dans l'axe $x$.

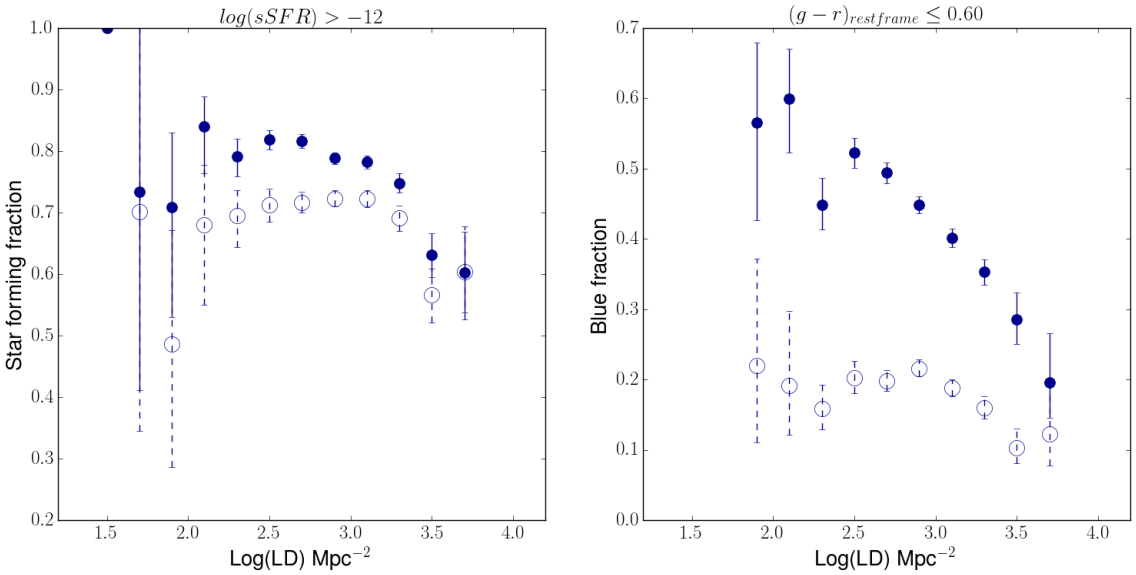


Figure 6: Fraction de galaxies actives dans le processus de formation stellaire dans différents intervalles de LD, calculée avec la sSFR (panneau de gauche) et la couleur rest-frame (panneau de droite) dans le domaine de décalage spectroscopique vers le rouge $0.2 \leq z < 0.3$. Les fractions obtenues en utilisant l'échantillon limité en magnitude observée sont représentées avec des symboles pleins, celles obtenues en utilisant un échantillon limité en masse sont représentées par des symboles vides.

Par contre, la fraction des galaxies en transition ne varie pas dans la même gamme de LD. Ces différences significatives entre l'environnement *global* et *local* sont intrinsèquement liées à (1) la signification physique différente des deux paramétrisations, et (2) aux différents mécanismes physiques agissant sur les galaxies qui se trouvent dans le puit de potentiel d'un halo de matière noire (selon la definition de l'environnement *global*) ou une fois exposées aux interactions avec d'autres galaxies dans les régions denses et fortement peuplées (selon la definition de l'environnement *local*).

Pendant les premières phases de mon doctorat, j'ai complété le travail de ma thèse de master, et je joins le texte intégral de l'article qui a été publié dans l'annexe de cette thèse (Guglielmo et al. 2015). Les résultats sont étroitement liés aux questions scientifiques traitées dans mon projet de doctorat, et abordés dans une approche complémentaire qui a reconstruit l'histoire de formation stellaire des galaxies dans l'Univers local dans les amas de galaxies et dans le champ pour étudier la dépendance de l'environnement, de la masse stellaire et de la morphologie observée.

# Perspectives

Insérée dans le contexte du grand sondage XXL, cette thèse fournit des informations importantes sur le lien entre la formation et l'évolution de propriétés des galaxies et l'environnement à une époque fondamentale pour l'assemblage de la masse stellaire dans les amas de galaxies. Cependant, plusieurs aspects doivent être analysés plus en details afin d'acquérir une compréhension plus générale des phénomènes physiques liés à l'environnement.

Dans le cadre de l'étude de la GSMF, la publication complète des données GAMA dans la région couverte également par le sondage XXL (G02) vient d'être réalisée dans Baldry et al. (2018), et je prévois de poursuivre la collaboration avec cette équipe pour pouvoir me rapporter directement à leurs résultats sur ce sujet.

De plus, j'ai récemment commencé à utiliser pour la comparaison de la GSMF (présentée dans cette thèse), les données HSC (Aihara et al. 2017) dans les intervalles de décalage spectroscopique vers le rouge les plus élevés (échantillonnés dans le Chapitre 5).

Une poursuite naturelle de l'analyse présentée est de compléter l'étude des propriétés spectrales des galaxies en fonction de la LD, suivant le schéma de l'analyse conduite sur l'environnement *global*. La possibilité de combiner la multitude d'informations qui dérive des spectres de galaxies et de la photométrie est fondamentale pour la détermination de l'échelle temporelle du quenching et des processus qui conduisent à l'arrêt de la formation stellaire. Une analyse détaillée de la présence d'une population de galaxies post-starburst, c.-à-d. une population de galaxies qui sont récemment devenues passives, serait également fondamentale pour comprendre le processusdominant conduisant à la formation de la population passive dans des environnements différents.

Le sondage XXL offre aussi un échantillon unique de superamas, qui permet l'étude systématique de l'influence et de l'abondance de ces objets et, plus géneralement, qui permet d'investiguer l'évolution des galaxies membres de ces structures à très grande échelle.

En outre, la disponibilité d'un code de spectral fitting si efficace permet d'explorer une approche complémentaire, en traçant l'histoire stellaire des galaxies individuelles, et d'étudier comment l'histoire de la formation stellaire s'est déroulée dans les groupes et les amas en rayons X, et dans des accroissements de different ampleur en termes de densité locale de galaxies. Cette technique était déjà utilisée dans Guglielmo et al. (2015) pour un échantillon de galaxies à bas décalages vers le rouge dans les amas et dans le champ. Cela permettrait également de comparer avec la population de l'Univers local.

Enfin, pour compléter le scénario, je prévois de comparer les observations avec des simulations. Ce projet va ouvrir un nouveau domaine par rapport à ce qui a été réalisé dans cette thèse, et à cet égard, nous commençons à collaborer avec deux groupes de simulations: le projet EAGLE (Schaye et al. 2015, et en particulier Katsianis et al. 2017 sur la comparaison entre les théories et les prédictions sur l'évolution du SFR), et les simulations IllustrisTNG (Pillepich et al. 2018).

# Publications

## First author publications

**(1) Guglielmo, V.**, Poggianti, B. M., Moretti, A., Fritz, J., Calvi, R., Vulcani, B., Fasano, G., and Paccagnella, A. (2015).
*The star formation history of galaxies: the role of galaxy mass, morphology and environment.*
MNRAS, 450, 2749.

**(2) Guglielmo, V.**, Poggianti B. M., Vulcani B., Adami C., Gastaldello F., Ettori S., Fotoupoulou S., Koulouridis E., Ramos Ceja M. E., Giles P., McGee S. and XXL collaborators (2017).
*The XXL Survey: XXII. The XXL-North spectrophotometric sample and galaxy stellar mass function in X-ray detected groups and clusters.*
A&A in press: arXiv:1710.04667.

**(3) Guglielmo, V.**, Poggianti B. M., Vulcani B., Moretti A., Fritz J., Gastaldello F., Adami C., Caretta C.A., Willis J., Koulouridis E., Ettori S., Ramos Ceja M. E., Giles P., and XXL collaborators (2018a).
*The XXL Survey: XXX. Characterisation of the XLSSsC N01 supercluster and analysis of the galaxy stellar populations*
A&A submitted.

**(4) Guglielmo, V.**, Poggianti B. M., Vulcani B., and XXL collaborators (2018b).
*The role of the environment in shaping the stellar population properties of galaxies at $0.1<z<0.5$.*
In preparation.

**(5) Guglielmo, V.**, Poggianti B. M., Vulcani B., and XXL collaborators (2018c).
*The star formation history and stellar mass assembly history of galaxies at $0.1<z<0.5$ as*

*a function of global and local environment.*
In preparation.

## Other publications

**(6)** Farahi A., **(5) Guglielmo, V.**, Evrard A. E., Poggianti B. M., Adami C., Ettori S., Gastaldello F., Giles P.A., Maughan B.J., Rapetti D., Sereno M., and XXL collaborators (2017).
*The XXL Survey: XXIII. The Mass Scale of XXL Clusters from Ensemble Spectroscopy*
A&A in press: arXiv:1711.07066.

**(7)** Adami C., Giles P., Koulouridis E., Pacaud F., Caretta C.A., Pierre M., Eckert D.,Ramos Ceja M. E., Gastaldello F., Fotoupoulou S., **Guglielmo V.**, and XXL collaborators (2017).
*The XXL survey: XX. The 365 cluster catalogue*
A&A in press.

**(8)** Chiappetti L., Fotopoulou S., Lidman C., Faccioli L., Pacaud F., Elyiv A., Paltani S., Pierre M., Adami C., Alis S. , Altieri B. , Baldry I., Bolzonella M., Bongiorno A., Brown M., Driver S., Elmer E., Franzetti P., Grootes M., **Guglielmo, V.** and XXL collaborators (2017).
*The XXL survey: XXVII. The 3XLSS point source catalogue.*
A&A submitted.

**(9)** Pierre M., Adami C., Birkinshaw M., Chiappetti L., Ettori S., Evrard A., Faccioli L., Gastaldello F., Giles P., Horellou C., Iovino A., Koulouridis E., Lidman C., Le Brun A., Maughan B., Maurogordato S., McCarthy I., Miyazaki S., Pacaud F., Paltani S., Plionis M., Reiprich T., Sadibekova T., Smolcic V., Snowden S., Surdej J., Tsirou M., Vignali C., Willis J., Alis S., Altieri B., Baran N., Benoist C., Bongiorno A., Bremer M., Butler A., Cappi, A. Caretta C., Ciliegi P., Clerc N., Corasaniti P. S., Coupon J., Delhaize J., Delvecchio I., Democles J., Desai Sh., Devriendt J., Dubois Y., Eckert D., Elyiv A., Farahi A., Ferraril C., Fotopoulou S., Forman W., Georgantopoulos I., **Guglielmo, V.** and XXL collaborators (2017).
*The XXL survey: First results and future.*
A&A 338, 334.

**(10)** Pierre M., Pacaud F., Adami C., Alis S., Altieri B., Baran N., Benoist C., Birkinshaw M., Bongiorno A., Bremer M., Brusa M., Butler A., Ciliegi P., Chiappetti L., Clerc N., Corasaniti P. S., Coupon J., De Breuck C., Delhaize J., Delvecchio I., Democles J., Desai Sh., Devriendt J., Dubois Y., Eckert D., Elyiv A., Ettori S., Evrard A., Faccioli L., Farahi A., Ferrari C., Finet F., Fotoupoulou S., Fourmanoit N., Gandhi P., Gastaldello F., Gastaud R., Georgantopoulos I., Giles P., Guennou L., **Guglielmo V.**, and XXL

collaborators (2016).
*The XXL Survey: I. Scientific motivations - XMM-Newton observing plan - Follow-up observations and simulation programme.*
A&A 592, A1.

# 1 ASTROPHYSICAL CONTEXT

In this chapter I will give an overview of the main astrophysical topics that are important for the contextualisation and development of this thesis. The first section is dedicated to the presentation of the world model predicting the formation and evolution of the structure in the Universe starting from the small primordial density fluctuation at the era of recombination, under the action of gravity. The observable Universe made of stars and galaxies, which are gathered in more and more massive structures from groups, to clusters and superclusters, forms within dark matter halos where the star formation process takes place since the very early phase of the Universe, from the cooling and collapse of molecular gas. Star formation builds up the wide variety of galaxies that are observed today, which evolve together with the structures in which they are embedded. The introduction proceeds with the detailed description of observables and measurable quantities used to describe the galaxy population and its interaction with environment. Galaxies experience a variety of environments from their birth and during their entire lifetime. The interaction with the potential well of the structure they're embedded in and/or with the other member galaxies, as well as the physical processes triggered by the hot gas permeating massive galaxy systems, may affect their observed properties. The physical processes acting in dense environments such as groups and clusters and their influence on galaxy stellar activity, dynamics and morphology are also described in this chapter. Finally, observational evidences, constraints and methodologies used in the literature and which will be implemented throughout this thesis to unveil the main unresolved questions on galaxy evolution related to environment are presented from an observational perspective.

## 1.1 Structure and galaxy formation

The formation and evolution of structures from small to large scale is determined by the dominant force in the Universe, gravitation. The accepted theory of gravitation is the theory of General Relativity, formulated by Albert Einstein in 1915 and based on two postulates: (1) our place in the Universe is not distinguished from other locations

and (2) the distribution of matter around us is isotropic, at least on large scales. World models following the so-called *cosmological principle*, stating that the Universe is spatially homogeneous and isotropic on large enough scales (the Friedmann-Lemaître models) obey the laws of General Relativity. The Universe that originates is not static and expands following the Hubble expansion law[1]. Essentially, these models are characterised by three parameters:

1. the current expansion rate of the Universe, quantified through the Hubble constant $H_0$;

2. the current mean matter density of the Universe $\rho_m$, often parametrised by the dimensionless density parameter

$$\Omega_m = \frac{8\pi G}{3H_0^2}\rho_m \tag{1.1}$$

3. and the density of the so-called vacuum energy, described by the cosmological constant $\Lambda$ or by the corresponding density parameter of the vacuum

$$\Omega_\Lambda = \frac{\Lambda}{3H_0^2} \tag{1.2}$$

According to the Friedmann-Lemaître models, the Universe used to be smaller and hotter in the past, and cools down continuously as an effect of the expansion. If we assume that the known laws of physics were also valid in the past we can trace back the cosmic expansion and get the Big Bang model of the Universe, according to which our Universe has evolved out of a very dense and very hot state, the so-called Big Bang.
According to this world model, a number of theoretical predictions have been observationally verified (Schneider 2006):

1. The fraction primordial constituent atoms of the Universe is fixed by the "big-bang nucleosynthesis". Helium formed about three minutes after the Big Bang and contributes with about 25% and hydrogen about 73% with all other elements constituting less than 2%. The mass fraction of helium in metal-poor objects such as molecular clouds, the seeds of future star formation where the chemical composition has not been significantly modified by processes of stellar evolution, is about 24%.

2. The number of neutrino families is derived from the exact fraction of helium, in a relationship of direct proportionality: the more neutrino species exist, the larger the fraction of helium will be. The precise determination of the primordial helium abundance in the Universe enabled to constrain the number of neutrino types to three (Pagel 1988; Pagel & Simonson 1989; Olive et al. 1990), and this result was later confirmed by particle accelerator experiments.

[1]The Hubble law express the direct proportionality between the distance of galaxies and their recessional radial velocity as measured from the observer ($v = H_0 \cdot d$, where $v$ is the radial velocity given in km/s, $H_0$ is the Hubble constant and $d$ is the distance from the observer in Mpc).

3. In the first 300000 years after the Big Bang, the temperature of the Universe was high enough to allow the electrons and protons to be free and separated in a highly ionised plasma state. The matter plasma was opaque to electromagnetic radiation due to Thomson scattering by free electrons, which efficiently reduced the mean free path each photon could travel before being scattered by another electron. As a consequence expansion, when the Universe cooled to about 3000 K, the plasma combined to neutral atoms and photons started to propagate freely, the Universe became transparent as a consequence of *recombination* (z$\sim$1000). The first and oldest photons escaping at the epoch of recombination constitute the so called Cosmic Microwave Background (CMB) radiation. As a result of cosmic expansion, this radiation has cooled down to about $T_0 \sim 2.73$ K. This microwave radiation is nearly perfectly isotropic. The CMB was predicted in 1946 by George Gamow, and it was then discovered by Arno Penzias and Robert Wilson in 1965.

4. Direct observations reveal instead that the local Universe is far from a condition of general spatial homogeneity and isotropy and shows a tendency for the hierarchical aggregation of its components. The density of the structures increases in the vicinity of clusters but the great majority of the total volume of the Universe is in lower density regions. The reconciliation between this theoretical assumption and direct observations is possible when considering large enough spatial scales. Indeed, no evidence of structures with linear dimensions $\gtrsim 100\mathrm{h}^{-1}$Mpc have been found to date.

The presence of structures in the Universe on smaller scales finds its origin and physical explanation in the presence of small anisotropies in the density field of the Universe at the epoch of recombination, observed as temperature fluctuations of the order of $\Delta T/T \sim 10^{-5}$ in the CMB radiation. In fact, the COBE satellite was the first to observe these predicted anisotropies. Later experiments, especially the WMAP and Planck satellites, observed the structure of the microwave background at much improved angular resolution and verified the theory of structure formation in the Universe in detail. The low amplitude of the CMB anisotropies implies that the inhomogeneities must have been very small at the epoch of recombination, whereas today's Universe features very large density fluctuations, at least on scales of clusters of galaxies. Hence, the density field of the cosmic matter must have evolved, driven by gravitational instability, in that an overdense region withstands expansion due to its self-gravity. Therefore, any relative overdensity becomes amplified in time. The growth of density fluctuations in time will then cause the formation of large-scale structures, and the gravitational instability is also responsible for the formation of galaxies and clusters.
From a theoretical perspective, even though the formation and evolution of dark matter halos is unambiguously determined under the action of gravity, complex numerical simulations are needed to model the non linear interplay between gravity, gas pressure and radiation. Furthermore, important ingredients are still lacking when the baryonic component is taken into account and simulations are forced to rely on several physical assumptions.

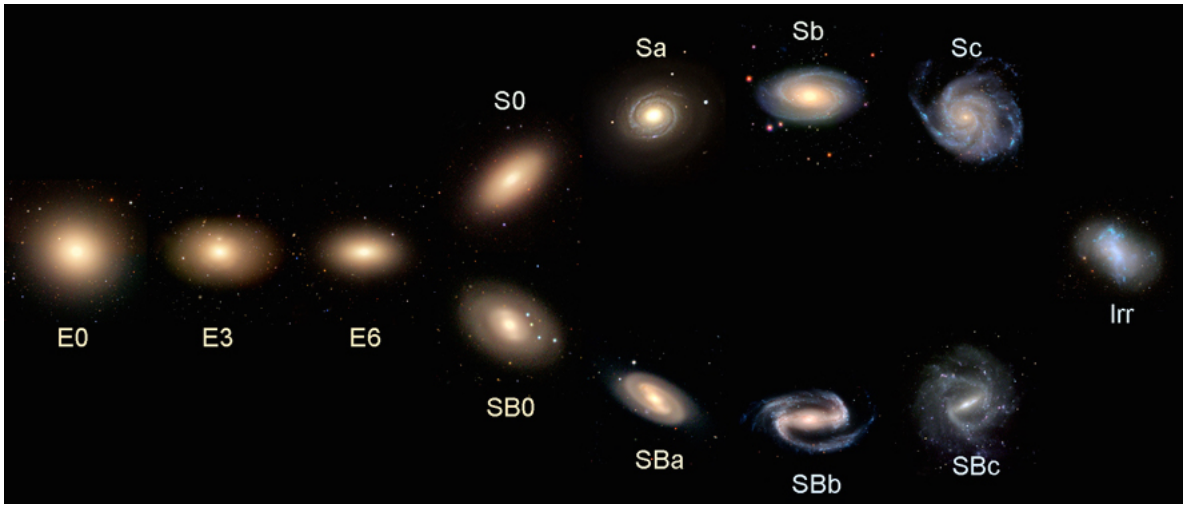


Figure 1.1: Schematic representation of the Hubble tuning fork of morphological classification (from GalaxyZoo.com). Galaxies are divided into ellipticals (E), lenticulars (S0s), spirals (without (S) and with (Sb) a bar) and irregulars.

Observations, in turn, suffer from the severe limitation that the spatial distribution of dark matter on large scale is not directly observable. Observables, i.e. stars and gas, constitute $\lesssim$20% of the total matter distribution and $\lesssim$5% of the total energy. In the context of structure evolution, the relation between the dark and luminous matter is currently only approximately understood and from an observational point of view this relation has to result from a detailed understanding of galaxy formation and evolution.
Historically, the reconciliation between the theoretical cosmological framework of structure formation and the observed properties of the galaxy population was not trivial. These diverse properties exhibited by galaxies are exemplified in the Hubble sequence classification scheme (Hubble 1926), which grouped galaxies of various morphologies into a tuning fork diagram (see figure 1.1) and distinguished four main types:

- Elliptical galaxies (E), characterised by spheroidal shape, massive and dominated by red/old stellar populations. Sub-classes are obtained on the basis of their ellipticity, i.e. the ratio between the major and minor axis;

- Lenticular galaxies (S0s) have smoothed light profiles dominated by a spheroidal bulge in the center and a lens/disc in the outskirts;

- Spiral galaxies (S) have a disc structure, are bluer due to young stellar populations from ongoing star formation, and are divided into barred and normal spirals depending on the presence of a bar. Sub-classes are obtained on the basis of the bulge to disc ratio and the characteristics of the spiral arms;

- Irregular galaxies are characterised by an irregular shape, sometimes with evidence of gravitational disruption in the form of tidal tails.

The idea that the relative timescale for star formation and for dynamical evolution are important for the origin of the Hubble sequence is an old one (Gott & Thuan 1976), and is based on the observational evidence that many properties of the galaxy population change along the sequence. Red elliptical "early-type" galaxies are the oldest and most massive galaxies, and preferentially inhabit dense regions of the Universe such as galaxy clusters, while blue star-forming "late-type" galaxies are less massive and more frequent in less dense regions of space (Dressler 1980, see section 1.7.1).

The model initially proposed for explaining this dichotomy is called "Monolithic collapse", represented in the left side of Figure 1.2, in which the formation of galaxies occurs at high-redshift from a rapid burst of star formation when massive gas clouds collapse (Eggen et al. 1962; Larson 1974, 1975), after which the galaxy passively evolve until the present day, with negligible additional star formation and/or morphological changes. This proposed scenario seemed to fit the characteristics exhibited by elliptical galaxies, which formed early in the Universe history and rapidly evolved, until their star formation ended.

Subsequent observational evidences did not confirm this scenario and lead instead to the so called "hierachical" paradigm, represented in the right side of Figure 1.2. This model predicts that smaller structures form first and then merge into larger systems ("bottom-up" formation scenario), though leaves some apparent inconsistencies with observations. Indeed, it has long been known that galaxies do not share this trend, at least in their star formation history. Moreover, the average mass of star forming galaxies declines with decreasing redshift. This phenomenon, named "downsizing" by Cowie et al. (1996), is not necessarily in contrast with the hierarchical clustering of dark matter halos. It has been suggested that internal feedback mechanisms could reconcile this anti-hierarchical behaviour of galaxies with the standard dark matter bottom-up model (Bower et al. 2006): the suppression of late gas condensation in massive halos due to the AGN activity gives rise to shorter formation timescales for more massive galaxies (De Lucia et al. 2006), while supernovae could efficiently delay the star formation in low mass systems, in qualitative agreement with the observed trends.

Finally, the results of the observations performed over the last decades favour a hybrid hierarchical model (Stanger 2009). The commonly adopted Universe model is the ΛCDM, it is grounded following the cosmological principle and provides a good explanation of the observed galaxy populations. In this hybrid model, which is a combination of the models outlined in Figure 1.2, cold dark matter halos collapse under the action of the gravitational force in correspondence of the initial density peaks in the dark matter flow, and galaxies form within halos from the cooling of hot gas from the very earliest times in the Universe. From that moment on, galaxies and their host halos are expected to evolve simultaneously, so that galaxy properties must be tightly correlated to the history of the halo. As already mentioned earlier in this chapter, the observed clumps of matter in the CMB are thought to have formed the cores of the first protogalaxies (or gas clouds) that would eventually mature into the galaxies we see in the Universe today. The first protogalaxies are thought to have merged to form larger structures. Stars formed in these larger structures and the first population of galaxies followed. Spheroidal shaped galaxies formed from these galaxies in case of merging events occurring during their condensation. As they condensed

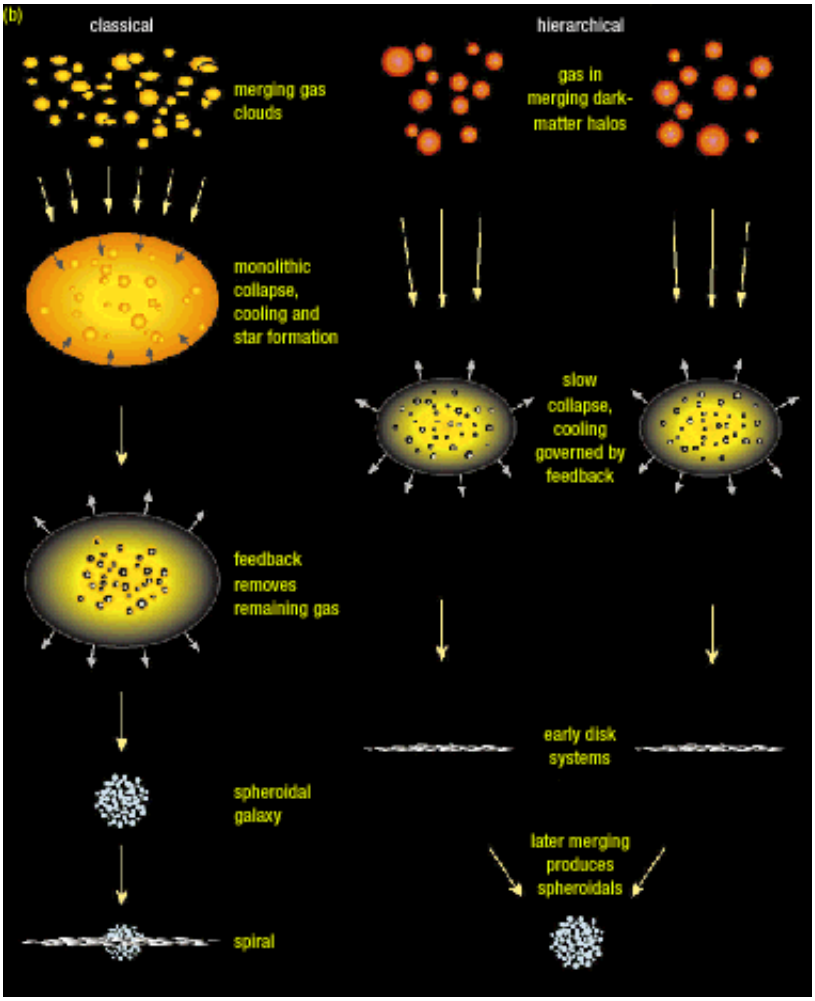


Figure 1.2: Schematic view of the two opposed models of structure formations proposed for explaining the population of galaxies observed in the nearby Universe. On the left side, the monolithic collapse model, on the right side the hierarchical structure formation scenario (Image source http://www.jeffstanger.net/Astronomy/galaxyformation.html).

further a disc would form leading to spiral galaxies, which today host spheroidal bulges at their centers as remnants of their past form. If major mergers only occurred after the time period of collapse then elliptical galaxies form. These spheroidal structures in galaxies contain approximately half the stars in the observable Universe and provide a valuable window into galaxy evolution.

Concerning theoretical studies in galaxy formation and evolution, a lot of effort has been invested in modelling gaseous collapse or accretion, with the aim of understanding the star formation process on one side, and the dynamical evolution leading to the observed shapes. In the hybrid hierarchical model, if gas collapses inwards (accretes) in a smooth fashion it builds discs and stars form slowly. The merger of these discs would lead to spherical

systems and if there is sufficient gas a slow accretion would again form a disc. One of the strengths of this model is that there is no prediction about the epoch of formation of the various galaxy types and galaxies can evolve through many forms throughout their history.
The main open questions of this branch of astrophysics regard the interplay among the physical star formation processes operating in the build up of galaxy stellar mass. In particular, significant effort has been invested in acquiring an overall view of which physical processes drive the star formation activity in galaxies and how this impacts their stellar history, observed properties, and to what extent these physical processes are related to the type of environment a galaxy inhabits.

## 1.2 Star formation process

The baryonic gas contained in the dark matter halos in which galaxies reside undergoes cooling processes on shorter timescales than the age of its parent halo. As a consequence, the gas is not supported by pressure anymore and starts streaming toward the halo center, increasing its density. In case of efficient cooling mechanisms, when the density of the gas overcomes the density of the dark matter in the halo center, the gas becomes gravitationally unstable and collapses. This cooling process can lead to the formation of cold and dense clouds (molecular clouds) in which star formation takes place. High resolution observations in the Milky Way and other nearby galaxies demonstrate that the star formation process occurs within such dense molecular clouds (Blitz 1993; Williams et al. 2000), and in particular several observational evidence support the connection between the overall rate of star formation of a galaxy and its capacity of generating dense molecular clouds. Furthermore, observations of the carbon monoxide (CO) line, the main observational probe of molecular clouds, in starburst[2] galaxies show that they are associated to the massive presence of molecular gas ($10^8 - 10^{10} M_\odot$) confined on small regions with dimensions typically lower than 2 kpc. Because relevant spatial and temporal timescales of the formation of single stars are short compared with the formation and evolution of galaxies, the star formation process can be studied in terms of statistical relations between the star formation rate and the global properties of the gas involved.
The star formation rate (SFR) is defined as the mass in stars per year generated by a galaxy, measured in $M_\odot\,yr^{-1}$. Given that observational indicators of star formation are all sensitive to the presence of massive stars, the extrapolation to the total SFR, which includes also the contribution of low mass stars, requires the assumption of an initial mass function (IMF). The IMF $\xi(M)$ is an empirical function that describes the mass distribution of a stellar population in terms of the initial mass of the stars, that is the mass they were formed with. Statistically, the IMF is proportional to the probability of a star to be formed with a certain mass within an ensemble of stars of the same age and same metallicity.

[2]A starburst galaxy is a galaxy undergoing high rates of star formation compared to the average timescales and rates of star formation in most other galaxies of the same mass.

The techniques developed for measuring the SFR evaluate the birth rate of massive stars ($M \gtrsim 10 M_{\odot}$), whose effective temperature during the main sequence phase is higher than ∼20000 K. Thus, the star formation process is associated with an intense UV radiation field. The energetic photons of this radiation ionise the hydrogen and other elements in the progenitor cloud, and further recombination produces strong emission lines, such as the Balmer (in the visual domain) and Lyman (UV) sequence lines. The UV radiation field is partially absorbed by the dust, which is abundant within the clouds where the star formation process takes place, and that radiates the energy absorbed at mid- and far-IR wavelengths. Finally, massive stars at the end of their evolutionary phase can explode as supernovae: relativistic electrons are accelerated as a consequence of the explosion and emit synchrotron radiation at radio frequencies. In case of binary systems, the accretion of SN remnants which are compact objects (neutron stars, black holes) originates X-ray radiation.
Furthermore, observations of the specific SFR, that is the SFR per unit mass, in galaxies of different stellar mass showed that the specific SFR of low mass galaxies is on average higher than that of high-mass ones. This is related to the *downsizing* effect: more massive galaxies formed a high fraction of their stellar mass in the elder epochs and on short timescales, while less massive galaxies have longer formation and evolution timescales (Cowie et al. 1996; Gavazzi et al. 2006; De Lucia et al. 2007; Sánchez-Blázquez et al. 2009).

## 1.3 Galaxy masses

Galaxy mass is a fundamental parameter that has be found to correlate with many other properties, such as galaxy colours, metallicity, internal structure, dynamics, and star formation. Two main definitions of galaxy mass can be adopted:

1. Stellar mass. By definition, for a given single stellar population (SSP) three different kinds of stellar mass can be distinguished (Renzini 2006; Longhetti & Saracco 2009):

   - The initial mass of the SSP, at age zero; this is nothing but the mass of gas turned into stars (M1);

   - The mass locked into stars, both those which are still in the nuclear-burning phase, and remnants such as white dwarfs, neutron stars and stellar black holes; it is commonly referred to as M2;

   - The mass of stars in the nuclear-burning phase; this value is called M3.

   It should be noticed that the difference between these three definitions is a function of the stellar age and of the IMF.

2. Dynamical mass. This definition is based on the relation existing between the rotational velocity or velocity dispersion of the systems and the radius within which the computation is performed. The dynamical mass accounts for the contribution

of stars, gas, and dark matter and can expressed by the formula $M_{dyn} = v^2 R/G$, where $R$ is the radius and G the gravitational constant. The computation of the velocity $v$ is performed by means of rotational curves in spiral galaxies and velocity dispersion for ellipticals. Therefore, the method requires the analysis of absorption and emission lines from galaxy spectra, which in most cases reduces its applicability.

Throughout my thesis, I will only consider stellar masses and, in particular, I will always adopt the definition M2.

### 1.3.1 Methods for the determination of stellar masses

The determination of galaxy stellar masses is of fundamental importance in the characterisation of a galaxy sample, and the most widely used methods are based on galaxy colours and spectral energy distribution (SED):

- **Correlation between absolute luminosity, stellar mass and colour.** The method is based on the use of precise spectrophotometric models for the determination of the correlation between the mass-to-light ratio of a galaxy and the optical colour of the integrated stellar population (Bell & de Jong 2001; Zibetti et al. 2009). The general relation can be expressed as

$$log(M/L_X) = a_X + b_X \times (X - Y) \tag{1.3}$$

where $X$ and $Y$ are two photometric bands in which absolute magnitudes are computed, $a_X$ and $b_X$ are tabulated constants which depend on the filters used, on galaxy colours and spectral type. The derived stellar mass is not biased by the systematics affecting dust-reddening estimates though it quite strongly depend on the IMF assumption. *In this thesis, this method is going to be applied for the computation of the stellar mass completeness limit in Chapter 3.*

- **SED fitting.** This method is based on the reconstruction of the SED of a galaxy by means of the comparison of photometric estimates in several observed filters or derived from a galaxy spectrum with empirical SED curves derived from theoretical libraries of SSP templates.
*SED fitting is going to be used throughout this thesis for estimating galaxy stellar masses in the sample of galaxies presented in Chapter 4.*

- **Full spectral fitting.** This method aims at reconstructing the main properties of a galaxy such as its stellar mass, star formation history and age starting from its observed spectrum. The spectrum is considered as to be the sum of the spectra of SSPs of different ages and contributing to the overall mass budget with a certain SFR over a period of time. The mass each SSP is responsible for is then added together, thus the final stellar mass of a galaxy is the integral over the time of the mass formed by each SSP.
*Stellar masses derived by means of full spectral fitting are also used in this thesis.*

It is important to notice that, overall, different methods of estimating stellar masses agree reasonably well within the errors (e.g. Bell & de Jong 2001; Bolzonella et al. 2010).

### 1.3.2 Specific SFR

The stellar mass can be linked to the SFR into the specific star formation rate (sSFR), that is the SFR per unit of galaxy stellar mass, i.e. sSFR = SFR/M. By definition, the sSFR dimensionally is the inverse of the time for a galaxy to double its stellar mass ($[sSFR] = yr^{-1}$). This quantity is an indicator of the contribution of the current star formation process to the stellar mass growth of galaxies. Low sSFRs indicate that the processes of star formation were more active in the past, while high sSFRs mean that a significant fraction of the stellar mass of the galaxy is currently being built.

## 1.4 Galaxy Environment

Galaxies do not randomly populate the Universe, and their spatial distribution is a consequence of the physical formation processes and of the tendency of structures to aggregate in overdense regions.
The parameters that are commonly used to define a galaxy environment can be subdivided in two broad categories: those related to the host halo of a galaxy (e.g. halo mass), and those describing the environment on local phenomena scales (e.g. local density or mass overdensity). In the first case they generally refer to *global* environment, in the second case to *local* environment.
According to the *global* environment definition, the most massive and most populous galaxy agglomerates are called galaxy clusters, while the less massive and less populous ones are called galaxy groups. The distinction among the two regards either the number of member galaxies, the imposition of an upper mass limit to the structure, or even systemic velocity dispersion. Clusters of galaxies are typically identified as galaxy associations with masses greater than $10^{14}M_{\odot}$ and velocity dispersion $\sigma \gtrsim 400$km/s, and with more than 50 bright members within a volume of few magaparsecs. Their high surface density and the elevated number of bright member galaxies make them identifiable at huge distances and particularly suitable as cosmological tracers. Groups have masses in the range $10^{12.5}M_{\odot} < M < 10^{14}M_{\odot}$ and velocity dispersions $\sigma \lesssim 400$km/s. Recent studies have found that the fraction of galaxies located in groups increases with cosmic time, up to the Local Universe values (Huchra & Geller 1982; Tully 1987; Eke et al. 2004b; Berlind et al. 2006; Knobel et al. 2009). Today, over 50% of galaxies are in groups, span a wide range in local density, and show properties that range from cluster-like to field-like (Zabludoff & Mulchaey 1998). Therefore groups are a key environment to investigate galaxy evolution and to provide a clear framework to study the nature of the physical mechanisms that lead to galaxy transformation. Even though galaxy groups are more numerous than more massive structures, they are much more difficult to detect because of their lower density contrast with respect to the background galaxy population. As clearly outlined

in Calvi et al. (2011), the difficulties in obtaining large, unbiased samples of groups have forced most studies to use small samples selected, for example, from the Hickson compact group catalogue (Hickson et al. 1989), from the CfA redshift survey (Geller & Huchra 1983; Moore et al. 1993), and from X-ray surveys (Henry et al. 1995; Mulchaey et al. 2003; Popesso et al. 2004). Only with the advent of large galaxy redshift surveys, such as the Two Degree Field Galaxy Redshift Survey (2dFGRS), the Sloan Digital Sky Survey (SDSS) and the Canadian Network for Observational Cosmology Redshift Survey (CNOC2), has it become possible to generate large group catalogues in the local Universe (e.g. Huchra & Geller 1982; Ramella et al. 1989, 1997; Hashimoto et al. 1998; Ramella et al. 1999; Tucker et al. 2000; Martínez et al. 2002; Balogh et al. 2004; Eke et al. 2004a; Calvi et al. 2011; Moustakas et al. 2013; Miniati et al. 2016) and at intermediate redshift (Carlberg et al. 2001; Wilman et al. 2005b; Giodini et al. 2012; George et al. 2013). At $z < 1$, for example, COSMOS (Scoville et al. 2007) is one of the most studied fields.

At optical wavelengths groups and clusters appear as over-densities of galaxies with respect to the field average density moving in a common gravitational potential well. However, the detection of groups and clusters of galaxies via spectroscopic surveys is affected by contamination due to projection effects. Since the development of X-ray imaging techniques of sufficient quality, high-mass groups and clusters have started to be identified as extended X-ray emitters. Their dark matter halos, in fact, have trapped hot plasma (intracluster medium, ICM) where the deflection of free electrons caused by the interaction with the electric field of protons produces the so-called *bremsstrahlung* radiation emitting at X-ray frequencies. Studies of dozens of galaxy clusters show that the X-ray luminosity of the hot gas increases with the total mass of the cluster, with typical X-ray luminosities in a wide range of values from $10^{43}$ to $10^{45}$ erg/s. This makes clusters the most luminous X-ray sources in the Universe, with the exception of quasars. The advantage of relying on this kind of observations for identifying structures in the Universe is the possibility of tracing the potential well in which galaxy processes related to environment occur, and directly measuring X-ray related quantities such as temperatures and luminosities which can be used as proxies for the mass of the halo.

Groups and clusters of galaxies, in turn, tend to cluster together in superclusters, which are the largest density enhancements originated by density perturbations on a scale of about 100 $h^{-1}$ Mpc ($\mathrm{H_0 = 100h\,km\,s^{-1}Mpc^{-1}}$) (see Bahcall & Soneira 1984 for the original definition), and which extend to tens of megaparsecs, tracing the large-scale structure of the Universe.

The largest and richest superclusters, which may contain several tens of rich (Abell) clusters, are the largest coherent systems in the Universe. At large scales a dynamical evolution takes place at a slower rate, and the richest superclusters have retained the memory of the initial conditions of their formation, and of the early evolution of structures (Kofman et al. 1987). Rich superclusters have high density cores that are absent in poor superclusters (Einasto et al. 2007). The core regions of the richest superclusters may contain merging X-ray clusters (Bardelli et al. 2000; Rose et al. 2002; Belsole et al. 2004). The formation of rich superclusters had to begin earlier than that of the smaller structures; they are the sites of early star and galaxy formation (e.g. Mobasher et al. 2005), and the

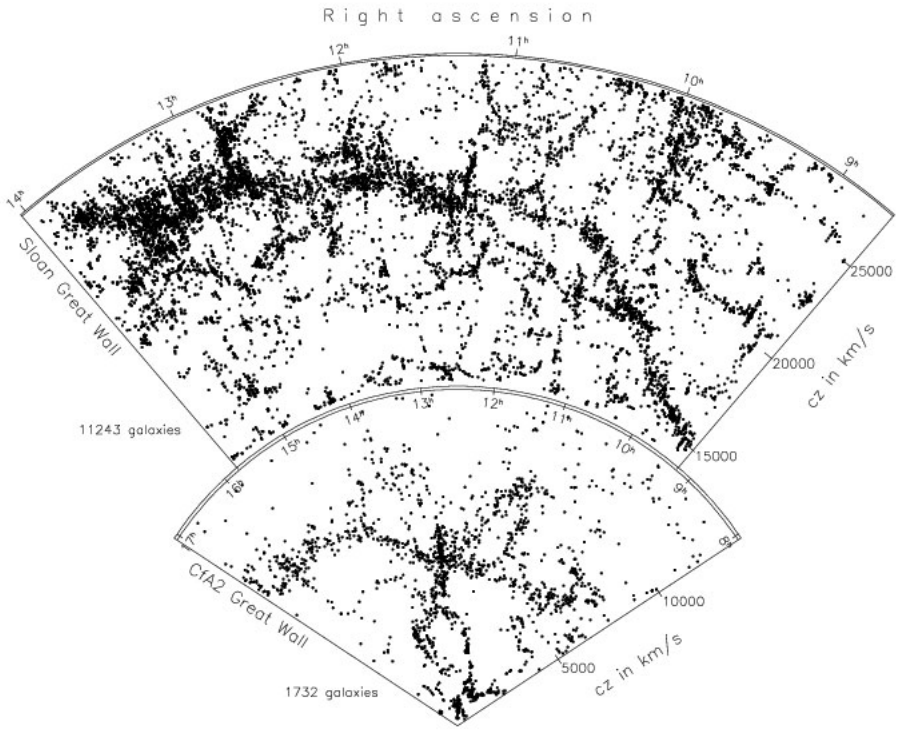


Figure 1.3: The image show the Universe up to 2 billion light years away from the Solar System (about 613 Mpc), as mapped by the Sloan Digital Sky Survey (SDSS York et al. 2000). The smaller image superposed is an earlier representation performed by the CfA redshift survey (Huchra & Geller 1982).

first places where systems of galaxies form (e.g. Venemans et al. 2004; Ouchi et al. 2005). The Sloan Great Wall (Figure 1.3) is the richest system of galaxies in the nearby Universe (Vogeley et al. 2004; Gott et al. 2005; Nichol et al. 2006). It consists of several rich and poor superclusters connected by lower density filaments of galaxies, representing a variety of global environments from the high density core of the richest supercluster in the SGW to a lower density poor supercluster at the edge of the SGW. The superclusters in the SGW differ in morphology and galaxy content, which suggests that their formation and evolution is diversified (Einasto et al. 2010). Furthermore, Einasto et al. 2010 analysed the presence of substructure in rich clusters, and found signs of possible mergers, infall or rotation that suggest that rich clusters in different superclusters of the Sloan Great Wall, including the cores of superclusters, are not yet virialised. Thus, the richest clusters in the SGW are still assembling.

A considerable amount of galaxies at all epochs, however, is distributed in low-density filamentary or sheets- like structures, and are usually called field galaxies. These structures usually surround large regions that contain very few, or no, galaxies, called voids.
Moving onto the definition of *local* environment, in the literature several authors usually propose *ad hoc* prescriptions either in terms of the local galaxy number density, that is the number of galaxies per unit volume or projected area around the galaxy of interest, and which can be calculated following several methods (e.g. Kovač et al. 2010; Cucciati et al. 2010; Muldrew et al. 2012; Vulcani et al. 2012; Darvish et al. 2015; Fasano et al. 2015). Specifically, the computation of projected local galaxy density (LD) is commonly used. It is usually derived from the circular area A that in projection on the sky encloses the N closest galaxies brighter than an absolute V magnitude $M_{lim}^{V}$ . The projected density is then $\Sigma = \mathrm{N/A}$ in number of galaxies per square megaparsec. The choice of the number of galaxies N depends on the redshift and is frequently assumed 5 for field samples (Tanaka et al. 2004) and 10 for cluster samples (Poggianti et al. 2008). Alternatively, a fixed aperture around any of the galaxies in the sample can be considered and the local density is then computed as the number of galaxies falling inside divided by the area of the aperture. *The last method is going to be used for computing the LD in this thesis.*

## 1.5 Physical processes acting in dense environments

Many processes come into play when a galaxy experiences the physical conditions occurring in a dense environment (Boselli & Gavazzi 2006; De Lucia et al. 2007; Boselli et al. 2016; De Lucia et al. 2010). These phenomena can be divided into three broad categories regarding the interaction between a galaxy and the cluster ICM, galaxy-galaxy gravitational interactions and tidal interactions between the galaxy and the cluster potential. Other mechanisms are also related to the presence of Active Galactic Nuclei (AGN) and the formation of the brightest cluster galaxy (BCG). An overview of the different regimes of action of most important processes is given in Figure 1.4 taken from Moran et al. 2007. A more detailed description of each of this phenomena and their characteristic timescale for the suppression of star formation in galaxies is given in the following paragraphs.

### 1.5.1 Interaction with the ICM

#### Gas starvation/strangulation

Current theories of galaxy formation suggest that when a galaxy is accreted onto a larger structure, the gas supply can no longer be replenished by cooling that is suppressed by the removal of the hot gas halo associated with the infalling galaxy (Larson et al. 1980; Balogh et al. 2000). This phenomenon is defined 'starvation' (or 'strangulation') and it is expected to affect a galaxy star formation history on a quite long timescale and therefore to cause a slow declining activity. This process was introduced to explain the transformation from spirals to S0s and represents an important element of semi-analytic models of galaxy formation. On time scales of a few Gyr, the star formation would exhaust the available

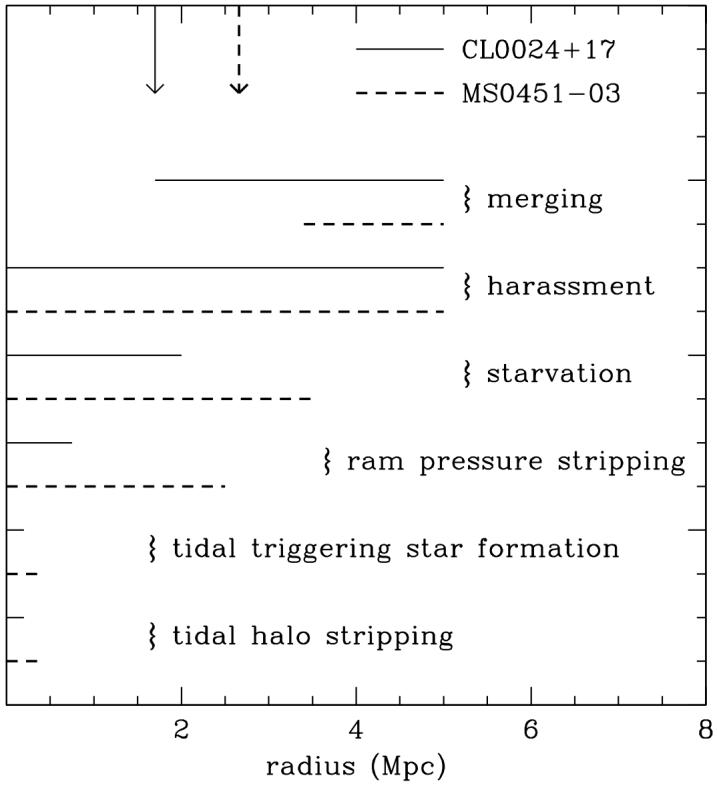


Figure 1.4: Diagram representing the radial range of action of the principal physical mechanisms responsible for the variation of galaxy properties in dense environments. Solid and dashed lines correspond to the two clusters studied by Moran et al. (2007).

gas, quenching further star formation activity. If this process is combined with a relatively efficient supernovae feedback, galaxies that fall into a larger system consume their cold gas very rapidly, moving onto the red-sequence on quite short timescales (De Lucia 2007). Strangulation has been proposed to be efficient also in galaxy-group interactions, where the halo gas stripping can remove warm and hot gas from a galaxy halo, and efficiently cutting off the gas supply for star formation (Larson et al. 1980; Cole et al. 2000; Balogh et al. 2000; Kawata & Mulchaey 2008).

### Ram pressure stripping

Galaxies travelling through a dense ($10^{-3} - 10^{-4}$atoms cm$^{-3}$) and hot ($10^7 - 10^8$ K) ICM suffer a strong ram-pressure stripping that can sweep cold gas out of the stellar disc (Gunn & Gott 1972). Depending on the binding energy of the gas in the galaxy, ram-pressure stripping can effectively remove the interstellar medium (ISM) if it overcomes the gravitational pressure anchoring the gas to the disc. Ram-pressure stripping is expected to be more important at the center of massive clusters because of the large relative velocities and higher densities of the intra-cluster medium (De Lucia 2007). The efficiency of this

process depends on several factors, such as the inclination of the galaxy disc with respect to trajectory (face-on interactions are more efficient) or the type of orbit, with radial orbits being more effective due to the higher velocities. Moreover, ram pressure is expected to be more active in removing gas from low mass objects than from massive spirals. Extreme examples of gas stripping are the so-called 'jellyfish galaxies' (e.g. Fumagalli et al. 2014; Fossati et al. 2015; Ebeling et al. 2014; Poggianti et al. 2016, 2017). Before leading to a complete gas ablation, ram pressure produces significant compression ahead of the galaxy and the possible formation of 'tentacles' of material behind the main body of the galaxy.

#### Thermal evaporation

Another mechanism to slow down the star formation rate of galaxies is thermal evaporation of the cold gas in disc galaxies via heat conduction from the surrounding hot ICM (Cowie & Songaila 1977; Cowie et al. 2003). If the ICM temperature is high compared to the galaxy velocity dispersion, at the interface between the hot ICM and the cold ISM, the temperature of the ISM rises rapidly and the gas evaporates. The mass loss rate is proportional to the dimension of the galaxy and to the density and temperature of the ICM. A typical galaxy (with a radius of 15 kpc and $5 \times 10^9 M_\odot$ of atomic gas) can be completely stripped on timescales of the order of some $10^7 - 10^8$ yr.

### 1.5.2 Galaxy-galaxy gravitational interactions

#### Mergers

Galaxy mergers and more in general strong galaxy-galaxy interactions are rare phenomena in massive clusters because of the high velocity dispersion of these systems. Galaxy interactions are expected to be common in groups in which the velocity dispersion is typically not much larger than that of the constituent galaxies (Hashimoto et al. 1998; Severgnini & Saracco 2001). Thus, mergers in the infalling group environment may represent an important 'pre-processing' step in the evolution of cluster galaxies. Close tidal encounters among group member galaxies can strongly alter the galaxy structure (Toomre & Toomre 1972) and may result in star-formation quenching. Specifically, numerical simulations (Mihos 2004) have shown that close interactions can lead to a strong internal dynamical response driving the formation of spiral arms and, in some cases, of strong bar modes. Sufficiently close encounters can completely destroy the disc, leaving a remnant whose properties resemble those of an elliptical galaxy. This phenomenon drives the gas toward the center of galaxies, where it can trigger a burst of star formation and fuel the central black hole, the feedback from which can heat the remaining gas and eventually quench star formation.

#### Harassment

Galaxy harassment is a mechanism that strips a galaxy of part of its mass and drives a morphological transformation as a consequence of repeated fast encounters, coupled

with the effects of the global tidal field of the cluster (Spitzer & Baade 1951; Farouki & Shapiro 1981; Moore et al. 1996, 1998). A detailed study on the impact of harassment in the properties of galaxies was conducted in Moore et al. (1996), which concluded that harassment has the potential to change any internal property of a galaxy within a cluster, including the gas distribution and content, the orbital distribution of stars, and the overall shape. It is expected to have an important role in the formation of dwarf ellipticals, in the transformation of gas-rich spirals into gas-poor lenticular galaxies, or in the destruction of low surface brightness galaxies in clusters, but is less able to explain the evolution of luminous cluster galaxies. In addition, at the typical velocity dispersions of bound groups, galaxy-galaxy harassment (i.e. frequent galaxy encounters) leads to the morphological transformation of disc galaxies. Indeed, it results in the loss of the galaxy's gaseous component, partly ablated and partly falling into the center, entailing a dramatic conversion of discs into spheroidals.

### 1.5.3 Tidal interactions with the cluster potential

Not only tidal interactions between galaxies can induce some relevant perturbation, but also tidal interactions between galaxies and the whole cluster potential, inducing gas inflow, bar formation, nuclear and perhaps disc star formation. Models by Fujita (1998); Valluri (1993); Henriksen & Byrd (1996) showed that tidal compression of galactic gas via interaction with the cluster potential can accelerate molecular clouds of disc galaxies falling towards the core, increasing the star formation rate. The efficiency of this process depends on the cluster to galaxy mass ratio, the distance of the galaxy from the center and the galaxy radius. The first galaxies to experience this kind of interaction are large galaxies passing within few hundreds of kpc of the cluster center. The net result could be a first increase of the nuclear activity of cluster galaxies and eventually a decrease of the total gas consumed through star formation events, while a complete removal of the gas due directly to the interaction is unlikely. At group scales, the combinations of tides and ram pressure stripping efficiently remove the gas from spirals, quenching the star formation in galactic discs, while triggering it in the arms and at the leading edge of gaseous disc, with the net result of a suppression of star formation on timescales of several Gyr (Moore et al. 1996).

### 1.5.4 Pre-processing in groups

It is important to notice that many of the physical processes outlined above acting at the level of group environment are relevant because of the so called 'pre-processing' phase a galaxy undergoes when it falls into a group that is successively accreted by a cluster. In numerical simulations, in fact, massive clusters have accreted up to 50% and 45% of their stellar mass and galaxies, respectively, through galaxy groups (McGee et al. 2009). Hence, being fundamental building blocks of both mass and galaxy population in clusters, galaxy groups could play a significant role in shaping the evolution of cluster galaxies as well, if confirmed to be favourable locations for star formation quenching.

## 1.6 Major drivers of galaxy evolution

From an observational perspective, to address outstanding questions on the evolution of galaxies one needs homogeneous and sizeable galaxy samples, covering a wide redshift range, and with reliable measurements of galaxy rest-frame colours, luminosities and masses. The evolutionary history of isolated galaxies - by definition free as much as possible from environmental influences - can then be used as the benchmark for exploring the presence of environment-dependent influences taking place in group and cluster galaxies. Over the last decades, the advent of large surveys of galaxies from low- to high- redshifts and in all environments allowed to inspect a wide variety of galaxy populations and constraint galaxy properties over the cosmic epochs, improving our understanding of the processes that shape galaxies.

The question of which variables are needed to fully define galaxy evolution is usually considered in terms of either *nature* or *nurture* processes. This corresponds to asking whether galaxy evolution is driven mainly by internal processes and characteristics, imprinted at galaxy birth, or environment has a specific effect in shaping galaxy evolution, because of specific mechanisms taking place in dense regions, where external influences have better chances to be relevant. Among a galaxy internal properties, galaxy stellar mass is considered the main contributor, as galaxies are characterised by a wide range of total stellar masses whose role in the determination of galaxy properties is crucial. For example, Kauffmann et al. (2003) found that colour, specific star formation rate, and internal structure are strongly correlated with galaxy stellar mass. Among external processes, the major actors are considered to be the environment in which a galaxy is found during its lifetime and mergers.

Several works in the literature have tried to disentangle between the dichotomy of the *nature* versus *nurture* paradigm, and convincing results have been obtained on their relative importance at different cosmic epochs and galaxy stellar mass regimes.

This concept is represented in a very intuitive way in the left panel of Figure 1.5 from Peng et al. (2010), in the context of the build-up of the passive population. Galaxy stellar mass leads the quenching of star formation at all cosmic epochs above a certain stellar mass (which slowly increases with time), while the low-mass regime is dominated by environmental quenching in the recent history of the Universe ($z<0.5$) and by merging processes in the past. Focusing on galaxies in the local Universe, the diagram is observationally motivated by the trends represented in the right panel of Figure 1.5. In the figure, which analyses a sample of low-redshift galaxies in the Sloan Digital Sky Survey (SDSS, York et al. 2000), the variation in the fraction of red galaxies is represented as a function of environment, parametrised as local overdensity of galaxies, and stellar mass. It emerges that galaxies become redder in any given environment when increasing their stellar mass, and in turn, the red fraction increases when galaxies reside in denser environments at fixed stellar mass.

These results are supported by many studies in the literature which found that environment seems to be more relevant for lower mass galaxies, at least as far as quenching is concerned: galaxies in denser environments tend to be redder than galaxies in less dense

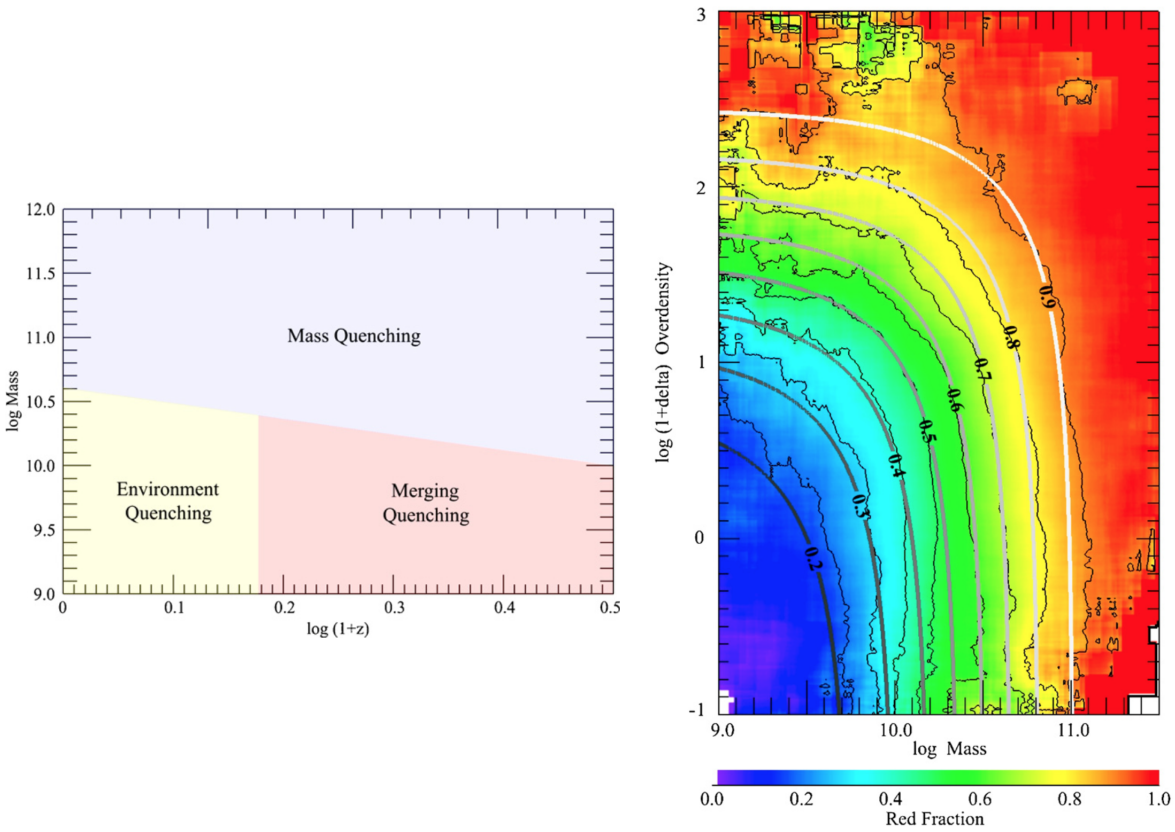


Figure 1.5: Left panel: Diagram showing the dominant mechanism for the quenching of galaxies as a function of mass and redshift in typical environments (Peng et al. 2010). According to the authors, merging and environmental quenching reflect both the underlying merger of dark matter halos. Right panel: Fraction of red galaxies in the SDSS sample studied in Peng et al. 2010 as a function of stellar mass and environment.

environments (Haines et al. 2007; Cooper et al. 2010; Pasquali et al. 2010; Peng et al. 2010, 2012; McGee et al. 2011; Sobral et al. 2011; Muzzin et al. 2012; Smith et al. 2012; Wetzel et al. 2012; La Barbera et al. 2014; Lin et al. 2014; Vulcani et al. 2015). In contrast, on average, more massive galaxies have formed their stars and completed their star formation activity at higher redshift than less massive galaxies, regardless of environment.

However, it has become more and more evident that in general, a detailed quantification of the influence of different environmental physical processes is complicated by the fact that one cannot easily separate "nature" from "nurture" (De Lucia et al. 2012), as well as the controversy regarding the primacy of *stellar mass versus environment*. According to what previously described in detail in Section 1.1, in fact, dark matter collapses into haloes in a bottom-up fashion: small systems form first and subsequently merge to form progressively larger systems. As structure grows, galaxies join more and more massive systems, therefore experiencing a variety of environments during their lifetime. In this

context, the nature-nurture debate appears to be ill posed, as these two elements of galaxy evolution are inevitably and heavily interconnected (De Lucia et al. 2012).
As for the nurture scenario, the bunch of physical processes illustrated in Section 1.5 might be effective in suppressing star formation and affecting the morphology of cluster galaxies. In principle, they should be coupled with a *history bias* that is an integral part of the hierarchical structure formation of cosmic structure. Until about a decade ago, this effect was believed to play a minor role: early numerical work found no dependence of the clustering of dark matter haloes on their properties, such as concentration or formation time (Lemson & Kauffmann 1999; Percival et al. 2003). Taking advantage of high-resolution simulations, however, recent studies have demonstrated that halo properties like concentration, spin, shape and internal angular momentum exhibit clear environmental dependencies (e.g. Avila-Reese et al. 2005). Haloes in overdense regions form statistically earlier and merge more rapidly than haloes in regions of the Universe of average density (Gao et al. 2005; Maulbetsch et al. 2007). This differential evolution is bound to leave an 'imprint' on the observable properties of galaxies that inhabit different regions at any cosmic epoch. In this context, a crucial missing ingredient for a correct interpretation of the observed environmental trends is represented by a detailed characterisation and quantification of the *environmental history* of group and cluster galaxies.

## 1.7 The variation of galaxy properties with environment

### 1.7.1 Morphology-Density relation

The first observational evidence in nearby clusters quantifying systematic differences of galaxy properties with local environment is the so called morphology-density relation (MDR). The MDR is the observed variation of the proportion of different Hubble types with local density, with ellipticals being more common in high-density regions, spirals being more common in low-density regions, and S0s remaining constant over the total population within the cluster virial radius regardless of density (Dressler 1980; Dressler et al. 1997). Figure 1.6 represents recent results regarding the MDR of galaxies in a sample of nearby clusters (WINGS) as a function of the projected LD, computed using the 10 nearest neighbours of the galaxy sample with $M_V$ <-19.5. In general, whereas about 70% of field galaxies are spirals, clusters are dominated by early-type galaxies, in particular in their inner regions. Furthermore, the fraction of spirals in a cluster depends on the distance to the center and increases for larger radii. Results obtained in the SDSS showed that the fraction of spirals decreases from ∼65% at low densities to about 35% in regions of high galaxy density. In contrast, the fraction of ellipticals and S0 galaxies increases toward higher densities, with the increase being strongest for ellipticals. A qualitatively similar, but quantitatively different MDR is present in galaxy clusters up to z=1 (Dressler et al. 1997; Treu et al. 2003; Postman et al. 2005). At redshift z ∼ 1, Tasca et al. (2009) instead did not find any variation in galaxy morphology (i.e. early versus late type) as a

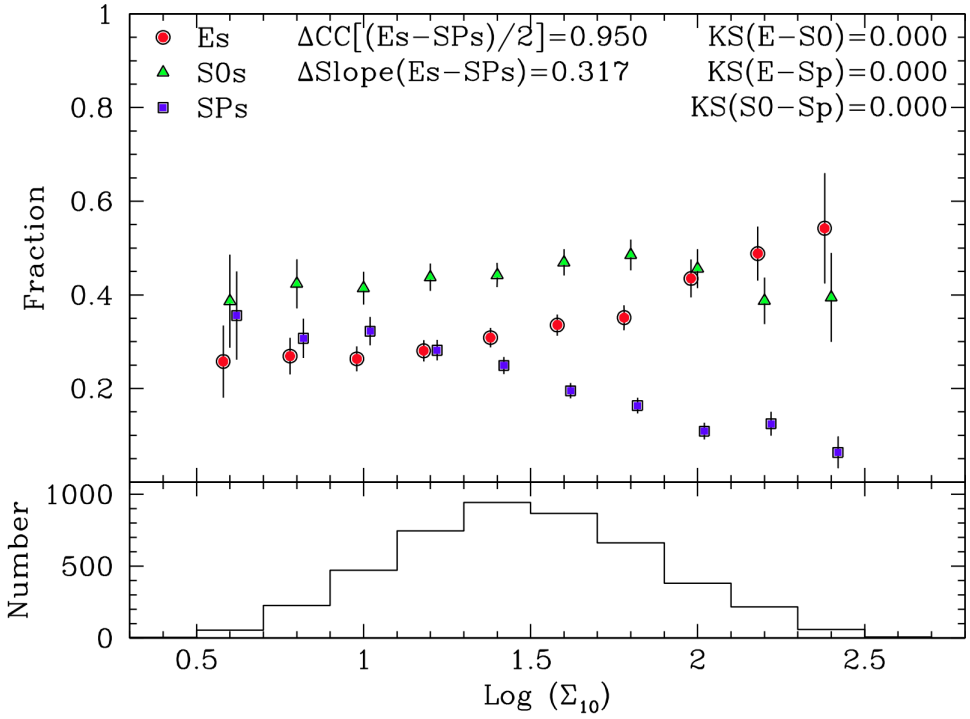


Figure 1.6: Relation between the morphological type T and the local density of galaxies (upper panel) and histogram of local density (lower panel) in low-redshift galaxies with $M_V$ <-19.5 belonging to WINGS clusters. Full red dots, green triangles and blue squares refer to elliptical (E), lenticular (S0) and spiral (SP) galaxies, respectively (from Fasano et al. 2015).

function of local galaxy density for $\log(M/M_\odot) > 10.5$.

It was subsequently found that a similar MDR also exists in nearby groups (Postman & Geller 1984; Postman et al. 2005), with the late-type fraction increasing with increasing mass of the group and the early-type fraction increasing with decreasing distance to the group center. Differences from the MDR of clusters were detected in low-redshift X-ray selected groups: massive groups have lower percentages of spirals than clusters (Helsdon & Ponman 2003), while compact groups have higher spiral fractions (Mamon 1986; Hickson et al. 1988). This piece of evidence triggered many studies that investigated whether pre-processing in groups could lead to the observed evolution in the MDR, directly acting on the formation of the S0 population. Thus, the cluster population that was accreted from groups should present similar trends. Wilman et al. (2009) analysed the morphological composition of galaxies in CNOC2 groups (Wilman et al. 2005b), a sample of ∼200 kinematically selected galaxy groups detected by means of a friends-of-friends percolation algorithm at 0.12<z<0.55, with the aim of addressing directly the importance of S0 formation in galaxy groups at intermediate redshift, finding indeed a much higher fraction of S0s in groups than in the lower density field. The fraction of elliptical galaxies at fixed

luminosity is not significantly enhanced in groups compared to the field and finally spiral galaxies have a strong suppression in groups. Optical and X-ray groups show at least the same fraction of S0s compared to cluster in a wide range of redshifts from z∼0 to z∼0.8 (Dressler 1980; Dressler et al. 1997; Fasano et al. 2000), as well as the lack of any strong radial trend. Wilman et al. (2009) concluded that pre-processing in low-mass groups is likely to dominate the formation of S0s, leading to an evolution in the global and cluster S0 fraction as more S0s are formed and accreted onto clusters by the present day.

### 1.7.2 SFR/sSFR mass relations

One way to shed light on the processes responsible for quenching is to compare the SFR of galaxies of a given stellar mass in different environments. The existence of a strong correlation between SFR/sSFR and stellar mass has been established from z = 0 out to at least z ∼ 3, with a roughly constant scatter of ∼0.3 dex out to z∼1 (Brinchmann et al. 2004; Daddi et al. 2007; Noeske et al. 2007; Salim et al. 2007; Vulcani et al. 2010; Rodighiero et al. 2011; Whitaker et al. 2012; Sobral et al. 2014; Speagle et al. 2014). The locus of points in which galaxies are located according to this tight relation is called 'main sequence' (MS). The smooth evolution of this dominant MS galaxy population suggests that most galaxies form stars through secular processes by gas accretion from the intergalactic medium. Thus, the evolution of the cosmic star formation history (SFH) is primarily determined by a balance between gas accretion and feedback processes, both closely related to galaxy mass, while stochastic events such as merger-driven starbursts play a relatively minor role. Outliers above the MS are defined as starbursts (e.g. Rodighiero et al. 2011). Star formation episodes in these galaxies are violent and rapid, likely driven by mergers (e.g. Elbaz et al. 2011; Wuyts et al. 2011; Nordon et al. 2012). Despite the much more vigorous star formation activity observed in starbursts, according to recent studies (e.g. Rodighiero et al. 2011; Sargent et al. 2012; Lamastra et al. 2013), these galaxies account for only ∼10% of the cosmic SFR density at z∼2. Since at any redshift most of the galaxies are located on the MS, most studies cannot investigate the dependence of physical quantities (e.g., dust content) on stellar mass and SFR independently, since these two quantities are degenerate along the MS.

On average, galaxies on this 'star formation sequence' were forming stars at much higher rates in the distant universe relative to today (e.g. Madau et al. 1996); for a given mass, the SFR has been decreasing at a steady rate by a factor of ∼30 from z∼2 to z=0 (Daddi et al. 2007), although it appears to be roughly constant from z∼7 to z∼2 (González et al. 2010). Whitaker et al. (2012) found that the slope of the SFR-mass relation evolves gradually with z while the normalization has a stronger evolution, as it is shown in Figure 1.7.

Different relations can be found in the literature, and many of these differences may arise from different criteria used to select star-forming galaxies. Actually, it is well known that a significant fraction of galaxies have very low SFRs, well below the star formation sequence. Furthermore, there exists a population of dusty star-forming galaxies with similar rest-frame optical colours to these quiescent galaxies. The selection of star-forming galaxies

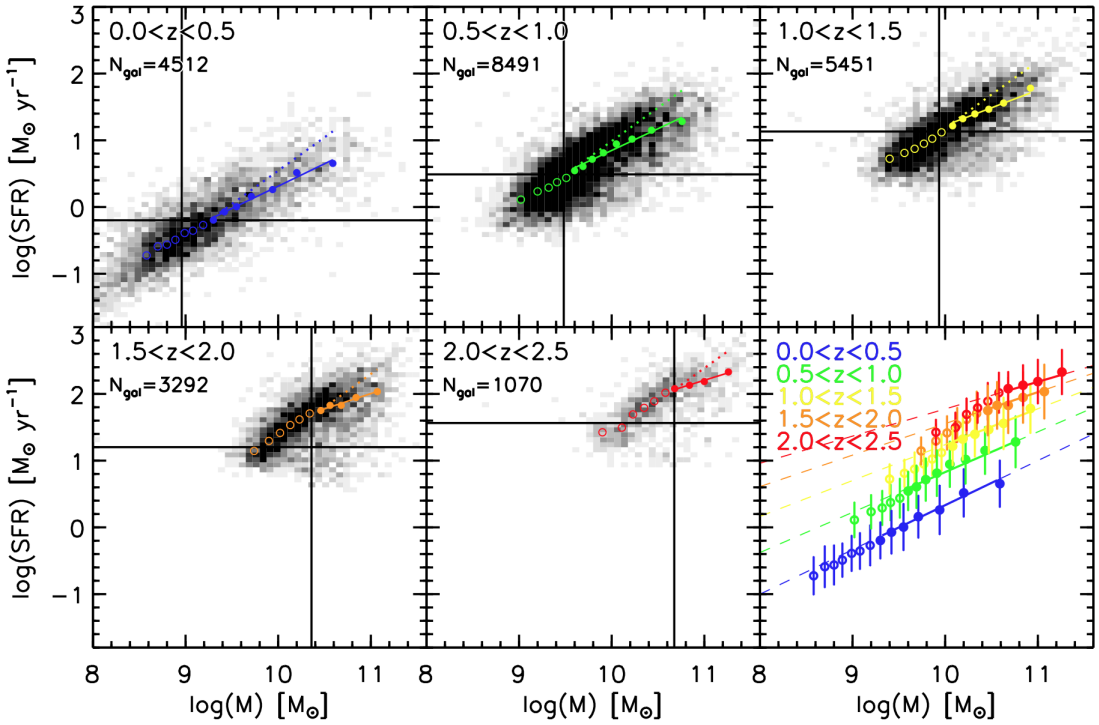


Figure 1.7: Figure 1 in Whitaker et al. (2012): SFR mass sequence for star-forming galaxies with a nonlinear slope at 0<z<2.5 (dotted line is linear in the logarithmic plane). The running medians and scatter are colour-coded by redshift, with a power-law fit above the mass and SFR completeness limits (solid lines in bottom, right panel).

and the treatment of quiescent galaxies can influence the measured relation and its scatter. Besides the selection criteria to cull star-forming galaxies, such differences include the SFR and mass diagnostics, and in particular the star formation histories adopted for the SED fits. Studies based on local samples (Brinchmann et al. 2004; Salim et al. 2007; Elbaz et al. 2007, for the SDSS) have illustrated a relationship between the SFR and stellar mass at low-z and have identified two populations: galaxies on a star-forming sequence and 'quenched' galaxies with little or non detectable SFR.

Since the SFR-Mass relation is the result of the balancing of inflows of cosmological gas and outflows due to the feedback it is expected to be sensitive to any physical mechanism affecting the amount of gas available for star formation. Lin et al. (2014), Jian et al. (2017) found for example that the sSFRs of star forming galaxies in the clusters are only moderately lower than those the field (< 0.2-0.3 dex) and the difference becomes insignificant at groups scales. Similarly, Peng et al. (2010) and Wijesinghe et al. (2012), using local galaxy field samples, showed that the local density mostly changes the fraction of passive galaxies but has little effect on the SFR-Mass relation.

This implies that the quenching of star formation is a relatively fast transition. On the other hand, von der Linden et al. (2010, z<0.1) and Haines et al. (2013, 0.15<z<0.3)

found evidence that galaxies in clusters have lower SFRs than galaxies of similar mass in the field. A population of galaxies with reduced SFR at given mass was discovered in clusters by Patel et al. (2009) at z<0.8, Vulcani et al. (2010) at 0.4<z<0.8 and Paccagnella et al. (2016) at 0.04<z<0.07.

### 1.7.3 Star formation properties and galaxy fractions

As for the build up of the passive population, expressed in terms of quenching efficiency, the process seems to be stronger in clusters, which exhibit a higher fraction of red early-type and a lower fraction of blue late-type galaxies than the field (e.g. Dressler 1980; Poggianti et al. 1999; Bai et al. 2009; Vulcani et al. 2013), suggesting that they are extremely effective in cutting off the galaxy's ability to form stars. In an evolutionary scenario, for example, Poggianti et al. (2006) and Iovino et al. (2010), showed that galaxy clusters and groups have seen an evolution in their star forming galaxy fractions, that is stronger than in the field, and that the evolution from blue star forming to red passive takes place sooner in dense environments and massive halos. This scenario implies that the fraction of red passive galaxies in clusters increases earlier than in the field, supporting again the environmental quenching.
Focusing on the star forming population, a general consensus on the properties of active galaxies in the cluster population with respect to the field has not been reached yet. In contrast to the results regarding the presence of a population with reduced SFR in clusters, some studies have suggested that the difference in the star formation activity between field and clusters is primarily driven by the relative red fraction, instead of the properties of the star forming population (Muzzin et al. 2012; Koyama et al. 2013; Lin et al. 2014; Jian et al. 2017).
In a *global* environment perspective, the common group-scale environments and their evolution over time are still poorly known. At intermediate redshift, the members of optically selected groups (Wilman et al. 2005b) and even more massive X-ray-selected groups (Jeltema et al. 2007) vary strongly on a group-to-group basis, from elliptical/passive galaxy dominated to spiral/star-forming galaxy dominated. This does not appear to be as well correlated with velocity dispersion or local density as in low-redshift groups (Postman & Geller 1984; Zabludoff & Mulchaey 1998; Poggianti et al. 2006). Therefore, it is likely that this is a critical regime and epoch, in which important evolutionary processes have been felt by galaxies in some but not all groups, as a function of their environmental history.
For instance, at z<1 in the COSMOS field, Presotto et al. (2012) didn't find any strong correlation between the fraction of red/blue galaxies and the distance from the group center, in galaxies with $\log(M/M_{\odot}) \geq 10.6$, while galaxies with $9.8 \leq \log(M/M_{\odot}) \leq 10.6$ show a radial dependence in the changing mix of red and blue galaxies. The trend interests poor groups, whereas richer groups do not display any obvious behaviour of the blue fraction. As for mass segregation, it is visible only in rich groups, while poorer groups host an heterogeneous population of galaxies with different stellar masses as a function of radius. George et al. (2013) found a decline of low-mass star-forming and disc-dominated galaxies from field to groups. Such behaviour is accompanied by an increase in the

quenched fraction of intermediate type (disc+bulge) galaxies from field to groups, while bulge-dominated systems show only weak evolution. Giodini et al. (2012) found significant differences in the build-up of the quenched population from field to group galaxies at low stellar masses, while no differences are found for star-forming galaxies.

Important insights about the properties and the processes operating in groups that lead to the suppression of the star formation are given in the context of the CNOC2 survey (Wilman et al. 2005b). As far as individual groups are considered, Wilman et al. (2005b) found a significant enhancement in the fraction of passive galaxies within groups with respect to field galaxies at the same redshift, even in smallest groups. Furthermore, the incidence of the passive population only weakly correlates with the velocity dispersion of the structure ($\sigma_{200}$) or the group concentration. In the stacked group population, the fraction of passive galaxies is larger compared to the field sample at the same redshift, and the difference is even enhanced when bright galaxies in high $\sigma_{200}$ groups are taken. Comparing the CNOC2 sample with nearby groups from the 2dFGRS Percolation-Inferred Galaxy Group catalogue (2PIGG, Eke et al. 2004b,a), Wilman et al. (2005a) highlighted an increase in the fraction of group galaxies with significant OII emission lines from low-to-intermediate redshift (from 29% up to 58%). The trend is parallel and is maintained systematically lower compared to the field across the full range. In order to explain the observed evolution, the authors computed the probability of a star forming galaxy in the group environment experiencing a truncation, which is modelled to be $\sim$0.3 per Gyr, and according to which environmental dependences start to be important only at z>0.45.

To further refine the *global* environment frame, in the last few years besides the aforementioned studies relating the cluster and group populations, an increasing interest is focused on even bigger structures: superclusters. Studying the properties of superclusters helps us to understand the formation, evolution, and properties of the large-scale structure of the Universe (Hoffman et al. 2007; Araya-Melo et al. 2009; Bond et al. 2010, and references therein), ranging from rich, large superclusters containing many massive clusters extending over 10-20 Mpc down to less massive structures containing groups and poor clusters of the order of $10^{13} - 10^{14} M_{\odot}$ each (e.g. Einasto et al. 2011, and references therein).

The majority of supercluster catalogues in the literature are based on optical data, and only in the last few years searches for superclusters based purely on X-ray detection have been pursued out to z $\leq$ 0.4 (Chon et al. 2013).

Even rarer than systematic studies on the characterisation of the properties of supercluster structures as a whole (Einasto et al. 2011 in the SDSS survey; Verdugo et al. 2012; Geach et al. 2011; Schirmer et al. 2011; Lubin et al. 2009; Kartaltepe et al. 2008; Tanaka et al. 2007 at z$\geq$0.4) are the studies of stellar population properties of galaxies that inhabit such environments. A connection between supercluster environment and star formation has started to emerge (Lietzen et al. 2012; Costa-Duarte et al. 2013; Cohen et al. 2017; Luparello et al. 2013). At low-redshift, using SDSS data, Lietzen et al. (2012) found that within the superclusters a larger number of elliptical galaxies is found in the higher-density environments than at lower densities. Recently, Cohen et al. (2017) have analysed the relationship between star formation, the amount of cluster substructures and supercluster environment in a sample of 107 nearby galaxy clusters using data from SDSS, finding a

significant inverse correlation between the density of the supercluster environment and the fraction of star forming galaxies within clusters. Furthermore, at redshift z∼1 Luparello et al. (2013) showed that galaxies in groups residing in superstructures have larger stellar mass content and larger time-scale for star formation than the typical values found in groups not belonging to superstructures, regardless of the distance to the group centre. They concluded that, according to the assembly bias scenario, groups in superstructures formed earlier than elsewhere.
Although a few isolated very high redshift superclusters are known (e.g. Gal & Lubin 2004; Swinbank et al. 2007; Guzzo et al. 2007; Gilbank et al. 2008; Kim et al. 2016), Pompei et al. (2016) is one of the first example of detection of a superstructure at $z \geq 0.43$ in a homogeneous X-ray sample from the XXL Survey (Pierre et al. 2016).
Moving onto the definition of *local* environment, in the local Universe Baldry et al. (2006) found that the fraction of galaxies in the red sequence is higher in denser environments at any given mass in the range $9.0 < \log(M/M_{\odot}) < 11.0$. Similar results have been confirmed also at higher redshift (e.g. Scoville et al. 2007; Cucciati et al. 2010, 2017), where many studies showed that all features of the global correlation between galaxy colour and environment measured at $z \sim 0$ (the so called 'galaxy bimodality') are already in place at $z \sim 1$, with blue galaxies on average occupying regions of lower density than red galaxies (e.g. Coil et al. 2008; Cooper et al. 2006, 2010; Cucciati et al. 2006). At these redshifts, Scoville et al. (2017) analysed the ratio between star forming and passive galaxies defined using the colour-colour diagram (NUV-r) vs. (r-K), finding that it was higher in the lowest local density regime than in the highest, although with decreasing significance from lower to higher masses. They could conclude that also the inverse of the sSFR is higher in denser environments.
In contrast to these studies, Scodeggio et al. (2009) showed that while there is evidence for a colour-density relation at fixed luminosity at z $\sim$ 1, at intermediate redshifts when fixing the stellar mass no colour-density relation holds anymore.

## 1.8 The galaxy stellar mass function

In the majority of the works of the literature presented so far, global environment and stellar mass are considered separately (see e.g. Iovino et al. 2010; Peng et al. 2010), to disentangle how galaxy properties change as a function of stellar mass, fixing the environment, and as a function of environment fixing the galaxy mass. However, studies of galaxy properties as a function of mass often ignore the possibility that the galaxy mass distribution itself may vary with environment (Vulcani et al. 2013).
Among the many galaxy properties that can be studied, the galaxy stellar mass function (GSMF) is an important diagnostic tool for performing a census of galaxy properties, and provides powerful means of comparison between the populations of galaxies in different environments. In particular, its shape and its evolution provide important insights into the processes that contribute to the growth in stellar mass of galaxies with time and that drive the formation and evolution of galaxies in different environments (Giodini et al.

2012).

The GSMF has been extensively studied in deep fields for galaxies of different colours and morphological types (Bundy et al. 2006; Baldry et al. 2008; Pozzetti et al. 2010; Vulcani et al. 2011) and in different environments (e.g. Balogh et al. 2001; Yang et al. 2009; Calvi et al. 2013; Vulcani et al. 2011, 2012, 2013, 2014b; Davidzon et al. 2016; Muzzin et al. 2013; van der Burg et al. 2015; Nantais et al. 2016). Its shape has been described by a Schechter or a double Schechter function (Schechter 1976). When fitted to the data, the shape of this function changes both as a function of galaxy type (star-forming/passive, or morphological type) and of environment.

When considering the *global environment*, both in the local Universe and at higher redshift, it has been shown that the shape of the GSMF shows only little variation from isolated systems to massive clusters (e.g. Calvi et al. 2013; Vulcani et al. 2013; van der Burg et al. 2015; Nantais et al. 2016, but see Yang et al. 2009). What varies with environment is the maximum galaxy stellar mass reached by the GSMF, which is higher in more massive halos (Whiley et al. 2008; Lin et al. 2010; Vulcani et al. 2012; Calvi et al. 2013; Shen et al. 2013; Vulcani et al. 2014b). In fact, the relation between the most massive galaxy of a halo and halo mass can be used to infer the halo mass calibrating this relation from simulations (Shankar et al. 2006; Wang et al. 2006; Moster et al. 2010; Leauthaud et al. 2012).

The dependence of the shape of the GSMF upon global environment has been largely investigated at different redshifts from group scales up to the cluster environment. Calvi et al. (2013) considered a sample of nearby clusters from the Wide Field Nearby Galaxy cluster Survey (WINGS, Fasano et al. 2006) and compared it with that of the general field, further subdivided into group, binary and single systems by means of a Friend-of-Friend (FoF) algorithm. The analysis does not point out any difference among the shape of the GSMF in any of the aforementioned environments, even comparing isolated systems with massive clusters. The same results are obtained at $0.3<z<0.5$ by Vulcani et al. (2013) when comparing the cluster and field galaxy population in the IMACS Cluster Building Survey (ICBS, Oemler et al. 2013b,a) and at $0.4<z<0.8$, when looking at galaxies in clusters and groups within the ESO Distant Cluster Survey (EDisCS, White et al. 2005).

In an evolutionary perspective, Muzzin et al. (2013) analysed the evolution of the GSMF in the COSMOS/UltraVISTA general field from $z\sim0.2$ up to $z\sim4.0$, separating also galaxies into star forming and quiescent. This study points out that the stellar mass density of the quiescent population increases twice faster than star forming one, and that at $z>2.5$ the star forming population dominates at all masses. No evolution in the high mass end is registered, meaning that high mass galaxies are already in place at high redshift and thus formed the bulk of their stellar mass at extremely old epochs. Vulcani et al. (2011) found that the evolution in groups and clusters proceeds similarly to the field: the high mass end of the GSMF is already in place in clusters at $z\sim0.8$ and since then galaxies with stellar mass in the range $10^{10.2} \leq M/M_{\odot} \leq 10^{10.8}$ underwent a significant growth. Morphological types have proportionally more massive galaxies in high redshift clusters than in the low redshift counterpart, and the strongest evolution occurs among S0 galaxies.

In contrast to the invariance of the stellar mass assembly with the global environment,

local density estimates point out the dependence of the shape of GSMF on *local* environment, which results to be steeper in less dense environments (e.g. Baldry et al. 2006; Bolzonella et al. 2010; Vulcani et al. 2012; Davidzon et al. 2016; Etherington et al. 2016). Both in the local Universe and at higher redshift, more massive galaxies are preferentially found at higher densities (e.g. Hogg et al. 2003; Kauffmann et al. 2004; Blanton et al. 2005; Bolzonella et al. 2010; Cucciati et al. 2010; Vulcani et al. 2012; Davidzon et al. 2016), where also the fraction of early type galaxies is higher.

## 1.9 This thesis

In the increasing amount and quality of the observations and surveys aimed at resolving the complex scenario of the galaxy stellar mass assembly and star formation history and its relation with their host halos (namely, the group/cluster potential well) it is fundamental to deal with uniform and statistically significant data samples. In particular, the possibility of relying on consistent data spanning significant environment and redshift ranges of the galaxy population enables the custom definition of the main properties, setting the stage for unbiased self-consistent scientific results. By taking advantage of a homogeneous sample of X-ray groups and clusters, one of the aim of this thesis is to systematically study the properties of galaxies embedded in halos of different mass, with particular attention to the processes and timescales that lead to the formation of the passive population. The originality of the studies carried out in this thesis with respect to previous results driven by similar motivation is the possibility of conducting a systematic study in X-ray emitting groups observed in the XXL Survey (Pierre et al. 2016), that also provides unprecedented combination of X-ray quantities on extended structures with spectroscopic and photometric information of galaxy populations from low- to intermediate-redshifts. As outlined in the previous sections, the physical processes operating in groups are still poorly understood. For example, to what extent do gravitational interactions and the intra-group medium determine the morphology and star-formation properties of galaxies residing in and around groups? The main objectives are to study the dependence of galaxy properties such as SFR, SFH, stellar mass assembly, colour of galaxies as a function of the derived X-ray properties of their host structures, with the possibility of combining and comparing them with local density informations and tracing their redshift evolution.

The XXL X-ray catalogue of structures, the measurement and derivation of the main groups and clusters properties from X-ray observations and the main results achieved during the first phase of characterisation of the sample is presented in **Chapter 2**. In the same chapter, I also present the first achievement of this thesis, that is the creation of the spectrophotometric catalogue of galaxies by merging photometric and spectroscopic information on galaxies coming from different surveys and observing runs.

Then, I proceed in **Chapter 3** with the description of the techniques adopted for estimating the main galaxy properties from observed data on the galaxies themselves and on their host halo. Throughout the chapter I introduce the definition of global environment from

X-ray properties of groups and clusters and I then present the main techniques exploited for deriving stellar masses, absolute magnitudes, star formation properties and ages of the galaxy sample.
**Chapter 4** presents the released spectrophotometric catalogue containing all the relevant properties of galaxies derived in the previous chapters. The first scientific result obtained from the released catalogue is the study of the galaxy stellar mass function in four different redshift bins from z=0.1 up to z=0.6 and comparing high-X-ray luminosity groups and clusters, low-X-ray luminosity groups and clusters and the field. These results are presented in **Chapter 5**.
A natural consequence of the comparison of galaxy stellar mass function is the study of the stellar populations and star formation properties of galaxies. I start by focusing the attention on the richest supercluster of galaxies identified in the XXL Survey, at redshift z$\sim$0.3, and compare star formation properties, ages and colours in different environments identified within the region surrounding the supercluster. The results are presented in **Chapter 6**.
Finally, the techniques and expertise gained in Chapter 6 together with the higher sample statistics allowed to enlarge and complete the study of the star formation and colour properties of galaxies in the whole XXL field and in three redshift intervals from z=0.1 up to z=0.5. The results obtained in this phase are presented and discussed in **Chapter 7**.
As an appendix to the thesis I also include the publication of the work carried out during my Master Degree, which was finalized during the first year of PhD. This work is relevant for the aims and scientific questions investigated during this PhD thesis.
Throughout the thesis, I assume $H_0 = 69.3, \mathrm{km\,s^{-1}\,Mpc^{-1}}$, $\Omega_M = 0.29$, $\Omega_\Lambda = 0.71$ (Planck Collaboration et al. 2014, Planck13+Alens). I adopt a Chabrier (2003) initial mass function (IMF) in the mass range 0.1-100 $M_\odot$ for all mass estimates and related quantities.

The work presented in this thesis was mainly carried out with my PhD supervisor, Dr. Bianca M. Poggianti. This PhD project is a co-tutorship of thesis between the University of Padova and the University of Aix Marseille, where I spent six months during my second year of PhD, directly collaborating with my co-supervisor, Dr. Christophe Adami at the Laboratoire d'Astrophysique de Marseille. Finally, important results have been achieved thanks to the close collaboration with Dr. Benedetta Vulcani, the second co-supervisor of this thesis. Frequent and essential interactions with the XXL collaborators have also been fundamental for the achievement of the results presented here.

# 2

# THE DATA SAMPLE

## Content

In this chapter I will describe the X-ray observations of the XXL Survey (PI Marguerite Pierre) and the multiwavelength database and catalogues that are used in this work. While the scientific analysis will be based only on the XXL North field (XXL-N), for the sake of completeness in the following I will also report on the data for the XXL South field (XXL-S). At the time of writing, the galaxy spectroscopic coverage of the latter field is insufficient to allow detailed analysis.
In Section 2.1 I will provide details about X-ray observations and the target selection criteria adopted in order to build the groups and clusters (G&C) database, together with a description of the information and quantities that can be recovered. In Section 2.2 I will present the optical imaging and photometric redshift (photo-z) catalogues. Starting from this section, I will also include my contribution leading up to the creation of the final spectrophotometric sample. In the last section, I will describe the XXL spectroscopic database and the building of the final spectroscopic catalogue of galaxies.
I refer to the Chapters 3 and 4 for a detailed description on the spectrophotometric catalogue and for the computation of the spectroscopic completeness, of galaxy stellar masses, stellar mass completeness limits and the definition of global environment.

## 2.1 X-ray groups and clusters

### 2.1.1 Survey strategy and X-ray observations

The XXL Survey (Pierre et al. 2016), is an extension of the XMM-LSS 11 $\mathrm{deg}^2$ survey (Pierre et al. 2004), and is made up by 622 XMM pointings covering a total area of $\sim 50\,\mathrm{deg}^2$ reaching a sensitivity of $\sim 5 \times 10^{-15}\mathrm{erg\,s^{-1}\,cm^{-2}}$ in the [0.5-2] keV band for point sources. The main goal of the survey is to provide a well-defined sample of G&C out to a redshift of one and suitable for precision cosmology studies. Indeed, the survey was designed to provide competitive stand-alone constraints (with priors from the primary cosmic microwave background, CMB) on the Dark Energy evolving equation of state

using X-ray G&C. As shown in recent studies, this challenging goal may be properly achieved only by self consistently fitting (1) the evolution of G&C physics as usually encoded in the scaling relations, (2) the selection effects impinging on the data set, and (3) the cosmological parameters (see detailed discussions in Pacaud et al. 2007; Mantz et al. 2010). Moreover, at intermediate redshift, XXL provides a unique census of the group and cluster population.
Given that XXL detected G&C cover a rather low-halo mass range even beyond the local Universe (e.g. Pascut & Ponman 2015) and that such a population have barely been studied in literature up to date, scaling relations based on integrated G&C properties are of fundamental importance in this work.
The description of the practical requirements and of the observing strategies which prevailed in the definition of the XXL X-ray sample are fully described in Pierre et al. (2016). First, the XMM observatory is an ideal instrument to map large areas of the sky thanks to its unrivaled collecting area (2000 $\mathrm{cm}^2$ at 1 KeV), large field of view (30 arcmin), which together with its angular resolution ($\sim$ 6 arcsec FWHM on axis) enable resolving G&C of galaxies at any redshift, provided that the S/N is sufficient. Second, massive halos are extended sources at all wavelengths, so samples identified on the sky are subject to confusion due to projection and mis-centering. With respect to detections in the optical, infrared and millimeter domains, the X-ray selection benefits from the density squared scaling of the gas emission, which makes the sources less susceptible to projection and improves centering. Finally, relative to serendipitous archival searches, contiguous samples provide improved measurements of large-scale clustering and simplify determination of the selection function and organisation of the multiwavelength follow-up. The choice of the XXL field was motivated by several reasons:

- The need for extragalactic fields of having a good XMM visibility as well as accessibility by the ESO telescopes;

- The splitting in two areas of 25 $\mathrm{deg}^2$ each was found to be a good trade-off between the necessity both to probe large scales and to have some assessment of the cosmic variance; further, splitting makes the X-ray and follow-up observations easier to schedule;

- The opportunity of benefiting from an already existing XMM coverage;

- The availability of deep imaging multi-band optical data and spectroscopy;

- Within the two regions, the possibility of selecting a low galactic absorption area.

The final selected areas, shown in figure 2.1, were (1) the so-called North region: the XMM-LSS field, with 10 ks observations over 25 $\mathrm{deg}^2$ in the CFHTLS-W1 Field (2h23 -05d00) with 11 $\mathrm{deg}^2$ previously covered with XMM exposures of 10-20 ks (Pierre et al. 2004) plus the XMM-Subaru Deep Survey (Ueda et al. 2008) and (2) the so-called South region: the BCS/XMM field with the same 10 ks exposure time as the north, covering another area of 25 $\mathrm{deg}^2$ (23h00 -55d00). The flux limit for 10ks observations is $5\times10^{-15}$ and

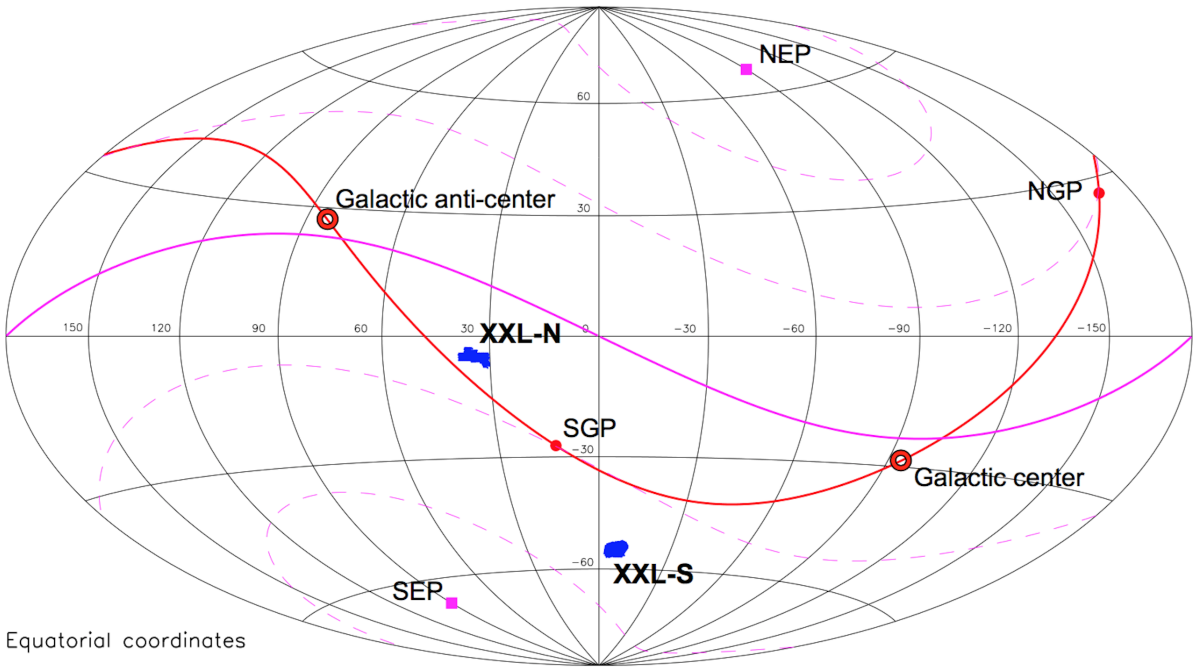


Figure 2.1: Map of the sky in equatorial coordinates showing in blue the two regions of the X-ray XMM pointings. The North and South ecliptic poles are indicated with the acronyms NEP, SEP; the North and South galactic poles are indicated with the acronyms NGP, SGP.

$2 \times 10^{-14}$erg s$^{-1}$ cm$^{-2}$ in the soft ([0.5-2] keV) and hard ([2-10] keV) bands, respectively. Hereafter I will refer to the XXL XMM-LSS and BCS fields as to XXL-N and XXL-S respectively.

A detailed plot of the final layout of X-ray pointings in the two XXL-N and -S regions is shown in figure 2.2. Each pointing is represented by a circle having a diameter of 20 arcmin: blue circles show the pre-XXL observations and, out of these, light-blue circles indicate observations done in mosaic mode. The red circles stand for the XXL AO-10 observations (December 2010, 2.9 Ms allocated time), all of which were done in mosaic mode[1]. Already existing observations completed to 10 ks within the AO-10 time-allocation are marked by a small filled red circle. Maps of dust column density calibrated to E(B-V) reddening in magnitude (Schlegel et al. 1998) are superposed to the pointings.

[1]Since no raster, dithering or tracking modes were included in the original design of the telescope, a target region larger than the field of view can only be achieved by a series of individual, independent observations, each having its own operational and instrument overheads. The technique adopted by XMM-Newton when the scientific case requires this kind of observations (galaxy clusters, supernova remnants, crowded fields, solar system objects) is called mosaic mode, and has been defined to keep a high observing efficiency when large fields are observed for relatively short integration times.

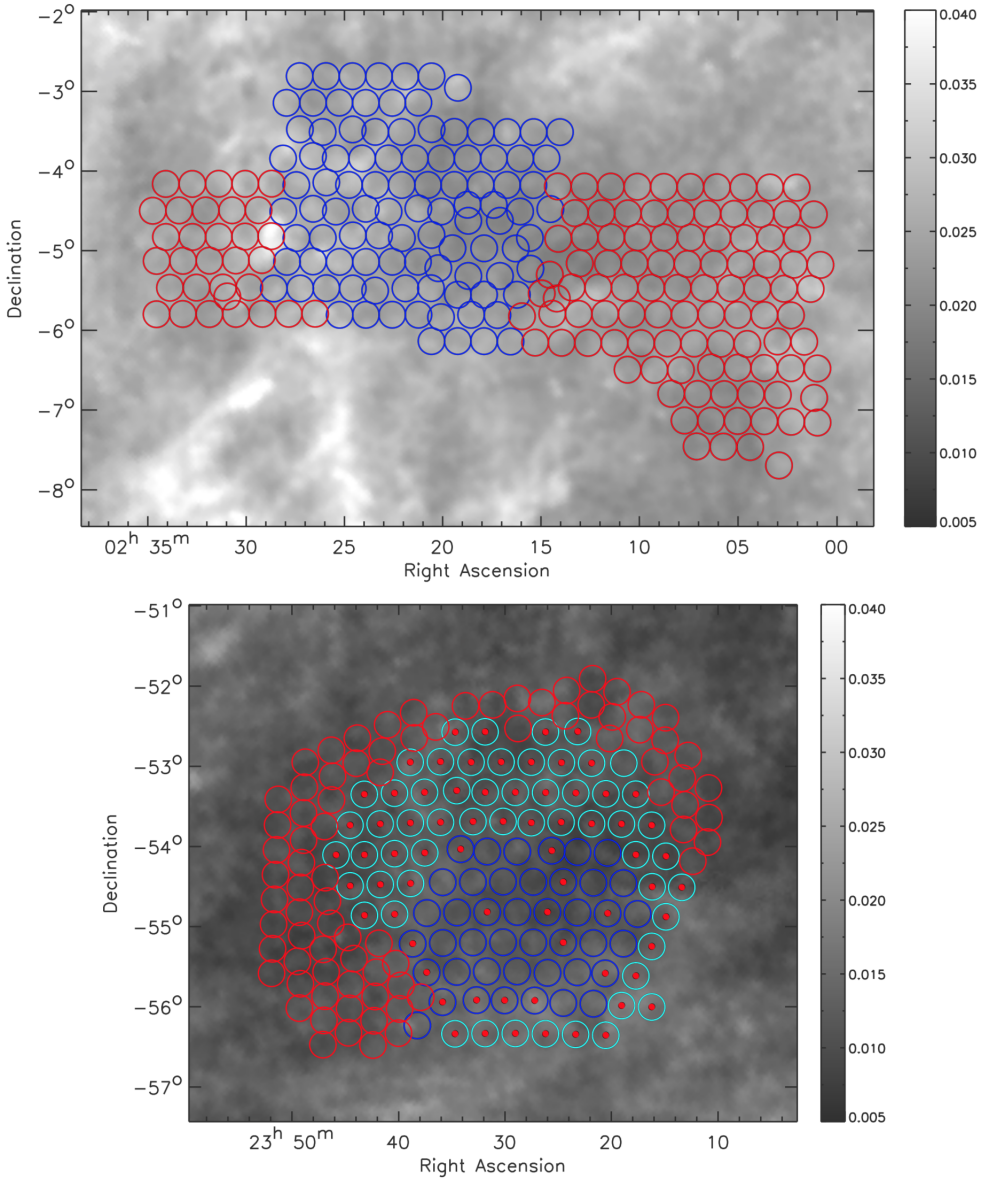


Figure 2.2: Final lay-out of the X-ray XMM observations in the two XXL regions, the XXL-N field in the top panel and the XXL-S field in the bottom panel. In the background the maps of dust column density calibrated to E(B-V) reddening in magnitude is shown (Schlegel et al. 1998); the circles have a diameter of 20 arcmin: the blue circles show the pre-XXL observations and, out of these, light-blue circles indicate observations done in mosaic mode. The red circles stand for the XXL AO-10 observations, all of which were done in mosaic mode. Already existing observations completed to 10 ks within the AO-10 time-allocation are marked by a small filled red circle.

### 2.1.2 XXL G&C Database

The data processing of X-ray observations and the sample selection are described in detail in Pacaud et al. (2016). The source detection algorithm is based on the fact that at high galactic latitude and medium X-ray sensitivity the great majority of sources are point like AGNs (95 %) and extended G&C of galaxies. Data were processed with the XAMIN v3.3.2 pipeline for the detection and classification of X-ray faint extended sources, a dedicated pipeline already used in the pilot XMM-LSS project (Pacaud et al. 2006; Clerc et al. 2012) to generate and process images, exposure maps and detection maps. XAMIN is a maximum-likelihood profile-fitting procedure, using either *pnt*, a point source PSF, or EXT, an extended source model assuming a beta-profile with a constant slope of 2/3, according to the classification of the source in the best band (the extended_source_class parameter). The procedure is based on two parameters named `ext` and `ext_stat`, which are both functions of the structure apparent size, flux and local XMM sensitivity: a detection enters the extended candidate list when it has an `ext` greater than $5''$ and a likelihood of extent `ext_stat` greater than 15. Extensive simulations enabled the creation of different classes for structures on the basis of the level of contamination from point-sources:

- **C1** class includes the highest surface brightness extended sources, with a likelihood of extent `ext_stat` $> 33$, and a likelihood of detection `ext_det_stat` $> 32$ and are identified to be almost uncontaminated by point sources that are misclassified as extended.

- **C2** class includes sources with $15 <$ `ext_stat` $< 33$ showing a 50% contamination rate. C2 G&C are fainter than the C1 ones. Contaminating sources include saturated point sources, unresolved pairs, and sources strongly masked by CCD gaps, for which not enough photons were available to permit reliable source charaterisation.

- **C3** class includes sources at the survey sensitivity limit, and so is likely to contain G&C at high redshift. C3 G&C are faint objects, corresponding to (optical) clusters associated with some X-ray emission, too weak to be characterised; the selection function of the C3 sample is therefore undefined, as well as other X-ray properties.

The list of C1, C2, C3 detections are hosted in the Saclay database (administered by Jean Paul Le Fèvre), which contains 455 analysable extended sources: 207 ($\sim$ 46%) of them are classified as C1 sources, 194 ($\sim$ 43%) are C2 and the remaining 51 ($\sim$ 11%) are C3 sources. Among the 455 XXL G&C, 264 are in the XXL-N area.
A description of the columns of a standard output catalogue downloaded from the database and which are useful for this work is given below:

- **tag** Internal source identifier (n**** for northen (LSS) field, s**** for southern (BCS) field)

- **xlssc** G&C name for external use (publications, citations, on-line catalogues)

- **type** G&C classification: C1, C2, C3

- **name(*)** Short name for internal use

- **full name** Following XMM-Newton format: XMMU JHHMMSS.s+DDMMSS

- **RA** Right Ascension as calculated by the pipeline (J2000)

- **DEC** Declination as calculated by the pipeline (J2000)

- **Status** Redshift status:
1 - 'inexistent': no cluster in the spectroscopic redshift space
2 - 'pending': awaiting the results from the spectroscopic runs
3 - 'photometric': photometric redshift measurement
4 - 'tentative': if 1 or 2 plausible cluster spectroscopic redshifts are found within 500 kpc, also considering the photometric information.
5 - 'provisional': awaiting final confirmation by the follow-up manager (same information as for "confirmed" is potentially available).
6 - 'confirmed': G&C definitively confirmed: either at least 3 concordant redshifts within 500 kpc or spectroscopic redshift for the central galaxy (BCG).

- **quality** Number assigned by the moderator after inspection of the X-ray/optical overlays:
1 - 'unlikely', is a default value prior to moderator evaluation
2 - 'possible'
3 - 'good candidate'
4 - flag to indicate that it has been observed in the IR (XMM-LSS project)
5 - preselected for the XXL-100 brightest sample (175 objects, see Sect. 2.1.3)
6 - XXL-100 brightest sample (in terms of pipeline total count-rate - irrespective of the C1/C2 classification.)

- **redshift** Redshift value (photometric or spectroscopic)

- **PN** Detector indicator

- **total counts** Number of counts in the PN detector observed in band B2 (0.5-2 keV)

- **total rate** Total count rate in the PN detector observed in band B2 (0.5-2 keV)

- **total flux (*)** Total flux in the PN detector in band B2 (0.5-2 keV)

- **MOS1+2** Detector indicator

- **total counts** Number of counts in the MOS detectors observed in band B2 (0.5-2 keV)

- **total rate** Total count rate in the MOS detectors observed in band B2 (0.5-2 keV)

- **total flux (*)** Total flux in the MOS detectors in band B2 (0.5-2 keV)

Where (*) indicates columns which are not visible in visitor and surveyor modes.

### 2.1.3 XXL-100 brightest catalogue

A subsample of 100 structures was selected from the entire sample (all classified as C1 and C2), containing the highest signal-to-noise objects. Specifically, the 100 brightest XXL G&C sample consists of 96 C1 and 4 C2 G&C with fluxes greater than $3 \times 10^{-14} erg\,sec^{-1}\,cm^{-2}$ within a 60″ aperture, almost equally distributed between the two XXL fields: 51 in XXL-N and 49 in XXL-S. The bright XXL G&C catalogue released in Pacaud et al. (2016) provides direct measures from the X-ray spectra of G&C, as well as from scaling relations investigated in several papers in the first XXL press release. The quantities that are either directly measured or derived/used to calibrate scaling relations are:

- the spectroscopic redshift.

- C60: net XMM counts in the [0.5-2] keV band within the 60″ aperture used for the sample selection.

- F60: flux relative to C60 in units of $10^{-14} erg\,s^{-1}\,cm^{-2}$.

- $T_{300kpc}$: temperature in a 300 kpc aperture derived from the Luminosity-Temperature relation investigated in Giles et al. (2016).

- $r_{500,MT}$[2]: overdensity radius with respect to the critical density in Mpc, obtained from the relation between the mass as estimated from the weak-lensing and the temperature ($M_{500,WL} - T_{300kpc}$), investigated in Lieu et al. (2016).

- $L^{XXL}_{500,MT}$: rest-frame luminosity within [0.5-2] keV in $r_{500,MT}$ in units of $10^{43} erg\,s^{-1}$.

- $M_{500,MT}$: mass within $r_{500,MT}$ in units of $10^{13} M_{\odot}$, obtained from the $M_{500,WL} - T_{300kpc}$ scaling relation of Lieu et al. (2016) and the temperatures measured in Giles et al. (2016).

### 2.1.4 G&C spectroscopic confirmation and X-ray properties from direct measurements and scaling relations

The spectroscopic confirmations of the nature of the candidate G&C and of their redshift were performed using an iterative semi-automatic process, very similar to the one already used for the XMM-LSS survey (e.g. Adami et al. 2011). The procedure is described in detail in Adami et al. 2018, and can be summarized as follows.

- Within the X-ray contours, the available spectroscopic redshifts from the XXL spectroscopic database (see Sec. 2.3) were selected;

[2] $r_{500,scal}$ is defined as the radius of the sphere inside which the mean density is 500 times the critical density $\rho_c$ of the Universe at the G&C's redshift; $M_{500,scal}$ is then by definition equal to $4/3\pi 500 \rho_c r^3_{500,scal}$.

- these redshifts were sorted by ascending order to identify significant gaps ($\Delta z$ >0.003) in their distribution;

- if one or more concentrations in both physical and redshift space appeared (more than 3 galaxies), the aggregate of galaxies closer to the X-ray center or that including BCG-like were selected as "group population". For the vast majority of the cases, a single concentration emerged (see Adami et al. 2018 for a more precise discussion on multiple systems). The procedure for identifying of the BCG is manual: if the galaxy is clearly the brightest one on the image, and it is close to the X-ray center, then, it is considered as a potential BCG. The clusters that were confirmed only on a BCG-based criterion underwent further checks a posteriori taking advantage of the AAOmega spectroscopic run, which showed that this procedure did not introduce systematic uncertainties in the redshift estimate. Only a few cases (less than 3%, described in Adami et al. 2018), produced wrong redshift estimate.

- If no concentration appeared, a single galaxy with measured redshift which was likely to be a BCG was selected. This did not exclude superposition effects, but the probability of such a configuration is low.

- If none of the two previous criteria was satisfied, the candidate structure could not be confirmed. If one of the two previous criteria was satisfied, the median value of the redshift of the preliminary "G&C population" was assumed to be the G&C redshift. This allowed us to compute the angular radius of a 500 kpc (physical) circle.

- The whole process was repeated with all available redshifts within a 500 kpc radius instead of those within the X-ray contours to obtain the final G&C redshift.

This procedure identified 341 spectroscopically confirmed G&C in the whole XXL sample, 202 of which in the XXL-N. Among the latter, 27 were confirmed considering only the BCG, 44 considering the BCG and another concordant galaxy. The final fractions of spectroscopically confirmed C1, C2 and C3 G&C in the whole (XXL-N) sample are 54% (52%), 35% (30%) and 11% (18%), respectively. Given the high uncertainties on X-ray properties derived for C3 G&C (whose list of spectroscopically confirmed objects is given in Table G.1 of Adami et al. 2018), in this thesis I will consider only C1+C2 G&C. Adami et al. (2017) publish 341 confirmed G&C plus all C1 non-confirmed X-ray extended sources, for a total of 365 structures, and release the complete catalogue of spectroscopically confirmed C1+C2 G&C.
In Table 2.1 the first 20 entries of the table are reported as example. For each source, the table provides the following information:

- The IAU xlssc identifier (between 1 and 499, or 500 and 999 for XXL-N or XXL-S respectively);

- RA and DEC;

Table 2.1: List of spectroscopically confirmed C1 and C2 G&C of galaxies. Col.1: official xlssc name. Col.2 and 3: X-ray structure coordinates. Col.4: G&C mean redshift. Col. 5: number of measured spectroscopic redshifts (X: means redshift is computed from X-ray spectroscopy directly). Col. 6: XXL class. Col. 7: gas mass inside a physical radius of 500 kpc along with lower and upper uncertainties. Col. 8: $R_{500}$. Col. 9: X-ray temperature with lower and upper uncertainties. Col. 10: $L^{XXL}_{500,MT}$ X-ray luminosity and uncertainty in the [0.5-2] keV energy range. Col. 11: X-ray flux and uncertainty as in XXL paper II and in the [0.5-2]keV band. Col. 12, flags: "+" means the G&C was already published in the XMM-LSS releases, * means that we have a note on this G&C in the appendix, $l$ means that the considered G&C is above the flux completeness limit ($\sim 1.3\ 10^{-14}$ erg s$^{-1}$ cm$^{-2}$), F means that the structure is a candidate fossil group. Complete table is available in the electronic version of Adami et al. (2017). Blank places are undetermined values.

| xlssc | RA | DEC | z | $N_{gal}$ | Class | $M_{gas,500kpc}$ $10^{11}$ | $R_{500}$ | $T_{300kpc}$ | $L^{XXL}_{500,MT}$ $10^{42}$ | $F_{60}$ $10^{-15}$ | flag |
|---|---|---|---|---|---|---|---|---|---|---|---|
| | deg | deg | | | | M$\odot$ | kpc | keV | erg/s | erg/s/cm$^2$ | |
| 199 | 30.192 | -6.708 | 0.339 | 2 | 1 | $73^{+4}_{-6}$ | 644 | $2.1^{+0.2}_{-0.3}$ | 32±3 | 67±5 | $l$ |
| 200 | 30.331 | -6.830 | 0.333 | 2 | 1 | $48^{+3}_{-3}$ | 653 | $2.1^{+0.3}_{-0.4}$ | 16±2 | 31±3 | $l$ |
| 114 | 30.425 | -5.031 | 0.233 | 6 | 2 | $40^{+3}_{-3}$ | | | | 35±8 | $l$ |
| 179 | 30.482 | -6.574 | 0.608 | 5 | 1 | $43^{+11}_{-12}$ | | | | 14±4 | $l$ |
| 113 | 30.561 | -7.009 | 0.050 | 9 | 1 | $8^{+1}_{-1}$ | | | | 115±8 | $l$ |
| 174 | 30.592 | -5.899 | 0.235 | 8 | 1 | $41^{+3}_{-4}$ | 570 | $1.5^{+0.1}_{-0.1}$ | 8±1 | 25±4 | $l$ |
| 094 | 30.648 | -6.732 | 0.886 | 3 | 1 | $106^{+12}_{-12}$ | 581 | $3.0^{+0.5}_{-0.6}$ | 224±32 | 48±5 | $+l$ |
| 196 | 30.728 | -7.652 | 0.136 | 8 | 1 | $26^{+2}_{-3}$ | 563 | $1.3^{+0.1}_{-0.2}$ | 4±1 | 32±4 | $l$ |
| 178 | 30.753 | -6.285 | 0.194 | 2 | 2 | $29^{+3}_{-5}$ | 655 | $0.8^{+0.1}_{-0.1}$ | 3±1 | 17±3 | $l$ |
| 156 | 30.766 | -7.101 | 0.336 | 4 | 2 | $33^{+3}_{-3}$ | | | | 28±4 | $l$ |
| 157 | 30.865 | -6.929 | 0.585 | 5 | 1 | $70^{+7}_{-7}$ | 721 | $3.2^{+0.8}_{-0.7}$ | 42±7 | 19±3 | $l$ |
| 197 | 30.923 | -7.785 | 0.439 | 2 | 1 | $107^{+5}_{-5}$ | 755 | $3.0^{+0.4}_{-0.5}$ | 76±9 | 97±7 | $l$ |
| 096 | 30.973 | -5.027 | 0.520 | 6 | 1 | $89^{+5}_{-5}$ | 951 | $5.0^{+0.9}_{-0.5}$ | 63±8 | 36±4 | $*+l$ |
| 155 | 31.134 | -6.748 | 0.433 | 2 | 1 | $36^{+4}_{-5}$ | 576 | $1.8^{+0.3}_{-0.3}$ | 16±3 | 23±3 | $l$ |
| 173 | 31.251 | -5.931 | 0.413 | 3 | 1 | $47^{+4}_{-4}$ | 930 | $4.3^{+0.3}_{-0.3}$ | 17±2 | 24±3 | $l$ |
| 177 | 31.290 | -4.918 | 0.211 | 7 | 2 | $37^{+3}_{-3}$ | | | | 22±4 | $l$ |
| 102 | 31.322 | -4.652 | 0.969 | 3 | 1 | $138^{+7}_{-7}$ | 638 | $3.9^{+0.8}_{-0.9}$ | 167±25 | 42±4 | $+l$ |
| 106 | 31.351 | -5.732 | 0.300 | 14 | 1 | $83^{+3}_{-3}$ | 777 | $2.8^{+0.2}_{-0.3}$ | 43±3 | 91±4 | $+l$ |
| 107 | 31.354 | -7.594 | 0.436 | 3 | 1 | $67^{+4}_{-5}$ | 672 | $2.4^{+0.4}_{-0.4}$ | 49±6 | 56±5 | $+l$ |
| 160 | 31.521 | -5.194 | 0.817 | 4 | 2 | | | | | 6±4 | |

- The redshift (z) and the number of galaxies used for the redshift determination ($N_{gal}$);

- The class: C1, C2 only;

- Basic X-ray and X-ray related quantities for the G&C of the present release ($M_{gas,500kpc}$, $r_{500,MT}$ , $T_{300kpc}$, $L^{XXL}_{500,MT}$ , and X-ray flux, details in the following subsection);

- A flag indicating whether there is a note on the G&C in one of the appendices

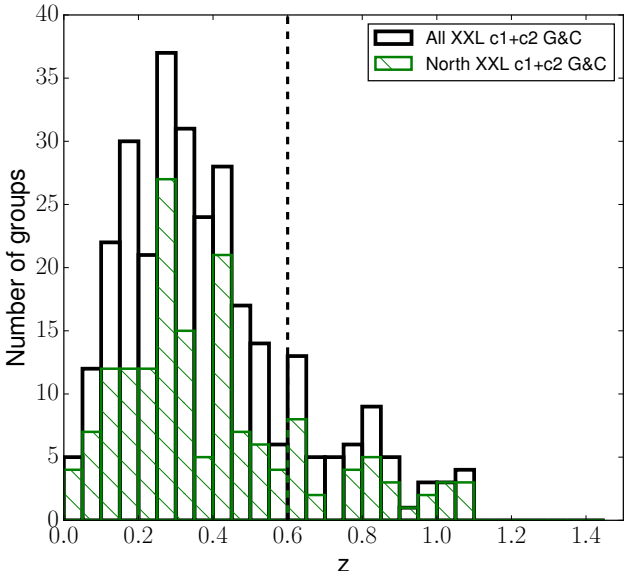


Figure 2.3: Redshift distribution of all the 302 spectroscopically confirmed XXL G&C (black), and of the 164 in the XXL-N area (green). The vertical black dashed line corresponds to $z = 0.6$, the maximum redshift of G&C considered in this thesis.

of Adami et al. (2017), whether the G&C was already published in Pacaud et al. (2016) or in former XMM-LSS releases, and whether the G&C is a member of the flux limited sample.

The redshift distribution of the C1+C2 G&C sample is shown in Fig. 2.3, where the histogram of the XXL-N sample is overlaid in green. A large fraction of X-ray G&C are located at z $\leq$ 1.0, and in particular the median redshift of the sample is $z = 0.339$ ($z = 0.335$ when only the XXL-N field is considered).

### X-ray direct measurements

The 222 C1+C2 (233 C1+C2+C3) G&C with flux brighter than $\sim$1.3 $\times 10^{-14}$ erg s$^{-1}$ cm$^{-2}$ underwent dedicated X-ray luminosity and temperature measurements, and corresponding quantities are reported in Table 2.1. Full details on the analysis of the G&C X-ray properties can be found in Giles et al. (2017, in preparation), and in the following the main steps of the spectral analysis are outlined.

As a conservative approach, the extent of the G&C emission was defined as the radius beyond which no significant G&C emission is detected using a threshold of $0.5\sigma$ above the background level. Due to the low number of counts and low signal-to-noise of many of the G&C past the XXL-100-BC, a detailed modeling of the background was performed following the method outlined in Eckert et al. (2014), instead of a simple background subtraction. $L^{XXL}_{500,MT}$ is defined as the [0.5-2.0] keV band (G&C rest frame) luminosity within $r_{500,MT}$. Such luminosities are extrapolated from 300 kpc (see below) out to

$r_{500,MT}$ by integrating under a $\beta$-profile assuming a core radius $r_c = 0.15\, r_{500,MT}$ and an external slope $\beta$=0.667 (see Pacaud et al. 2016). Values for G&C $r_{500,MT}$ are calculated using the mass-temperature relation obtained in Lieu et al. (2016). Given that the G&C considered at this stage are much fainter sources than those considered in Pacaud et al. (2016), it was not possible to measure X-ray temperatures for all of them. Several G&C either were located in pointings affected by flaring, or had very low counts, or were contaminated by point sources, or were at very low redshift with a consequent bad spatial coverage. Gas masses were analytically computed following the procedure outlined in Eckert et al. (2016). Briefly, surface-brightness profiles in the [0.5-2] keV band were extracted starting from the X-ray peak using the PROFFIT package (Eckert et al. 2011). The surface-brightness profiles are then deprojected by decomposing the profile onto a base of multiscale parametric forms, and are then converted into gas density profiles using X-ray cooling functions calculated using the APEC plasma emission code (Smith et al. 2001). Finally, the recovered gas density profiles are integrated over the volume within a fixed physical scale of 500 kpc. Note that in Table 2.1 gas masses are given only for G&C with an uncertainty on the flux F60 lower than one third of the flux itself. X-ray photometry was computed adopting the same procedure used to estimate aperture fluxes in a radius of 60″ (F60), by estimating the count-rates in X-ray pointings and modeling the signal in a user defined background annulus around the source with a linear fit to the local exposure map. Count-rates are converted into global fluxes using average energy conversion factors.

### G&C parameters from scaling relations

In order to have homogeneous estimates of the complete G&C sample, global properties were estimated via scaling relations based on the $r$ = 300 kpc count-rates (see Adami et al. 2018). The $L^{XXL}_{500,scal}$, $L^{bol}_{500,scal}$, $T_{300kpc,scal}$, $M_{500,scal}$ and $r_{500,scal}$ values used in the current thesis are also extracted from **?**, and the first 20 entries of Table F.1 which is released with the paper are given in Table 2.2.

The estimates of the global properties of the groups were derived as follows. The procedure considers as input values the XMM count rates in the $0.5-2$ keV band extracted within 300 kpc from the G&C centers, computed using the total counts and exposure data obtained in source and background apertures. Then, the methods iterates on the gas temperature $T_{300kpc,scal}$ to recover $r_{500,scal}$ (using the $M-T$ relation for the sample "XXL+COSMOS+CCCP" in Table 2 of Lieu et al. 2016) and a luminosity $L^{XXL}_{500,scal}$ (using the best-fit results for the relation $L^{XXL}_{500,scal}-T_{300kpc,scal}$, with "XXL" fit, in Table 2 of Giles et al. 2016) that was integrated up to $r_{500,scal}$ by adopting a $\beta-$model with parameters $(r_c, \beta) = (0.15\, r_{500,scal},\, 2/3)$. The iteration stopped when the input and output values of $T_{300kpc,scal}$ agreed within a tolerance value of 5 K. Usually this process converges in a few steps (2-3 iterations) and provides estimates and relative errors propagated from the best-fit results of the X-ray temperature ($T_{300kpc,scal}$), $r_{500,scal}$, $M_{500,scal}$, the luminosity in the 0.5-2.0 keV range ($L^{XXL}_{500,scal}$), and the bolometric luminosity ($L^{bol}_{500,scal}$). A comparison between the measured cluster temperatures and those obtained from the scaling relations

Table 2.2: List of X-ray parameters from scaling relations (see text) for the confirmed C1 and C2 G&C of galaxies. Col.1: XXL name of the galaxy structure. Col. 2: X-ray temperature and uncertainty (in the [0.5:2] keV band). Col. 3: radius corresponding to the 500 matter density contrast along with its uncertainty. Col. 4: total mass at the 500 matter density contrast along with lower and upper values. Col. 5: Bolometric X-ray luminosity and uncertainty.

| xlssc | $T_{300kpc,scal}$ keV | $r_{500,scal}$ kpc | $M_{500,scal}$ $10^{13}$ M$\odot$ | $L^{bol}_{500,scal}$ $10^{42}$ erg/s |
|---|---|---|---|---|
| 1 | 4.2±0.5 | 819±94 | 30±11 | 250±21 |
| 2 | 3.7±0.6 | 692±84 | 21±8 | 200±25 |
| 3 | 4.4±0.7 | 745±97 | 29±12 | 360±44 |
| 5 | 2.7±0.6 | 499±69 | 11±5 | 120±20 |
| 6 | 6.3±0.7 | 1151±138 | 66±24 | 650±30 |
| 8 | 1.6±0.2 | 579±54 | 7±3 | 17±3 |
| 9 | 1.8±0.2 | 605±59 | 9±3 | 23±5 |
| 10 | 2.8±0.3 | 773±74 | 18±6 | 72±7 |
| 11 | 0.8±0.1 | 435±41 | 2±1 | 2±1 |
| 13 | 2.0±0.2 | 635±57 | 10±3 | 26±3 |
| 18 | 1.5±0.2 | 548±50 | 6±2 | 14±2 |
| 20 | 2.3±0.3 | 625±64 | 11±4 | 47±9 |
| 21 | 0.9±0.1 | 460±41 | 3±1 | 3±1 |
| 22 | 3.1±0.3 | 835±79 | 22±7 | 91±4 |
| 23 | 2.5±0.3 | 716±67 | 14±4 | 50±5 |
| 25 | 2.9±0.3 | 812±76 | 20±6 | 73±4 |
| 27 | 2.4±0.2 | 710±65 | 13±4 | 43±4 |
| 28 | 1.5±0.2 | 545±53 | 6±2 | 12±3 |
| 29 | 4.6±0.9 | 675±97 | 27±12 | 480±46 |
| 30 | 1.8±0.3 | 496±54 | 7±3 | 25±5 |

is displayed in Figure 2.4 (Adami et al. 2018); the observed scatter around the 1:1 line simply reflects the intrinsic scatter of the luminosity temperature relation. Note that the uncertainties of the scaling relations and count rates were propagated to the errors on the considered derived X-ray quantities.

In this thesis, I will mainly focus on the 164 C1+C2 G&C in the XXL-N field, reported in Figure 2.5. In the figure, the trend of $M_{500,scal}$, $r_{500,scal}$ and the temperature with redshift are shown. The sub-panels on the right show the distributions of the same quantities. The upper panel refers to $M_{500,scal}$, whose median value is $(9.54 \pm 0.80) \times 10^{13} M_{\odot}$ for the whole sample. This indicates that roughly half of the G&C should be properly qualified as clusters, since they have a mass $M_{500,scal} \geq 10^{14} M_{\odot}$. The remaining half of them are more properly groups. The distribution of $r_{500,scal}$ (middle panel of the figure) resembles that of $M_{500,scal}$, as expected given that these two quantities are closely related.

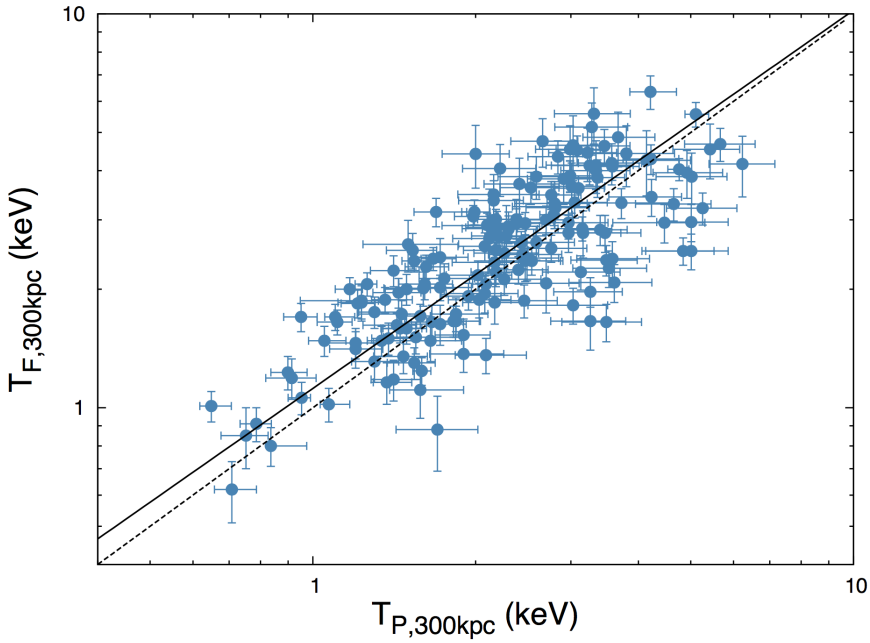


Figure 2.4: Comparison between the true temperature measurements (y-axis) and estimates from the scaling relations (x-axis). The dotted and solid lines show the 1:1 relation and the actual linear regression best fit to the data respectively.

Throughout the scientific analysis, I will separate G&C in two classes according to their X-ray luminosity to study separately the properties of high and low luminosity G&C. The two classes of high and low X-ray luminosity are shown with different colours in all panels (red and green dots, according to the legend). The adopted threshold value is $L^{XXL}_{500,scal} = 10^{43}\,erg\,s^{-1}$ (the red dashed horizontal line in the bottom panel of the figure), the median value of the X-ray luminosity of the whole sample and which approximately corresponds to a virial mass of $10^{14} M_{\odot}$. Overall, selection effects emerge: at z>0.6 the survey detects only the most massive G&C.

G&C at $z \leq 0.6$ will be used in the scientific analysis that will be presented in the next chapters. In this redshift range, G&C span a wide range of both virial masses ($8.72 \times 10^{12} \leq M_{500,scal}(M_{\odot}) \leq 6.63 \times 10^{14}$) and X-ray luminosities ($2.27 \times 10^{41} \leq L^{XXL}_{500,scal}(erg\,s^{-1}) \leq 3.5 \times 10^{44}$).

### 2.1.5 Superclusters

The search for superclusters has been conducted in Adami et al. (2017). The paper presents the search for physical associations between individual clusters of galaxies, and arbitrarily called "superclusters" the associations of at least three clusters. Cluster pairs (association of only two clusters) are not considered as superclusters.

A total of 35 superclusters were identified by means of a FoF algorithm charaterised

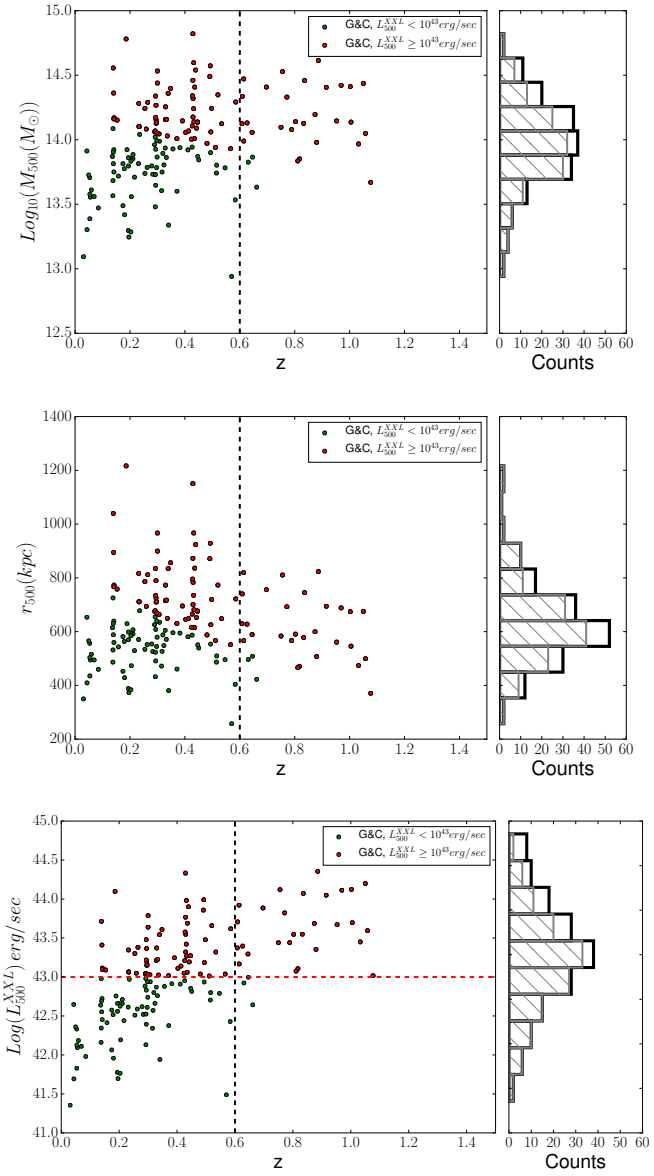


Figure 2.5: Main panels: $M_{500,scal}$ (upper), $r_{500,scal}$ (middle), $L^{XXL}_{500,scal}$ (bottom) versus redshift for the 164 XXL-N C1+C2 G&C with estimates of $M_{500,scal}$ and $r_{500,scal}$ ($M_{500}$, $r_{500}$ and $L^{XXL}_{500}$ in the figures). The distribution of the same quantities is shown in the corresponding right panels, where black histograms refer to all G&C in the sample, and gray hatched histograms are for $z \leq 0.6$ G&C. In the main panels, the vertical black dashed line corresponds to $z = 0.6$, the maximum redshift of G&C considered in this thesis. High-luminosity G&C ($\log(L^{XXL}_{500,scal}) \geq 43$ erg/sec) are marked in red, low-luminosity G&C in green. In the bottom panel, the horizontal red dashed line corresponds to the luminosity used to separate the G&C into two classes (see text for details).

Table 2.3: List of detected super-cluster candidates with the FoF approach from Adami et al. (2017). Columns are: ID, old name of some previously detected superclusters in Pacaud et al. (2016) Coordinates (J2000 equinox), mean redshift, multiplicity, the reliability index from the Voronoi tessellation approach (R), and list of the members.

| Name | Old | $RA(deg)$ | $DEC(deg)$ | $z_{mean}$ | m | R | Members (xlssc cluster numbers) |
|---|---|---|---|---|---|---|---|
| XLSSsC N18 | | 30.429 | -6.879 | 0.336 | 3 | 3 | 200, 156, 199 |
| XLSSsC N02 | e | 32.054 | -6.658 | 0.430 | 11 | 4 | 086, 172, 082, 085, 093, 084, 083, 092, 155, 107, 197 |
| XLSSsC N03 | | 33.037 | -4.758 | 0.139 | 8 | 2 | 162, 095, 060, 112, 138, 118, 176, 201 |
| XLSSsC N06 | f | 33.151 | -5.570 | 0.300 | 5 | 4 | 098, 117, 167, 111, 161 |
| XLSSsC N12 | | 34.140 | -5.003 | 0.447 | 4 | 4 | 110, 187, 144, 142 |
| XLSSsC N21 | | 34.418 | -5.034 | 0.651 | 3 | 3 | 059, 080, 195 |
| XLSSsC N11 | | 34.430 | -4.865 | 0.340 | 3 | 2 | 058, 192, 086 |
| XLSSsC N15 | | 34.465 | -4.607 | 0.291 | 4 | 3 | 180, 126, 137, 202 |
| XLSSsC N17 | | 34.770 | -4.241 | 0.203 | 3 | 3 | 077, 193, 189 |
| XLSSsC N13 | | 35.220 | -4.666 | 0.513 | 3 | 2 | 183, 131, 124 |
| XLSSsC N19 | | 35.630 | -5.147 | 0.380 | 3 | 2 | 132,067,017 |
| XLSSsC N04 | | 35.809 | -4.159 | 0.828 | 8 | 3 | 047,032,184,069,071,003, 015, 064 |
| XLSSsC N16 | | 36.155 | -3.453 | 0.174 | 3 | 2 | 043, 035, 182 |
| XLSSsC N20 | | 36.161 | -4.241 | 0.433 | 3 | 2 | 006, 012, 026 |
| XLSSsC N10 | | 36.290 | -3.411 | 0.329 | 4 | 4 | 009, 023, 129,010 |
| XLSSsC N07 | | 36.447 | -5.143 | 0.496 | 5 | 4 | 049, 020, 053, 169, 143 |
| XLSSsC N05 | a | 36.493 | -4.142 | 0.055 | 6 | 2 | 054, 125, 011, 191, 052, 062 |
| XLSSsC N08 | b | 36.909 | -4.159 | 0.141 | 4 | 1 | 050, 090, 087, 041 |
| XLSSsC N14 | | 36.919 | -4.406 | 0.616 | 3 | 3 | 089, 001, 145 |
| XLSSsC N01 | d | 36.952 | -4.775 | 0.296 | 14 | 4 | 024, 149, 150, 022, 104, 140, 148, 168, 088, 027, 028, 008, 070, 013 |
| XLSSsC N09 | | 37.383 | -5.232 | 0.190 | 4 | 1 | 091, 151, 074, 123 |
| XLSSsC S04 | | 362.695 | -55.135 | 0.131 | 4 | 1 | 570, 511, 569, 568 |
| XLSSsC S10 | | 365.240 | -56.143 | 0.469 | 3 | 2 | 598, 558, 559 |
| XLSSsC S02 | | 365.696 | -53.939 | 0.321 | 6 | 3 | 599, 563, 548, 614, 632, 585 |
| XLSSsC S11 | | 365.917 | -52.967 | 0.534 | 3 | 3 | 626, 562, 508 |
| XLSSsC S09 | | 366.969 | -53.990 | 0.384 | 3 | 4 | 624, 573, 574 |
| XLSSsC S01 | c | 367.142 | -54.103 | 0.171 | 12 | 3 | 565, 600, 601, 514, 536, 623, 627, 535, 635, 629, 620, 520, 518 |
| XLSSsC S03 | | 367.392 | -55.421 | 0.273 | 5 | 4 | 519, 524, 588, 612, 610 |
| XLSSsC S05 | | 367.910 | -54.651 | 0.210 | 4 | 1 | 577, 586, 608, 595 |
| XLSSsC S12 | | 368.449 | -55.882 | 0.808 | 3 | 3 | 583, 521, 575 |
| XLSSsC S13 | | 368.828 | -54.186 | 0.099 | 3 | 1 | 544, 515, 590 |
| XLSSsC S08 | | 369.350 | -52.915 | 0.355 | 3 | 2 | 504, 545, 555 |
| XLSSsC S06 | | 369.601 | -53.530 | 0.275 | 4 | 3 | 526, 591, 557, 622 |
| XLSSsC S07 | | 370.462 | -53.355 | 0.334 | 3 | 4 | 593, 501, 503 |
| XLSSsC S14 | | 371.145 | -54.519 | 0.202 | 3 | 2 | 636, 554, 530 |

by a Voronoi tesselation technique, which will be available in the XXL Master Catalogue browser [3] and at the Centre de Données astronomiques de Strasbourg[4] (CDS) (Chiappetti et al. 2017, submitted).
In the following paragraph, details about the procedure adopted for the superclusters identification will be given.

### FoF detected superclusters

All spectroscopically confirmed C1, C2, and C3 G&C are involved in the search for superclusters in the two XXL-N and XXL-S fields, performed by Adami et al. (2017). The

[3]http://cosmosdb.iasf-milano.inaf.it/XXL
[4]http://cdsweb.u-strasbg.fr

analysis is restricted to the $0.03 \leq z \leq 1.00$ redshift range.
First, a classical three-dimensional FoF was performed to estimate the critical linking length, $\ell_c$, for each field, the one that maximizes the number of superclusters (see, for instance Einasto et al. 2001). This lead, respectively for XXL-N and XXL-S, 27 and 29 $h_{70}^{-1}$ Mpc. Note that performing a FoF analysis by using this value for the linking length would work only for a sample with an homogeneous distribution in redshift. A proper methodology would require a weighting function to weight $\ell_c$. To do this, the authors investigated the density distribution of G&C at different redshifts, used as a tracer of their selection function.
Cluster space densities were measured by dividing the cluster sample in ten bins of redshift and calculating the respective cosmological volumes. The density falls roughly exponentially from z$\sim$0.03 up to z$\sim$0.7, reaching then a plateau until the the last bin that is found to be undersampled. A pure exponential form (given in Equation 2.2) was used to fit the redshift intervals in the range $0.22 \leq z \leq 0.71$, which was found to reproduce closely the exponential plus plateau G&C density behavior.
Thus, each targeted G&C underwent a "tunable" FoF algorithm (Chow-Martínez et al. 2014), which includes an exponential fit for appropriately weighting $\ell_c$ and computing the local linking length, $\ell(z)$, expressed with the following:

$$\ell(z) = \left[\frac{3}{4\pi\, d(z)}\right]^{1/3} \ell_c \tag{2.1}$$

where

$$d(z) = e^{-5.724\, z} \tag{2.2}$$

is the normalised density (weighting) function.
The procedure identifies 21 superclusters in the XXL-N field and 14 in XXL-S, considering only supercluster candidates with a multiplicity (number of G&C members) greater than or equal to 3 (see Table 2.3). An XXL-internal denomination "XLSSsC" was adopted for XXL superclusters to avoid any confusion with individual regular G&C. The centre of each supercluster was calculated as being the geometrical centre of the member G&C. All superclusters described in this section have sizes lower than 60 Mpc, which corresponds to the median value of the largest superclusters found in the local Universe (Chow-Martínez et al. 2014).
A list of the G&C pairs detected with the same FoF-based-procedure just described is also given in the Appendix of Adami et al. (2017) (Table E.1): the list includes 16 G&C pairs in XXL-N and 23 in XXL-S.
Note that the use of a "tunable" linking length allows to detect supercluster candidates even at z$\geq$0.6, where the completeness of the sample drops. Indeed, the algorithm assumes an "additional density" at such redshifts in order to maintain the value of the mean density similar to that of nearby clusters. This mechanism enhances the linking length and therefore the probability of finding "connected" structures. Note that these high-redshift superclusters have to be taken with caution, and are not going to be used in

any of the scientific analysis presented in this thesis. Finally, it is worth noting that at z∼0.8, i.e. the redshift of the most distant supercluster detected in Adami et al. (2017), the linking length is ∼80 Mpc, similarly to the largest superclusters known in literature, namely the Horologium-Reticulum supercluster, whose size measures 95 Mpc (Fleenor et al. 2005).
A 3D Voronoi tessellation technique (Icke & van de Weygaert 1987; Söchting et al. 2012) was then applied to G&C in both XXL fields in order to assess the reliability of the supercluster detection procedure used in the previous paragraph.
Finally, the results of this procedure were compared either to the set of superclusters found in Pacaud et al. (2016) with a different method and to the supercluster found among the XXL-100 brightest cluster sample, finding that the same structures are identified and therefore validating the procedure described in this section. The only noticeable exception is XLSSsC N08 (Table 2.3): the members originally assigned in Pacaud et al. (2016) are now partly associated to XLSSsC N03, not detected in Pacaud et al. (2016) due to the lower number of spectroscopically confirmed G&C in the XXL sample.

## 2.2 Photometric and photo-z databases

The scientific potential of the XXL survey relies heavily on its associated multiwavelength programme. For the XXL-N field, it is possible to resort on different and deep photometric observations. The largest contribution comes from the CFHT Legacy Survey (Veillet 2007, CFHTLS) Wide1 (W1) T0007 data release. Observations were obtained with the 3.6m Canada-France-Hawaii Telescope (CFHT), using the MegaCam wide field optical imaging facility. The MegaCam camera consists of 36 CCDs of $2048 \times 4612$ pixels each and covers a field-of-view of 1 deg$^2$ with a resolution of 0.186 arcsec per pixel. The data cover the observed wavelength range 3500Å$< \lambda <$ 9400Å in the $u^*$, $g'$, $r'$, $i'$, $z'$ filters. Note that the MegaCam filter $i'$ was broken during the survey and a new $i'$ band filter was introduced ("$y'$"). Both filters are considered and included separately in the catalogues.
W1 only covers the XXL region $30.17771 \leq RA(deg) \leq 38.8223$ and $-11.22814 \leq DEC(deg) \leq -3.70516$. To cover part of the remaining regions, observations done by the MegaPipe Group GRZ programme (Gwyn 2008) in the $g$, $r$, $z$ bands were exploited. These observations cover the following areas:

- Field A: $35.10541 \leq$ RA (deg) $\leq 36.09985$,
  $-3.78505 \leq$ DEC (deg) $\leq -2.73612$,

- Field B: $36.06188 \leq$ RA (deg) $\leq 37.05696$,
  $-3.78826 \leq$ DEC (deg) $\leq -2.73855$.

A visual representation of the ensemble of the W1, Field A and B will be given at the end of this section, where I will present the final spectrophotometric catalogue, in Figure 2.11. For the W1 Field, the preferred catalogue to use is the one containing photometric redshifts (photo-z) computed from the Laboratoire d'Astrophysique de Marseille (LAM)

in collaboration with Terapix using the SED fitting software LePhare[5] (Arnouts et al. 1999, 2002; Ilbert et al. 2006). The code consists of a set of Fortran programs and computes photometric redshifts with a standard $\chi^2$ method using SED fitting technique. The Terapix[6] T0007 release of finely calibrated stacks and catalogues and photometric redshift data are publicly available and can be downloaded from the Canadian Astronomy Data Centre (CADC). The version of the photo-z catalogue considered in this work consists of 4613209 sources where the overlapping regions between the observing tiles have been removed through a S/N criterion, and therefore multiple objects have already been removed.
Listed here below the columns from the whole CFHTLS-W1-T0007 catalogue which are relevant in the following:

- **ID:** unique ID for each source, from the merged catalogue from Terapix (digit1=1 for wide, digit2=field, digit3-4=tile, digit6-*=original Id).

- **RA:** J2000, in deg.

- **DEC:** J2000, in deg.

- **flag:** photometric flag from Terapix.

  – flag=0 clean;

  – flag=1 if star according to sextractor (only at observed magnitudes i,y<21);

  – flag>1 if the source falls in a masked region.

- **StarGal:** star/galaxy classification based on the morphology, magnitude and $\chi^2$ (1: star, 0: gal).

- **Final photo-z:** the value assumed corresponds to:

  – z = zPDF if galaxy (median of the maximum likelihood distribution, column 11);

[5] www.lam.oamp.fr/arnouts/LEPHARE.html

[6] Traitement Élémentaire Réduction et Analyse de PIXel (Bertin & Tissier (2007)): it is an astronomical data reduction centre dedicated to the processing of very large data flows from digital sky surveys (e.g. CFHTLS, WIRDS or WUDS, NGVS, CFHQSIR, KIDS/VIKING, UltraVISTA) and giant panoramic visible and near infrared cameras (e.g. MegaCam and WIRCam at CFHT, or OmegaCam on the VST and VIRCam on VISTA at ESO/Paranal). TERAPIX is located at IAP (Institut d'Astrophysique de Paris, website http://terapix.iap.fr).

  - z=0 if star;

  - z=9.99 if strange object (possible QSO/AGN, less than 3 filters for the fit, or reduced $\chi^2$ >100);

  - z=-99.9 if masked area (flag>1).

- `zPDF`**:** photo-z measured using the galaxy templates. Median of the maximum likelihood distribution.

- `zPDF_l68`**:** lower limit of the zPDF measure, corresponding to the 68% confidence level.

- `zPDF_u68`**:** upper limit of the zPDF measure, corresponding to the 68% confidence level.

- `chi2_zPDF`**:** reduced $\chi^2$ (-99 if less than 3 filters) at zPDF (doesn't include the N(z) prior in the $\chi^2$).

- **u:** Observed auto magnitude, already corrected for Milky Way extinction, $u^*$ filter.

- **g:** Observed auto magnitude, already corrected for Milky Way extinction, $g'$ filter.

- **r:** Observed auto magnitude, already corrected for Milky Way extinction, $r'$ filter.

- **i:** Observed auto magnitude, already corrected for Milky Way extinction, old $i'$ filter.

- **y:** Observed auto magnitude, already corrected for Milky Way extinction, new $i'$ filter ($y'$ hereafter).

- **z:** Observed auto magnitude, already corrected for Milky Way extinction, $z'$ filter.

- **u_err:** error on observed $u^*$ magnitude.

- **g_err:** error on observed $g'$ magnitude.

- **r_err:** error on observed $r'$ magnitude.

- **i_err:** error on observed $i'$ magnitude.

- **y_err:** error on observed $y'$ magnitude.

- **z_err:** error on observed $z'$ magnitude.

Table 2.4: Zero-point corrections for the CFHTLS-W1 field. Offsets need to be subtracted to each band.

| $u^*$ | $g'$ | $r'$ | $i'$ | $y'$ | $z'$ |
|---|---|---|---|---|---|
| 0.00978 | -0.04726 | -0.02308 | -0.00567 | -0.01864 | 0.06455 |

First, the Terapix photometric flag reported in (col.5) of the catalogue was used to remove stars (flag=1) and sources in masked regions (flag>1), leading with 4341315 sources over the total. Also bright objects (with observed magnitude $r' \leq 20$) with bad photometric redshift measurements were removed from the sample, in order to avoid high levels of contamination from spurious sources, such as saturated stars.

Observed magnitudes have been corrected for zero-point offsets which are given in the CFHTLS-T0007 explanatory document, and that have been computed by comparing the observed and modeled fluxes from a subsample where spectroscopic redshifts were available. The values of the zero-point corrections that I adopted to correct observed magnitude depend on the band of observation and are given in Tab. 2.4.

No photo-z estimates are available for the Field A and Field B regions. I verified that also observed magnitudes in the two fields A and B were already corrected for zero-point offsets, by using a common subsample of galaxies with the W1 Field, and I created a unique photometric catalogue removing the overlap regions between W1, Field A and Field B: the final number of sources is 4508438.

Then, I complemented the sample with other photo-z measurements in the W1 Field (Sotiria Fotoupoulou, private communication, SF catalogue hereafter). The catalogue contains aperture magnitudes in $g'$, $r'$, $i'$, $z'$, $J'$, $H'$, $K'$ bands for 4887 galaxies. Using a common subsample of the SF catalogue and of the CFHTLS W1 catalogue, I performed a linear fit between aperture magnitudes from SF and total magnitudes from CFHTLS in order to derive a conversion factor for each one of the filters $g'$, $r'$, $i'$, $z'$: the offsets and slopes of the relations are written in each panel of Figure 2.6 and are used to convert aperture magnitudes into total ones for the 4887 matched objects. It is important for the scientific analysis of this thesis to point out that the aperture to total magnitude correction derived from Figure 2.6 refers to the most general spectrophotometric sample, which includes all redshifts and observed magnitudes. Indeed, I applied the correction before performing any cut and analysis on the sample. In order to test *a posteriori* the methodology, I proceeded in several ways.

First, I computed the aperture to total magnitude correction using only the sample I am going to consider in the scientific analysis (i.e. cutting in magnitudes and in the redshift ranger: r$\leq$20.0 and 0.1<z<0.6), and I compared the resulting total magnitudes with the previous estimates. The result is given in the left panel of Figure 2.7, showing the redshift-stellar mass plane, where all galaxies I will consider from Chapter 5 are shown and the data points are colour coded according to the difference in the total magnitude estimates in the r-band (Delta_r). The data that should be considered for this comparison are those above the black line, that is in the mass complete sample. As noticeable from the plot,

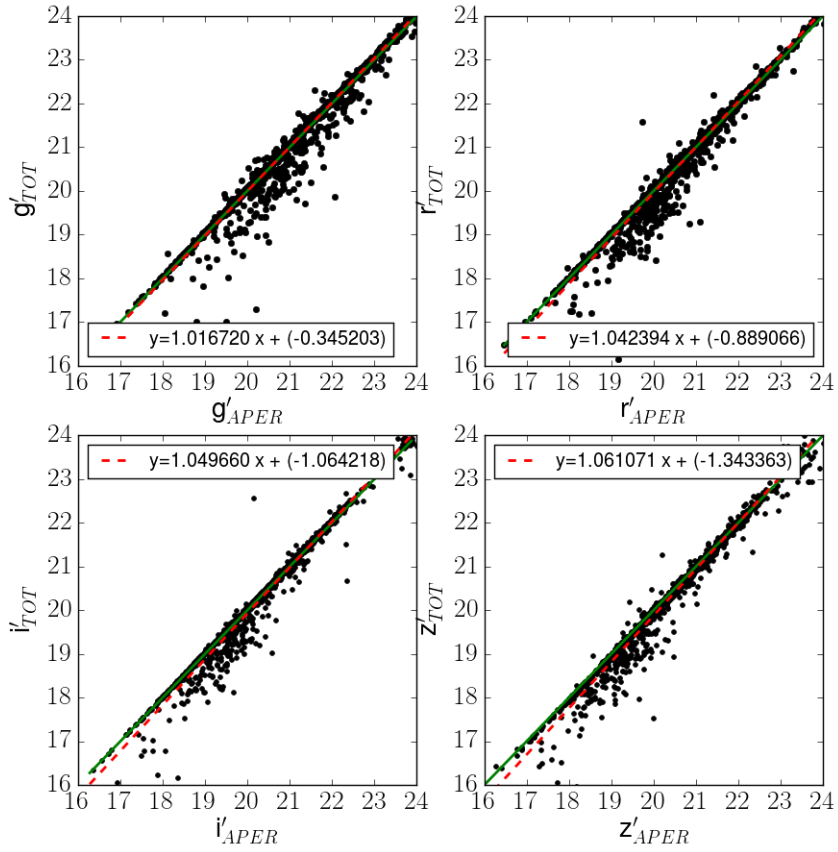


Figure 2.6: Relation between aperture and total magnitude for the SF photometric catalogue (see text for details). Each panel refers to a different band, the red line is the linear fit which was used to convert aperture magnitudes into total ones for the whole SF catalogue, and the green line is the 1:1 relation.

the differences are small and are distributed around a mean value of 0.15 magnitudes.

Second, from Figure 2.6 I isolated all the objects lying on the 1:1 line, that is those having a star-like light profile. I noticed by looking at their colours and magnitudes that they are blue and bright galaxies which are likely to be central starburst galaxies, and therefore their light profile is peaked towards the center.

Third, I tested the differences between total magnitudes as computed here with those computed with a completely independent method by Fotopoulou et al. (2016) for the galaxies in common, probing that differences in the results are negligible. An histogram of the difference between the two estimates is given in the right panel of Figure 2.7.

Finally, I verified that the correction I applied is not affecting the scientific results. In the final sample only 0.8% of galaxies (a tenth of which are in G&C) over the total have

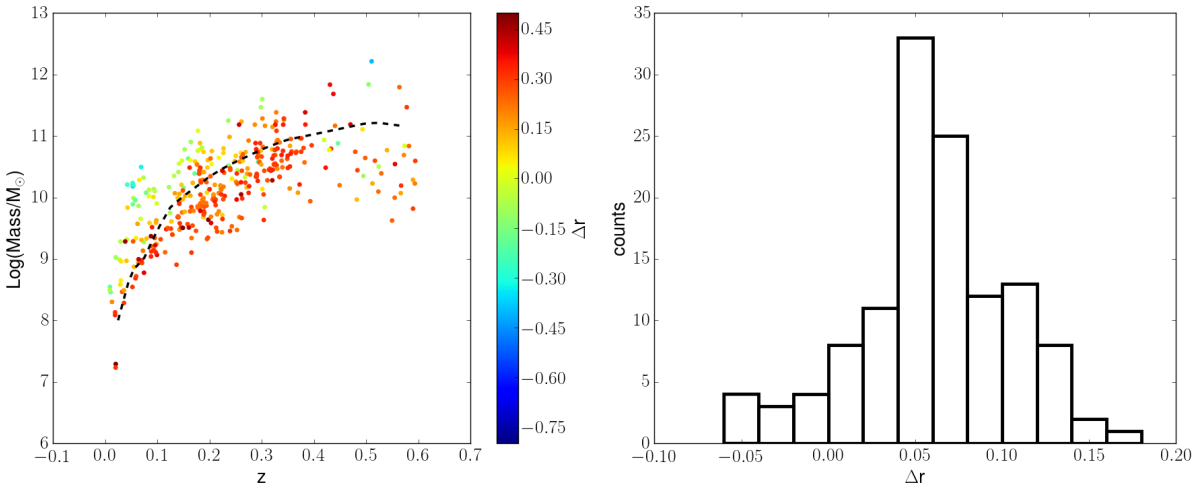


Figure 2.7: Left panel: comparison between the aperture-to-total magnitude correction computed using the whole sample and that used in the scientific analysis. Galaxies are shown in the stellar mass-redshift plane and colour coded for the difference in total r-band magnitude. The black dashed line represent the stellar mass limit at each redshift, defining the minimum mass of galaxies in the mass complete sample at each redshift. Right panel: Difference between the total magnitudes computed by the method described in this thesis and an independent method in Fotopoulou et al. (2016).

total magnitudes obtained from the correction of aperture magnitudes. Here below I give some statistics divided in redshift bins about this sample which will prove that they will not affect the final results:

- $0.1 \leq z < 0.2$: 99 galaxies over 5322 (1.8%), 94/4402 (2%) in the field and 5/920 (0.5%) in G&C.
- $0.2 \leq z < 0.3$: 59 galaxies over 5156 (1.1%), 54/4654 (1.1%) in the field and 5/502 ($\sim$1%) in G&C.
- $0.3 \leq z < 0.4$: 26 galaxies over 2655 (<1%), 21/2468 (0.85%) in the field and 5/187 (2.6%) in G&C.
- $0.4 \leq z < 0.6$: 9 galaxies over 2736 (0.3%), 7/2595 (<0.3%) in the field and 2/141 (1.4%) in G&C.

Errors on total magnitudes are computed by combining in quadrature the mean error on the estimates calculated in 0.5 magnitude bins and the root mean square (rms) of the aperture-to-total magnitude relation shown in Figure 2.6, calculated using the same binning in magnitude.

The total number of sources contained in the photometric catalogue is the sum of the W1, Fields A, B and SF catalogues and is 4513325.

Note that all magnitudes used are Sextractor `MAG_AUTO` magnitudes (Bertin & Arnouts 1996) in the AB system corrected for Milky Way extinction according to Schlegel et al. (1998).

Table 2.5: Surveys included in the first release of the CeSAM XXL database and contributing to our galaxy sample. Entries in the first column are reported as appear in the SpecOrigin column in the original database, and in the second column they have been grouped into main surveys and observing programmes relative to a given instrument or telescope. The *Field* column indicates which XXL area is covered by the survey (North (N), South (S), or both), and the *Type* column indicates the source of the data: E (External), PI (XXL or XMMLSS PI).

| SpecOrigin in the spectroscopic database | Parent survey and References | Field | Type |
|---|---|---|---|
| AAT_AAOmega | Lidman et al. (2016) - XXL Paper XIV | S | PI XXL |
| AAT_AAOmega_GAMA | GAMA, Baldry et al. (2018) | N | E |
| AAOmega2012 | Adami et al. (2018) - XXL Paper XX | N | PI XXL |
| Akiyama | Akiyama et al. (2015) | N | E |
| Alpha_compilation | Adami et al. (2011) | N | PI XMMLSS + E |
| ESO_Large_Programme | Adami et al. (2018) - XXL Paper XX | N+S | PI XXL |
| LDSS03 | Adami et al. (2011) | N | PI XMMLSS |
| Magellan | Adami et al. (2018) - XXL Paper XX | N | E (XXL agreement) |
| Milano | Adami et al. (2011) | N | PI XMMLSS + E |
| NED | | N+S | E |
| NTT | Adami et al. (2011) | N+S | PI XMMLSS |
| SDSS_DR10 | SDSS, Ahn et al. (2014) | N | E |
| Simpson | Simpson et al. (2012) | N | E |
| SNLS | Balland et al. (2017, in preparation) | N | E |
| Stalin | Stalin et al. (2010) | N | E |
| Subaru | Akiyama et al. (2015) | N | E |
| VIPERS/XXL | VIPERS, (Scodeggio et al. 2016) | N | E |
| VVDS_Deep | VVDS, Le Fèvre et al. (2005) | N | E |
| VVDS_UD | VUDS, Le Fèvre et al. (2015) | N | E |
| XMMLSS | Adami et al. (2011) | N | PI XMMLSS |
| WHT | Koulouridis et al. (2016) - XXL Paper XII | N | PI XXL |

Note that whenever I will make use of photo-z estimates throughout the thesis I will specify the selection criteria starting from the sample built here.

## 2.3 Spectroscopic database

The galaxy spectroscopic information is hosted in the CeSAM (Centre de donnéeS Astrophysiques de Marseille) database in Marseille[7]. The database contains data for both the XXL G&C and the galaxies in the same area. Besides some XXL dedicated observing runs (Adami et al. 2018), many other surveys have observed the galaxies in this field and the database includes them all. In particular, all redshifts from the VIMOS Public Extragalactic redshift survey (VIPERS), covering the redshift range $0.4 < z < 1.2$, were made

[7]http://www.lam.fr/cesam/

available for this analysis prior to the recent public release (Scodeggio et al. 2016). As a result, there is a wide variety of spectra of different quality and origin to deal with. The final spectroscopic data release (CeSAM-DR2) is public and can be downloaded directly from the database; the complete list of the surveys and observing programmes included is given in Table 2.5. The samples included in the table refer to both XXL fields, but, as here I focus only on the XXL-N, I present the results only for this region.
The sample contains 134604 sources; 25421 of them refer to multiple observations of the same objects from different surveys, but the multiple measurements are not flagged in CeSAM. To remove the duplicates, I defined two different selection criteria, both based on sets of priorities on observational properties of galaxies. The first set regards the origin of the considered spectrum (the *SpecOrigin* column in the database catalogue). The different surveys are divided into three classes of priority (*origin flag*: 1, 2, 3), based on the availability of spectra in the database and on their quality: the smaller the value the higher the priority. The list of the surveys with their attributed *origin flag* is given below:

1. (AAT_AAOmega, entirely in the South), AAT_AAOmega_GAMA, ESO Large Programme, AAOmega2012, NTT, WHT, XMMLSS, SDSS_DR10.
2. VIPERS/XXL, VVDS_UD, VVDS_deep.
3. Akiyama, Alpha_compilation, LDSS03, Milano, NED, SNLS, Simpson, Stalin, Subaru, Magellan.

The second set of priorities is chosen on the basis of the reliability of the redshift measurement, as given by each survey (the $z_{flag}$ column in the database catalogue). I grouped all the possible values assumed by this flag in the different surveys into five classes (*quality flag*: 0, 1, 2, 3, 4): the larger the value the higher the precision and reliability of the redshift estimate. In the following I list all the original *flags* as they are in the CeSAM XXL spectroscopic database and the corresponding *quality flag* (the first number of the list) as they are in the final catalogue that is released in Guglielmo et al. (2017) (see Chapter 4).

0. -99.99 ($z_{flag} <$ -13.0 in the routine), 0, 20;
1. 1, 11, 21, 31, 311, -11;
2. 2, 9, 12, 19, 22, 29, 32, 39, 312, 319, 219, 75;
3. 3, 13, 23, 33, 313;
4. 4, 5, 14, 24, 34, 314.

The selection for multiple measurements is then based on a consequential criterion that considers both priorities: the redshift of the entry with smaller *origin flag* is considered and, if more entries have the same *origin flag*, the *quality flag* is considered, giving priority to the largest value.

10165 out of 25421 objects with multiple redshift are selected using this method. In a further 3123 cases both flags coincide: for these, one spectrum is selected interactively and 1158 single objects are finally included in the catalogue.
The "cleaned" spectroscopic catalogue is the ensemble of the catalogue of single spectra found in the parent catalogue (109183 sources), of the zflag/SpecOrigin selected objects (10165 sources) and of the hand selected ones (1158 sources), and therefore it contains 120506 galaxies. Overall, the uncertainties on the galaxy redshift in the database vary from 0.00025 to 0.0005, computed from multiple observations of the same object and depending on the sample used (more details on the XXL spectroscopic database are given in Adami et al. 2018); I consider the largest value in this range as the typical redshift error for all objects.
The main surveys contributing to the final spectroscopic catalogue are, in decreasing order of importance: VIPERS with 51% of all redshifts; GAMA (Galaxy And Mass Assembly) with 27% of all redshifts; SDSS with 10% of all redshifts; VVDS+VVUD with 7% of all redshifts; XMMLSS with $\sim 1\%$ of all redshifts; ESO + WHT observations with $\sim 0.5\%$ of all redshifts.
The redshift distribution of the "cleaned" catalogue of galaxies is shown in the left panel of Figure 2.8: the vertical red dashed line corresponds to $z = 0.6$, the maximum redshift of G&C considered in this work. In the right panel, the main surveys contributing to the "cleaned" sample are shown separately: as it is evident from the histograms, in the redshift domain below the $z = 0.6$ cut, the main contributors to the catalogue are, in decreasing order of importance: GAMA (51%), VIPERS (26%), SDSS (13%), and VVDS+VVUD (4%). Indeed, the first peak in the redshift distribution going from low- to high- redshift is due to GAMA galaxies, whose number is negligible at higher redshifts. The second peak, instead, is due to the growing contribution of VIPERS redshifts which reach their maximum number just beyond the $z = 0.6$ threshold and therefore have lower incidence in the final sample. Furthermore, as will be pointed out in the following chapters, the magnitude distribution of VIPERS galaxies is shifted towards fainter magnitudes than those that included in the magnitude limited sample of this work: hence, the number of VIPERS sources finally involved is negligible.

### WHT Observations

I was personally involved in a spectroscopic observing run aimed at providing further spectroscopic redshifts (Lonoce, private communication) in the center of a supercluster (XLSSsC N01) at $z \sim 0.3$ in the XXL-N field. Observations were conducted with the AF2 multifiber spectrograph at the 4.2m William Herschel Telescope (WHT, La Palma Island, Spain) during 8 nights from the 22th to the 29th of January, 2017, during a campaign belonging to the WEAVE project. These data and their analysis will be presented in Lonoce et al. 2017, in preparation[8].
AutoFib2+WYFFOS (AF2) is the multi-object, wide-field, fibre spectrograph working at the Prime focus of the 4.2m William Herschel Telescope (WHT). It contains 150 science

[8]see http://www.ing.iac.es/weave/science.html for more information on the WEAVE project.

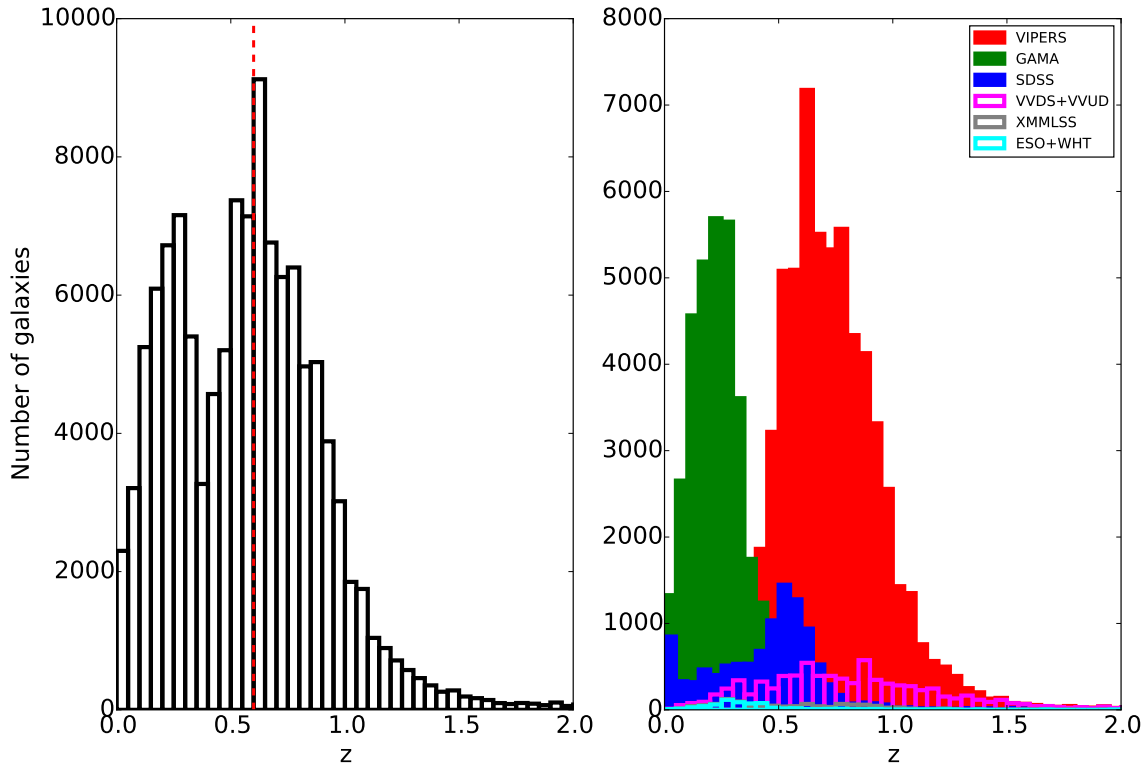


Figure 2.8: Left panel: redshift distribution of the "cleaned" spectroscopic sample of galaxies (120506) from the CeSAM XXL spectroscopic database relative to the XXL-N field. The vertical red dashed line corresponds to $z = 0.6$, the maximum redshift of G&C considered in this work. Right panel: redshift distribution of the main surveys included in the same sample.

fibers each of 1.6 arcsec diameter, and 10 fiducial bundles for acquisition and guiding. At the Prime focus, the fibers are placed onto a field plate by the robot positioner Autofib2 at user-defined sky coordinates. Object light is transmitted along fibers 26 metres in length to the Wide Field Fibre Optical Spectrograph (WYFFOS). Observations were carried out using two gratings, one covering the blue and one covering the red portion of the spectrum, and having a window of 200 Å of superposition:

- 10h00 (30 exposures of 1200 sec each) using R1200R grating, centered at 6350 Å and covering the range 5700-7000 Å with a resolution of 2.0 Å.

- 07h20 (22 exposures of 1200 sec each) using R1200B grating, centered at 5200 Å and covering the range 4500-5900 Å with a resolution of 2.2 Å.

Important technical details related to the telescope and the instrument are listed in Table 2.6.
The fiber positioning is subject to limitations: there is a minimum fibre spacing of about 30 arcsec, and the radially moving rods that hold the fibers are not allowed to cross. The

Table 2.6: Main parameters for the current AUTOFIB2 plus WYFFOS system.

| | |
|---|---|
| *Prime Focus* | |
| Field diameter | 1 degree |
| Unvignetted field | 40 arcmin |
| Plate scale | 17.6 arcsecmm$^{-1}$ (57.0 $\mu$marcsec$^{-1}$) |
| Focal ratio | f/2.81 |
| | |
| *AUTOFIB2* | |
| Fiducial fibres | ten 7-fibre guide bundles, 1 arcsec resolution |
| Science fibres (Large) | $126 \times 153\mu$m diameter (2.7 arcsec) |
| Cycle Time | $\sim$16 sec/fibre |
| Positioning accuracy | Better than 10 $\mu$m (absolute) |
| Science fibres length | 26m |
| | |
| *WYFFOS* | |
| Collimator | f/8.2; $f$=820 mm |
| Short Camera | f/1.2; $f$=132 mm |
| Dispersion: Reflection mode | 11.5 - 0.8 Åpixel$^{-1}$ |
| Resolving Power: Echelle mode | $\sim$8000 |
| Pixel size | 24 $\mu$m |

first important part of the observation planning is to create the mapping between the objects that will be observed during a particular WYFFOS exposure and the fibres that will observe them. Simulations using *af2_configure* have to be done in order to charaterise the aforementioned limitations and produce the optimal configuration that meets the scientific requirements of the observations. In its most general mode it will take an input file with the coordinates (RA, DEC) of the objects, create a fibre to object mapping using a placement algorithms, and then allow the user to edit the placement interactively. Three files are required for input to the program: a fibre information file, a telescope information file and an object field file.
AutoFib2 has two basic type of fibers, programme or fiducial. The former are used for the programme objects and the latter for fiducial or guide objects. Both of these types of fibers are assigned a status according to one of these criteria:

Missing: the fiber is physically missing.

Disabled: the fiber has been disabled.

Dead: the fiber has very low transmission.

Ok: the fibre can be used for placement.

This file also contains other information such as the park position of each fibre and their current x,y positions.

The telescope information file is provided with *af2_configure* and stores the scale and distortion of the field of the telescope.
The only input file required of the user is the file which contains the coordinates of the objects to be observed, hereafter the *field file*. The *field file* can be arbitrarily named by the user, as long as it has the extension '.fld'. It has two sections: the header and the object information. The header contains general information about the field that is going to be observed, among the others the name of the field, the date of observations, the equinox of the field centre and its coordinates RA and DEC. The object table includes the following quantities:

- **Name:** This should be any alphanumeric string representing the object name.

- **RA:** The hours and minutes must be expressed as integers; the seconds should be expressed as a real.

- **DEC:** The degrees and minutes must be expressed as integers; the seconds should be expressed as real.

- **Type:** This is the object type and can assume one of three values:

**P-** Programme object.

**F-** Fiducial object.

**S-** Dedicated sky patch.

- **Weight:** The user can weight the objects in order to increase the chance that a particular object will be allocated. The weighting can be according to any arbitrary scheme so long as the value is expressed as a real number which is greater than or equal to zero. Weights will be interpreted in the sense that a higher numerical value corresponds to a higher weight.

- **Magnitude:** This is an estimate of the magnitude of the object in any band and it is optional.

- The rest of the line can be filled with any other information about the object.

As an example, the following lines are selected from the *field file* relative to the observations of the XLSSsC N01 supercluster:

1111_155819 2 28 25.75 -5 0 37.11 P 25.0 19.48

1 2 26 54.73 -4 41 1.89 F 99.0 14.06

The weight parameter was set to 99.0 for spectroscopic objects and for stars, and to 25.0 for photo-z candidates. Magnitudes are expressed in the Johnson-Cousins photometric system, I_AB band.

Focusing on the object type, in the following I will give details about the procedure I followed for the preparation of the target catalogue. The centroid coordinates of the observed substructure of G&C belonging to the XLSSsC N01 supercluster, i.e. the coordinates of the center of the observed field are: $\mathrm{RA_{cen}} = 36.9125$, $\mathrm{DEC_{cen}} = -4.7875$, $\mathrm{z_{cen}} = 0.299$.

**Target selection:**

I selected the scientific targets from spectroscopic and photo-z putative members of a substructure of G&C within XLSSsC N01 supercluster. Note that the astrometry is the same for both the spectroscopic and photo-z samples and is given by the CFHTLS catalogue. A first selection criterion is based on the extension of the unvignetted Field of View (FoV) of the prime focus (20 arcmin of circular radius), which corresponds to a projected distance of $\sim 0.33\,\mathrm{deg}$ in the plane of the sky. I considered only targets within a circular radius of 0.33 deg with respect to the field center. Spectroscopic members are selected in the redshift range $0.285 \leq \mathrm{z} \leq 0.32$, and are galaxies whose spectroscopic redshift lies within $3\sigma$ from their G&C mean redshift, where $\sigma$ is the velocity dispersion of their host G&C, and located within a projected distance of $3 \times r_{200}$ with respect to each G&C center. Photo-z putative members are galaxies located within a projected distance of $3 \times \mathrm{r_{200}}$ with respect to each G&C center, and whose photo-z lies within $1\sigma_{photo-z}$ with respect to the spectroscopic redshift of each G&C. $1\sigma_{\mathrm{photo-z}} = 0.04$ is the typical error on the photo-z estimate, computed as a redshift-dependent quantity: $0.031 \times (1+\mathrm{z_{GC}})$, $z_{GC}$ being the mean redshift of the supercluster. Among all selected objects, I considered as good candidates for observations only those with a magnitude $I_{AB} \leq 20.5$. The total number of scientific targets given as input to the configuration program is 269, 93 of which are spectroscopic members and the rest are photo-z putative members.

**Fiducial stars selection:**

It is important to point out that the astrometry should be the same for fiducial and science targets in order to ensure the most accurate positioning of the fibers given their reduced diameter. Nevertheless, the CFHTLS sample lacks sufficiently bright stars, with magnitude $\mathrm{V_{AB}} \leq 15$ either because they're saturated or because their astrometry is not accurate enough. I selected fiducial stars from the SDSS dr12 catalogue, with the following requirements: they have to be within a square of 30 arcmin (i.e. 0.5 deg) semi-length in RA and DEC with respect to the centroid of the substructure, in the magnitude range: $13 < V_{AB} < 16$ and with a total proper motion close to zero, i.e. $\mathrm{pm_{tot}} = \sqrt{\mathrm{ra,pm^2 + dec,pm^2}} \leq 10.0$ mas/yr. I applied a proper corrections to the SDSS astrometric system in order to correct for small differences with respect to the CFHTLS one.

**Sky:**

Sky fibers were finally added manually in random positions.

Figure 2.9 represents the final selection of targets within the unvignetted area of AF2, shown with a red circle: all G&C pertaining to XLSSsC N01 supercluster are represented

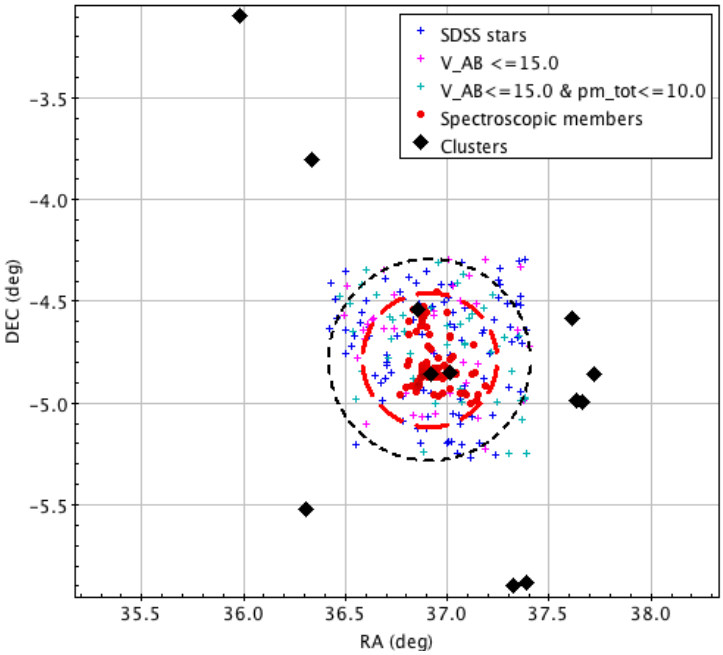


Figure 2.9: XLSSsC N01 supercluster field: G&C pertaining to XLSSsC N01 supercluster are represented with black diamonds. The unvignetted field of view of the prime focus of WHT is shown with a red circle. Galaxies already known as being spectroscopic members of the structure with $I_{AB} \leq 20.5$ are represented with red dots. Fiducial stars with $13 < V_{AB} < 16$ extracted from the SDSS dr12 are represented with blue crosses and are located on a wider area of 30 arcmin in the focal plane, represented with a black circle: among them, the subsample with $V_{AB} \leq 15$ is shown with magenta crosses, and a further subsample with $V_{AB} \leq 15$ and the lowest proper motions $pm_{tot} < 10$ mas/yr are shown with cyan crosses.

with black diamonds, already known spectroscopic members with $I_{AB} \leq 20.5$ are represented with red dots. Fiducial stars with $13 < V_{AB} < 16$ are represented with blue crosses and are located on a wider area of 30 arcmin in the focal plane, represented with a black circle: among them, the subsample with $V_{AB} \leq 15$ is shown with magenta crosses, and a further subsample with $V_{AB} \leq 15$ and the lowest proper motions $pm_{tot} < 10$ are shown with cyan crosses.
The *af2_configure* software finally selected 60 scientific targets, 6 fiducial stars and 23 sky fibers. An excerpt of the output configuration file '.cfg' generated is given here below, and the corresponding setup of AF2 is shown in Figure 2.10: the dark coloured fibers rods hold fiducial bundles; plusses denote objects, star symbols denote fiducial stars, and open circles denote background or sky positions.

⋆ Telescope info from wht_prime.dat

⋆ Field diameter (mm) 205.00

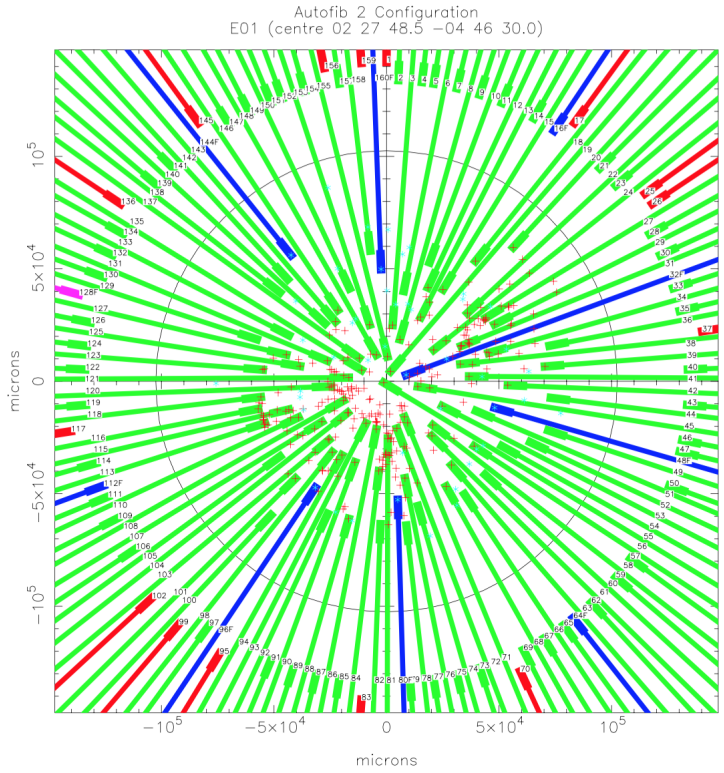


Figure 2.10: Final configuration of the AF2 fibers in the observed field. The dark coloured fibers rods hold fiducial bundles; plusses denote objects, star symbols denote fiducial stars, and the remaining green fibers are background or sky positions. Fibers which are not located beyond the black circle are either parked or disabled fibers and are not going to be used during the observations.

⋆ Telescope scales as follows: 17.643 320.00 2.0000

TARGET XLSSsC N01

UTDATE 2017.1

EQUINOX 2000.0

SKYPA 36.00

FIBRES SMALL

CENTRE 02 27 48.5 -04 46 30.0

HA 0.0

1 DISABLED

2 PARKED

3 111965 2 28 3.18 -4 40 5.58 P 99.0 19.00

4 PARKED

5 PARKED

6 PLACE_XY 02 28 8.882 -04 35 39.688 7676 40127

7 PARKED

8 1111_235014 2 27 55.69 -4 41 2.54 P 25.0 20.24

9 PARKED

10 PLACE_XY 02 28 6.700 -04 30 43.322 19138 52868

11 PARKED

12 114924 2 27 59.72 -4 33 28.01 P 99.0 19.88

13 1102_15277 2 27 53.68 -4 37 5.84 P 25.0 20.11

14 PARKED

15 1102_29559 2 27 52.78 -4 32 31.32 P 25.0 20.36

16 PARKED

17 DISABLED

18 2645 2 27 47.74 -4 27 8.92 P 99.0 20.41

19 1111_217690 2 27 49.86 -4 45 8.25 P 25.0 20.07

20 1102_61416 2 27 36.14 -4 22 57.51 P 25.0 19.27

The first ten lines recall the input information described at the beginning of the section, then the status of each fiber is described: scientific targets and fiducial stars are written as in the input file, sky fibers are positioned by hand in the 'PLACE_XY' lines. Fibers which are not used are either 'PARKED' or 'DISABLED'.
The WHT observations yielded 59 spectra of galaxies in the XLSSsC N01 supercluster field, from which 52 could be measured. Of these, 17 new redshifts (Lonoce, private communication) were obtained from photo-z putative candidates. These redshifts were added to the spectroscopic catalogue I used, to produce the spectrophotometric catalogue described below.

## 2.4 Matching spectroscopy with photometry

As last step, I matched the photometric catalogue described in Section 2.2 resulting from the combination of the CFHTLS W1 field with Field A, B and SF catalogues, with the "clean" spectroscopic catalogue described in Section 2.3 plus the redshifts measured in the WHT observing run. I performed a match in coordinates between the two catalogues

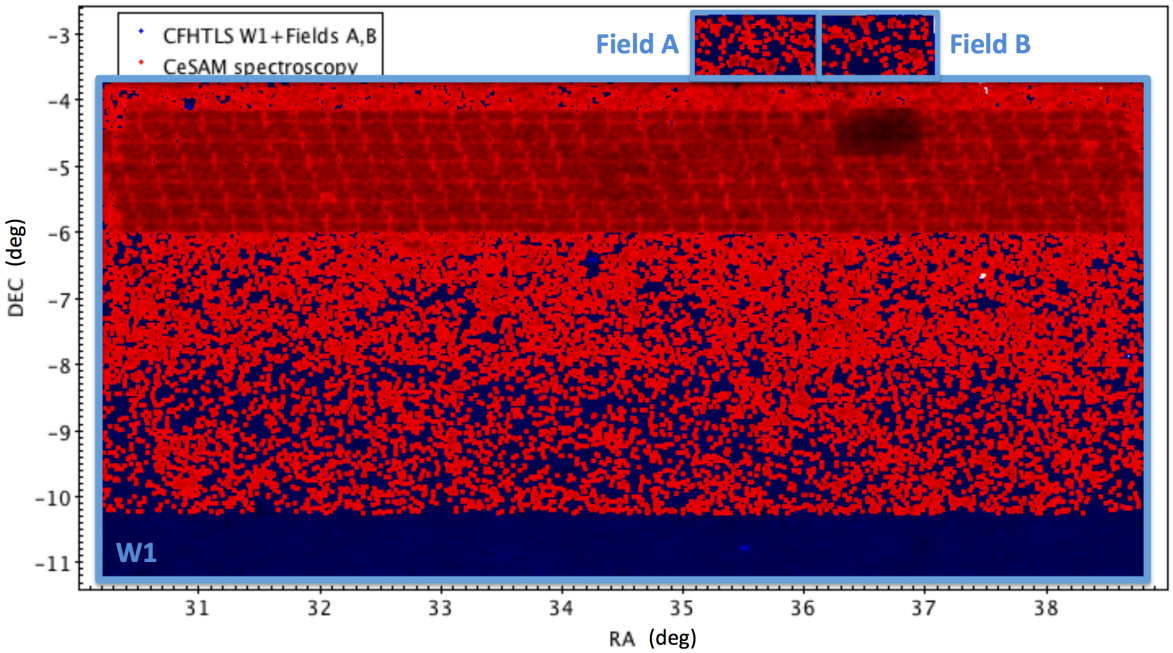


Figure 2.11: CFHTLS W1, Fields A and B photometric catalogue, in blue, and CeSAM spectroscopic catalogue restricted to the photometric area, in red. Different signatures in the spatial distribution of the galaxies within the spectroscopic catalogue correspond to different sampling of the area performed by different surveys. In particular, the denser chess-board pattern in the upper part of the field ($-6 \lesssim DEC \lesssim -4.25$) corresponds to the VIPERS data and the majority of the other red points are from the GAMA survey.

within a maximum tolerance radius of 1 arcsec, obtaining 113749 galaxies. Then I excluded targets with redshifts $z \sim 0$ to avoid being contaminated by stars, and 113240 galaxies constitute the final catalogue.
In Figure 2.11 the CFHTLS W1, Fields A and B photometric catalogue (4508438 sources) is shown together with the spectroscopic sample in the same region in the sky (114467 sources). Note that no redshift cut was applied in the spectroscopic catalogue that is shown in the figure.

# 3

# DERIVED PROPERTIES OF GALAXIES

## Content

In this chapter I will discuss the methods adopted to compute the properties of the galaxy samples presented in Chapter 2. Specifically, I will introduce the definition of global environment according to the virial properties of G&C, and the two codes used to derive the main properties of galaxies. Starting from the redshift and observed photometry I could apply a SED fitting code (LePhare, Arnouts et al. 1999; Ilbert et al. 2006) to derive absolute magnitudes and stellar masses for the whole spectrophotometric catalogue described in the end of Chapter 2. Stellar population properties are derived from full spectral fitting technique by taking advantage of the software SINOPSIS (Fritz et al. 2007, 2011, 2017). The code was applied to a selection of good quality and high resolution spectra from the whole sample in order to derive the current star formation rate, the star formation history, average stellar ages and the equivalent width of all emission and absorption lines characterising each spectrum. I will describe the relevant quantities used in this thesis in the end of the chapter.

## 3.1 Definition of the environments

To determine which galaxies are part of G&C, the computation of the velocity dispersions of the structures is first needed. Starting from the $M_{500,scal}$ computed from scaling relations (see Chapter 2), I calculated $M_{200}$ using the relations given in Balogh et al. (2006), which are based on the concentration-mass relation derived through cosmological numerical simulations in Dolag et al. (2004):

$$\frac{M_{200}}{M_{500,scal}} = \begin{cases} 1.30 & \text{if} \quad 8\times10^{12}M_{\odot} < M_{500,scal} \leq 5\times10^{13}M_{\odot} \\ 1.35 & \text{if} \quad 5\times10^{13}M_{\odot} < M_{500,scal} \leq 2\times10^{14}M_{\odot} \\ 1.40 & \text{if} \quad M_{500,scal} > 2\times10^{14}M_{\odot} \end{cases}$$

Then, the velocity dispersion $\sigma_{200}$ can be obtained from $M_{200}$ using the relation given in Poggianti et al. (2006) (originally given in Finn et al. 2005), which is based on the virial

theorem:

$$\sigma_{200} = 1000\,\mathrm{km\,s^{-1}} \cdot \left( \frac{M_{200}}{1.2 \cdot 10^{15} M_{\odot}} \cdot \sqrt{\Omega_{\Lambda} + \Omega_0 (1+z)^3} \cdot h \right)^{1/3} \tag{3.1}$$

Note that these velocity dispersions are derived from X-ray-based mass estimates and are more reliable than values obtained from galaxy redshifts, especially for structures containing just a few members.
Finally, $r_{200}$ is derived from $r_{500,scal}$, simply dividing the latter by 0.7, according to the relation adopted in Ettori & Balestra (2009).
A galaxy is considered member of a G&C if its velocity $v_{gal} = c(z_{gal} - z_{G\&C})/(1 + z_{G\&C})$ lies within $\pm 3\sigma_{200}$ where $z_{gal}$ is the spectroscopic redshift of the galaxy and $z_{G\&C}$ the redshift of the G&C, and if its projected distance from the G&C centre is a given fraction of $r_{200}$, according to the scientific goal of the study. Throughout the scientific analysis of this thesis I will use either (a) a projected distance $< 3\,r_{200}$, (b) or from 1 to 3 $r_{200}$ ("outer membership" region), or (c) $< 1.5\,r_{200}$ or even $< 1.0\,r_{200}$ ("inner membership" region).
The adopted definition of membership is suited in case of low statistical number of G&C members, as for the samples treated in this thesis. This same definition was previously adopted in the context of the WINGS survey in e.g. Moretti et al. (2017), and further refined in Biviano et al. (2017), who accurately computed the level of contamination due to interlopers, and found that the resulting more refined values of the velocity dispersion $\sigma_{200}$ lowered by a factor 10%. Confidently enough, such a contamination error would not be able to affect our scientific results given the low number of galaxies identified as members of the single G&C, especially in the outskirts.
As a general definition, the field sample is the ensemble of all galaxies not belonging to any G&C. Note that, due to the detection limit and sensitivity of X-ray observations, at higher redshift only higher mass G&C are detected. As a consequence, galaxies that belong to lower mass structures at these redshifts (i.e. groups which are below the adopted X-ray thresholds, including C3 objects) are included in the field sample, and can in principle contaminate it.

## 3.2 Spectrophotometric models

Two different approaches have been undertaken for deriving the main properties of galaxies starting from observed quantities. I computed stellar masses and absolute magnitudes through a SED fitting code, LePhare[1]. Star formation histories, average stellar ages, equivalent widths of emission and absorption lines of galaxies were derived by analysing their integrated spectra by means of the spectrophotometric code SINOPSIS[2].
The main features of the codes, as well as a detailed description of input/output parameters will be detailed throughout the chapter.

[1]http://www.cfht.hawaii.edu/ arnouts/lephare.html
[2]http://www.crya.unam.mx/gente/j.fritz/JFhp/SINOPSIS.html

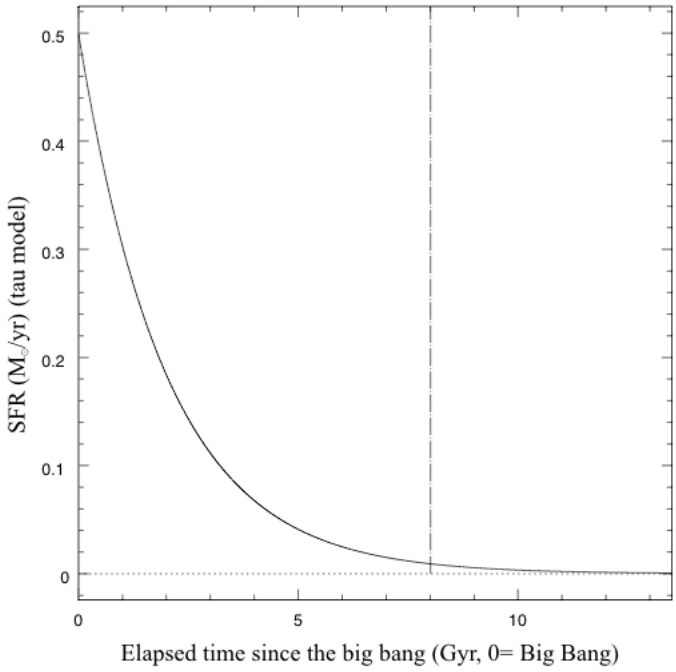


Figure 3.1: Bruzual & Charlot exponentially declining SFH with $\tau$=2 parameter. The vertical line corresponds to the age of 8 Gyr. From that moment on, the galaxy has a negligible SFR.

### 3.2.1 LePhare

LePhare (Arnouts et al. 1999; Ilbert et al. 2006) is a set of fortran programs mainly developed to compute photometric redshifts and to perform SED fitting. The method is based on the comparison between the observed colours of galaxies with those expected from template SEDs. In this thesis, I ran the code to compute physical properties of galaxies, namely stellar masses and absolute magnitudes, keeping the spectroscopic redshift fixed as input parameter in order to improve the quality of the physical outputs.
The package is composed of three parts:

1. A preliminary phase to select the SED models, the set of filters and to compute the template magnitudes, using stand-alone programs. They allow to extract basic informations relative to the filters($\lambda_{mean}$, AB-corrections, attenuation) and SEDs (k-correction vs z, colour-colour diagrams). Operatively, at this stage the user must complete the following steps:

   - Selection of a list of SEDs relative to stars, QSOs, and galaxies.
   I used the default LePhare lists for the stellar and QSO libraries, which are a composite ensemble of different prescriptions from the literature (e.g. in the stellar

library a number of SED relative to main sequence stars are taken from Pickles 1998, low-mass stars from Chabrier et al. 2000 and white dwarfs from Bohlin et al. 1995). The galaxy library was built from Bruzual & Charlot (2003) models, considering an exponentially declining star formation histories SFH $\propto 1/\tau \cdot \exp(-t/\tau)$, where $t$ is the time since the age of formation, set at 13.5 Gyr, and $\tau$ is the decay time, i.e. the timescale of the star formation process.
All free parameters governing the spectral synthesis models are summarised in Table 3.1.

Out of the whole library of available models, 27 Bruzual & Charlot (2003) models

Table 3.1: Parameters used for the library of templates.

| | |
|---|---|
| IMF | Chabrier |
| SFH prescription | Exponential |
| Time-scales $\tau$ (Gyr) | 0.1, 0.3, 1, 2, 3, 5, 10, 15, 30 |
| Redshift intervals | ranging from 0.0 to 1.8, with a spacing of 0.02. |
| Metallicity | $Z_\odot$ |
| E(B-V) | 0., 0.05, 0.1, 0.15, 0.2, 0.25, 0.3, 0.35 |
| Extinction law | Calzetti et al. (2000) |
| Cosmology | $H_0 = 69.3$, $\Omega_m = 0.29$, $\Omega_\lambda = 0.71$ |

were selected, that is 9 SFHs with different $\tau$ values for each of the 3 metallicity values: Z=0.004, Z=0.008, Z=$Z_\odot$ = 0.02. Finally, all the possible values for $\tau$ (extensively written in the third line of Table 3.1) with solar metallicity were selected, the redshift step was set to 0.02 up to redshift 1.8 and several reddening values E(B-V) were exploited, listed in the corresponding line of Table 3.1. Galaxy models were extinguished using the Calzetti et al. (2000) extinction law for $\tau > 2$ star formation histories (i.e. extinguishing all star forming galaxies which show active star formation up to z $\sim$ 0.5, $\sim$8 Gyr from the Big Bang). According to the exponentially declining SFH model adopted, and as evident from Figure 3.1 this corresponds to the SFH of a galaxy whose star formation activity is negligible at z $\leq$ 0.5. Galaxies with more rapidly declining SFHs are not extinguished by the code.

- Selection of a set of filters.
The same set of filters contained in the observed data should be used, so I selected CFHTLS Megacam $u^*$, $g'$, $r'$, $i'$ (old i), $y'$ (new i), $z'$ filters. As explained in Chapter 2, the $i'$ filter was broken during the observations for the survey, and this set of filters contain both of them.

- Computation of theoretical absolute magnitudes, in those filters, for each SED and redshift.

This phase requires several parameters that have to be set in order not to exceed the dimension of the library, defined as:

$$\text{Number of models} \times \text{Number of ages} \times \text{Number of SFHs} \times \text{Number of z} - \text{steps} \times \\ \times \text{Number of extinction laws} \times \text{Number of E(B} - \text{V)}.$$

2. As last step, taking as inputs at least two observed magnitudes and a spectroscopic redshift, the photometric redshift code performs a simple $\chi^2$ fitting method comparing the observed fluxes $F_{obs}$ (and relative uncertainties) with the preferred SED templates $F_{temp}$:

$$\chi^2 = \sum_i \left( \frac{F_{obs,i} - s \times F_{temp,i}}{\sigma_i} \right)^2 \tag{3.2}$$

where $F_{obs,i}$ and $\sigma_i$ are the observed flux and its uncertainty in a given $i$ photometric band; $F_{temp,i}$ is the template flux in the same filter. The template fluxes are normalized to the observed ones by choosing the factor $s$ that minimises the $\chi^2$ value ($\partial\chi^2/\partial s = 0$):

$$s = \sum_i \frac{F_{obs,i} \times {F_{temp,i}}^2}{\sigma_i^2} \Big/ \sum_i \frac{F_{temp,i}^2}{\sigma_i^2} \tag{3.3}$$

It requires precise format for the input catalogues, which can be either the basic input (SHORT) or the extended version (LONG). The LONG format is used when the spectroscopic redshift is kept fixed, and the columns must be ordered as follows:

- ID: identification number (integer) of each galaxy;

- Observed magnitudes with relative errors: either in the mag1, mag2, ...magN, err1, err2, ...errN (MMEE) or in the mag1, err1, mag2, err2, ...magN, errN (MEME) order. Magnitudes must be in Vega or AB system and also fluxes can be used instead of magnitudes. The input catalogue must include the same number of couple (magnitude, error) values as the number of filters used to create the libraries, and the filters must follow the same order as in the library;

- CONTEXT value, that is an integer which specifies which combination of passbands can be used for each object. It is defined as $\sum_{i=1}^{i=N} 2^{i-1}$, where $i$ is the filter number as ordered in the input catalogue and in the library, and N is the total number of filters. According to the catalogues used in this work, the context is defined according to the passbands specified in Table 3.2;

- Z-SPEC: spectroscopic redshift of each galaxy;

- STRING: all the remaining columns in the input catalogue; The contribution from emission lines can be added to the fit (`ADD_EMLINES` parameter) and finally the redshift is fixed (ZFIX=YES in the parameter file, as defined in the input catalogue LONG format).

Table 3.2: Computation of the "CONTEXT" column for the input catalogue.

| Passband | $u^\star$ $g'$ $r'$ $i'$ (old $i'$) $y'$ (new $i'$) $z'$ |
|---|---|
| Filter number (i) | 1 2 3 4 5 6 |
| Filter Context ($2^{(i-1)}$) | 1 2 4 8 16 32 |

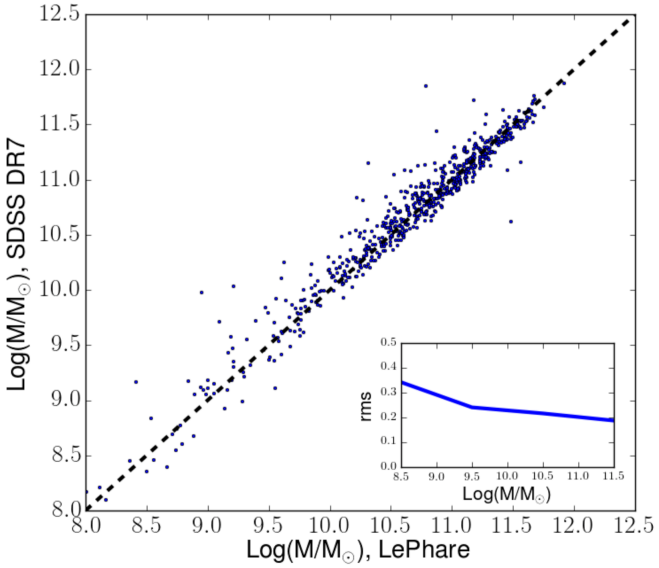


Figure 3.2: Comparison between the stellar mass values computed with LePhare (this work) and the stellar masses from the SDSS DR7. The inset shows the root mean square (rms) as a function of mass between the two estimates.

3. The results obtained from the previous steps can be used to generate simulated multi-colour catalogues.

### Relevant outputs for this thesis

In this work, LePhare outputs that will be considered in the following chapters are absolute magnitudes in the observed filters and stellar masses. The final stellar mass value is the output stellar mass from the Maximum Likelihood (ML) analysis (MASS_MED), which has an associated error, instead of the stellar mass corresponding to the minimum $\chi^2$, which is computed for all galaxies having a measured magnitude at least in one band. I will make use of LePhare stellar masses in the stellar mass function analysis presented in Chapter 5, and of absolute magnitudes in all the chapters in which I will analyse the observed properties of galaxies, i.e. Chapter 5, 6 and 7.

### Stellar masses

The program successfully computed stellar masses for 108168/113240 galaxies (95.5% of the sample). The mean and median error on the stellar mass estimates are computed from the minimum and maximum stellar mass estimate of LePhare (MASS_INF and MASS_SUP), and are respectively 0.3 dex and 0.2 dex.
To test mass estimates, the values obtained with LePhare were compared with the masses obtained fitting the photometry following the methodology presented in Kauffmann et al. (2003); Salim et al. (2007); Brinchmann et al. (2004), for a subsample of 740 galaxies galaxies in common with the SDSS DR7. The comparison shown in Figure 3.2 shows a good agreement between the stellar masses. The dispersion of the relation as a function of the stellar mass, given in the inset, is comparable with the error on stellar masses computed from LePhare. This test confirms the reliability of the LePhare configuration adopted.

### Stellar mass completeness limits

The stellar mass completeness limit is, at a given redshift, the minimum stellar mass above which the sample galaxies can be considered complete (i.e. not affected by any selection bias) at any stellar mass. The maximum redshift range I will consider throughout the thesis is $0.1 \leq z \leq 0.6$, and the dominant spectroscopic survey in this interval is the GAMA survey, whose magnitude completeness limit is r=19.8. I translated this magnitude in out CFHTLS magnitude system obtaining a magnitude completeness limit of $r'$=20. Hence, I will adopt this magnitude limit in order to compute the stellar mass limit of the galaxy sample. Note that this assumption is then verified and fully justified by the spectroscopic completeness computation I will perform in the next chapters. This limit is strongly redshift dependent, so to compute it the entire redshift range must be divided into several intervals. In order to reconcile the temporal extension of each interval with the sample statistics, which varies as a function of redshift, I considered fixed redshift bins of $\Delta z = 0.03$ up to $z = 0.09$, and bins with a fixed number of galaxies (2000) in the redshift range $0.09 < z \leq 0.6$. When computing stellar mass limits, galaxies are not separated according to their environment.
Considering only the galaxies entering the magnitude limited sample ($r \leq$20.0) and focusing on one redshift interval at the time, I computed the mass limits as follows (and are reported in Figure 3.3):

- I built $(g-r)_{rest-frame}$ vs. $M_r$ rest-frame colour-magnitude diagram for galaxies entering the sample. Excluding the 5% reddest galaxies to eliminate outliers, the rest-frame colour limit $(g-r)_{rest-frame,lim}$ is defined as the colour of the reddest galaxy in the sample.

- The so called red sequence is then identified, selecting galaxies with $(g-r)_{rest-frame,lim} - 0.15 < (g-r)_{rest-frame} < (g-r)_{rest-frame,lim}$. The absolute magnitude limit $M_{r,lim}$ is defined as the absolute r-band magnitude of the faintest galaxy in the interval.

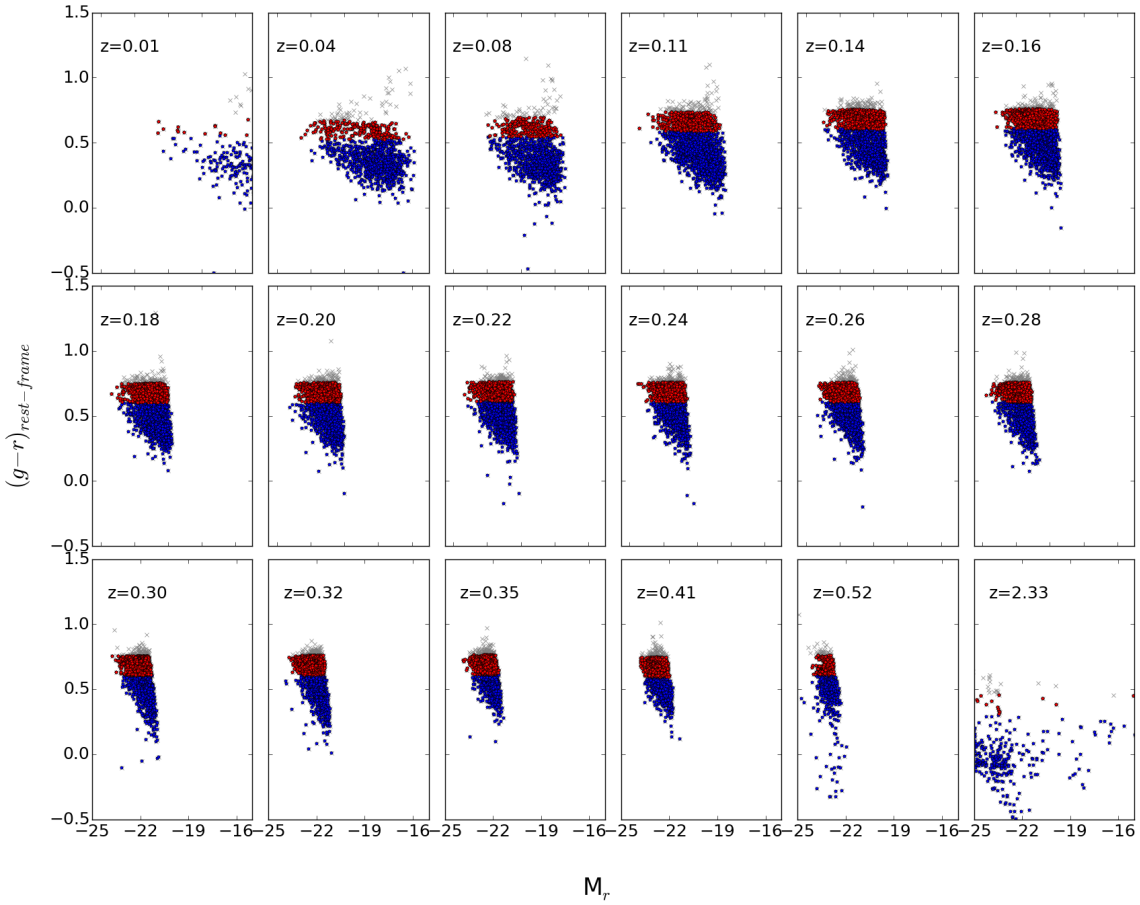


Figure 3.3: Colour-magnitude diagram for galaxies in all the redshift bins considered during the stellar mass limit determination. Gray crosses are the 5% reddest galaxies excluded as outliers in the first step of the mass completeness limit computation. Red points represent the 0.15 width colour stripe used in order to define the absolute magnitude limit starting from the rest frame colour limit, as explained in the text. Blue points are all other objects which are not considered for the mass limit computation.

- Finally, I computed the mass limit following the prescription of Zibetti et al. (2009):

$$\mathcal{M}_{lim,M_\odot} = -0.840 + 1.654(g-r)_{rest-frame,lim} + 0.4(M_{r,\odot} - M_r) \tag{3.4}$$

  where the absolute magnitude of the Sun is $M_{r,\odot} = 4.64$.

As a result of the procedure, Figure 3.3 shows the colour-magnitude diagram for galaxies in all the redshift ranges considered: gray crosses are the 5% reddest galaxies excluded as outliers in the first step of the computation. Red points represent the 0.15 width colour stripe used in order to define the absolute magnitude limit starting from the rest frame colour limit and blue points are all other objects which are not considered for the mass limit computation. It must be pointed out that the first and the last redshift sub-intervals

Table 3.3: Table resuming the results of the mass limit computation. The first three columns are respectively the lower, upper limits and the centre of the redshift bins considered in the procedure; the fourth column is the rest-frame colour limit, namely the colour of the reddest galaxy in the sample, excluding outliers; the fifth column is the absolute magnitude limit, that is the faintest absolute magnitude of a galaxy whose colour is within $(g-r)_{rest-frame,lim} - 0.15 < (g-r)_{rest-frame} < (g-r)_{rest-frame,lim}$, and finally the last column is the value of the derived stellar mass limit.

| $z_{inf}$ | $z_{sup}$ | $z_{cen}$ | $(g-r)_{rest-frame,lim}$ | $M_{r,lim}$ | $log(M_{lim}/M_{\odot})$ |
|---|---|---|---|---|---|
| 0.000 | 0.030 | 0.015 | 0.702 | -11.885 | 6.931 |
| 0.030 | 0.060 | 0.045 | 0.672 | -16.171 | 8.596 |
| 0.060 | 0.090 | 0.075 | 0.694 | -17.644 | 9.221 |
| 0.0900 | 0.1365 | 0.1133 | 0.736 | -18.631 | 9.686 |
| 0.1365 | 0.1458 | 0.1412 | 0.755 | -19.300 | 9.985 |
| 0.1458 | 0.1717 | 0.1588 | 0.759 | -19.556 | 10.094 |
| 0.1717 | 0.1902 | 0.1809 | 0.751 | -19.996 | 10.257 |
| 0.1902 | 0.2089 | 0.1995 | 0.757 | -20.216 | 10.354 |
| 0.2089 | 0.2280 | 0.2184 | 0.762 | -20.398 | 10.436 |
| 0.2280 | 0.2459 | 0.2369 | 0.759 | -20.573 | 10.501 |
| 0.2459 | 0.2659 | 0.2559 | 0.758 | -20.806 | 10.592 |
| 0.2659 | 0.2901 | 0.2780 | 0.758 | -21.071 | 10.698 |
| 0.2901 | 0.3043 | 0.2972 | 0.756 | -21.292 | 10.783 |
| 0.3043 | 0.3308 | 0.3176 | 0.761 | -21.488 | 10.870 |
| 0.3308 | 0.3661 | 0.3485 | 0.763 | -21.646 | 10.936 |
| 0.3661 | 0.4453 | 0.4057 | 0.746 | -21.967 | 11.037 |
| 0.4453 | 0.6000 | 0.5226 | 0.760 | -22.703 | 11.354 |
| 0.600 | 4.060 | 2.330 | 0.455 | -15.042 | 7.785 |

are not going to be used in the scientific analysis of the following chapters, in that they do not have enough statistics in order to provide a reliable estimate of the stellar mass completeness limit.

The quantities resulting from each step listed above are given in Table 3.3 for all the intervals in which the sample has been divided.

The number and spacing of the redshift sub-intervals adopted to compute the stellar mass completeness limit was also varied considering narrower and broader extensions of the bins, in order to test the variability of the resulting colour, absolute magnitude and stellar mass limits. The analysis on the dependence of these derived quantities with redshift (namely, the $M_{r,lim}$ and $log(M_{lim}/M_{\odot}$ as a function of redshift) pointed out that the average trend was nearly unchanged while statistical fluctuations arose due to the increasing and decreasing number of galaxies per bin. Therefore, I am confident that the width of the redshift intervals used in this computation are not biasing the results on the stellar mass completeness limit as a function of redshift.

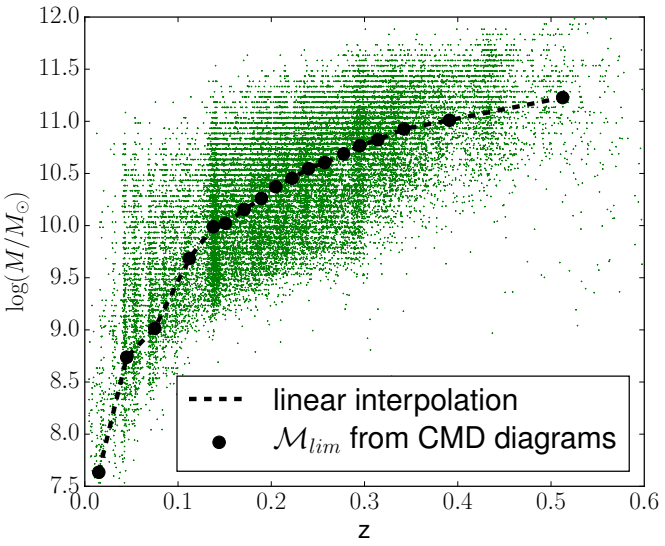


Figure 3.4: Stellar mass completeness limit as a function of redshift. Black points represent the measured limit, as explained in the text. Black dotted line is the linear interpolation to the points. Green dots represent the whole galaxy sample.

Finally, excluding the last redshift bin, I make use of an interpolation method to obtain the mass limit at each desired redshift (Figure 3.4). In the Figure, the whole galaxy sample is shown with green dots, as a representation of the loss of galaxies occurring when a mass limited sample is considered with respect to a magnitude limited one, as a function of redshift.

### 3.2.2 SINOPSIS

SINOPSIS (**SI**mulati**N**g **OP**tical **S**pectra w**I**th **S**tellar population models, Fritz et al. (2007, 2011, 2017)) is an improved and extended version of the code developed by Poggianti et al. (2001) to reproduce the stacked optical spectra of a sample of Luminous Infrared Galaxies of different spectral types. The goal of this model is to reconstruct the SFH of galaxies, hence the amount of stars formed at each epoch throughout the galaxy evolutionary history.
With respect to other spectrophotometric and full spectral fitting models, e.g. STARLIGHT (Cid Fernandes et al. 2005), STECKMAP (Ocvirk et al. 2006), VESPA (Tojeiro et al. 2007), GOSSIP (Franzetti et al. 2008), ULySS (Koleva et al. 2009), POPSYNTH (MacArthur et al. 2009), FIREFLY (Wilkinson et al. 2015), FIT3D (Sánchez et al. 2016), the latest version of SINOPSIS (Fritz et al. 2017) has several improvements and advantages, which are going to be fully detailed throughout the section.
The fitting code is based on a stellar population synthesis technique that reproduces the main features of observed galaxy spectra in the Ultra-Violet (UV) to Near-InfraRed (NIR)

Table 3.4: List of photometric windows, defined by their respective lower and upper wavelength, where the continuum is calculated to compare observed and model spectrum.

| # | $\lambda_{inf}$ (Å) | $\lambda_{sup}$ (Å) |
|---|---|---|
| 1 | 4600 | 4750 |
| 2 | 4845 | 4853 |
| 3 | 4858 | 4864 |
| 4 | 4870 | 4878 |
| 5 | 5040 | 5140 |
| 6 | 5210 | 5310 |
| 7 | 5400 | 5500 |
| 8 | 5650 | 5800 |
| 9 | 5955 | 6055 |
| 10 | 6150 | 6250 |
| 11 | 6400 | 6490 |
| 12 | 6620 | 6690 |
| 13 | 6820 | 6920 |
| 14 | 7110 | 7210 |

spectral range. Until now it has been applied to derive physical properties (stellar mass, dust attenuation, star formation history, mean stellar ages, etc.) of galaxies in many samples (Dressler et al. 2009; Vulcani et al. 2015; Guglielmo et al. 2015; Paccagnella et al. 2016, 2017; Poggianti et al. 2017) and the code was validated by means of comparison with both simulated spectra (Fritz et al. 2007) and other datasets and models (Fritz et al. 2011, 2014).

The code requires as input the observed spectrum, the spectroscopic redshift and, eventually, photometry.

The first step is to measure the average flux in several portion of the continuum without significant line features (Table 3.4) and at the same time the equivalent width (EW) of emission/absorption lines (i.e. the hydrogen lines of the Balmer series plus the [OII] 3727Å line).

The second step is the building of a model spectrum: from a set of $\sim$ 200 mono-metallicities SSP spectra with ages spanning the range between $10^4$ and $14 \times 10^9$ years, SINOPSIS creates a new set, with a reduced number of model spectra, by binning the models of the original grid with respect to the SSP age. In this way, the number of theoretical spectra shrinks to only 12 (Table 3.5), for any given metallicity value. The choice of the age bins is made based on presence and intensity of spectral features as a function of age (see Fritz et al. 2007, for more details).

The final model spectrum is obtained as a combination of all 12 SSP spectra, as shown

Table 3.5: The ages and durations ($\Delta$T) of the set of averaged SSP spectra used in SINOPSIS, as it was built according to the criteria explained in the text. Here $\Delta$T is the time interval over which the SFR is assumed to be constant.

| Age Interval (yr) | $\Delta$T (yr) |
|---|---|
| (0-2) $\times 10^6$ | $\times 10^6$ |
| (2-4) $\times 10^6$ | $\times 10^6$ |
| (4-7) $\times 10^6$ | $\times 10^6$ |
| (7-20) $\times 10^6$ | $\times 10^7$ |
| (2-6) $\times 10^7$ | $\times 10^7$ |
| (6-20) $\times 10^7$ | $\times 10^8$ |
| (2-6) $\times 10^8$ | $\times 10^8$ |
| (6-10) $\times 10^8$ | $\times 10^8$ |
| (1-3.2) $\times 10^9$ | $\times 10^9$ |
| (3.2-5.6) $\times 10^9$ | $\times 10^9$ |
| (5.6-10) $\times 10^9$ | $\times 10^9$ |
| (1-1.41) $\times 10^{10}$ | $\times 10^9$ |

in the formula:

$$L_{mod}(\lambda) = \sum_{i=1}^{N_{SSP}} M_i \times L_i(\lambda) \times 10^{-0.4 \times A(\lambda) \times R_v \times E(B-V)_i} \tag{3.5}$$

where $N_{SSP}$ is the number of SSPs used, $M_i$ and $L_i(\lambda)$ are the values of stellar mass and luminosity per unit of stellar mass of the *i-th* SSP, $A(\lambda)$ represents the extinction law, $E(B-V)_i$ is the colour excess assigned to the *i-th* SSP and finally $R_v$ is the ratio of total to selective absorption $A_V/E(B-V)$. Notice that only positive values for extinction are allowed.

The maximum number of free parameters in the equation is up to 24: 12 SFR +12 extinction values when all the SSPs are used. When no emission lines are measured in the observed spectrum, the 4 youngest SSPs and their relative extinctions are excluded and the number of free parameters reduces to 16. Note that precompiled libraries of models with a specific SFH pattern are not used, but the best combination of SFR/extinction for each SSP age that better reproduces observed features in the observed spectrum is searched for (Free Form, FF). Nevertheless, analytical SFHs can be used instead of the FF pattern, such as $\tau$ models, log-normal, double exponential, and exponentially declining SFHs. It should be pointed out that adopting such prescriptions for the SFH pattern increases the computational time. In fact, while decreasing the number of free parameters in the equation, they require the use of the whole set of SSPs instead of binning them into the final 12 ages of Table 3.5.

The principal ingredients used by SINOPSIS in order to build the model spectrum are given in the formula.

Note that a new set of SSP models is used (Bruzual & Charlot 2017, in preparation), with a higher spectral and age resolution, and a larger number of metallicity values (namely 13, from Z=0.0001 to Z=0.04, as compared to the 3 default values used before) with respect to libraries publicly available. This new models dataset includes the most recent version of the PADOVA evolutionary tracks from Bressan et al. (2012, PARSEC), and have been coupled with stellar atmosphere libraries from several sources depending on the wavelength coverage, on the luminosity, and on the effective temperature (see Gutkin et al. 2016, for the full compilation of the adopted stellar spectra). The evolutionary tracks include the treatment of the Wolf-Rayet phase, for stars typically more massive than $25M_{\odot}$. The assumed IMF is Chabrier (2003) with masses in the range 0.1-100 $M_{\odot}$ IMF.

Each SSP is weighted for a given value of stellar mass, and the effect of extinction is applied before they are added together to yield the final model. Note that the code accounts for differential extinction as a function of the stellar age to simulate a selective extinction effect (Calzetti et al. 1994; Poggianti & Wu 2000), where the light emitted by the youngest stellar populations is most likely to be affected by the presence of the dust that is typically abundant in star forming molecular complexes. Once a stellar population ages, it progressively gets rid of this interstellar medium envelop, either by means of supernova explosions, which will blow it away, or because of the proper motions of the star clusters, or by a combination of the two effects. This treatment of dust obscuration is not only a more realistic description of the real situation but is also required when one wants to reproduce also the intensity of emission lines, which are the most prominent features of the youngest stars and the most prone to dust extinction. The effect of dust extinction is included in the code by modelling it as a uniform dust layer in front of the source. While this is indeed a simplification, Liu et al. (2013) have demonstrated that adopting a slab, foreground dust screen, is a fair representation of the effects dust has on starlights at large scales. Furthermore, the mix of stellar ages and extinction can be naturally taken into account by the age-dependent way of treating dust attenuation that SINOPSIS allows. Different extinction and attenuation laws can be chosen including, among others, the attenuation law from (Calzetti et al. 1994), the average Milky way extinction curve (Cardelli et al. 1989), or the Small and Large Magellanic Clouds curves (Fitzpatrick 1986).

Concerning metallicities, one of the main hypotheses of the model is that all the stellar populations in a galaxy have a common metallicity value at any age. So a homogeneous value for the metallicity of theoretical spectra is adopted and the three different sets of metallicities that are ordinarily explored are sub-solar (Z=0.004), solar (Z=0.02) and super-solar (Z=0.05). Fitting an observed spectrum with a single value of the metallicity is equivalent to assuming that this value belongs to the stellar population that is dominating its light. It is clear that assuming a single value for the SSP metallicity is a simplifying assumption since, in practice, the stellar populations of a galaxy span a range in metallicity value. A check on the reliability of the mass and star formation histories derived using this method has been performed analysing synthetic spectra of different SFHs with metallicity that varies as a function of stellar ages, so to simulate the chemical evolution of the galaxy,

and it turns out that the way metallicity is treated does not introduce any bias in the recovered stellar mass or SFH (Fritz et al. 2007).

Differently from all the other available codes, SINOPSIS includes the emission from ionised gas in the interstellar medium in SSP models at ages $\lesssim 10^7$ yr (Balmer, Paschen, Brackett, Lyman series and forbidden lines of several elements: [OI], [OII], [OIII], [NII], [SII], [SIII]). SINOPSIS currently is the only spectral fitting code that includes SSPs with emission lines. This is a great advantage for a number of reasons: emission lines in the observed spectra need not to be masked for the fitting, a reliable value for dust extinction can be calculated (even when $H\beta$ is not observed), star formation rate can be automatically estimated as well, and finally correction for the underlying absorption in Balmer lines is performed in a self-consistent way, by simultaneously taking into account both the absorption and emission components. The calculation of the lines intensities is obtained by pre-processing the SSPs spectra energy distribution (SED) with ages $\leq 5 \times 10^7$ years through the photoionisation code CLOUDY (Ferland 1993; Ferland et al. 1998, 2013). The adopted parameters are those typical of a HII region (see also Charlot & Longhetti 2001): hydrogen average density of $10^2\,\mathrm{atoms\,cm^{-1}}$, a gas cloud with a inner radius of $10^{-2}$ pc, and a metal abundance corresponding to the metallicity of the relative SSP. The lines for which the luminosities are calculated include hydrogen of the Balmer (from H$\alpha$ to H$\epsilon$), Paschen (from Pa$\alpha$ to Pa$\delta$), Brackett (from Br$\alpha$ to Br$\delta$), and Lyman (Ly$\alpha$ and Ly$\beta$) series. Luminosity of UV and optical forbidden lines from various other elements (such as [OI], [OII], and [OIII], [NII], [SII] and [SIII]) are calculated as well. One of the outputs includes also the pure stellar emission, that is of the model spectrum without the nebular emission lines component. These are calculated from the best fit parameters but using instead the SSP set with pure stellar emission.

An example of the result of the fitting procedure performed by SINOPSIS is given in Figure 3.5, where two galaxies of different spectral type and redshift are analysed: from left to right, the spectrum of an early-type galaxy and that of a late-type galaxy are considered. In both panels, the observed spectrum is shown in black, and vertical gray hatched areas are the continuum bands in which the average flux has been measured by the code. In the lower sub-panels, the spectra of the SSPs employed by the code in order to reproduce the observed spectrum are shown with different colours: their ages are written next to their spectra and the final best-fit model spectrum is superposed to the observed one in red in the upper panel. As it is noticeable from the plot, the possibility of measuring both absorption and emission lines when fitting the spectrum allows to reproduce with a much greater fidelity the data, and therefore constrain physical properties much more precisely.

The observed errors on the continuum flux are computed by taking into account the local spectral signal-to-noise ratio, while uncertainties on the equivalent widths are derived mainly from the measurements method. The $\chi^2$ is measured for each model spectrum created at any iteration, considering all the features: an Adaptive Simulated Annealing algorithm search for the best combination of parameters (namely, the SFR and extinction) that minimises the $\chi^2$ between the observable measured at the beginning and the corresponding quantities from the model:

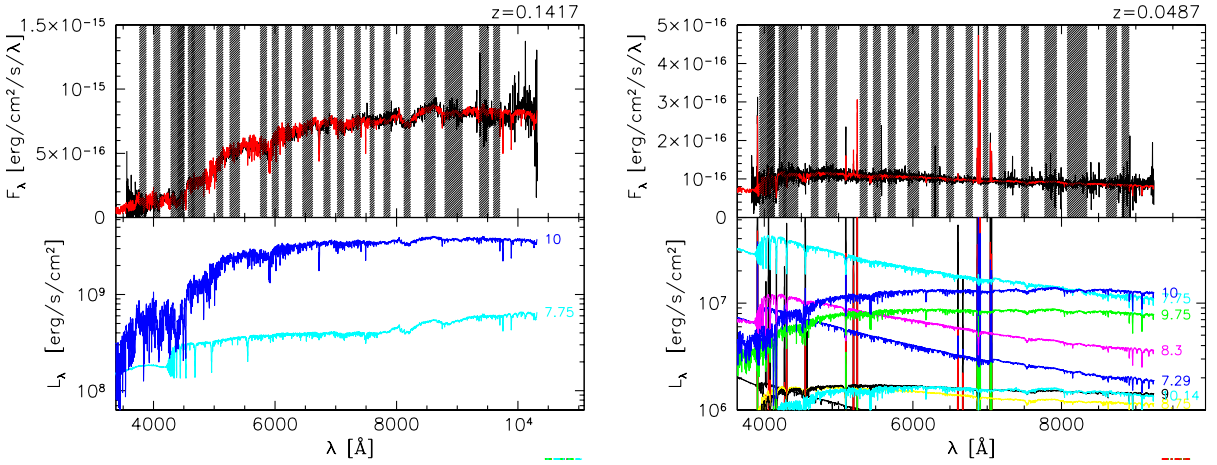


Figure 3.5: Example of the full spectrum fitting performed by SINOPSIS for an early-type (left) and late-type (right) galaxies, at the redshift indicated on top of each plot. In the upper panel of both plots, the original spectrum of the galaxy is shown in black; the final fit is superposed to the original one in red and vertical gray hatched areas are the continuum bands in which the average flux has been measured by the code. In the lower panel of both plots, the spectra of the SSPs employed by the code in order to reproduce the observed spectrum are shown with different colours; the logarithm of their age (in yr) is written next to each one.

$$\chi^2 = \sum_{i=1}^{N} \left(\frac{M_i - O_i}{\sigma_i}\right)^2 \tag{3.6}$$

where $M_i$ and $O_i$ denote the quantities measured from the model and observed spectra, respectively, $\sigma_i$ the observed uncertainties and N the total number of observed constraints. Due to the presence of extinction, the search of the combination of parameters that minimises the differences between the observed and model spectrum is a non-linear and under-determined problem, in that the number of constraints (i.e. observables) is lower than the number of parameters. The solution given with this method is non-unique, due to the limited wavelength range under analysis, together with the age-metallicity degeneracy and the already mentioned non-linearity and underdetermination. Such a degeneracy must be considered in the computation of errors to be attributed to the output: for each observed spectrum, 11 realisations of the model spectrum are performed starting from different initial conditions in the parameter space (SFR, extinction), the $\chi^2$ is computed at each iteration and the algorithm drives the solution towards the minima. Error-bars are then associated to all physical quantities measured by the code, such as stellar mass, SFR, extinction and ages: the minimum and maximum value of each parameter in different realisation are considered as upper and lower limits, and the median is considered as final value.

The code performances as a function of spectral resolution and noise have been extensively

tested in Fritz et al. (2007). Spectra with a resolution ranging from 4Å to 9Å(FWHM) were considered in the context of the WINGS survey, and they are fully compatible with the GAMA spectra used in this thesis. SDSS spectra are of better resolution, thus the same conclusions can be applied. As for the dependence of the quality of the spectral fitting on the signal-to-noise ratio (SNR), two extreme cases of poor and high SNR were exploited in Fritz et al. (2007), who concluded that with increasing SNR the uncertainties in the derived physical quantities are on average slightly smaller, the mass formed per age bin is more precise (in particular in the second age bin) and the recovered value of the metallicity are more correct, in the sense that there is less degeneracy in the quality of the fits obtained with different values of the metallicity of the SSPs. As a general conclusion, however, Fritz et al. (2007) state that the SNR is not driving the intrinsic degeneracy of the solutions, and that the characteristic features of a spectrum can be reproduced by different mixing of stellar population of different ages.

### Physical properties of galaxies

The code gives as outputs the SFR in 12 ages corresponding to the set of SSPs, the SFR in four broad bins, absolute and observed magnitudes from the model, stellar masses, luminosity weighted (LW) and mass weighted (MW) ages, dust attenuation and the value of all measured EWs.
Among them, the main physical properties of galaxies that are going to be used in this thesis are the galaxy stellar masses, SFR, SFH, and average ages.

### Stellar mass

As already introduced in Chapter 1, the use of spectral synthesis techniques leads, for a given SSP, to three different kinds of stellar mass (Renzini 2006; Longhetti & Saracco 2009). The difference between these three definitions is a function of the stellar age and of the IMF. SINOPSIS provides masses calculated using all of the aforementioned definitions, but only the masses defined according to definition 2 will be used in the next chapters. Given that the theoretical spectra are given in luminosity per unit of solar mass, to compute the values of stellar mass the model spectrum is converted to flux by accounting for the luminosity distance factor and the K-correction (which is naturally performed by fitting the spectra at their observed redshifts).

### Star formation rate and star formation history

The search for the best fit-model, as already discussed above in this section, is performed using 12 SSPs of different ages, obtained, in turn, by binning a much higher age-resolution stellar age grid. The star formation history is then given as the star formation rate in the 12 bins that is computed by dividing the stellar mass of a given age bin by its duration. The definition of stellar mass that is applied at this stage is that named M1, i.e. the initial mass of the SSP, at age zero, which corresponds to the mass of gas turned into stars. However, there is an intrinsic degeneracy in the typical features of spectra of

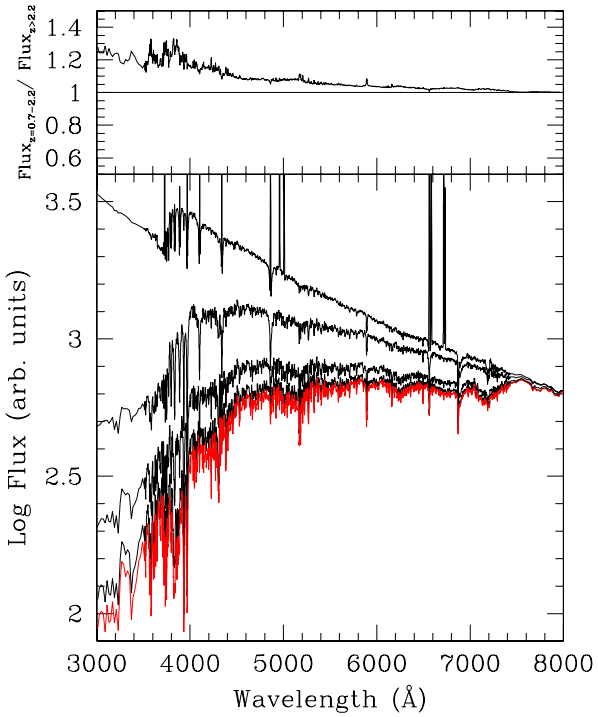


Figure 3.6: *Bottom*: comparison between spectra of stellar populations of the five significant age intervals derived from a further binning of the 12 SSP ages as those adopted in Guglielmo et al. (2015). The age of the populations (and the redshift) is decreasing from the bottom to the top of the panel. The oldest spectrum is plotted in red. Spectra are in arbitrary units and are normalized at 8000 Å. *Top*: ratio between the spectra of the two oldest populations.

similar age and this degeneracy increases for older stellar population spectra. There is, hence, an intrinsic limit to the precision of this method in determining the age of the stellar populations that compose a spectrum. This means that we may be not able, in general, to distinguish between patterns of SFH and extinction that differ in the ages of the dominant stellar populations by small amounts, and also that similar spectral features can be obtained with different linear combination of parameters. A direct visualisation of this issue is given in the main panel of Figure 3.6, that shows the spectra of stellar populations with ages reflecting the five age intervals adopted in the paper. The oldest spectrum, corresponding to the start of the SFH, $\sim$ 14 Gyr ago, is plotted in red in order to be distinguished from the second oldest one, which is very similar: the ratio of the fluxes of the two spectra is plotted in the upper panel of the figure, and shows 20 per cent level differences noticeable only in the short wavelength domain. The plot shows that the average spectra in each time interval are significantly different one from another, and this is how their contribution to the integrated spectrum can be distinguished by the model.

The only exception is the similarity between the spectra of the two oldest populations. For this reason results for stellar populations older than 5/6 Gyr should be taken with great caution, considering the possible 'spilling' between the SFR reconstruction of the two oldest populations. Moreover, the current SFR value is taken to be the one referring to the time interval ranging from 0-20 Myr and is calculated by fitting the equivalent width of emission lines that are directly related with the star formation process, that is Hydrogen (H$\alpha$ and H$\beta$) and Oxygen ([OII] at 3727Å). The lines luminosity is entirely attributed to star formation processes neglecting other mechanisms that can produce ionizing flux. In this way, for LINERS and AGNs the SFR values may be overestimated.

### Average ages

The code provides also an estimate of the average age of a galaxy, weighted on the stellar populations that compose its spectrum. Given that the mass-to-light ratio changes as a function of the age, there are two different definitions that can be given: the MW-age and the LW-age (see also Fernandes et al. 2003). The latter is directly derived from the spectrum, being weighted in this way towards the age of the stellar populations that dominate the light, while the first definition requires the knowledge of the mass distribution as a function of stellar age, i.e. the SFH. The LW average logarithmic age is given by:

$$\langle log(T) \rangle_L = \frac{1}{L_{tot}(V)} \times \sum_{i=1}^{N_{SSP}} L_i(V) \times log(t_i) \tag{3.7}$$

where $L_i(V)$ and $L_{tot}(V)$ are the rest-frame luminosities of the *i-th* SSP and of the total spectrum in the V-band, respectively, and $t_i$ is the age of the *i-th* SSP.
The MW average logarithmic age is given by:

$$\langle log(T) \rangle_M = \frac{1}{M_{tot}} \times \sum_{i=1}^{N_{SSP}} M_i \times log(t_i) \tag{3.8}$$

where, similarly, $M_{tot}$ and $M_i$ are the total mass and the mass of the *i-th* SSP, respectively. Hence, while the LW-age gives an estimate of the age of stars that dominate the optical spectrum, being in this way more sensitive to the presence of young stars, the MW-age is more representative of the actual average age of a galaxy stellar populations. To compute these values the finest age grid (12 ages) are averaged.

### Relevant outputs for this thesis

SINOPSIS ran on the subsample of spectra provided by the SDSS and GAMA surveys, which are flux calibrated and have the best available spectral quality: the resolution of the SDSS spectra is 3.0 Å and for the GAMA spectra is 4.5 Å. Furthermore, in the magnitude complete sample and in the redshift range I will consider in this thesis, these surveys are the main contributors to the galaxy spectrophotometric sample.

I will take advantage of the output parameters for studying in details the characteristics of the stellar populations of galaxies in different environments and in different redshift bins, which will be the main focus of Chapters 6 and 7. I will mainly consider the current SFR, the SFR and the stellar mass built in different age bins (i.e. the SFH), and the LW-age. I use the current SFR (SFR1 in the SINOPSIS output) to define the sSFR.

As discussed in Fritz et al. (2014), in the lowest resolution spectra of this thesis, i.e. GAMA spectra, emission lines can be measured down to a limit of 2 Å, while any emission measurement below this threshold is considered unreliable. In terms of sSFR, this sets a lower limit of $10^{-12.5}\mathrm{yr}^{-1}$. In this thesis, I will consider as star forming only galaxies with sSFR $> 10^{-12}\mathrm{yr}^{-1}$, and I have verified that moving this threshold does not affect the scientific results and trends. Three examples of GAMA spectra of a star forming (top), low-star forming (middle) and passive (bottom) galaxy are reported in blue in Figure 3.7. These spectra represent the three galaxy types that are going to be considered in the scientific analysis presented in Chapters 6 and 7. In each panel, the best fit spectrum from SINOPSIS is superposed in red.

Finally, it is worth showing a comparison between the stellar masses derived using LePhare and SINOPSIS. In fact, in the scientific analysis I will make use of both stellar mass estimates depending on the quantities and on the scientific analysis I will perform. The comparison between the stellar masses derived in two independent and different methods are given in Figure 3.8, as a function of the LePhare stellar mass: the y-axis shows the difference between the two stellar mass estimates divided by the stellar mass obtained from LePhare. From the plot, a systematic shift towards higher masses computed with SINOPSIS is noticeable, and this is likely to be due to the radical difference between the two approaches (SED versus spectral fitting), and I am confident that results obtained considering either LePhare or SINOPSIS stellar mass are compatible and comparable.

There are a few cases in which the two codes failed in fitting the input data, or some objects had to be excluded from the input sample. In the SED fitting procedure performed using LePhare, the caveat is most likely the insufficient number of magnitude bands given as input or a bad redshift estimate for the galaxy (e.g. if *quality_flag* is 0 or 1, see Chapter 2 for details). In the full spectral fitting technique used by SINOPSIS, the reason is twofold. The first issue is the absolute flux calibration of the fiber spectra, in fact while SDSS spectra have an absolute calibration, for the GAMA spectra only the shape of the continuum was recovered. To resolve this problem SINOPSIS requires as input the magnitude computed in a band which is directly computable from the spectrum, i.e. relative to a filter whose response curve is totally included in the wavelength range covered by the spectrum. With increasing redshift, this could not be the case for all the spectra, since some of them lacked the proper input magnitude. These galaxies were excluded from the input sample. The second issue concerns the fact that GAMA spectra are composed of a blue and red spectrum which are taken separately at the telescope from two branches of the spectrograph, and are sewed together using a common wavelength range. In case the common interval does not cover a sufficiently extended region and/or contains particular spectral features the superposition is not trivial and could lead to strange shapes in the continuum, which are hard to correct. Besides these main issues, the SNR could play

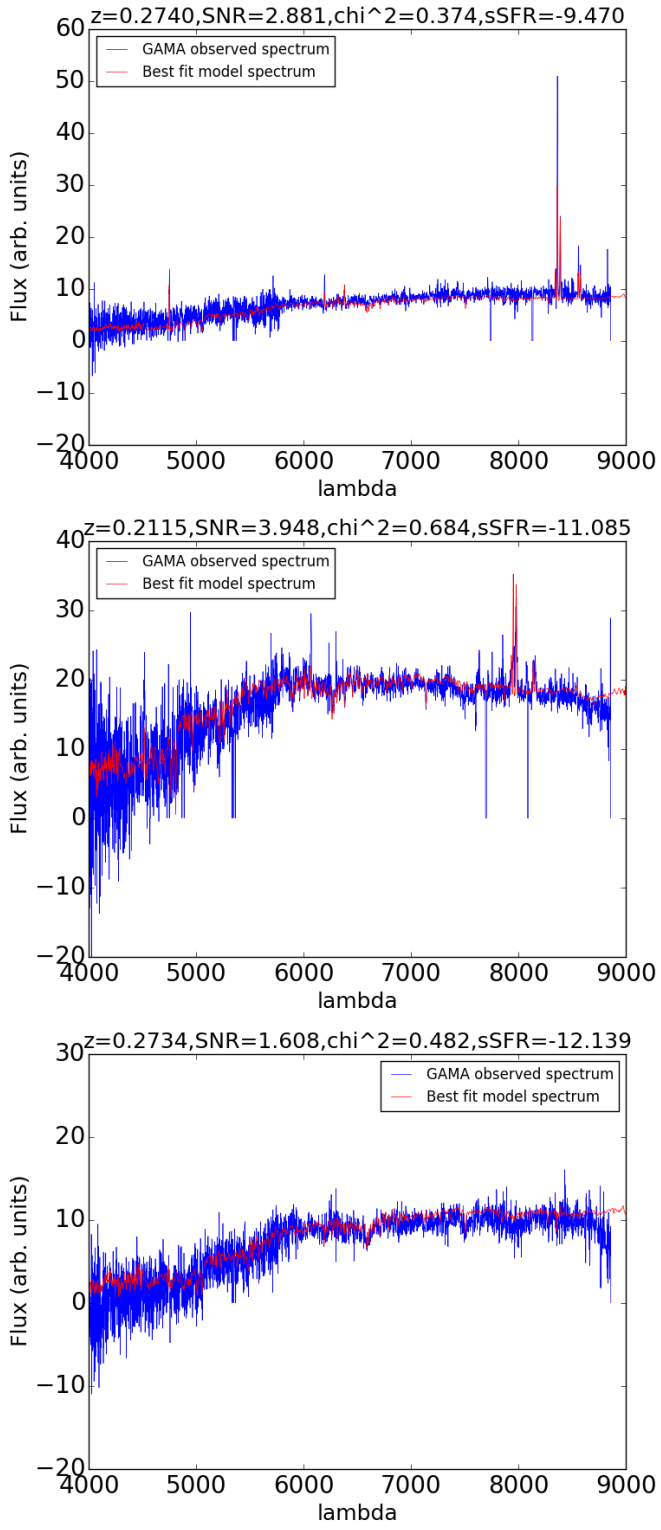


Figure 3.7: Example of the best fit spectrum obtained with SINOPSIS on three spectra from the GAMA survey, for a star-forming (top panel), low-star forming (middle panel) and passive (bottom panel) galaxy. The original spectrum is represented in blue and the best fit is superposed in red. On top of each panel it is reported the SNR of the input spectrum, the $\chi^2$ of the fit and the sSFR of the considered galaxy. The redshift of the galaxy is given in the legend.

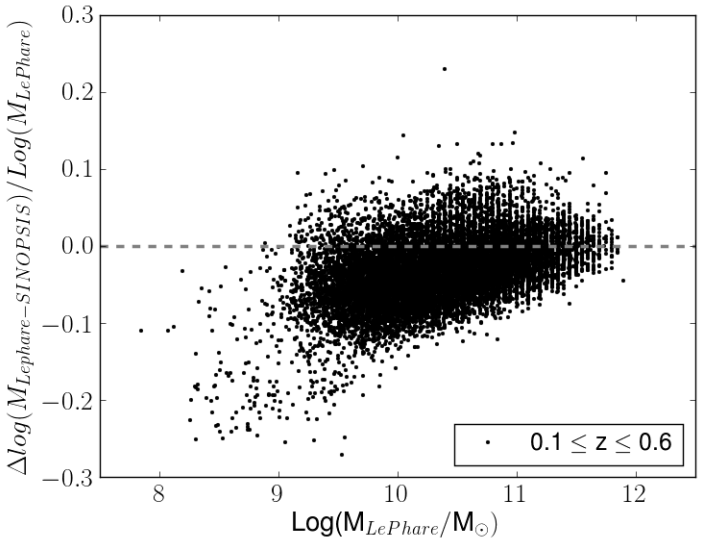


Figure 3.8: Comparison between the stellar masses as estimated through a SED fitting code using LePhare and through a full spectral fitting code, SINOPSIS. The LePhare stellar mass estimate is given in the x-axis; in the y-axis, the difference between the LePhare and SINOPSIS stellar mass estimates is divided by the LePhare stellar mass. The data point refer to the redshift interval $0.1 \leq z \leq 0.6$, as indicated in the legend. For a better visualisation, the y=0 line is also plotted in gray.

a role as already discussed in the previous sections of this chapter, and, concerning the GAMA spectra, spectra at higher redshift and/or lower luminosity, may lead to some difficulties.

The exact number of galaxies resulting from the SED and full spectral fitting analysis will be explicitly written in Chapter 5, 6 and 7 according to the sample that will be considered. In Chapter 4, I will present the release of a spectrophotometric catalogue of galaxies in the redshift range $0.1 \leq z < 0.6$, in which, among other properties, LePhare stellar masses are included. In Chapter 5, I will study galaxy stellar mass functions, that will be built starting from the released catalogue. In Chapter 6, I will investigate the star formation properties of galaxies which are derived from SINOPSIS, and therefore SINOPSIS stellar masses are going to be used for consistency. Finally, in Chapter 7, the study presented in the previous chapter will be enlarged to the whole XXL W1 Field, and, again, I will consider quantities obtained from SINOPSIS.

# 4

# THE RELEASED SPECTROPHOTOMETRIC CATALOGUE

## Content

In this chapter I will present the complete spectrophotometric sample of galaxies within X-ray detected, optically spectroscopically confirmed G&C and in the field. The main advantages of this sample compared to other existing catalogues at similar redshift are the much wider area in the sky, the X-ray detection and the spectroscopic confirmation of both the G&C and of its members, which assure robustness. The catalogue includes galaxies in a sample of 164 X-ray selected G&C from the XXL Survey in the North region (XXL-N), at $0.1 \leq z \leq 0.6$, with a wide range of virial masses ($1.24\times10^{13} \leq \mathrm{M}_{500,\mathrm{scal}}(\mathrm{M}_{\odot}) \leq 6.63\times10^{14}$) and X-ray luminosities ($2.27 \times 10^{41} \leq \mathrm{L}^{\mathrm{XXL}}_{500,\mathrm{scal}}(\mathrm{erg\,s^{-1}}) \leq 2.15 \times 10^{44}$).
The catalogue contains 22111 field and 2225 G&C galaxies with $r$ band magnitude $< 20.0$, which is the magnitude completeness limit. 95% of all G&C have at least 3 spectroscopic members, and 70% at least 10. Being a homogeneous census of galaxies within X-ray spectroscopically confirmed G&C at these redshifts, this sample allows environmental studies on the evolution of galaxy properties. Such catalogue is made publicly available to the community at CDS in Guglielmo et al. (2017). The Chapter describes in details the spectroscopic completeness analysis which is going to be used in the galaxy stellar mass function analysis, and overviews the main entries and galaxy characteristics that are released with the catalogue.

## 4.1 Environment

Chapter 3 describes the general procedure followed in order to assign galaxy membership to the G&C sample. As already specified at that stage, several membership definition can be adopted on the basis of the projected distance with respect to the G&C centre within which galaxies are considered as belonging to the structure.
For what concerns the released catalogue as well as the scientific analysis on galaxy

stellar mass function in Chapter 5, I define two membership radii: the 'outer' membership region, including all galaxies having a projected distance $< 3\,r_{200}$ with respect to the G&C centre, and the 'inner' membership region, containing galaxies having a projected distance $< 1.5\,r_{200}$ with respect to the G&C centre.
This method identifies 4180 (2656) members within 3 (1.5) $r_{200}$ in the cleaned spectroscopic sample. Note that some galaxies are assigned multiple memberships, that is they can belong to different G&C. This happens when two or more G&C are physically close in space. Specifically, when the outer membership is considered, 13%/2%/0.9%/0.6% of the galaxies in the sample simultaneously belong to two/three/four/five G&C. No galaxy belongs to more than five G&C.
Figure 4.1 shows the distribution of G&C as a function of the number of their members. Separate panels show the full sample and those G&C at $z \leq 0.6$, and the effects of using the inner and outer membership criteria are illustrated. Considering the outer membership definition, 95% of all G&C to have at least 3 spectroscopic members, and 70% have at least 10 members.

## 4.2 Spectroscopic completeness

When dealing with photometric and spectroscopic catalogues, it is important to know whether and for which subsample the spectroscopic sampling of the region is complete with respect to the photometric one. The spectroscopic completeness of a sample is commonly defined as the ratio between the number of reliable spectroscopic redshifts in a given region and the total number of galaxies within it (i.e. the number of galaxies in the photometric catalogue). In principle, the completeness ratio depends on the sampling of the spectroscopic surveys in different regions of the sky (being our spectroscopic catalogue an heterogeneous ensemble of data coming from different surveys), the observed magnitude and the colour of galaxies.
In order to deal with the first two factors mentioned above, the XXL-N field is divided in three stripes (arbitrarily named) according to the spatial distribution of the surveys (Figure 4.2):

- C-A area: the North-East region corresponding to the beginning of the G02 GAMA region: $30.17 \leq \mathrm{RA} \leq 38.83$ $-4.1715 \leq \mathrm{DEC} \leq -3.72$.
- C-B area: GAMA and VIPERS superposition area: $30.17 \leq \mathrm{RA} \leq 38.83$, $-6.0 \leq \mathrm{DEC} < -4.1715$.
- C-C area: South-East area: $30.17 \leq \mathrm{RA} \leq 34.0$, $-8.0 \leq \mathrm{DEC} < -6.0$.

The samples are then further subdivided according to the position in the sky and the magnitude, creating a grid of 1.0 deg width both in RA and in DEC (for a total of 22 cells), and considering intervals of 0.5 $r$-band observed magnitude. Given that some regions in the whole field of Figure 4.2 are not adequately sampled by the available spectroscopy (e.g. the C-C region, having lower spectroscopic coverage at any magnitude) histograms

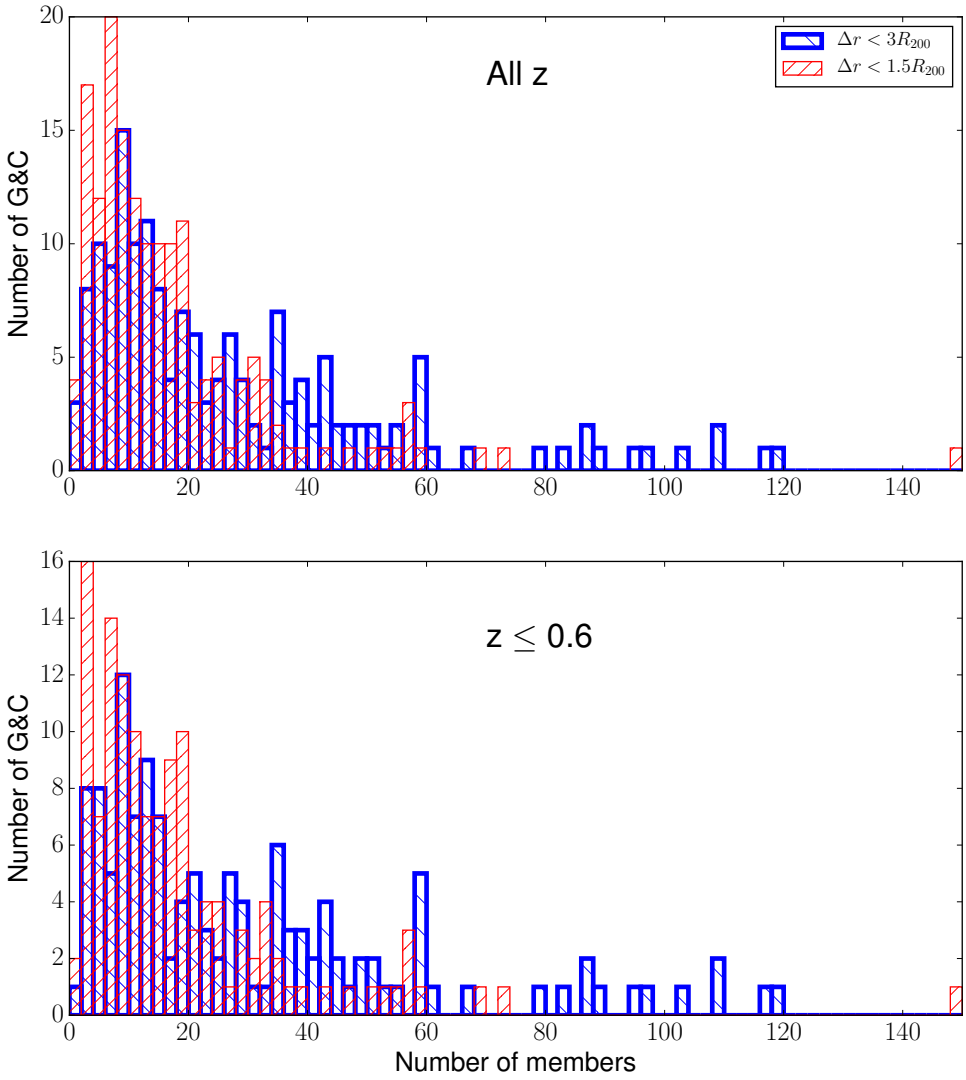


Figure 4.1: Number of members in XXL-N G&C at all redshift (top panel) and in the 132 XXL-N G&C at $z \leq 0.6$ (bottom panel), assigned to structures as described in Sec. 3.1. 4180 members within $3r_{200}$ (3619 at $z \leq 0.6$) are plotted in blue; 2656 members within $1.5r_{200}$ (2284 at $z \leq 0.6$) are plotted in red.

of galaxies are computed separately in each cell: the ratio of the spectroscopic to the photometric histograms gives the completeness in each region of the sky and in each magnitude bin within it. Completeness curves are obtained from the completeness ratio as a function of magnitude in each of the 22 cells, and are shown in Figure 4.3.

The final adopted magnitude limit, that is where the completeness drops dramatically, is $r = 20.0$ in the CFHTLS photometry (corresponding to GAMA $r = 19.8$), and GAMA data drive the curves at the magnitudes of interest.

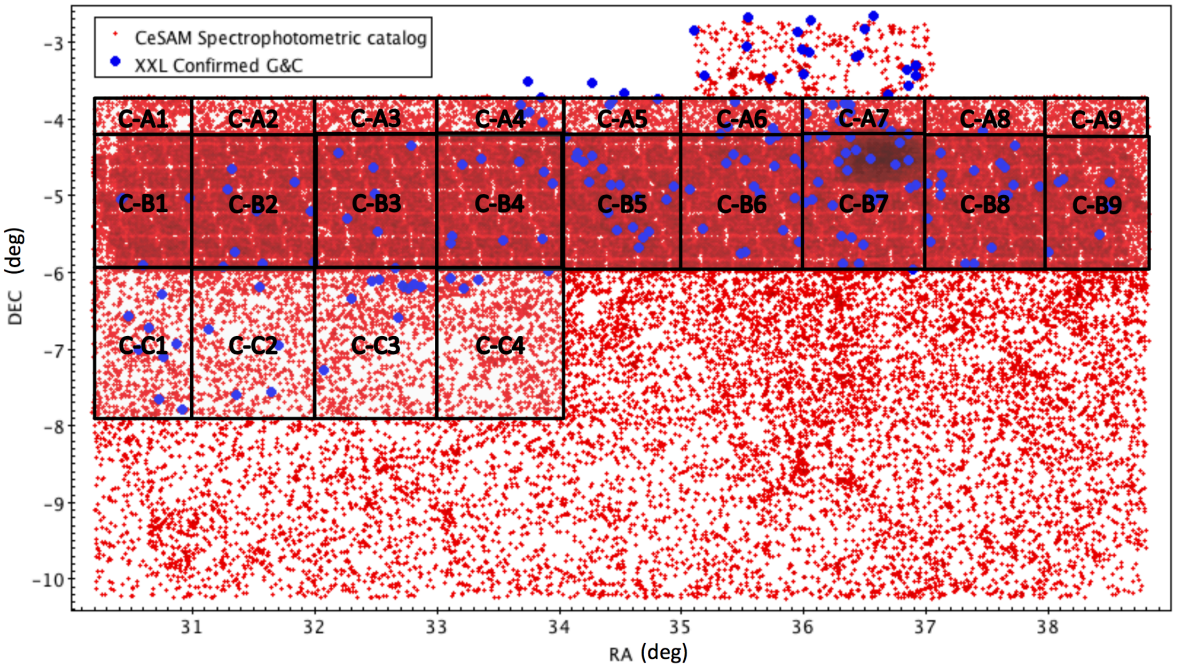


Figure 4.2: XXL-N area. Red dots show the galaxies in the spectrophotometric sample that is used to compute the spectroscopic completeness (Section 4.2) and blue dots represent X-ray confirmed G&C. The regions in which the spectroscopic completeness has been computed are overplotted with small boxes.

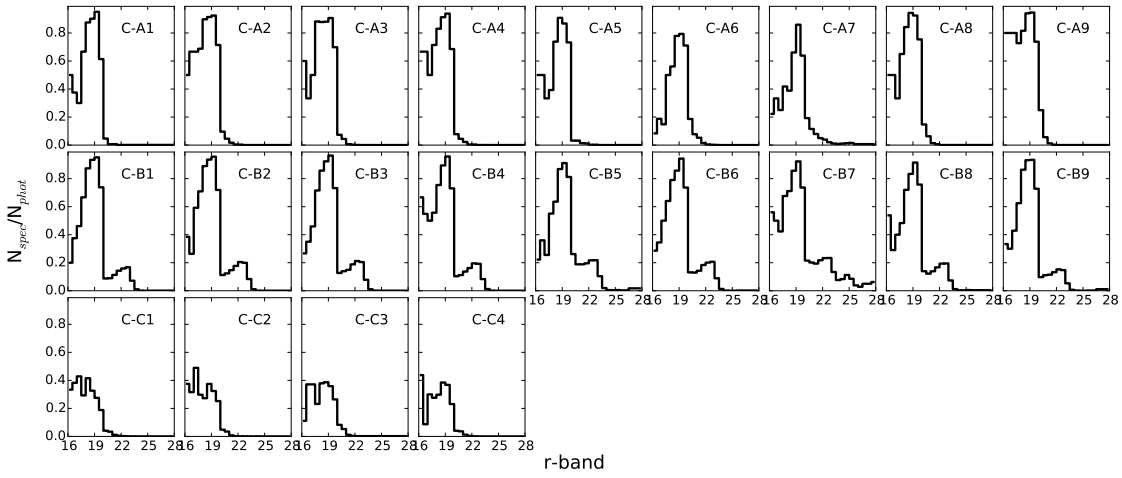


Figure 4.3: Completeness curves as a function of $r$-band magnitude in all the regions discussed in the main text and represented in Figure 4.2, as written in each panel.

Considering the magnitude limited sample including 28096 galaxies with $r \leq 20.0$, the total completeness values for the three regions are:

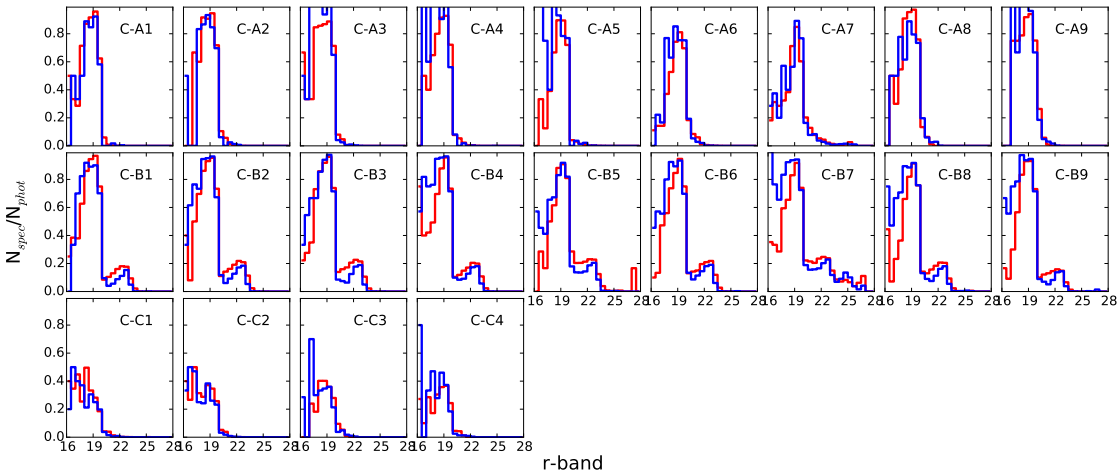


Figure 4.4: Completeness curves as a function of $r$-band magnitude and colour in all the regions discussed in the main text and represented in Figure 4.2, as written inside each panel. Galaxies are divided into blue and red according to their median observed (g-r) colour. In all the cases, the KS test on the histograms at $r \leq 20$ finds no significant differences between the considered samples.

- C-A: Number of galaxies in the spectrophotometric database = 3784, number of galaxies in the photometric database = 5292. Completeness =71.5±0.8% (Poissonian error);

- C-B: Number of galaxies in the spectrophotometric database = 15494, number of galaxies in the photometric database = 19944. Completeness =77.7±0.4%;

- C-C: Number of galaxies in the spectrophotometric database = 2497, number of galaxies in the photometric database = 8751. Completeness =28.5±0.6%.

I test the dependence of the spectroscopic completeness on galaxy colour, drawing completeness ratios as a function of magnitude for blue and red galaxies separately, following the procedure adopted for the entire sample. The sample is divided into blue and red galaxies, according to the observed (g-r) median colour ($(g - r)_{\rm median} = 0.61$) and the spectroscopic completeness computed for the two populations separately.
In Figure 4.4 the resulting completeness curves for blue and red galaxies (suitably coloured) are represented in all 22 cells in which spectroscopic completeness has been calculated.
I also test the dependence of the spectroscopic completeness on galaxy environment, to verify whether denser regions in the XXL area have the same sampling as the field. I consider separately galaxies falling into the projected area of G&C and galaxies in the remaining field sample (made of all galaxies with no X-ray G&C along the whole line of sight) in order to compute again the spectroscopic weights, following the same method explained previously in this section. As it is already detailed in the membership assignment section of this chapter (Sect. 3.1), the projected area of G&C is defined by

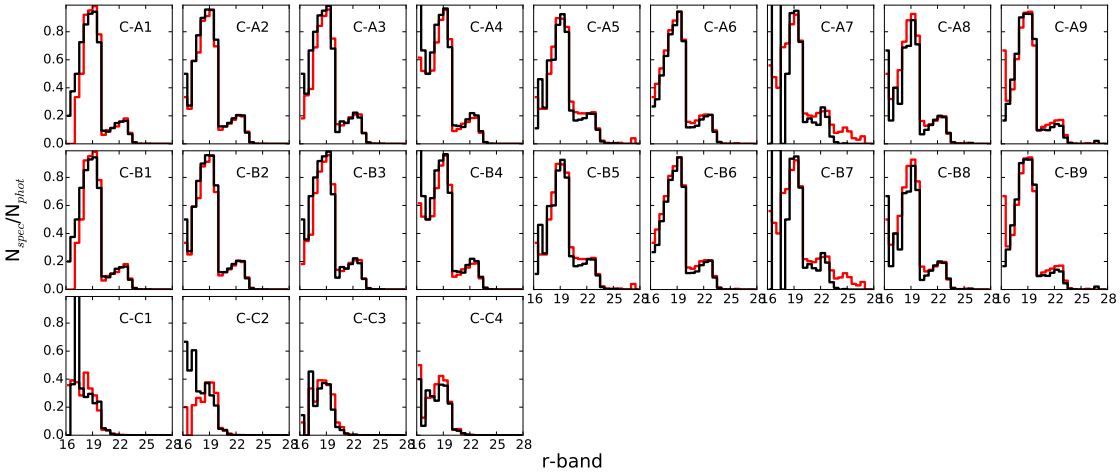


Figure 4.5: Completeness curves as a function of $r$-band magnitude and environment in all the regions discussed in the main text and represented in Figure 4.2, as written inside each panel. Galaxies in the projected area of G&C are shown in red, field galaxies are shown in black (see Sec. 3.1 for the definitions of the environments). In all the cases, the KS test on the histograms at r$\leq$20.0 finds no significant differences between the considered samples.

means of the virial radii of G&C. In particular, galaxies within $3 \times R_{200}$ from G&C centres and at all redshifts are considered at this stage.

As noticeable from Figure 4.5, a general very good agreement is found between the curves in all regions considered, suggesting that the spectroscopic data almost equally sample regions of different densities in the XXL area.

For a better understanding of the comparison, Figure 4.6 shows the curves in four representative regions that gather together contiguous cells showing no differences in their completeness curves. The first region includes the cells in the C-A stripe. The second one includes the cells in the C-B stripe, except for the C-B7 cell, where the presence of VVDS and VUDS surveys require a dedicated analysis. This cell alone constitutes the third region. Finally, the cells in the C-C stripe make up the fourth region. The curves in the four regions highlight how the coverage of the survey is different in different parts of the sky and how the choice of computing the completeness in each cell separately is indeed appropriate. A statistical Kolmogorov-Smirnov test (KS) is performed on the resulting completeness curves of Figure 4.6 at r$\leq$20.0. In the left panel of the figure, the dependence of the spectroscopic completeness on galaxy colours is checked: the comparison shows that the two galaxy samples have no significant differences, i.e. the probability that they are drawn from the same parent sample is high, suggesting that the spectroscopic completeness estimates are not biased against any colour. The p-values resulting from the KS test on the two samples are shown within each panel.

The right panel of the figure shows the analysis on the relation between spectroscopic completeness and environment. Overall, the p-values resulting from the KS test confirm

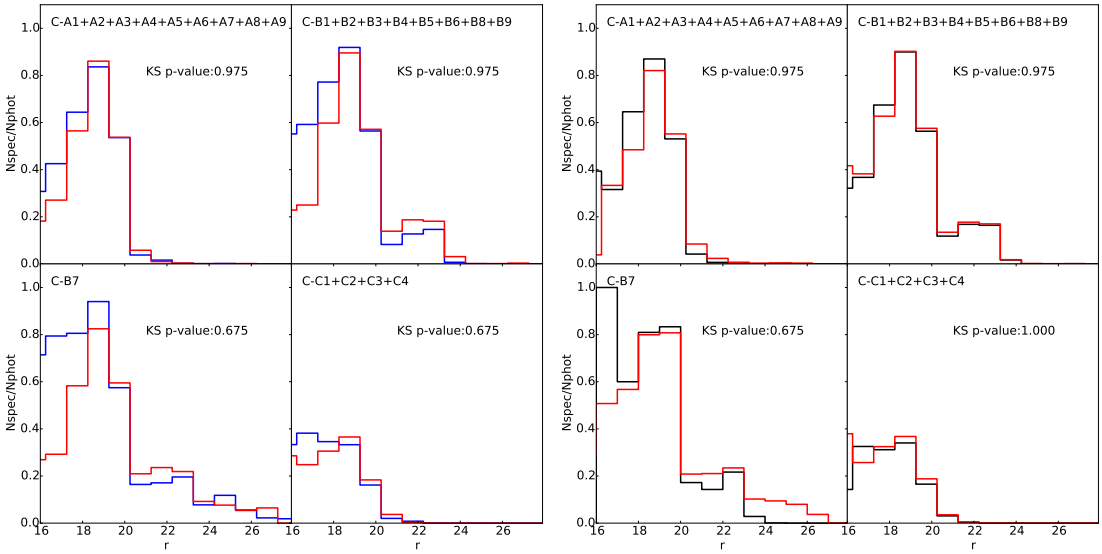


Figure 4.6: Completeness curves as a function of $r$-band magnitude and colour in the four representative regions discussed in the main text, as written inside each panel. In the left panel, galaxies are divided into blue and red according to their median observed (g-r) colour. In all the cases, the KS test on the histograms at r≤20.0 finds no significant differences between the considered samples, as shown by the p-values written in each panel. In the right panel, galaxies in the projected area of G&C are shown in red, field galaxies are shown in black (see Sec. 3.1 for the definitions of the environments). In all the cases, the KS test on the histograms at r≤20.0 finds no significant differences between the considered samples, as shown by the p-values written in each panel.

the conclusion already derived in Figure 4.5. However, there are two cases in which the KS test points out a significant difference between the G&C area and field sample: C-B: $36.0 < \mathrm{RA\,(deg)} \leq 37.0$ (C-B7) and C-A: $36.0 < \mathrm{RA\,(deg)} \leq 37.0$ (C-A7). Such discrepancy can be explained by taking into account that the considered areas in the sky are significantly dominated by field and G&C galaxies, respectively, and therefore the completeness curves of the less populated sample have not a statistically significant number of objects, neither in the photometric nor in the spectroscopic sample. The right panel of Figure 4.6 shows the completeness curves of field galaxies and of galaxies in the projected area of G&C in same the four representative regions used in the right panel for blue and red galaxies. As expected, C-B7 region shows a lower p-value with respect to the other curves, being however higher than the commonly adopted p-value used as threshold for considering the two samples statistically equivalent.

## 4.3 Description of the catalogue

The catalogue contains all relevant quantities described in this chapter for the subsample of galaxies with $0 < z \leq 0.6$, $r \leq 20.0$ and a derived stellar mass estimate.

Table 4.1: Statistics of the sample at $r \leq 20.0$. Numbers are given according to the redshift bins written in the first column of the table. The second column gives the total number of G&C in each redshift bin, the third column gives the number of galaxies in the G&C, while the fourth column gives the number of galaxies in the field. Numbers in parentheses are weighted for spectroscopic completeness.

| z | $N_{G\&C}$ | $N_{gals}$ in G&C | $N_{gals}$ in the field |
|---|---|---|---|
| 0.0-0.1 | 11 | 294 (393) | 2228 (3015) |
| 0.1-0.2 | 24 | 991 (1147) | 6125 (7868) |
| 0.2-0.3 | 37 | 634 (743) | 8134 (10708) |
| 0.3-0.4 | 22 | 212 (320) | 4206 (5791) |
| 0.4-0.6 | 38 | 94 (191) | 1418 (2301) |
| total | 132 | 2225 (2794) | 22111 (29683) |

The released sample is composed of 24336 galaxies, both in the field and in G&C, and the contribution of the different surveys is: 95% of redshifts come from GAMA (23178 galaxies out of 24336), 3% are from SDSS_DR10 (763 galaxies out of 24336) and the rest come from ESO Large Programme + WHT XXL dedicated observational campaigns (0.5%, 115 galaxies out of 24336) and VIPERS (0.2%, 48 galaxies out of 24336). The catalogue contains the astrometry from CFHTLS, the redshift, the name of the parent catalogue/survey, the *Origin flag* and *Quality flag* that were introduced in Sec. 2.3, all the membership related quantities, absolute magnitudes, stellar masses and completeness values. A detailed description of all the entries provided will be provided later in this section.
Table 4.1 presents some useful numbers characterising the sample. Overall, 22111 (29683 once weighted for incompleteness) galaxies enter the field sample, 2225 (3446 once weighted for incompleteness) galaxies enter the G&C sample, which includes 132 structures.
Here a description of the content of the released galaxy catalogue is given. The catalogue entries for a subsample of galaxies are given in Table 4.2 as an example. The different columns indicate:

- **Index:** galaxy identifier sequential number.

- **RAdeg:** right ascension (deg, J2000).

- **DEdeg:** declination (deg, J2000).

- **z:** redshift from the XXL spectroscopic database.

- **SpecOrigin:** parent survey/catalogue of the spectrum.

- **Origin_Flag:** flag dividing the surveys given in the SpecOrigin column into three classes of priority, as explained in the main text, Section 2.3.

- **Quality_Flag:** flag uniformly dividing zflag values into five classes according to the precision and reliability of the redshift estimate (Section 2.3).

- **DeltaR_r200_1:** distance in units of $r_{200}$ from the first G&C the galaxy is considered member of (for field galaxies, the value is set to zero).

- **DeltaR_r200_2:** distance in units of $r_{200}$ from the second G&C the galaxy is considered member of (for field galaxies or only single membership, the value is set to zero).

- **DeltaR_r200_3:** distance in units of $r_{200}$ from the third G&C the galaxy is considered member of (for field galaxies or only single/double membership, the value is set to zero).

- **DeltaR_r200_4:** distance in units of $r_{200}$ from the fourth G&C the galaxy is considered member of (for field galaxies or only single/double membership, the value is set to zero).

- **DeltaR_r200_5:** distance in units of $r_{200}$ from the fifth G&C the galaxy is considered member of (for field galaxies or only single/double membership, the value is set to zero).

- **Delta_v_1:** difference in recession velocity from the first G&C the galaxy is considered member of (for field galaxies, the value is set to zero).

- **Delta_v_2:** difference in recession velocity from the second G&C the galaxy is considered member of (for field galaxies or only single membership, the value is set to zero).

- **Delta_v_3:** difference in recession velocity from the third G&C the galaxy is considered member of (for field galaxies or only single/double membership, the value is set to zero).

- **Delta_v_4:** difference in recession velocity from the fourth G&C the galaxy is considered member of (for field galaxies or only single/double membership, the value is set to zero).

- **Delta_v_5:** difference in recession velocity from the fifth G&C the galaxy is considered member of (for field galaxies or only single/double membership, the value is set to zero).

- **XLSSC_3r200:** xlssc ID of the structure the galaxy belongs to. In case of multiple memberships, the multiple identification numbers are separated using the underscore symbol (_).

- **XLSSC_3r200_uniq:** xlssc ID of the closest G&C (i.e. the G&C that minimizes the projected distance between the G&C centre and the galaxy) the galaxy belongs to.

- **DeltaR_r200_uniq:** projected distance in unity of r200 of the closest G&C given in the previous column.

- **uMag:** rest-frame u-band absolute magnitude computed using LePhare, using spectroscopic redshift and observed magnitudes.

- **gMag:** rest-frame g-band absolute magnitude computed using LePhare, using spectroscopic redshift and observed magnitudes.

- **rMag:** rest-frame r-band absolute magnitude computed using LePhare, using spectroscopic redshift and observed magnitudes.

- **iMag:** rest-frame i-band absolute magnitude computed using LePhare, using spectroscopic redshift and observed magnitudes.

- **yMag:** rest-frame y-band absolute magnitude computed using LePhare, using spectroscopic redshift and observed magnitudes.

- **zMag:** rest-frame z-band absolute magnitude computed using LePhare, using spectroscopic redshift and observed magnitudes.

- **MASS_INF:** 16% lower value on the Maximum Likelihood (ML) analysis of LePhare

- **MASS_MED:** median value of the stellar mass from the ML analysis of LePhare.

- **MASS_SUP:** 16% higher value on the ML analysis of LePhare.

- **Compl_SM:** completeness computed using the subsample of the spectrophotometric catalogue including only the galaxies with a reliable stellar mass estimate by LePhare.

Note that, in all the columns, the value -99.99 is arbitrarily assigned when a value is not available.

Table 4.2: Subsample of 10 galaxies in the catalogue with their properties. The full table is going to be stored at CDS. The explanation of the different columns is given in Section 4.3. The column "Index" is repeated at the beginning of each part of the table in this example just for the sake of clarity.

| Index | RAdeg | DEdeg | z | SpecOrigin | Origin_Flag | Quality_Flag |
|---|---|---|---|---|---|---|
| 1378 | 31.63026 | -7.56776 | 0.4411 | ESO_LP | 1 | 400 |
| 940 | 34.36603 | -7.70509 | 0.0158 | AAT_AAOmega_GAMA | 1 | 400 |
| 93017 | 36.10000 | -4.18690 | 0.1065 | VIPERS_2DR | 1 | 400 |
| 1052 | 34.92736 | -7.66780 | 0.1082 | SDSS_DR10 | 1 | 400 |
| 59658 | 35.50422 | -4.80558 | 0.2050 | AAT_AAOmega_GAMA | 1 | 400 |
| 100987 | 30.54604 | -4.99444 | 0.2340 | AAT_AAOmega_GAMA | 1 | 400 |
| 99479 | 37.66412 | -4.96348 | 0.2867 | AAT_AAOmega_GAMA | 1 | 400 |
| 99777 | 37.65939 | -4.95309 | 0.2898 | AAT_AAOmega_GAMA | 1 | 400 |
| 99540 | 32.72662 | -6.22625 | 0.4218 | AAT_AAOmega_GAMA | 1 | 400 |
| 98614 | 32.80906 | -6.15934 | 0.4235 | WHT | 1 | 2 |

| Index | DeltaR_R200_1 | DeltaR_R200_2 | DeltaR_R200_3 | DeltaR_R200_4 | DeltaR_R200_5 |
|---|---|---|---|---|---|
| 1378 | 0.0 | 0.0 | 0.0 | 0.0 | 0.0 |
| 940 | 0.0 | 0.0 | 0.0 | 0.0 | 0.0 |
| 93017 | 0.0 | 0.0 | 0.0 | 0.0 | 0.0 |
| 1052 | 0.0 | 0.0 | 0.0 | 0.0 | 0.0 |
| 59658 | 0.0 | 0.0 | 0.0 | 0.0 | 0.0 |
| 100987 | 1.67932 | 0.0 | 0.0 | 0.0 | 0.0 |
| 99479 | 0.67039 | 0.47195 | 0.0 | 0.0 | 0.0 |
| 99777 | 2.04885 | 0.74780 | 0.64046 | 0.0 | 0.0 |
| 99540 | 1.17331 | 0.50395 | 2.61695 | 2.40155 | 0.0 |
| 98614 | 2.04803 | 1.53839 | 1.35872 | 1.27156 | 0.06218 |

| Index | Delta_v_1 | Delta_v_2 | Delta_v_3 | Delta_v_4 | Delta_v_5 | XLSSC_3r200 |
|---|---|---|---|---|---|---|
| 1378 | 0.0 | 0.0 | 0.0 | 0.0 | 0.0 | 0 |
| 940 | 0.0 | 0.0 | 0.0 | 0.0 | 0.0 | 0 |
| 93017 | 0.0 | 0.0 | 0.0 | 0.0 | 0.0 | 0 |
| 1052 | 0.0 | 0.0 | 0.0 | 0.0 | 0.0 | 0 |
| 59658 | 0.0 | 0.0 | 0.0 | 0.0 | 0.0 | 0 |
| 100987 | 116.6602 | 0.0 | 0.0 | 0.0 | 0.0 | 114 |
| 99479 | 1181.2538 | 1181.2538 | 0.0 | 0.0 | 0.0 | 149_150 |
| 99777 | 926.8587 | 464.1469 | 464.1469 | 0.0 | 0.0 | 148_149_150 |
| 99540 | 1050.5763 | 1698.2439 | 1259.8086 | 505.1972 | 0.0 | 082_083_085_086 |
| 98614 | 693.3804 | 1341.8223 | 1279.1928 | 902.8628 | 147.3492 | 082_083_084_085_086 |

| Index | XLSSC_3r200_uniq | DeltaR_r200_uniq | uMag | gMag | rMag | iMag | yMag | zMag |
|---|---|---|---|---|---|---|---|---|
| 1378 | 0 | 0.0 | -20.338 | -20.786 | -21.096 | -21.318 | -21.298 | -21.499 |
| 940 | 0 | 0.0 | -15.621 | -16.186 | -16.501 | -16.697 | -16.681 | -16.745 |
| 93017 | 0 | 0.0 | -15.513 | -15.680 | -16.458 | -16.596 | -16.572 | -16.811 |
| 1052 | 0 | 0.0 | -18.768 | -20.115 | -20.833 | -21.245 | -21.208 | -21.552 |
| 59658 | 0 | 0.0 | -19.542 | -20.130 | -20.461 | -20.632 | -20.614 | -20.802 |
| 100987 | 114 | 1.67932 | -19.357 | -20.204 | -20.811 | -21.150 | -21.118 | -21.415 |
| 99479 | 150 | 0.47195 | -20.448 | -21.184 | -21.647 | -22.024 | -21.996 | -22.264 |
| 99777 | 150 | 0.64046 | -20.217 | -21.439 | -22.112 | -22.513 | -22.481 | -22.790 |
| 99540 | 083 | 0.50395 | -20.558 | -21.734 | -22.344 | -22.658 | -22.631 | -22.893 |
| 98614 | 086 | 0.06218 | -20.873 | -22.149 | -22.812 | -23.126 | -23.098 | -23.360 |

| Index | MASS_INF | MASS_MED | MASS_SUP | Compl_SM |
|---|---|---|---|---|
| 1378 | 9.708 | 9.747 | 9.789 | 0.0346 |
| 940 | 8.502 | 8.536 | 8.578 | 0.0 |
| 93017 | 8.520 | 8.633 | 8.708 | 0.2331 |
| 1052 | 10.516 | 10.550 | 10.584 | 0.0 |
| 59658 | 9.569 | 9.608 | 9.642 | 0.7011 |
| 100987 | 10.119 | 10.174 | 10.254 | 0.6941 |
| 99479 | 10.167 | 10.202 | 10.236 | 0.8812 |
| 99777 | 11.016 | 11.050 | 11.084 | 0.8812 |
| 99540 | 11.016 | 11.050 | 11.084 | 0.0819 |
| 98614 | 11.166 | 11.200 | 11.234 | 0.2412 |

# 5 THE GALAXY STELLAR MASS FUNCTION

## Content

As first scientific exploitation of the galaxy sample described in Chapter 4, I characterise the stellar mass distribution and study the dependence of the galaxy stellar mass function (GSMF) on global environment and redshift.
The advantage of this work is that it is based on a large, homogeneous X-ray selected sample of G&C that are spectroscopically confirmed and span a wide range in X-ray luminosity, therefore uniformly probing a wide range of halo masses. I study the dependence on the environment dividing galaxies in the field from galaxies in the outer membership region of G&C in four redshift bins and I further divided the G&C sample in two classes of X-ray luminosity. I find no evidence for a dependence of the shape of the GSMF on environment (field vs G&C), and on X-ray luminosity, used as a proxy for the virial mass of the system. These results are confirmed by the study of the correlation between mean stellar mass of G&C members and $L^{XXL}_{500,scal}$.
The study is included in the second part of Guglielmo et al. (2017).

## 5.1 Galaxy sample

Here I make use of the catalogue of galaxies in X-ray selected groups and clusters (G&C) from the XXL Survey in the redshift range $0.1 \leq z \leq 0.6$; the lowest bin ($0 < z < 0.1$) was excluded because the catalogue includes only 11 groups at these redshifts. It is worth recalling that with respect to previous G&C catalogues at similar redshifts, the sample covers a much wider area in the sky, with the advantage of diminishing the cosmic variance, and includes G&C confirmed spectroscopically, which span a wide range in X-ray luminosity ($2.27 \times 10^{41} \leq \mathrm{L^{XXL}_{500,scal}(erg\,sec^{-1})} \leq 3.5 \times 10^{44}$) and therefore virial masses ($8.72 \times 10^{12} \leq \mathrm{M_{500,scal}(M_\odot)} \leq 6.64 \times 10^{14}$). G&C membership determinations are robust, being based on spectroscopic redshifts and on virial masses derived from X-ray quantities via scaling relations (Adami et al. 2018).
It is important to notice that galaxies in the regions classified as C3 by the XXL observa-

tions are included in the field sample. In principle, these could be source of contamination both for the field and for the G&C sample. As for the field sample, the presence of possible C3 members is not a source of contamination at all, given the reduced number of galaxies that could belong to these objects compared to the amount of galaxies in the field. Concerning G&C, I computed the galaxy stellar mass functions both including and excluding the putative C3 members from rough estimates of their virial masses and radii via scaling relations, and I verified that the final results are not affected at all.
As a reminder, the catalogue is a magnitude limited sample ($r \leq 20.0$) providing G&C spectroscopic memberships within 3 $r_{200}$, spectroscopic completeness weights, absolute magnitudes, stellar masses (and stellar mass limits as determined in Chapter 3.2.1). Table 5.1 summarises the sample of G&C and galaxies pertaining to the four analysed redshift bins ranging from $0.1 \leq z \leq 0.6$. Galaxies are split in different environments and spectroscopic completeness weighted numbers are given in parenthesis. The stellar mass completeness limit the samples at each redshift is also given in the table.

## 5.2 Results

### 5.2.1 The galaxy stellar mass function

I consider galaxies in the four broad redshift bins described in Table 5.1, and subdivided them into G&C members and field. Using the linear interpolation given in Figure 3.4, each redshift bin was assigned the stellar mass completeness limit corresponding to the lower end of each interval.
For this analysis, all galaxies in the outer membership region of G&C ($r \leq 3r_{200}$) are used.[1] To build the GSMF, galaxies are grouped in stellar mass bins of 0.2 dex width. In each mass bin, the number of galaxies is counted, and then divided by the width of the bin, to have the number of galaxies per unit of mass. In building histograms, each galaxy is weighted by its spectroscopic incompleteness correction, as determined in Section 4.2. The choice of the mass completeness limit outlined before introduces an additional partial incompleteness in each redshift bin which is redshift dependent. To further correct for such incompleteness, each redshift bin is subdivided into four sub-bins equally spaced in redshift and the proper mass completeness limit for each of these sub-bins is estimated. Figure 5.1 summarises all the steps of this correcting procedure, taking as example the GSMF of field galaxies in the $0.1 \leq \Delta z \leq 0.2$ interval. The mass distribution of each sub-sample is then computed separately and the lowest redshift sub-bin (e.g. $0.100 \leq \Delta z \leq 0.125$ in the figure) is assumed not to suffer from incompleteness. The deviations from the shape of the lowest redshift sub-bin observed in the other three sub-bins must be due to some incompleteness in the mass regime between the adopted and the proper mass limit. A statistical correction is then applied forcing the shape of the mass function in each of these sub-bins to be the same of that in the first sub-bin. Specifically, in each sub-bin in

[1] Note that the results presented in what follows will not change considerably when only galaxies within a distance $r \leq 1.5\, r_{200}$ are considered.

Table 5.1: Final sample used in the scientific analysis of this Chapter. Numbers are given according to the four redshift bins written in the first column of the two tables. The second column gives the stellar mass limit. Top table: Columns 3-5 contain the total number of G&C, and the number of G&C in the two X-ray luminosity bins in which the GSMF has been studied, which contain galaxies with stellar masses above the mass limit. Bottom Table: Columns 3-6 contain the number of galaxies above the stellar mass limit in G&C, divided again in luminosity classes, and the number of galaxies in the corresponding field sample; the quantities in parentheses refer to the number of galaxies weighted for spectroscopic completeness.

| z | $\mathcal{M}_{lim,M_\odot}$ | $N_{G\&C}$ | | |
|---|---|---|---|---|
| | | all | $L_{XXL}^{500} < 10^{43}$ erg/s | $L_{XXL}^{500} > 10^{43}$ erg/s |
| 0.1-0.2 | 9.6 | 21 | 16 | 5 |
| 0.2-0.3 | 10.4 | 34 | 17 | 17 |
| 0.3-0.4 | 10.8 | 24 | 11 | 13 |
| 0.4-0.6 | 11.0 | 38 | - | - |
| total | | 117 | 44 | 35 |

| z | $\mathcal{M}_{lim,M_\odot}$ | $N_{gals}$ in G&C | | | $N_{gals}$ in the field |
|---|---|---|---|---|---|
| | | all | $L_{XXL}^{500} < 10^{43}$ erg/s | $L_{XXL}^{500} > 10^{43}$ erg/s | |
| 0.1-0.2 | 9.6 | 920 (1116) | 420 (530) | 500 (586) | 4402 (6098) |
| 0.2-0.3 | 10.4 | 502 (751) | 182 (272) | 320 (479) | 4654 (6729) |
| 0.3-0.4 | 10.8 | 187 (351) | 85 (135) | 102 (216) | 2468 (4009) |
| 0.4-0.6 | 11.0 | 141 (531) | - | - | 2595 (13188) |
| total | | 1746 (3132) | 687 (937) | 922 (1281) | 14119 (30024) |

redshift, the best-fitting line to the set of counts in the mass range between the adopted mass completeness limit and the proper one is computed. For the first sub-bin, where the proper and adopted mass limit coincide by definition, the fit is performed on the same mass range adopted in the fourth sub-bin, which is the most incomplete. In each sub-bin the ratio of the fit in that sub-bin to the fit in the first sub-bin is taken and the factor is used to correct the number counts. Finally, the complete GSMF in each redshift bin is obtained by summing up all the corrected counts within each mass bin.

The adopted stellar mass completeness limit relative to the lowest sub-interval $0.100 \leq \Delta z \leq 0.125$ is shown with a vertical red dotted line. Data points of the redshift sub-intervals composing the whole redshift range considered here are plotted with different colours, and are listed in the legend. They are normalised to the area underlying the grey shaded region: the lower stellar mass corresponds to the mass complete regime of the highest redshift sub-interval, and the upper one corresponds to the maximum stellar mass value shared by the data points of all redshift sub-intervals. The linear fits applied for correcting the low-mass end slope of the GSMF of each sub-intervals are shown with black dashed lines. The total GSMF obtained summing up all data points without applying the statistical correction is shown with grey diamonds, and finally the corrected GSMF

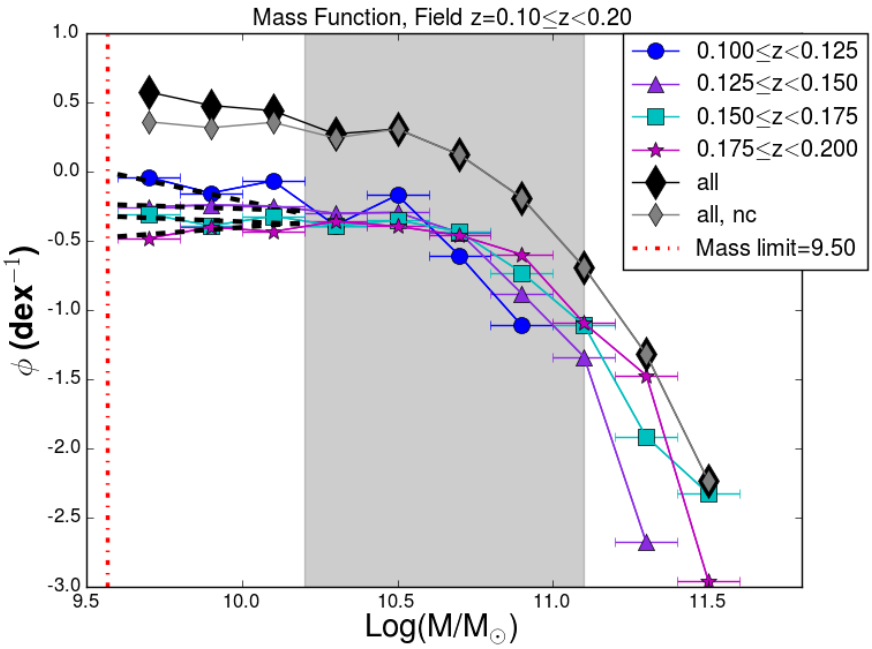


Figure 5.1: Example of the statistical correction applied to the GSMF in the low-mass end. The procedure is fully detailed in the main text, in Section 5.2.1. The figure refer to field galaxies in the redshift bin $0.1 \leq z \leq 0.2$. The adopted stellar mass completeness limit is shown with a vertical red dotted line and the value is given in the legend. Data points of the redshift sub-intervals composing the whole redshift range considered here are plotted with different colours, as it is shown in the legend. The grey shaded area shows the region in which the data points relative to different redshift sub-intervals have been normalised: the lower stellar mass of this area corresponds to the mass complete regime of the highest redshift sub-interval, and the upper one corresponds to the maximum stellar mass value shared by the data points of all redshift sub-intervals. The linear fits applied for correcting the low-mass end slope of the GSMF of each sub-intervals are shown with black dashed lines. The total GSMF obtained summing up all data points without applying the statistical correction is shown with grey diamonds, and finally the corrected GSMF is shown with black diamonds.

is shown with black diamonds.

Note that this further correction does not introduce any bias in the results that follow. Indeed, considering instead the most conservative limit (i.e. for each redshift bin, the mass limit of the highest redshift sub-bin) I obtained similar results, but with much larger uncertainties.

First, I compare the GSMF with other results from the literature, as shown in Fig. 5.2. To do so, I consider the sample of Moustakas et al. (2013), who exploited multi-wavelength imaging and spectroscopic redshifts from the PRism MUlti-object Survey (PRIMUS) over

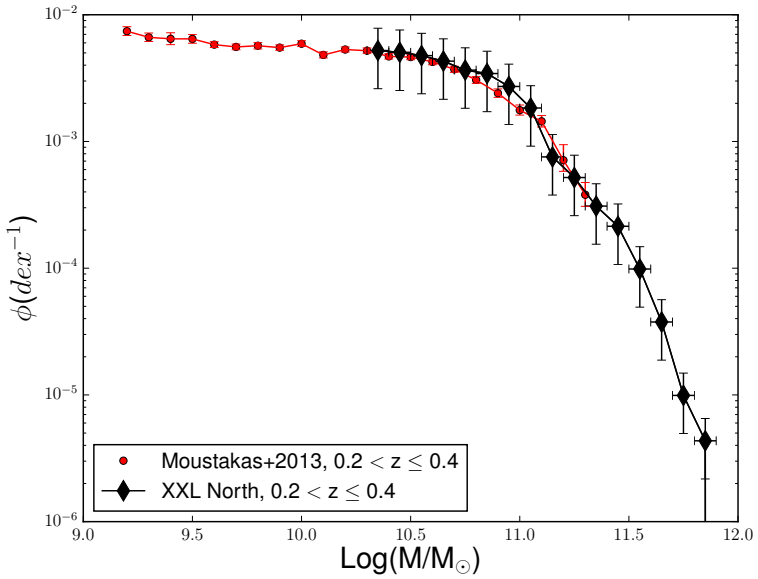


Figure 5.2: Comparison between the GSMF of XXL-N field galaxies in the redshift range 0.2-0.4 and the stellar mass function derived in Moustakas et al. (2013) in the same redshift range. The original normalisation of Moustakas et al. (2013) is maintained and the values of the GSMF of XXL-N field derived in this work are scaled to theirs in the common mass range, as described in the main text. Moustakas et al. (2013) survey is more sensitive to low-mass galaxies, but is smaller than XXL-N and does not probe the high-mass end of the galaxy population. Error bars on the data points are computed as described in Section 5.2.2.

five fields totaling $\sim 5.5$ deg$^2$ to characterise the mass functions in the redshift interval $0.2 < z < 1.0$. To increase their statistics, in this work the two redshift bins $0.2 < z < 0.3$ and $0.3 < z < 0.4$ are combined together in the mass range in common and their GSMF is contrasted to the one obtained from XXL data over the same redshift interval. This analysis makes use of both field and G&C galaxies together, mimicking the analysis of Moustakas et al. (2013). In this case, the original normalisation over the comoving volume given by Moustakas et al. (2013) is maintained and the values of the GSMF derived in this work were normalised to theirs in the mass range shared by the two curves. Figure 5.2 shows that the GSMF derived in this work compares remarkably well with the independent determination by Moustakas et al. (2013), indicating that systematics on the stellar mass determination are under control. It is possible now to proceed with the analysis.

### 5.2.2 GSMF in different environments and its evolution

The final GSMF are shown in Figure 5.3 and 5.5. GSMFs are normalised using the total integrated stellar mass in the mass range shared by the samples under comparison, so

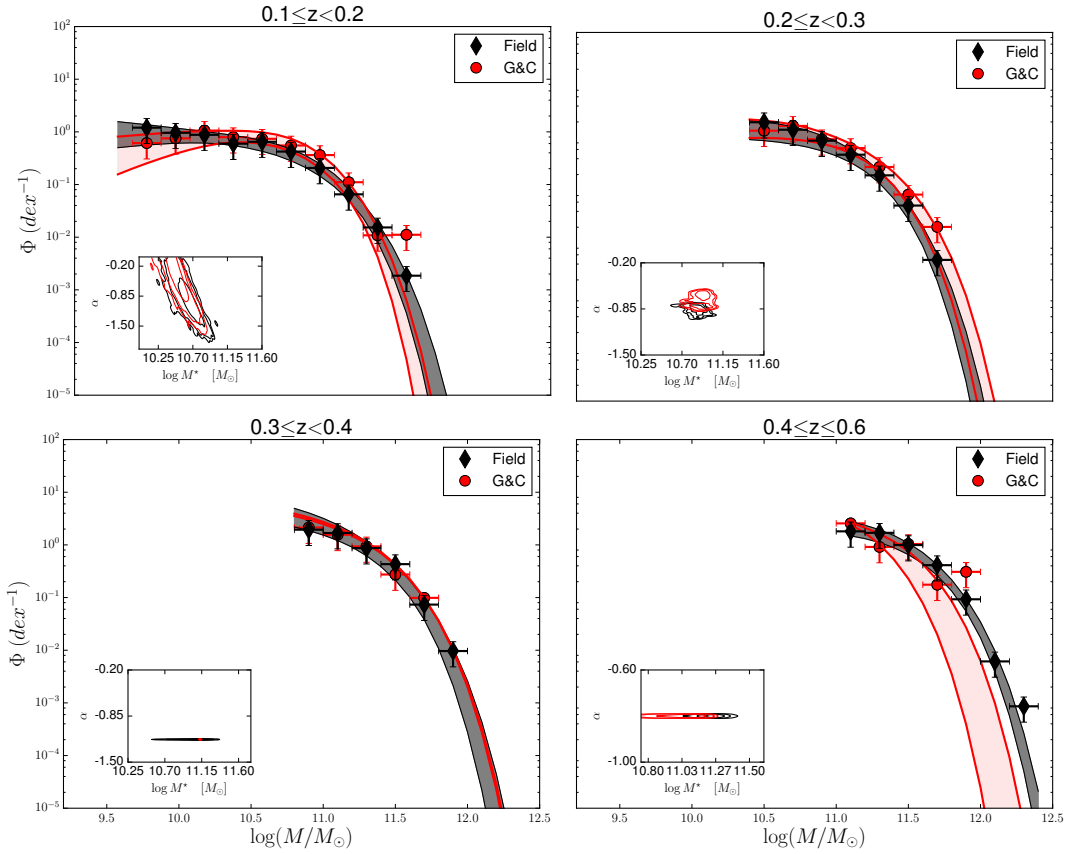


Figure 5.3: GSMF in different redshift ranges, as indicated in each panel, for galaxies in G&C (red points) and in the field (black diamonds). Only points above the mass completeness limit are shown. Error bars on the x-axis show the width of the mass bins, error-bars on the y-axis are derived from Poisson's statistics on the number counts together with cosmic variance contribution. Schechter fit functions are also shown as shaded areas, following the same colour scheme as the points. In the insets, 1, 2, 3 $\sigma$ contour plots on the Schechter fit parameters $\alpha$ and $M^*$ are also shown. At z$\geq$0.3, fixed values for the faint end slope $\alpha$ were set in order to perform Schechter fits.

that the total galaxy stellar mass in each histogram in that mass range is equal to one. Such a normalisation allows to focus the analysis on the shape of the GSMF and not on the number density, which is obviously very different across the different environments. In all the plots, error bars on the x-axis represent the width of the bins, error bars along the y-axis are computed adding in quadrature the Poissonian errors (Gehrels 1986) and the uncertainties due to cosmic variance, which are computed considering only field galaxies as follows. Following the procedure explained in Marchesini et al. (2009), the whole field is divided in 9 sub-regions and the number density of galaxies is computed in each region separately; the contribution to the error budget from cosmic variance is then $\sigma_{\rm cv} = \phi_{\rm i}/\sqrt{\rm n}$, where $i$ is any of the stellar mass bins in which the number density is computed and $n$ is the

number of sub-regions considered. The uncertainty due to cosmic variance is computed using the field sample was also applied to the GSMF in G&C. Only points above the mass completeness limit are shown.

The main goal of this chapter is to contrast the G&C and field GSMF, as shown in Figure 5.3, for galaxies at different redshifts. At each cosmic time, the mass distributions in the different environments present similar shape within the error bars. This result is in agreement with previous literature data, both in the local universe (e.g. Calvi et al. 2013) and at $z \sim 0.6$ (e.g. Giodini et al. 2012; Vulcani et al. 2013).

It is noticeable that with increasing redshift and going to higher stellar masses, the GSMF of the field sample changes from being below the G&C GSMF to be above at the highest redshifts. This trend could be due to the limited statistics of G&C at higher redshift and to the detection limit of X-ray observations, where the XXL survey is able to detect only bigger G&C.

In order to validate the previous statements on the dependence of the GSMF on environment at different redshifts, analytical fits to the data points have been performed, using a Monte Carlo Markov Chain method. The number density $\Phi$(M) of galaxies can be described by a Schechter function, given by the following equation:

$$\Phi(M_l) = \ln(10\Phi^\star)10^{(M_l - M_l^\star)(1+\alpha)} \exp(-10^{(M_l - M_l^\star)}) \tag{5.1}$$

where $M_l = \log(M/M_\odot)$, $\alpha$ is the low-mass end slope, $\Phi^\star$ is the normalisation, and $M_l^\star = \log(M^\star/M_\odot)$ is the characteristic mass. Schechter function fits are computed only above the completeness limits and the best-fit parameters are reported in Table 5.2.

A direct hint of the similarity of the GSMF of the samples considered is given by the inset plots included in all panels, which show the confidence contour at 1, 2, 3 $\sigma$ of the parameters that are significant for this analysis: $\alpha$ and $M^\star$. At $0.1 < z < 0.2$, Schechter fits agree within $1\sigma$ level, probing on a statistical ground that the shapes of the field and G&C GSMFs are very similar. Moving to higher redshifts, the significance of the results is lower, but still outstanding differences do not emerge. Contour levels on the Schechter parameters are superposed at the 2-3 $\sigma$ level. Note that at z>0.3, due to the limited mass range probed by the sample considered here, it is not possible to probe the slope of the GSMF and hence only the exponential tail of the mass distribution can be inspected. Hence, it was necessary to fix the $\alpha$ parameter to reduce the degeneracy and determine $M^\star$. The value chosen at this stage is the best value that can reproduce the data point distribution, both for field and for G&C galaxies separately.

It should be considered that comparisons of the parameters while fixing one of the two have to be taken carefully. Furthermore, note that at $0.4 \leq z < 0.6$ $M^\star$ is much less constrained in G&C than in the field, since there are no data points at $\log(M/M_\odot) > 12.2$. At lower masses, the two GSMFs clearly overlap.

Having assessed a similarity in the GSMF for galaxies in the different environments, the next step is to investigate its evolution with cosmic time. Figure 5.4 shows the variation of the GSMF with time for the ensemble of the field and G&C samples. Curves are normalised at the most massive data point at the lowest redshift bin ($0.1 \leq z < 0.2$, blue dots in the figure). In this way the assumption is that the most massive galaxies are

Table 5.2: Best-fit Schechter Function Parameters ($M^\star, \alpha$) for the GSMF in different environments and redshifts. Note that for $z \geq 0.3$ I fixed $\alpha$ in the fits, therefore it does not have errors. At $z > 0.4$, due to low number statistics,the sample could not be divided into Low and High $L^{XXL}_{500,scal}$ G&C.

| z | Environment | $\alpha$ | $\log(M^\star/M_\odot)$ |
|---|---|---|---|
| 0.1-0.2 | Field | -0.8 ± 0.4 | 10.6 ± 0.1 |
| | G&C | -0.01 ± 0.50 | 10.4 ± 0.1 |
| | G&C High $L^{XXL}_{500,scal}$ | 0.4 ± 0.7 | 10.3 ± 0.1 |
| | G&C Low $L^{XXL}_{500,scal}$ | 0.1 ± 0.5 | 10.4 ± 0.1 |
| 0.2-0.3 | Field | -0.80 ± 0.05 | 10.87 ± 0.06 |
| | G&C | -0.59 ± 0.08 | 10.98 ± 0.03 |
| | G&C High $L^{XXL}_{500,scal}$ | -0.87 ± 0.08 | 10.94 ± 0.04 |
| | G&C Low $L^{XXL}_{500,scal}$ | -0.72 ± 0.06 | 11.07 ± 0.06 |
| 0.3-0.4 | Field | -1.18 ± - | 11.1 ± 0.1 |
| | G&C | -1.18 ± - | 11.125± 0.007 |
| | G&C High $L^{XXL}_{500,scal}$ | -1.18 ± - | 11.1 ± 0.1 |
| | G&C Low $L^{XXL}_{500,scal}$ | -1.18 ± - | 10.69 ± 0.09 |
| 0.4-0.6 | Field | -0.8 ± - | 11.27 ± 0.05 |
| | G&C | -0.8 ± - | 11.07 ± 0.14 |

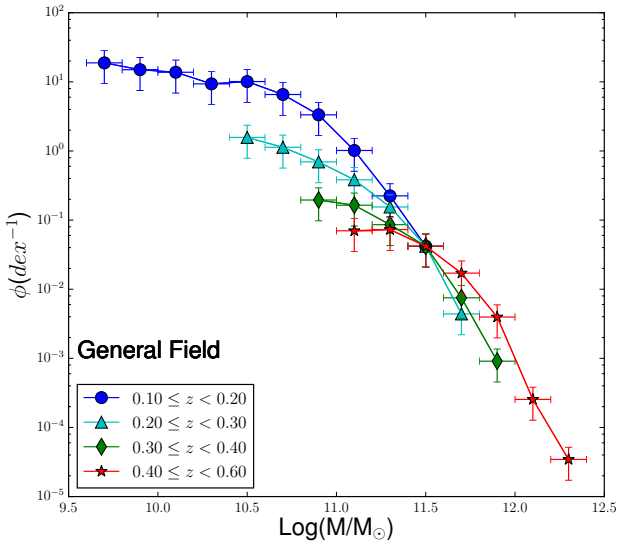


Figure 5.4: Evolution of the GSMF in the general field (pure field+G&C) with redshift. The curves are normalised at the number counts of the highest mass point of the GSMF at $0.1 \leq z < 0.2$ (blue curve).

already in place at $z \sim 1$ (see e.g. Fontana et al. 2004; Pozzetti et al. 2007). Although the mass range sampled at different redshift varies, the GSMFs in the figure show an

increase in the relative number of lower mass galaxies with decreasing redshift. These results are in agreement with previous findings (e.g. Marchesini et al. 2009; Moustakas et al. 2013; Muzzin et al. 2013; Ilbert et al. 2013; Vulcani et al. 2013) that showed that while the most massive galaxies are already in place at $z > 0.6$, the number of low mass galaxies proportionally increases going from higher to lower redshift. It was not possible to perform Schechter fits on these GSMFs because of the limited number of data points to rely on: in fact, in order to properly compare the fits, one should consider the stellar mass limit of the highest redshift bin. This condition does not allow to let both $\alpha$ and $M^\star$ parameters free to vary during the fit, as only the high mass end of the GSMF is sampled, and would force the assumption of a literature value for the faint end slope of the Schechter function $\alpha$, therefore preventing a direct study on the variation of the number of low mass galaxies.
The distribution of stellar mass in galaxies in G&C below $z < 1$ was investigated by Giodini et al. (2012), who exploited 160 X-ray detected galaxy G&C in the 2 deg$^2$ COSMOS survey at $0.2 < z < 1$ and determined G&C memberships with photometric redshifts. The main aim of their analysis was to shed light on the way the transition between the star forming and passive population occurs in different environments, and as a consequence a direct comparison with the results presented in this section cannot be done. For the low-redshift passive population, they find differences in the shape of the stellar mass function of passive galaxies between the groups and the field. On the other hand, they found that the stellar mass distribution of star forming galaxies is similar in the shape in all the environments. The analysis presented in this thesis is based on a much wider area, reducing the cosmic variance, and on spectroscopic redshifts. Giodini et al. (2012) also divided the sample into two subsamples of high- and low-mass G&C, and in different redshift ranges, probing a wider stellar mass range with respect to this study. Their distribution in X-ray luminosity and virial masses is narrower with respect to those considered here in the same redshift range, so that this analysis could exploit the dependence of the GSMF on environment also in more massive G&C. The two studies are complementary.

### 5.2.3 Dependence on X-ray luminosity

The previous section has shown how the environment has little effect on the overall galaxy stellar mass distribution at least above the adopted mass limit. Here I investigate whether the global properties of the G&C are related to the GSMF and to the typical stellar mass of the galaxies they host.
The G&C sample in this work spans a wide range of $L^{XXL}_{500,scal}$ (see Figure 2.5 in Chapter 2). It is therefore possible to consider separately galaxies in low luminosity G&C ($L^{XXL}_{500,scal} < 10^{43}\,\mathrm{erg\,s^{-1}}$) and high luminosity G&C ($L^{XXL}_{500,scal} > 10^{43}\,\mathrm{erg\,s^{-1}}$) and investigate whether the galaxy stellar mass distribution changes with X-ray luminosity. Figure 5.5 shows that galaxies in G&C characterised by different values of $L^{XXL}_{500,scal}$ have very similar mass distribution, emphasising once again how the global environment does not impact the GSMF in the mass range probed here. These findings are supported also by the analysis of the Schechter fit parameters, shown in the insets of Figure 5.5 (see also Table 5.2).

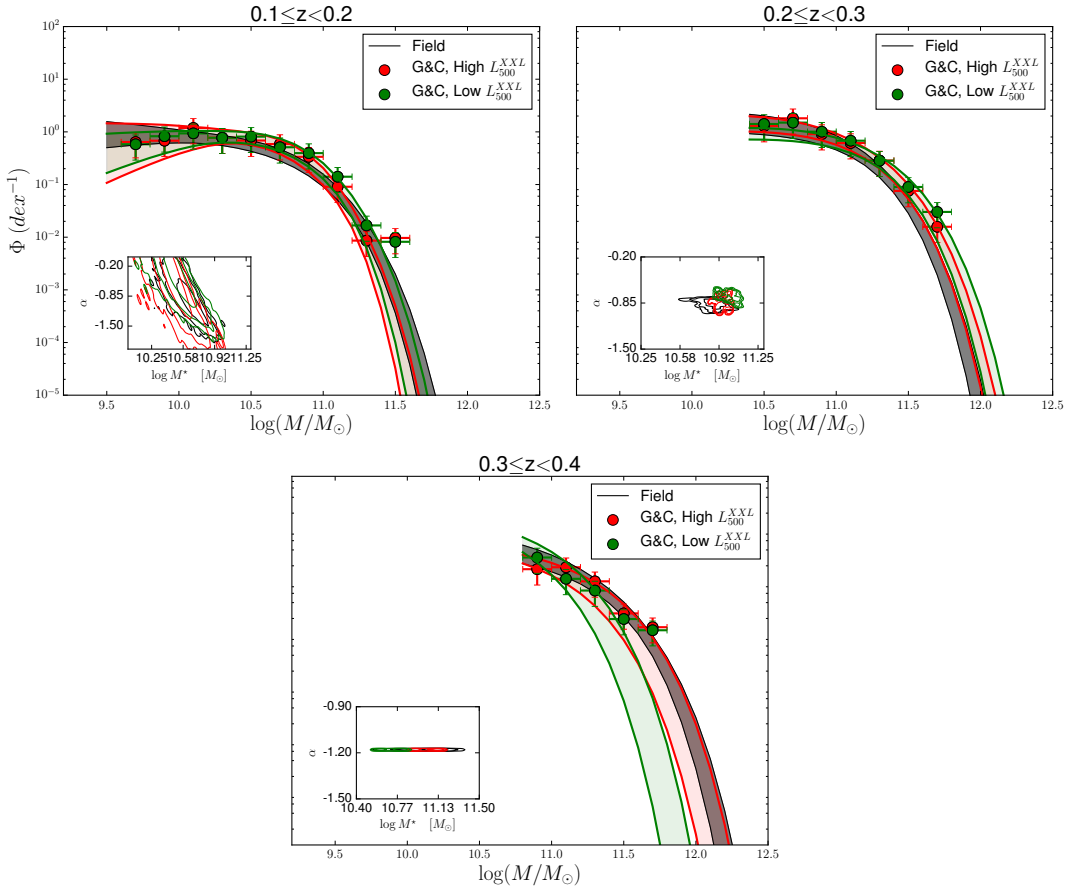


Figure 5.5: GSMF at different redshifts, as indicated in each panel, for galaxies in G&C with different X-luminosity and in the field (black diamonds). High X-ray luminosity G&C members ($L_{500,scal}^{XXL} > 10^{43}$erg s$^{-1}$) are plotted with red symbols, low X-ray luminosity G&C members are plotted with green symbols ($L_{500}^{XXL}$ in the figure). Only points above the mass completeness limit are shown. Error bars on the x-axis show the width of the mass bins, error-bars on the y-axis are derived from Poisson's statistics on the number counts together with cosmic variance contribution. Note that, due to low number statistics of the sample, this analysis is limited to redshift 0.4. At z≥0.3, fixed values for the faint end slope $\alpha$ were set in order to perform Schechter fits.

Note that in the sample given in Table 5.1, the number of low luminosity G&C at $z > 0.4$ is very small, therefore a statistically meaningful comparison at these redshifts is not possible.

Figure 5.6 shows the mean stellar mass of G&C members as a function of the G&C X-luminosity, in the four redshift bins. At each cosmic epoch, mean values are obtained only considering the galaxies that enter the mass complete sample at that redshift. The stellar mass limit of each redshift bin is taken to be the stellar mass limit of the highest redshift sub-interval within that bin. The mean value of the mean stellar mass is computed in

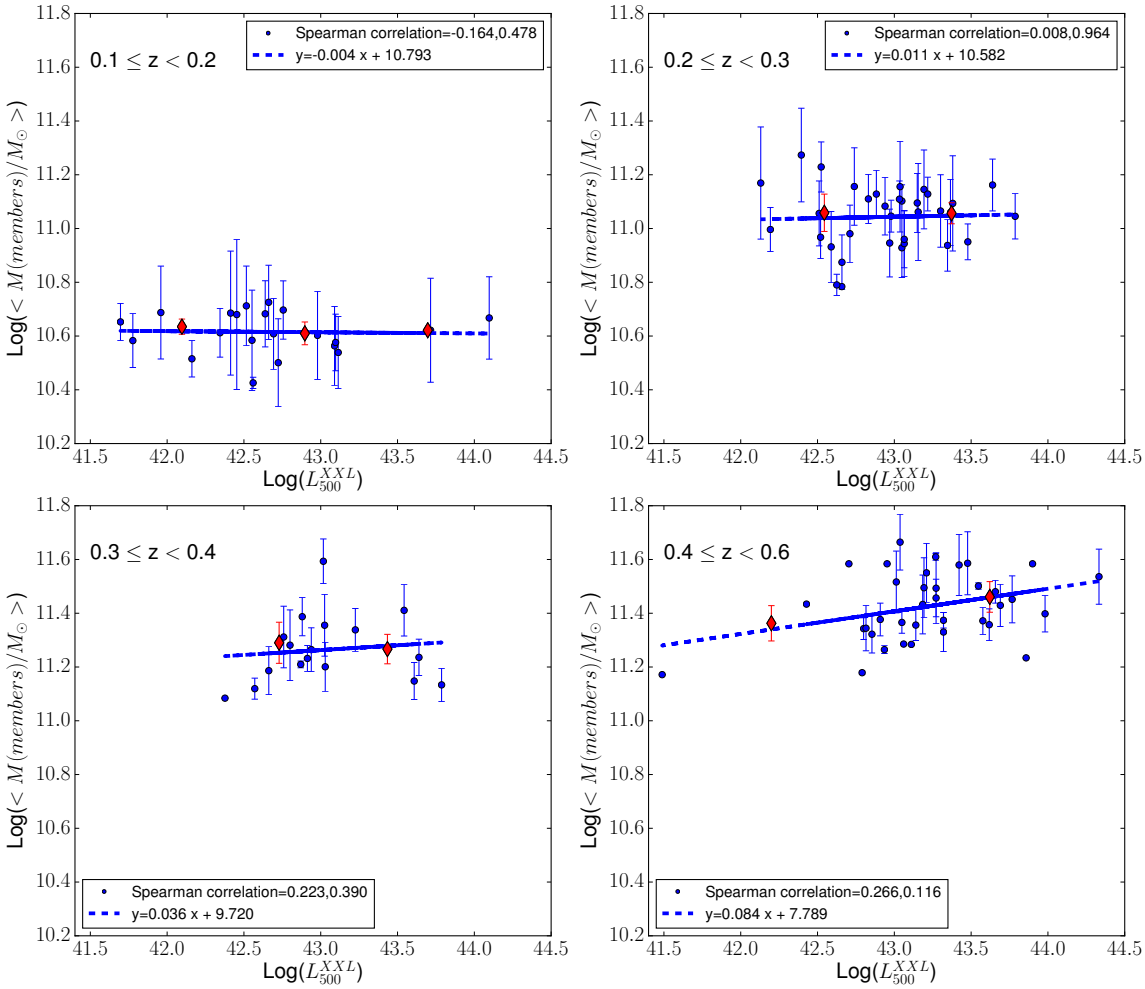


Figure 5.6: Correlation between the mean mass of member galaxies of G&C and the X-ray luminosity of the host G&C (blue dots) in the four redshift bins where the stellar mass function was computed. The mean value of the y-axis quantity was computed in equally populated bins of X-ray luminosity (three at $z = 0.1 - 0.2$, two in the other redshift intervals) and is shown with red diamonds. Least-squares fits are shown with dashed lines in the figure and least-squares fit parameters are shown in the legend.

equally populated bins of X-ray luminosity (three at 0.1≤z<0.2, two in the other redshift intervals). No strong correlations emerge, as also confirmed by the Spearman correlation test. The first value of the Spearman correlation that is shown in the legend of Figure 5.6 refers to the slope of the correlation, and the second one is the p-value. The latter shows that the correlations are not very tight at all redshifts except the highest one, which is also the only case in which a positive correlation is found. However, the presence of some outliers (e.g. at 0.3≤z<0.4) may influence these results, as well as the scarcity of data in some bins. Least-squares fits of the data are also shown with dashed blue lines in the plot

and the least-squares lines are written in the legend. The slope of the lines in all panels points out that, overall, trends are almost flat, supporting again the scenario that, at any given redshift, the global environment does not strongly affect galaxy masses.
At similar redshifts, Vulcani et al. (2014b) have shown that in clusters the mass of both the central galaxy and of the most massive satellite correlates with the velocity dispersion of the hosting halo (see also, e.g., Shankar et al. 2006; Wang et al. 2006; Moster et al. 2010; Leauthaud et al. 2010). They interpreted that evidence as sign that the environment has a strong effect on the mass of the central and most massive satellites. Indeed, the mass growth of these galaxies is known to be due to mergers and accretion from tidal stripping events, as well as different gas cooling and heating mechanisms. All these factors might depend on the size of the G&C (see, e.g., Coziol et al. 2009; Hopkins et al. 2010; Nipoti et al. 2012; Newman et al. 2012; Vulcani et al. 2014a).
Taken together, these results might indicate that the environment can only affect the mass of peculiar galaxies, like the most massive ones in the systems, but it is not able to impact the overall mass budget.
Since it is well known that galaxies in different environments and with different stellar masses have different star formation properties and are subject to different physical processes, one could expect different mass growth rates and timescales in different environments. The findings presented in this section instead suggest that at the redshifts and mass range considered here most of the galaxy mass have already been assembled, and that environment-dependent processes have had no significant influence on galaxy mass. This means that at least at $z \leq 0.6$, strangulation and other gravitational interactions, while affecting other galaxy properties like morphologies and star-forming properties, have a mild effect on galaxy mass, that have already been assembled, and hence on the galaxy mass distribution. Studies of the properties of the different galaxy populations in the different environments will help in understanding the impact of the different processes (see the next Chapter 6 and 7 of this thesis, and related papers: Guglielmo et al. 2018a, submitted; Guglielmo et al. 2018b,c in preparation).

## 5.3 Summary

In this chapter the catalogue of galaxies in X-ray selected G&C from the XXL Survey and in the field, assembled in Chapter 4 of this thesis was employed to analyse the GSMF of galaxies in G&C and in the field at different redshift. As previously found e.g. by Vulcani et al. (2013), no significant differences emerge between the shape of the GSMF in the different environments and for galaxies located in G&C with different X-ray luminosities. These findings suggest that at the redshifts considered here environment-dependent processes have had no significant influence on galaxy mass, at least in the mass range we are sampling.
In the following chapters, the spectrophotometric catalogue will be used to investigate the spectral features of galaxies as a function of redshift and environment, to derive the SFR and reconstruct the SFH within X-ray G&C and comparing them with those in the

corresponding field sample.

# 6

# CHARACTERISATION OF THE XLSSsC N01 SUPERCLUSTER AND ANALYSIS OF THE GALAXY STELLAR POPULATIONS

## Content

This chapter is focused on XLSSsC N01, a supercluster located in the XXL-North field centered in RA=36.952, DEC=-4.775, and centroid redshift z=0.2956 (Adami et al. 2018). This supercluster is the best candidate for environmental studies on galaxies being the richest one in the XXL-North field (14 groups and clusters; hereafter, G&C), and being located in a region of the sky with highly complete spectroscopic and photometric data.

The aim of this study is to present the XLSSsC N01 supercluster, characterise the G&C it is composed of and investigate the stellar populations properties of galaxies classified as members, or belonging to the surrounding filaments and field.

I study a magnitude limited sample ($r \leq 20$) and a mass limited sample ($\log(M/M_{\odot}) \geq 10.8$) of galaxies in the virialised regions and in the outskirts of 11 XLSSsC N01 G&C, in dense regions outside G&C (tracing filamentary structures) and in low-density field. For $r \leq 20$, the fraction of star forming/blue galaxies shows depletion within G&C virial radii. For $\log(M/M_{\odot}) \geq 10.8$, no trends with environment emerge, as massive galaxies are mostly already passive in all environments. No differences between field, filaments and G&C members emerge in the sSFR-mass relation in the mass complete regime. Finally, the LW-age-mass relation of passive populations within G&C virial radii show signatures of recent environmental quenching.

The results of this study are included in Guglielmo et al. (2018a, submitted).

## 6.1 Galaxy sample

### 6.1.1 Catalogue of the structures

For the purpose of this chapter, it is important to remind that XXL provides an unprecedented volume between $0.1 < z < 1$ with which is it possible to study the nature and evolutionary properties of groups, G&C, and superclusters of galaxies. Besides the extended ROSAT-ESO Flux-Limited X-ray Galaxy Cluster Survey (REFLEX II), it is the second survey which has detected several superclusters of galaxies even beyond $z = 0.4$. As already highlighted in Pacaud et al. (2016) and subsequently in Adami et al. (2018), the selection method used for XXL superclusters has the advantage of relying only on galaxy structures showing clear evidence of a deep potential well and further extend the volume used for such study ($z \geq 0.3$).

To have homogeneous estimates for the complete sample, I consider the following G&C parameters derived via scaling relations based on the $r = 300$ kpc count-rates (see Chapter 2 for details): the $L^{XXL}_{500,scal}$, $T_{300kpc,scal}$, $M_{500,scal}$ and $r_{500,scal}$. Furthermore, I make use of velocity dispersions ($\sigma_{200}$) derived from $M_{500,scal}$ using the procedure detailed in the environment definition (Section 3.1), which makes use of a relation based on the virial theorem given in Poggianti et al. (2006). Finally, I rely on the catalogue of superclusters built in Adami et al. (2018), containing 35 superclusters identified by means of a FoF algorithm characterised by a Voronoi tesselation technique: the complete list is available in Table 9 of that paper.

Among them, XLSSsC N01 is the largest supercluster identified in Adami et al. (2018), with an extension of $\sim 2$ deg in right ascension and $\sim 3$ deg in declination; the coordinates of the centroid of the structure are RA=36.954, DEC=-4.778 and redshift z=0.2956. The supercluster is composed of 14 spectroscopically confirmed G&C, whose main properties are described in Table 6.1: 9/14 are classified as C1, 3/14 are C2 , while only two of them classified as C3. In the following, I will consider only C1+C2 G&C for which X-ray count-rates provide good quality measurements of virial properties. Among these, I will exclude xlssc 028 because it is located outside of the region covered by our photo-z catalogue of galaxies (see Sect. 6.1.2).

Note that the XLSSsC N01 G&C $M_{500,\mathrm{scal}}$ masses range from $4 \times 10^{13}$ to over $2 \times 10^{14} M_{\odot}$, with half of the G&C having masses greater than $10^{14} M_{\odot}$, which corresponds to X-ray luminosities $L^{XXL}_{500,scal}$ greater than $10^{43}$ erg/s. This distribution of virial masses/X-ray luminosity does not differ from that characterised in the overall C1+C2 sample analysed in Chapter 2, meaning that at first sight, G&C assembling together to form a supercluster are not required to have peculiar values of virial masses or X-ray luminosities.

### 6.1.2 Galaxy catalogue

To characterise the properties of the galaxies in the XLSSsC N01 supercluster, I extract the useful information from the spectrophotometric catalogue presented in Chapter 4. In particular, I focus on the area covered by the supercluster (RA[35.25:38.0], DEC[-6.25:-

Table 6.1: X-ray and membership properties of G&C within XLSSsC N01 superstructure. Column 1 gives the IAU official name of G&C; column 2 is the classification of G&C according to the level of contamination as explained in Pacaud et al. (2016); column 3 is the spectroscopic redshift of the G&C; columns 4 and 5 contain the RA-DEC coordinates of the X-ray centre of G&C; columns 6, 7, 8, 9, 10 report all X-ray parameters derived through scaling relations from X-ray count-rates Adami et al. (2018): temperature ($T_{300kpc,scal}$), virial radius ($r_{500,scal}$), virial mass ($M_{500,scal}$), luminosity ($L^{XXL}_{500,scal}$). Velocity dispersion ($\sigma_{200}$) was measured in XXL Paper XXII using a relation based on the virial theorem given in Poggianti et al. 2006; column 11 and 12 report the number of spectroscopic members within $1r_{200}$ and $3r_{200}$ as assigned in section 4.1.

| xlssc | class | z | RA (deg) | DEC (deg) | $T_{300kpc,scal}$ (KeV) | $r_{500,scal}$ (Mpc) | $M_{500,scal}$ ($10^{13}M_\odot$) | $L^{XXL}_{500,scal}$ $10^{42}$(erg/s) | $\sigma_{200}$ (km/s) | $N_{gal,1r200}$ | $N_{gal1-3r200}$ |
|---|---|---|---|---|---|---|---|---|---|---|---|
| 008 | C1 | 0.2989 | 36.336 | -3.801 | 1.6±0.2 | 579±53 | 7±2 | 5.5±0.9 | $404^{+32}_{-38}$ | 12 | 6 |
| 013 | C1 | 0.3075 | 36.858 | -4.538 | 2.0±0.2 | 635±57 | 10±3 | 8.7±0.8 | $445^{+37}_{-46}$ | 31 | 22 |
| 022 | C1 | 0.2932 | 36.917 | -4.858 | 3.1±0.2 | 835±79 | 22±6 | 30.1±1.2 | $588^{+44}_{-53}$ | 38 | 50 |
| 024⋆ | C3 | 0.2911 | 35.744 | -4.121 | - | - | - | - | - | - | - |
| 027 | C1 | 0.2954 | 37.012 | -4.851 | 2.4±0.2 | 710±64 | 13±4 | 14.1±1.1 | $494^{+41}_{-51}$ | 15 | 13 |
| 028⋆ | C1 | 0.2969 | 35.984 | -3.098 | 1.5± 0.2 | 545±52 | 6±2 | 4.1±0.9 | $380^{+34}_{-43}$ | - | - |
| 070⋆ | C3 | 0.3008 | 36.863 | -4.903 | - | - | - | - | - | - | - |
| 088 | C1 | 0.2951 | 37.611 | -4.581 | 2.5±0.2 | 725±66 | 14±4 | 15.6±1.4 | $505^{+40}_{-48}$ | 16 | 10 |
| 104 | C1 | 0.2936 | 37.324 | -5.895 | 2.5±0.2 | 735±67 | 15±4 | 16.5±1.4 | $512^{+38}_{-45}$ | 7 | 35 |
| 140 | C2 | 0.2937 | 36.303 | -5.524 | 1.2±0.2 | 491±53 | 4±1 | 2.5±0.8 | $337^{+23}_{-27}$ | 2 | 11 |
| 148 | C2 | 0.2938 | 37.719 | -4.859 | 1.8±0.2 | 608±63 | 8±3 | 6.8±1.8 | $423^{+42}_{-55}$ | 11 | 23 |
| 149 | C2 | 0.2918 | 37.634 | -4.989 | 2.0±0.2 | 655±60 | 10±3 | 9.5±1.3 | $455^{+37}_{-45}$ | 8 | 11 |
| 150 | C1 | 0.2918 | 37.661 | -4.992 | 2.2±0.2 | 678±62 | 12±3 | 11.2±1.3 | $472^{+33}_{-39}$ | 9 | 0 |
| 168 | C1 | 0.2948 | 37.387 | -5.880 | 2.8±0.2 | 790±74 | 18±5 | 23.2±1.7 | $550^{+42}_{-51}$ | 12 | 3 |

⋆These G&C are excluded from this analysis either because they are classified as C3 or because of the lack of photometric data, as explained in the main text.

3.5]), and the redshift range $0.25 < z < 0.35$, for a total of 3759 objects. I remind that I was involved in dedicated spectroscopic observations using the AF2 multifiber spectrograph at WHT. The observations regarded a region covered by three G&C in the supercluster (xlssc 013, 022 and 027).

To derive the properties of galaxies and of their stellar populations, I exploited both LePhare and SINOPSIS. Absolute magnitudes are computed using LePhare, as described in Chapter 3. Galaxy stellar population properties have been derived by fitting the spectra with SINOPSIS.

Each galaxy in the sample is weighted for spectroscopic incompleteness as computed in Chapter 4. Note that in the whole XLSSsC N01 region the spectroscopic completeness does not vary when using the sample with the outputs from SINOPSIS, and that the completeness curves of the galaxies within G&C are statistically similar to those of galaxies in the field.

I applied the same magnitude cut and completeness weight to all samples and environments. As already mentioned in the previous chapters, the magnitude completeness limit is set to $r = 20.0$, which, at the redshift of XLSSsC N01, corresponds to an absolute magnitude of $M_r \sim -21.4$. In the magnitude complete sample, which selects 2429 galax-

ies out of 3759, the 97% of the galaxies come from the GAMA+SDSS survey (2323 and 27 galaxies, respectively), which provide the spectra which are going to be analysed in the following. The magnitude completeness limit is converted into a conservative mass completeness limit of $\log(M_{lim}/M_{\odot}) = 10.8$, following the procedure detailed in Section 3.2.1.

## 6.2 Characterisation of the XLSSsC N01 supercluster: the definition of environment

Figure 6.1 shows the spatial distribution of XLSSsC N01 G&C and galaxies. In the top panels, the centre of each of the G&C belonging to XLSSsC N01 is shown, along with the 3 $r_{200}$ circles indicating the G&C sphere of influences. The spectrophotometric sample of galaxies in the top right panel shows, with different colours, galaxies belonging to the four environments I use in this chapter. Based on virial properties of G&C together with redshifts of galaxies and their distance from the G&C within XLSSsC N01, I distinguish two membership regions:

- G&C virial members are galaxies whose spectroscopic redshift lies within $3\sigma$ from their G&C mean redshift, where $\sigma$ is the velocity dispersion of their host G&C and whose projected distance from the G&C centre is $< 1\, r_{200}$.[1] The number of G&C virial members is 130 (4.2% of the spectrophotometric sample). Virial members are reported in the top right panel of Figure 6.1 with dark orange diamonds.

- G&C outer members are galaxies whose spectroscopic redshift lies within $3\sigma$ from their G&C mean redshift, and whose projected distance from the G&C centre is between 1 and 3 $r_{200}$. The number of G&C outer members is 133 (4.3% of the spectrophotometric sample), and they are reported in the top right panel of Figure 6.1 with black stars.

In order characterise galaxies in different environments, I extend the definition of G&C members/outer members as follows. I considered the redshift range $0.25 \leq z \leq 0.35$, and removed galaxies belonging to other G&C in the same region, which are not members of the supercluster because of their redshift: 197 galaxies out of 3120 (6.3%) are removed from the sample, so that the remaining 3255 galaxies belong to a *general field* sample which is not contaminated by the presence of other X-ray G&C.
Then, I computed projected LD in order to further refine the *general field environment*. I considered all galaxies in the photo-z sample with an observed magnitude $r \leq 22.0$, and a photo-z in the range $0.25 \leq z_{phot} \leq 0.35$: $r$=22.0 is the fainter magnitude at which the error in the photo-z estimate is low ($photo{-}z_{err}/(1{+}z) \sim 0.03$), while the photo-z range is chosen on the basis of the scatter in the spectroscopic vs photometric redshift plane (plot not shown) in order to simultaneously minimise the contamination from galaxies with a

[1] I recall that $r_{200}$ derives from $r_{500}$, simply dividing the latter by 0.7, according to the relation adopted in Ettori & Balestra (2009).

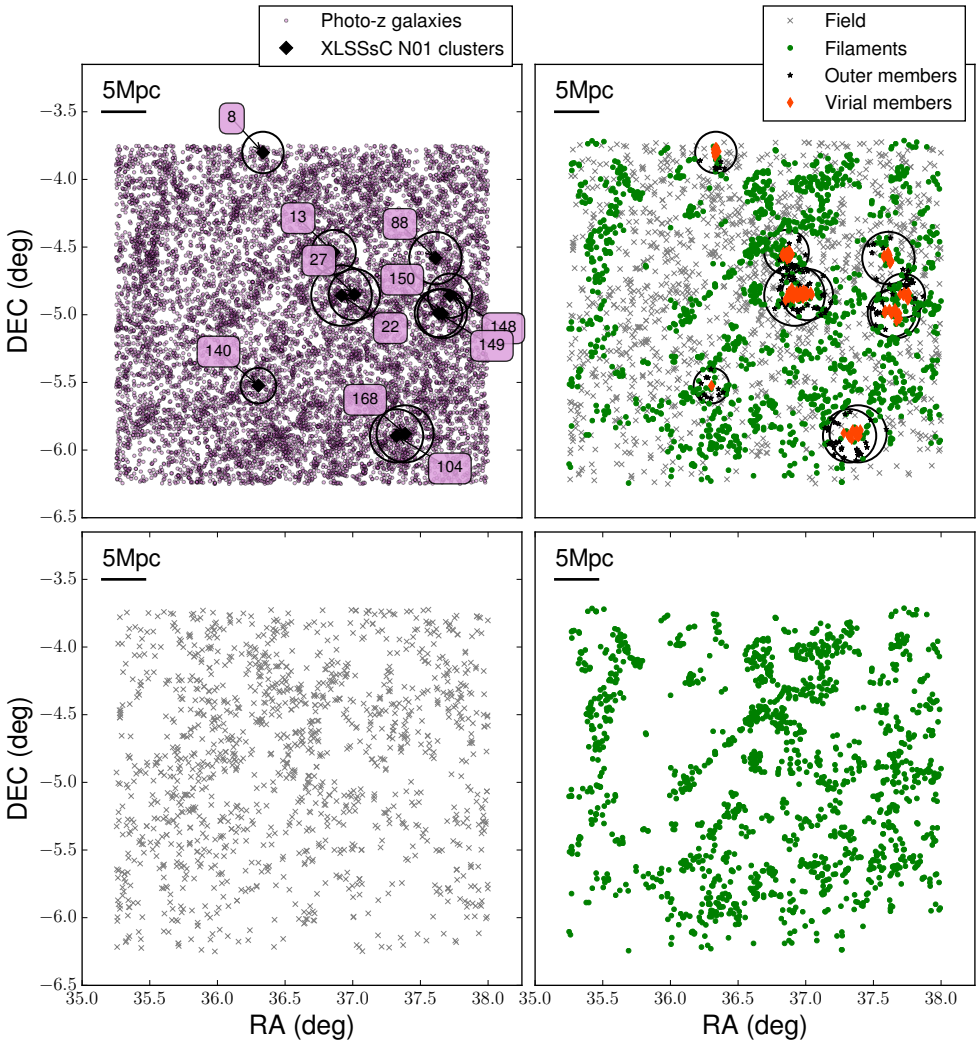


Figure 6.1: Sky distribution of galaxies in the XLSSsC N01 supercluster region. Top left panel shows as black points galaxies with a photo-z redshift in the range between 0.25 and 0.35 (used to compute the LD). Top right panel shows galaxies with a spectroscopic redshift, color coded according to their environment, as defined in Sec. 6.2. Grey crosses are field galaxies, green dots are galaxies in filaments, dark orange diamonds represent virial members and black stars are outer members. In the top panels, black circles show the projected extension in the sky of 3 $r_{200}$ for each G&C in the superstructure. The two bottom panels show the field and filament samples separately, with the same symbols as the top right panel.

photo-z within the selected range but with spectroscopic redshift outside of this range, and maximise the number of galaxies at the redshift of the supercluster. I included in the LD computation also galaxies with no reliable photo-z, but whose spectroscopic redshift is $0.25 \leq$ spec-z $\leq 0.35$. The photo-z sample of galaxies used in the LD computation is

shown in the top left panel of Figure 6.1. I defined the projected LD relative to a given galaxy as the number of neighbours in a fixed circular region in the sky of radius 1 Mpc at z=0.2956 (the redshift of XLSSsC N01). All galaxies in the photo-z sample are taken in a slightly larger rectangular region with respect to that defined in above in this section, in order to minimise the regions in which boundary corrections had to be performed: $35.0 \leq RA \leq 38.25$, $-6.5 \leq DEC \leq -3.5$.
The LD is defined as the ratio between the number counts of galaxies $N_c$ in the circle around the considered galaxy and the area $A$ of the circle itself. Count corrections are performed for galaxies in the proximity of the edges in the high declination side of the rectangle, by implementing a Monte Carlo method for computing the area of the circular segment that falls outside the field and dividing the LD estimate by the ratio $F_c\,(\leq 1)$ between the area actually covered by the data and the circular area.
I finally considered the histogram of the logarithm of the estimated LD to define two environments: galaxies with log(LD) higher than the median value of the distribution ($\log(LD/Mpc^{-1}) \gtrsim 3.3$) belong to "filaments", and galaxies with log(LD) lower than the median belong to the "field" sample. The number of galaxies belonging to filaments is 1436 (46.0%) and to the field is 1224 (39.2%).
Note that the definition of filaments is nothing but a custom denomination used to identify galaxies in the densest LD regions of the *general field*, motivated by the spatial distribution of galaxies in Figure 6.2 (see green dots in the top right and bottom right panels).
Figure 6.2 represents the photo-z sample of galaxies used to compute the LD, where each galaxy is colour coded according to its LD. The LD peaks in the regions where the G&C are located, indicated with black circles in the plot. The LD distribution for the field, the filaments and G&C virial and outer members is shown in Figure 6.3. By definition, the LD distributions of field and filament galaxies are separated at the median value of log(LD)$\sim$3.3. While the distribution of G&C virial members is distinct and shifted towards higher values, the distribution of outer members is broadened in the range of log(LD) going from the typical values of filaments and field to 3.7 (more typical value of G&C virial members).
The field and filament samples are reported together in the top right panel of Figure 6.1 along with virial/outer members, and separately in the two bottom panels of the same Figure, to better visualise and motivate their definition: indeed, the filament sample traces the presence of several structures around the G&C belonging to XLSSsC N01.
The redshift distribution of galaxies in the different environments is shown in the left panel of Figure 6.4. The right panel of the same figure zooms in the redshift distribution of the members, highlighting how the distribution is bimodal, with a second peak in redshift in correspondence of the xlssc 013 cluster.
From Figure 6.1, it emerges that several G&C are gathered together to form substructures within the supercluster region.
The redshift distribution of G&C virial members is divided into seven substructures according to their position in the sky and is shown in Figure 6.5, 6.6, 6.7, 6.8, 6.9, 6.10 and 6.11. The motivation for this subdivision is twofold: first, that G&C within each substructure have overlapping virial radii and redshift distribution of member galaxies,

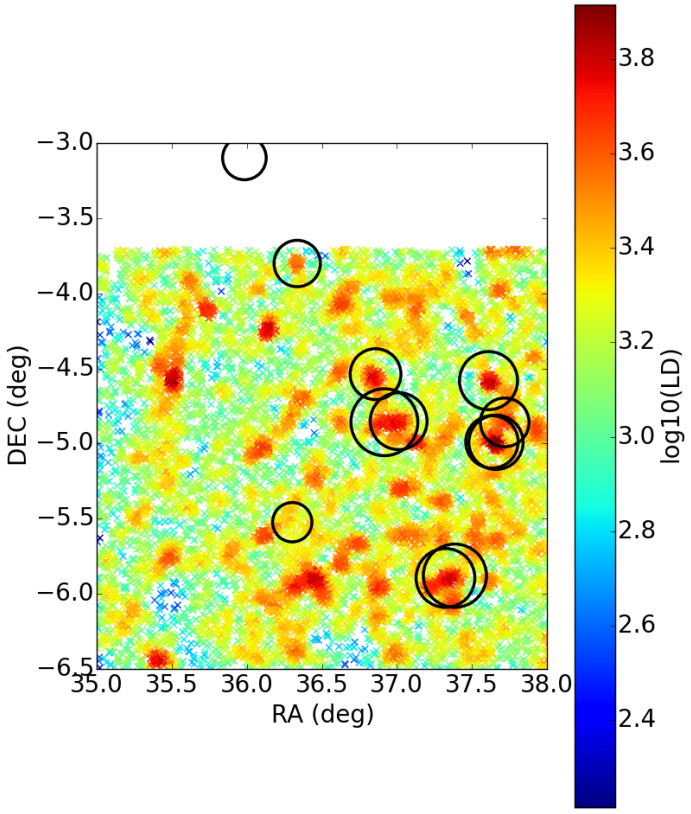


Figure 6.2: LD spatial distribution in the region surrounding XLSSsC N01 supercluster (RA-DEC plane). The logarithmic values of the local density are written in the colour bar next to the plot. Galaxies belong to the photo-z sample used to compute the local density, in the photo-z range $0.25 \leq z \leq 0.35$ and observed magnitude $r \leq$22.0. Black circles indicate the $3r_{200}$ radius of the G&C.

Table 6.2: Number of galaxies in the different environments, above the magnitude and mass completeness limit, respectively, for the sample with successful fits from LePhare and SINOPSIS. Numbers in parenthesis are weighted for spectroscopic incompleteness.

| | LePhare sample | | SINOPSIS sample | |
|---|---|---|---|---|
| | $r \leq 20$ | $\log(M_*/M_\odot) \geq 10.8$ | $r \leq 20$ | $\log(M_*/M_\odot) \geq 10.8$ |
| Virial members | 75 (96) | 62 (76) | 70 (84) | 48 (59) |
| Outer members | 99 (120) | 61 (74) | 100 (120) | 59 (71) |
| Filaments | 1159 (1427) | 633 (746) | 1215 (1470) | 607 (724) |
| Field | 958 (1189) | 450 (533) | 1024 (1252) | 438 (526) |

which are shared by more than one G&C in many cases. Second, the subdivision aims also at maximising the visibility of the X-ray contours related to each G&C or substructure, as shown in the figures.

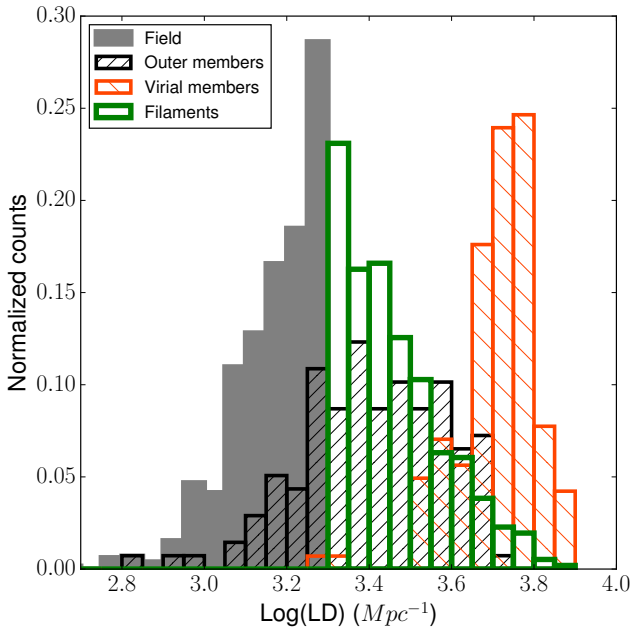


Figure 6.3: Normalized LD distribution as computed using the photo-z sample in the redshift range $0.25 \leq z_{phot} \leq 0.35$. The grey histogram represents the field, the green empty histogram represents galaxies in filaments, the black hatched histogram the G&C outer members and the orange hatched histogram the G&C virial members.

The final samples of galaxies that will be used in the scientific analysis are presented in Tab. 6.2. I report the number of galaxies in the spectrophotometric catalogue with LePhare and SINOPSIS outputs, respectively, in all the environments defined in this section, both in the magnitude limited and in the mass limited samples. I point out that I make use of both catalogues because SFRs are available only for the SINOPSIS sample, while the LePhare sample maximises the number of galaxies classified as G&C members. It is worth recalling that a discussion about the main reasons of fitting failures in the application of the two code to the data can be found in Section 3.2.2.

## 6.3 Stellar population properties versus environment

In this section I present the analysis of the stellar population properties of galaxies in different environments using both the magnitude complete sample ($r \leq 20.0$) and the mass limited sample ($\log(M/M_{\odot}) \geq 10.8$).
To distinguish between galaxies at different stages of their evolution, two different definitions of star forming and passive galaxies are exploited. The first definition is based on the current SFR and stellar mass as measured by SINOPSIS. I consider as star forming the galaxies with $sSFR > 10^{-11} yr^{-1}$ and as passive the remaining ones.
The second definition is based on galaxy colours as measured by LePhare. To identify

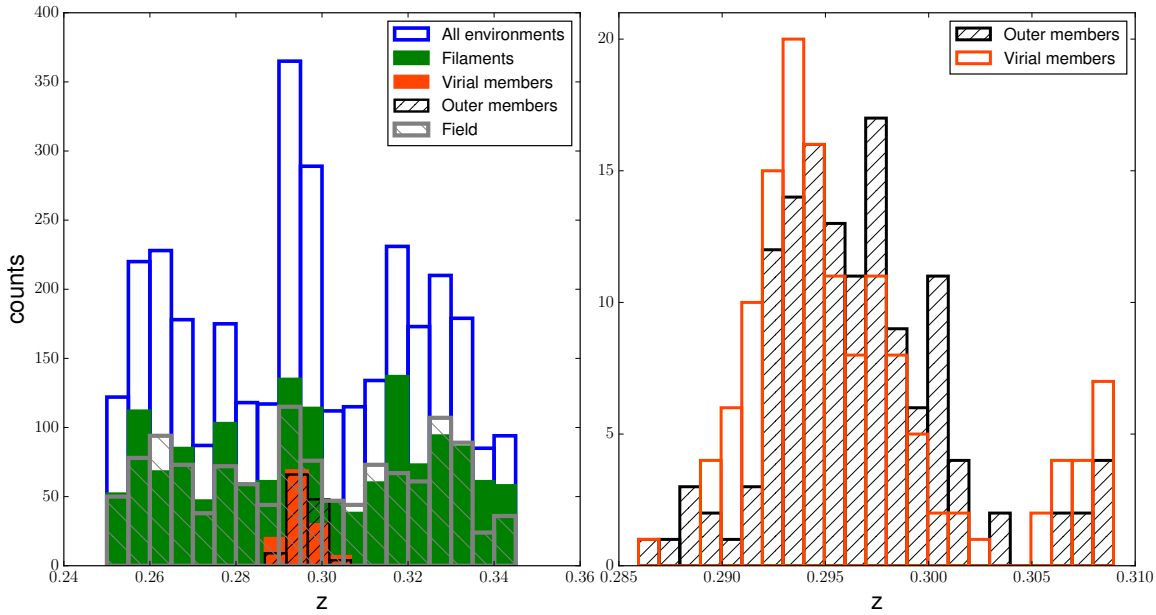


Figure 6.4: Redshift distribution of the spectrophotometric sample in the region including the XLSSsC N01 supercluster. Left panel: the whole spectroscopic sample is represented with the blue histogram, the grey distribution is for field galaxies, the green one is for galaxies in filaments and finally galaxies classified as virial and outer members are shown with the dark orange and black histogram, respectively. Right panel: zoom in on the virial and outer members, with the same colours used in the left panel. Details about the definition of different environments are given in Section 4.1.

the threshold in colour that best separates the blue and red populations, I investigated the correlation between sSFR, $(\mathrm{g}-\mathrm{r})_{\mathrm{rest-frame}}$ colour and $M_r$, as shown in Fig. 6.12 for the subsample of galaxies analysed by both LePhare and SINOPSIS. Passive galaxies, shown with red points, are mostly clustered at $(\mathrm{g}-\mathrm{r})_{\mathrm{rest-frame}} \geq 0.6$, while star forming galaxies, colour coded according to their sSFR, show a more spread distribution. Galaxies having $\log(sSFR/yr^{-1})$ >-9.8 most likely have $(\mathrm{g}-\mathrm{r})_{\mathrm{rest-frame}} < 0.6$, galaxies with bluer colours have on average $\log(sSFR/yr^{-1}) \sim -10$. I therefore consider as 'red', galaxies with $(\mathrm{g}-\mathrm{r})_{\mathrm{rest-frame}} > 0.6$, and 'blue' the rest. With this cut, 80% of passive galaxies are located in the red region of the diagram.

### 6.3.1 Dependence of the galaxy fractions on environment

I can now compute the fraction of blue and star forming galaxies, separately, in the different environments identified in the XLSSsC N01 region, as reported in Figure 6.13. Focusing on the star forming fractions (top left panel) in the magnitude-limited sample (shown with filled symbols), the fraction of star forming galaxies in virial members is $0.72^{+0.06}_{-0.05}$ whereas that in field galaxies is $0.79^{+0.01}_{-0.01}$; galaxies in filaments have an inter-

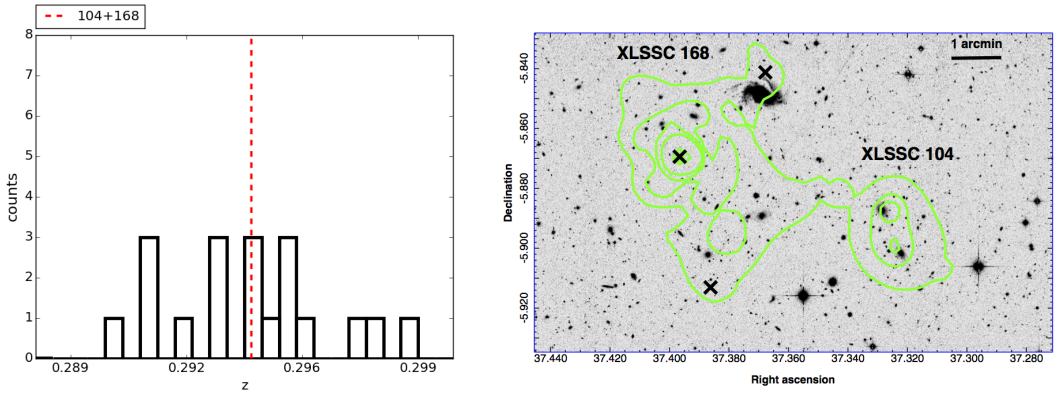


Figure 6.5: Left panel: Redshift distribution of the virial members grouped into the substructure composed by xlssc 104+ xlssc 168, as indicated in the labels. The redshift binning is the same in all histograms, and the x-axis extension depends on the redshift range covered by each substructure, for a better visualisation. The xlssc name of G&C composing each substructure is written on top of each panel. The mean redshift of the substructure is shown with a vertical red dashed line. Right panel: CFHTLS i-band image of the region surrounding xlssc 104 and xlssc 168 with X-ray contours superposed in green. Black crosses indicate the centre of the X-ray emission of point sources. The physical extension of the area in the sky is indicated within each panel.

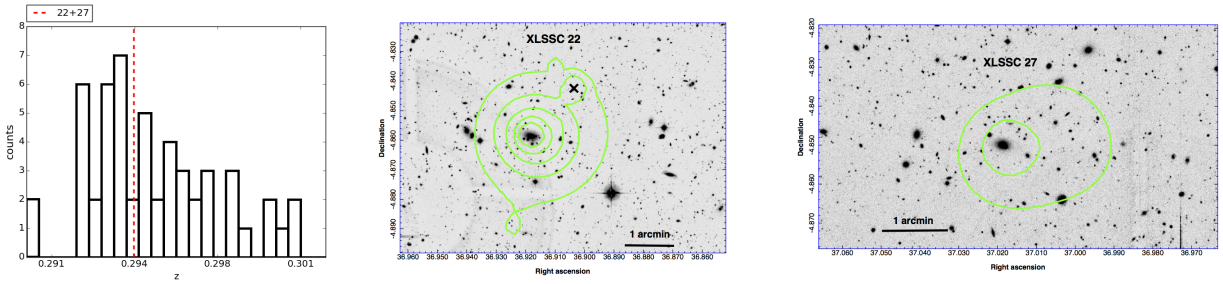


Figure 6.6: Same as Figure 6.5 but for xlssc 022 and xlssc 027.

mediate star forming fraction ($0.77^{+0.01}_{-0.01}$). The fraction of star forming galaxies in outer members is slightly higher with respect to the other environments ($0.80^{+0.04}_{-0.04}$) and in particular with respect to virial members.

Similar trends are visible when the rest-frame color is considered (top right panel of Figure 6.13), where the reduced size of error bars with respect to the star forming fraction panel at top left further confirms the results: in the magnitude-limited sample, the fraction of blue galaxies among the virial members is significantly lower than that in the other environments, being only $0.21^{+0.05}_{-0.04}$. By contrast, outer members and filaments have similar values within the error bars of $0.38^{+0.05}_{-0.05}$ in the former and $0.41^{+0.01}_{-0.01}$ in the latter, and

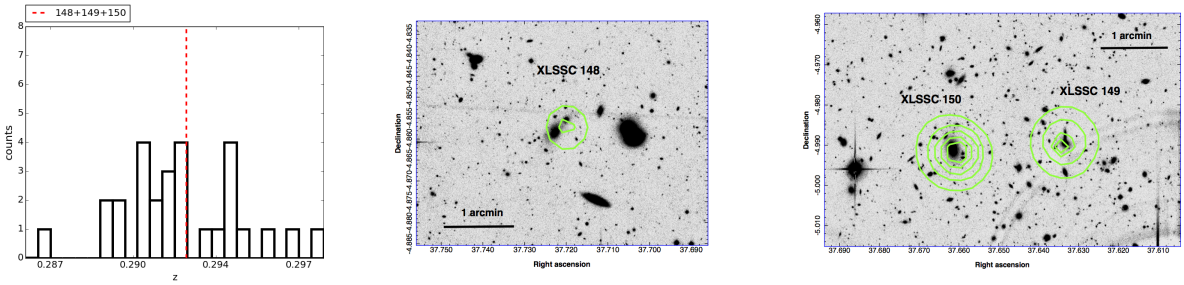


Figure 6.7: Same as Figure 6.5 but for xlssc 148, xlssc 149 and xlssc 150.

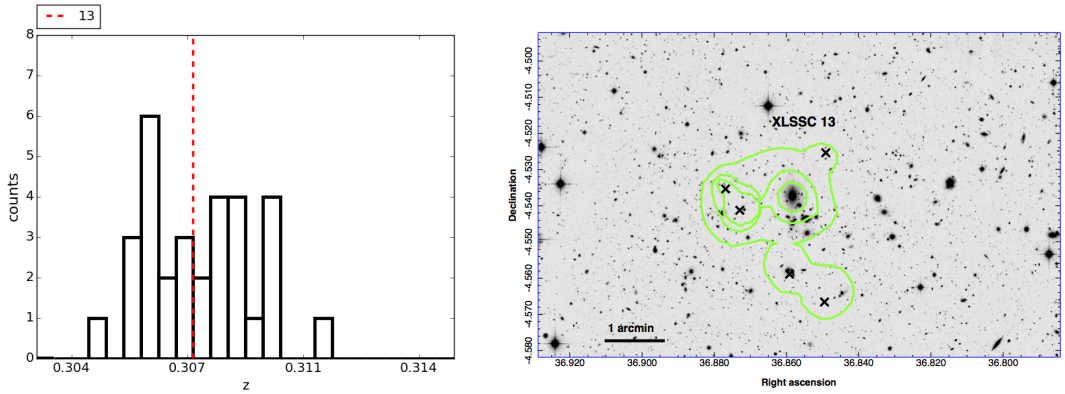


Figure 6.8: Same as Figure 6.5 but for xlssc 013.

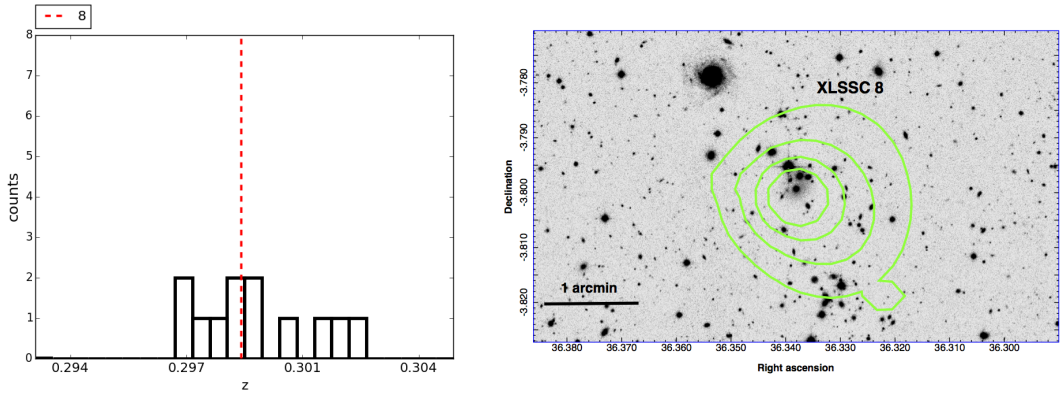


Figure 6.9: Same as Figure 6.5 but for xlssc 008.

galaxies in the field represent $0.47^{+0.02}_{-0.02}$ of the entire sample. The decrease in the fraction of blue galaxies from the field to the virial members population is a factor $\sim$2.3 and from outer to virial members a factor $\sim$1.8. When considering the mass limited sample (shown

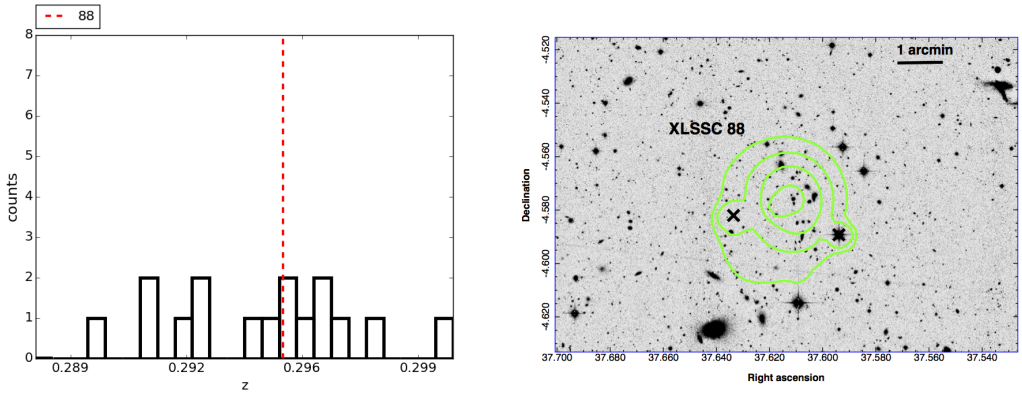


Figure 6.10: Same as Figure 6.5 but for xlssc 088.

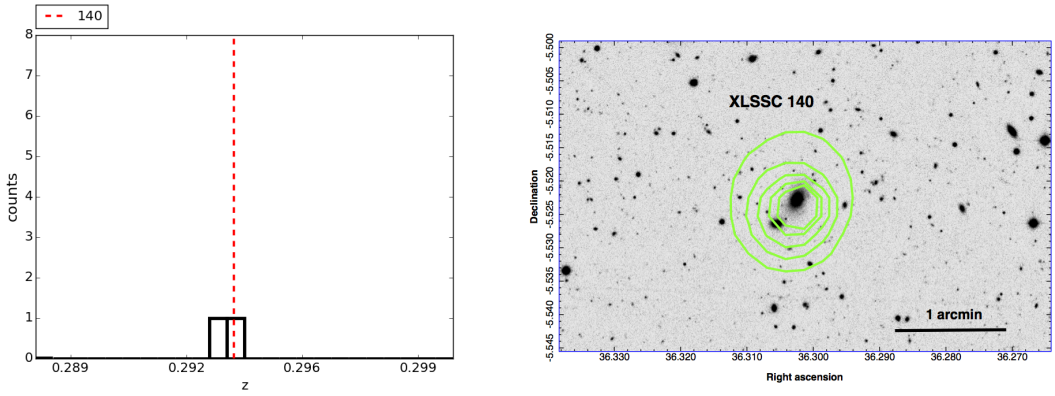


Figure 6.11: Same as Figure 6.5 but for xlssc 140.

with empty symbols and dashed error bars) the fractions decrease in all environments and the differences between different environments are smoothened. The only difference that is maintained is between the fraction of blue galaxies in G&C virial members and that in the pure field. The enhancement and subsequent decrease of the fraction of star forming/blue galaxies going from outer to virial members, both in the magnitude and in the mass complete regimes, points in the direction of an environmental effect that influences the evolution of these galaxies.

In the mass limited sample, any possible trend is washed out by the fact that our stellar mass limit at the redshift of the supercluster selects only high mass galaxies ($\log(M/M_{\odot}) \geq 10.8$), whose star formation activity, according to the downsizing scenario, was concentrated at earlier epochs and on shorter timescales before the onset of mass quenching. Indeed, the fraction of star forming/blue galaxies in the mass limited sample are always lower than their corresponding fraction in the magnitude limited sample in any of the considered environments.

Also, it can be noted that the fractions of blue and star forming galaxies are different.

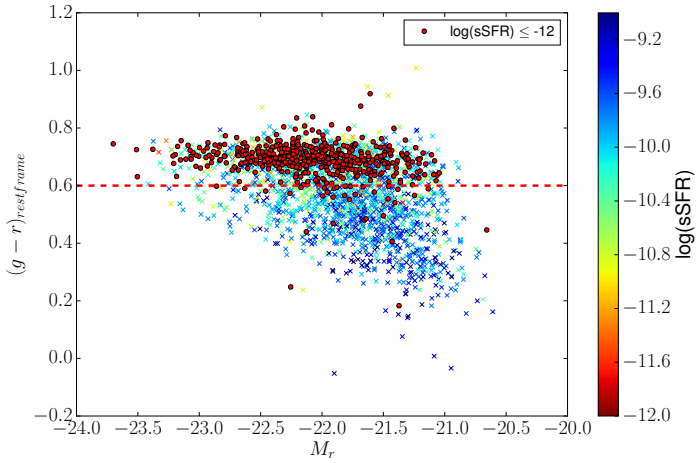


Figure 6.12: colour-magnitude diagram for galaxies in the magnitude limited sample for the subset with both SINOPSIS and LePhare outputs. Red points indicate passive galaxies, while galaxies with log(sSFR)>-11 are colour coded according to their sSFR. The red dotted line shows the separation between red and blue objects.

Besides the differences due to the different methods in which the two characteristics are derived, i.e. the SFR from spectroscopy and galaxy colours from photometry, it should be considered that the two definitions of "star forming" (sSFR) and "blue" (rest-frame colour) have different physical meanings. Indeed, while the SFR is a snapshot measuring the number of stars produced by the galaxy at the moment it is observed, the colour is sensitive also to the past history of the galaxy itself, especially the recent history, being determined by its predominant stellar population. Furthermore, colour is also influenced by other phenomena dealing with galaxies, e.g. metallicity and dust extinction.
Following the recipe given in Nantais et al. (2017) (previously formulated by e.g. van den Bosch et al. 2008), I define the "quenching-efficiency" parameter (Q.E.) of a given environment with respect to the field as:

$$Q.E. = \frac{F_{passive/red,i} - F_{passive/red,field}}{F_{starforming/blue,field}} \tag{6.1}$$

where $F_{passive/red,i}$ is the fraction of passive/red galaxies in that environment, $F_{passive/red,field}$ is the fraction of passive/red galaxies in the field and $F_{starforming/blue,field}$ is the fraction of star forming/blue galaxies in the field. Values of Q.E. in the different environments for the different subsamples are reported in the lower panels of Figure 6.13, below the corresponding fractions of star forming/blue galaxies they refer to.
The efficiency of the inner G&C regions in suppressing star formation stands out: the Q.E. assumes significantly higher values in G&C virial members. The trend is particularly significant using the colour fractions: the efficiency is highest in G&C virial members ($\sim$ 0.5), it decreases to $\sim$0.2 in outer members and to $\sim$0.1 in filaments.

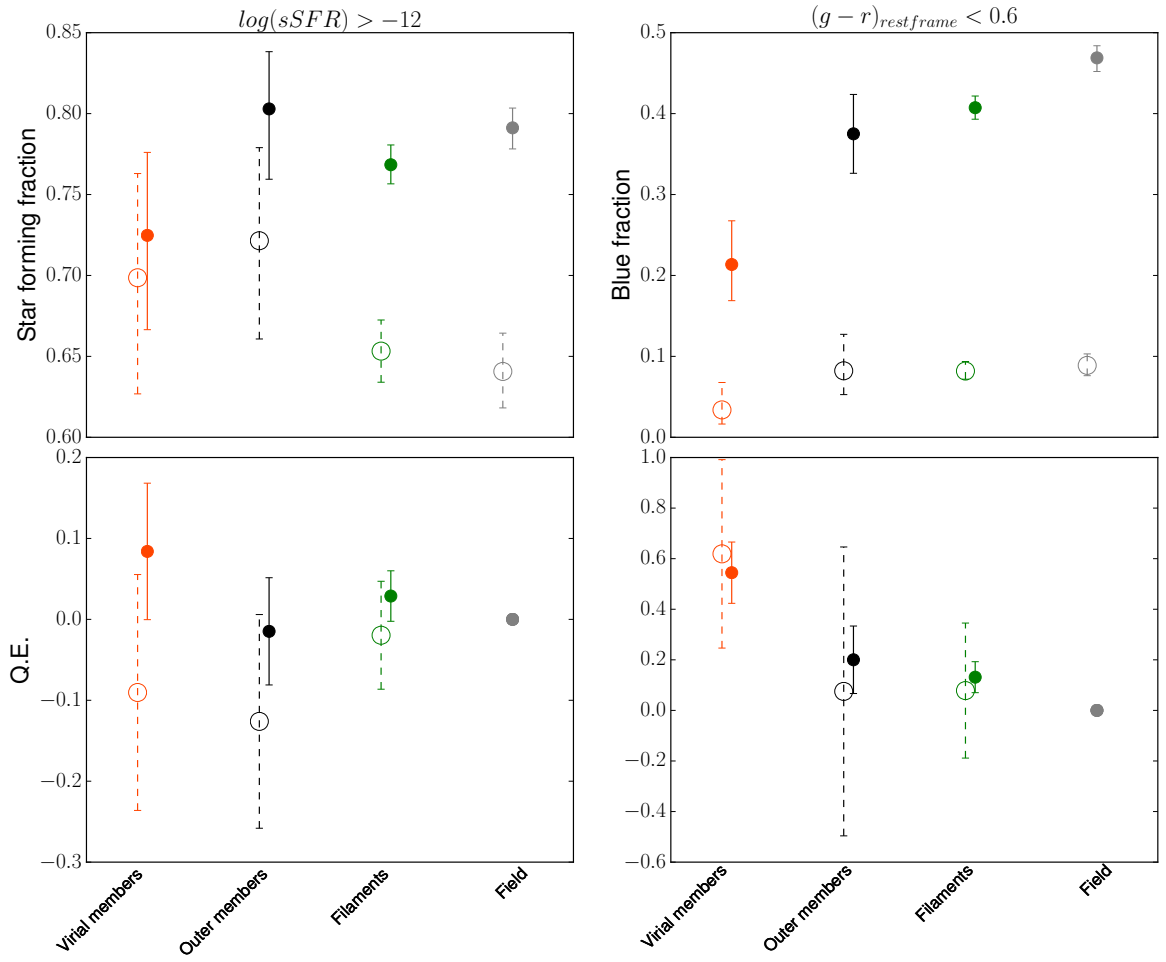


Figure 6.13: Fraction of star forming galaxies in different environments, computed with sSFR (left panel) and rest-frame colour (right panel). The fractions obtained using the magnitude limited sample are represented with filled symbols and solid errors, those obtained using the mass limited one are represented by empty symbols and dashed error bars. Errors are derived by means of a bootstrap[2] method. The two lower panels show the Q.E. in different environment, computed with equation 6.1 for both the star forming and blue samples. Errorbars on the Q.E. are derived from the errors in the star forming and blue fractions using the propagation of errors.

Values computed using the sSFR fractions are lower: the Q.E. is close to zero in all environments except as traced by virial members, where it reaches a value of $\sim 0.1$. Both in the magnitude and mass limited sample, outer members are characterised by a negative Q.E. (decreasing from $\sim$-0.01 to $\sim$-0.13 going from one sample to another), suggesting an enhanced star formation activity.

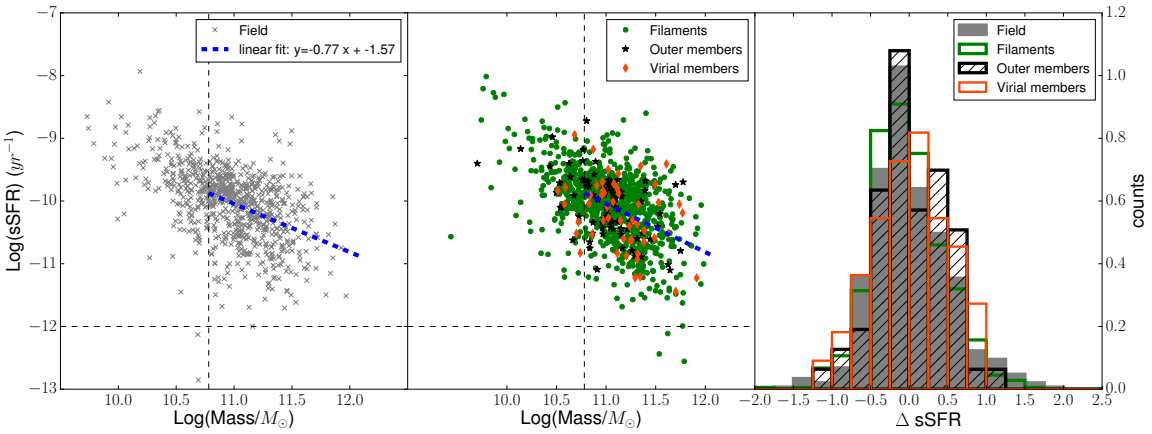


Figure 6.14: sSFR-mass relation for galaxies in the field (left panel) and galaxies in filaments and G&C virial and outer members (green dots, orange diamonds, and black stars in the central panel). The vertical and horizontal lines show the stellar mass limit and our adopted separation between star forming and passive galaxies. The blue dashed line is the fit to the relation of the sample including all the environments. The panel on the right shows the distribution of the differences between the galaxy sSFRs and their expected values according to the fit given their mass.

### 6.3.2 sSFR- and SFR-Mass relations in different environments

In the previous section I have detected a dependence of the star forming and blue fractions on environment. Here I correlate the galaxy star forming properties with the stellar mass, to further inspect the role of the environment.

Now, I investigate whether star forming galaxies living in different environments share similar correlations between the sSFR and their stellar mass. First, focusing on the sSFR, in Fig. 6.14 I show the sSFR-mass relation in the four environments introduced above. Very little differences are observed among the different samples, at least above the mass completeness limits. To better quantify the differences, I compute the linear regression fit considering altogether the different environments, above the mass completeness limit. I then plot the distribution of the difference between the sSFR of each galaxy and the value derived from the fit (right panel of Fig. 6.14). A KS statistical tests is performed to compare these distributions, and finds that they are all compatible with being drawn from a single parent sample (i.e., the p-values are above the significance level of 0.05). Overall, I conclude that the sSFR-Mass relation seems not to depend on global environment above the galaxy stellar mass limit in our sample, even considering extremely different environments such as X-ray G&C within XLSSsC N01 supercluster and the field (uncontaminated by X-ray groups or clusters).

Second, I focus on the SFR-Mass relation of star forming galaxies in the four defined environments, shown in Fig. 6.15. It is evident that galaxies in the different environments are similarly distributed in this plane. I perform a sigma-clipping linear fit to the relation

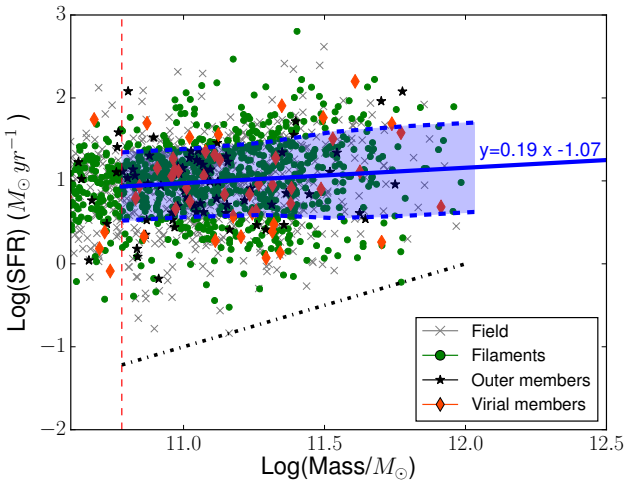


Figure 6.15: SFR-mass relation for galaxies in the field (grey crosses), in filaments (green dots), G&C virial (orange diamonds) and outer members (black stars). The red dashed vertical line shows the stellar mass limit. The blue line is the fit to the relation including all the environments, and the shaded areas correspond to $1\sigma$ errors on the fitting line. The black dashed line represents the log(sSFR/$yr^{-1}$)=-12 limit.

in the mass-complete regime, and compute $1\sigma$ confidence intervals which are shown as blue shaded areas around the solid blue fitting line. Following Paccagnella et al. (2016), I identify galaxies in transition between the star forming main sequence and the quenched population as those galaxies with $log(sSFR/yr^{-1}) > -12$ and SFR below -$1\sigma$ the SFR-mass fitting line. The fraction is computed as the ratio of this population to the population of galaxies with $log(sSFR/yr^{-1}) > -12$, in each environment. The results point out that the incidence of galaxies in transition is not environment dependent, being $0.19^{+0.03}_{-0.02}$ in the field, $0.16^{+0.02}_{-0.02}$ in filaments, $0.19^{+0.86}_{-0.68}$ in G&C outskirts and finally $0.18^{+0.10}_{-0.08}$ in the virial regions of G&C. This trend suggests that in the regions surrounding the XLSSsC N01 supercluster the migration from the star forming main sequence to the quenched stage occurs similarly from the innermost regions of G&C, to the outskirts and to the surrounding field.

### 6.3.3 LW-age in different environments

Differently from the current SFR and sSFR that give information on the ongoing efficiency of galaxies of producing stars, the LW-age provides an estimate of the average age of the stars weighted by the light observed. It reflects the epoch of the last star formation episode.

Figure 6.16 contrasts the median LW-age-Mass relation in G&C virial members, filaments and field, in the magnitude-limited sample (the galaxy stellar mass limit is shown with a vertical black dashed line). Medians are computed in non-independent stellar mass bins

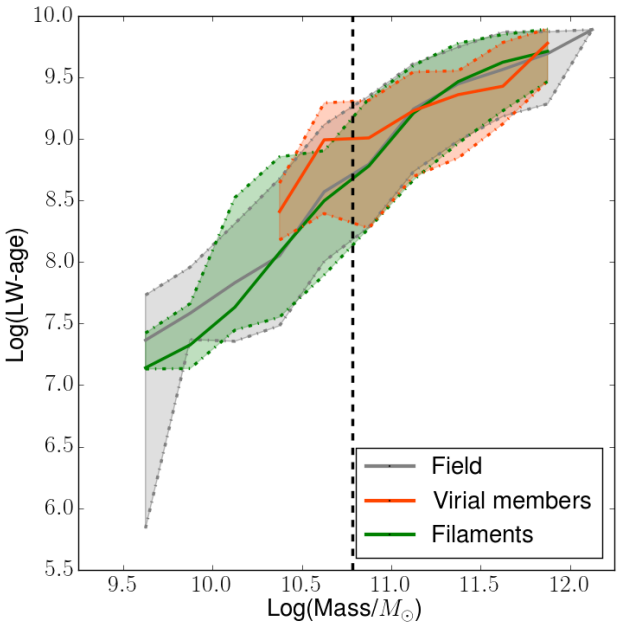


Figure 6.16: Median LW-age-mass relation computed in non-independent stellar mass bins for different environments, as shown in the legend. The stellar mass limit is shown with a vertical black dashed line. Shaded areas are the 16th and 84th percentiles, corresponding to $1\sigma$ errorbars.

in order to increase the statistics and shaded intervals correspond to the 16th and 84th percentiles, i.e. $1\sigma$ confidence interval. The mean LW-age values span the range from $\sim 1.8 \times 10^7 yr$ to $\sim 5.6 \times 10^9 yr$ in the magnitude limited sample, and from $\sim 10^9 yr$ to $\sim 5.6 \times 10^9 yr$ in the mass limited sample. Overall, the LW-age increases with the galaxy stellar mass in an environmental independent fashion. No dependences are found also when the outer members population is considered (not shown in the plot).

In order to evaluate any possible dependence on galaxy populations, I split galaxies into star forming/blue and passive/red using the same criteria adopted in the previous sections and I plot their median LW-age in the four panels of Figure 6.17. While neither the blue nor the red population show any variation in the median value of the LW-age with environment at any stellar mass, environmental dependences are visible in the passive and, possibly, star forming populations. Considering star forming galaxies, the LW-age of virial members is slightly higher than that of galaxies in filaments and in the field, indicating that their star formation was more active in the past than it is today. Much more clearly, when looking at the passive populations, a dependence on environment emerges, as the LW-age of passive galaxies in the virial regions of G&C is systematically lower than that of all other galaxies having the same stellar mass, indicating that these galaxies underwent a recent quenching of the star formation, most likely upon accretion onto the G&C.

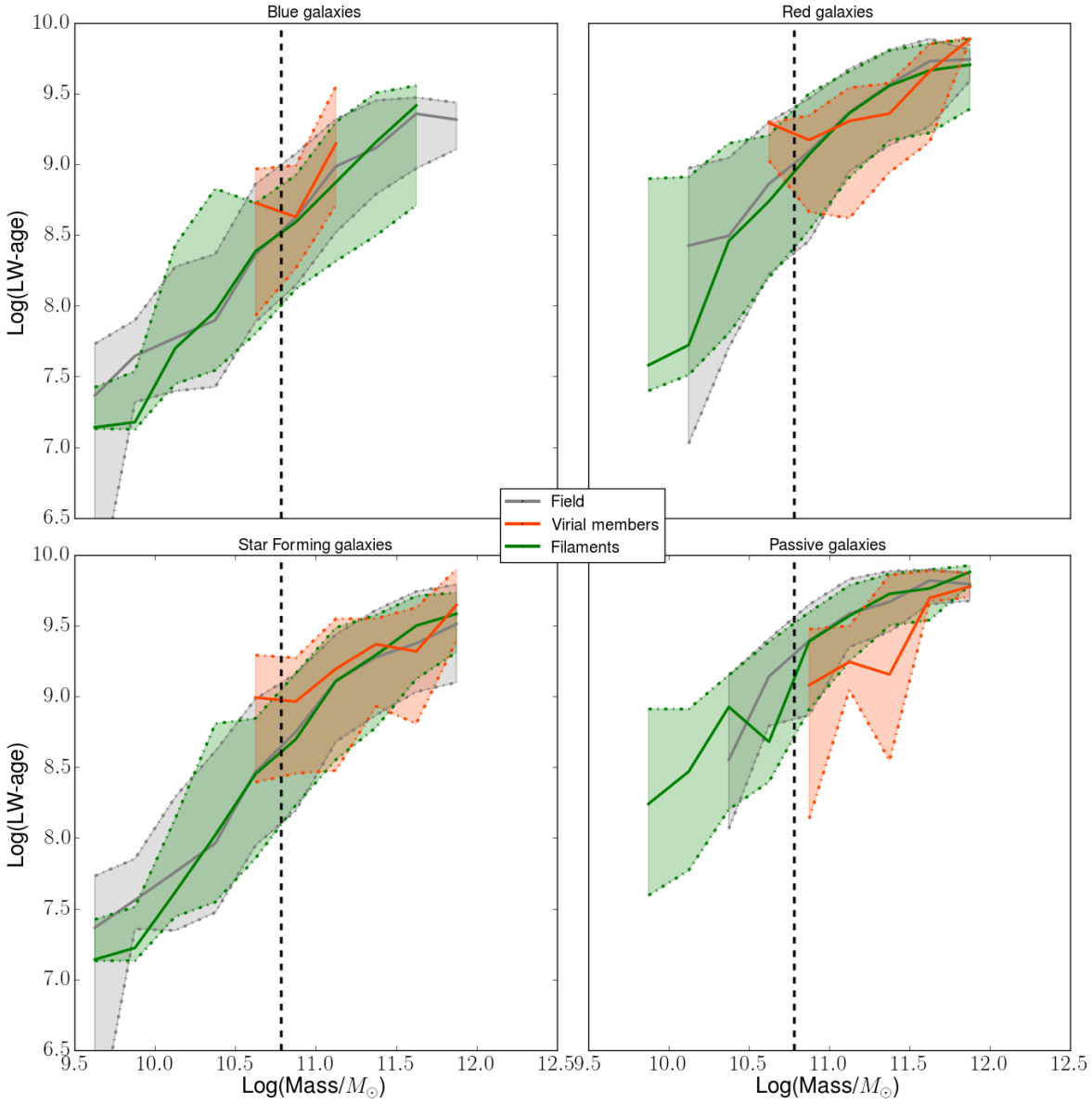


Figure 6.17: Median LW-age-mass relation computed in non-independent stellar mass bins for different environments, as shown in the legend, for star forming/blue and passive/red galaxies. The stellar mass limit is shown with a vertical black dashed line. Shaded areas are the 16th and 84th percentiles, corresponding to $1\sigma$ errorbars.

## 6.4 Discussion

In the previous sections I have analysed the the fraction of star forming galaxies, defined in terms of their sSFR, and the fraction of blue galaxies, defined in terms of their $(g - r)_{rest-frame}$ colour. I stress that these two definitions have different physical meanings.

The SFR is a snapshot measuring the number of stars produced by the galaxy at the moment it is observed, the colour is sensitive also to the past history of the galaxy itself, especially the recent history.

The effect of the environment is mainly visible in galaxies in the densest environments (G&C virial/outer members). Indeed, in the magnitude limited sample ($r \leq 20.0$), the fractions of star forming and blue galaxies are systematically lower among virial members than in the other environments, indicating star formation quenching in the G&C virialised regions. By contrast, there are hints that the fraction of star forming galaxies is enhanced among the outer members population, even with respect to filaments and field. Even though error bars prevent us from stating this on secure statistical grounds, this result suggests an enhancement of star formation when galaxies approach the G&C outskirts.

Similar results were previously found also by Tran et al. (2009), that compared the fraction of 24 $\mu$m sources in a supergroup with the field and a rich galaxy cluster at z $\sim$ 0.35, finding an enhancement in the number of star forming galaxies with $\mathrm{SFR_{FIR}} \geq 3\mathrm{M_{\odot}yr^{-1}}$ compared to cluster galaxies, which resulted to be a factor of $\sim$ 4. This population was identified as composed of luminous, member galaxies with masses around $10.0 \leq log(M/M_{\odot}) \leq 10.6$ outside the central regions of groups.

Turning the attention to the colour fractions, some additional environmental effects might emerge. In addition to an enhancement of the blue population in the outer members with respect to virial members, filaments behave similarly to outer members and have a lower incidence of star forming than the field. Overall, considering the colors, there is a monotonic trend of increasing star forming fractions from the G&C, to the filaments, to the field.

These findings are validated by the Q.E. parameter that was computed in all environments with respect to the pure field. In the local Universe, similar conclusions were drawn by Wetzel et al. (2012), who detected a significant quenching enhancement around massive clusters only for galaxies closer than 2 virial radii from the centre.

When looking at the mass limited sample ($\log M/M_{\odot} \geq 10.8$), the fractions of both star forming and blue galaxies are lower with respect to their corresponding value in the magnitude limited sample, quenching efficiency trends are flatter and differences between environments are not evident anymore.

In the mass limited sample ($\log M/M_{\odot} \geq 10.8$), the fractions of both star forming and blue galaxies are lower than their corresponding value in the magnitude limited sample, quenching efficiency trends are flatter and differences between environments are not evident anymore. The stellar mass limit selects only the high-mass end of the galaxy stellar mass function, thus the absence of environmental dependences suggests that the evolution of massive galaxies is mostly completed by this epoch, in agreement to what previously found (e.g. Brinchmann et al. (2004); Peng et al. (2010); Woo et al. (2013)). This scenario is consistent with the downsizing effect (Cowie et al. 1996), according to which galaxies with higher masses are on average characterised by shorter and earlier star formation processes, and become passive on shorter time-scales than lower mass galaxies.

I have also investigated the sSFR-mass relation, finding no difference among galaxies in the field, in filaments, and in G&C. These results differ from the findings of e.g. Vulcani et al.

(2010); Patel et al. (2009) at similar redshift, who identify a population of G&C galaxies with reduced sSFR with respect to the field, at any given stellar mass. Differences might be primarily due to the fact that here low-mass G&C are investigated, while previous works studied more massive structures. Indeed, e.g. Vulcani et al. (2010) found no differences between the sSFR-mass relation of groups and the field. Furthermore, the fact that the sSFR-mass relation does not show any dependence on environment while the fraction of star forming galaxies does, points towards fast quenching mechanisms leading to the formation of a passive population without any evidence of transition in the sSFR-mass diagram. Indeed, the fraction of galaxies in transition from being star forming to passive, being below $1\sigma$ the SFR-Mass relation, is similar throughout the different environments explored in the region surrounding XLSSsC N01.
Finally, I have explored the LW-age-mass relation, finding a systematic increase in the mean LW-age with increasing stellar mass, once again in agreement with the downsizing scenario. Furthermore, while the median LW-age-mass relation of the global population of galaxies is independent of environment, a clear signature of recent quenching of the star formation activity emerges in the passive population of galaxies in the virial regions of X-ray G&C, suggesting the action of environmental processes which are also responsible for the drop in the star forming fractions highlighted above.

## 6.5 Summary

In this chapter I have presented the characterisation of one of the superclusters identified in Adami et al. (2018) by means of a FoF algorithm on XXL X-ray G&C. The supercluster, named XLSSsC N01, has a mean redshift of 0.2956, is composed of 14 G&C covering a region of 37 Mpc in RA $\times$ 50 Mpc in DEC. Within this region, I characterised the environment of galaxies in 11 G&C in XLSSsC N01, distinguishing among G&C virial members, G&C outer members, filaments and field galaxies (which were defined based on their local density). I have then characterised the properties of the stellar populations of galaxies in these environments.
Overall, I detected a monotonic trend of increasing star forming/blue fractions from the G&C, to the filaments and to the field. In contrast, I found no difference among the sSFR-mass relation and LW-age-mass relation for galaxies in the field, in filaments, and in G&C. However, indications of recent quenching of the star formation activity are evident in the passive population of galaxies in the virial regions of X-ray G&C.
This study lays the groundwork for the investigation on the properties of stellar populations of galaxies within the whole sample of XXL superclusters, by taking advantage of the larger sample statistics and with the possibility of exploring a broader redshift range from $z = 0.1$ up to $z = 0.5$. This study will be the subject of the next Chapter.

# 7

# STAR FORMATION AND STELLAR POPULATION PROPERTIES OF 0.1$\leq z \leq$0.5 GALAXIES

## Content

The aim of this chapter is to extend the study on the star formation properties and colours of galaxies presented in the previous chapter, to acquire a general understanding of the phenomena that characterise and influence the observed properties of galaxies at different epochs and in different environments. Exploiting the techniques and strategies developed for the analysis on the XLSSsC N01 supercluster, here I characterise galaxies in three redshift bins from z=0.1 up to z=0.5, in X-ray G&C of different virial masses and X-ray luminosities and as a function of local density. The study is focused on computing the fraction of star forming and blue galaxies, the sSFR/SFR-mass relation, the LW-age, the mass assembly history and SFH of galaxies and finally the correlation between the total star formation rate and the virial mass of structures. This work will be presented in Guglielmo et al. 2018b,c (in prep.).

## 7.1 Galaxy sample

### 7.1.1 Catalogue of structures

The G&C catalogue that is used in this Chapter consists of the C1+C2 spectroscopically confirmed structures in the XXL-N field, at redshift 0.1$\leq$z$\leq$0.5. Note that, differently from the study presented in Chapter 5, I lower the upper limit of the redshift range, for the reasons that will be explained in the following sections.
The sample is composed of 111 G&C that are fully characterised in terms of X-ray luminosities, temperatures, virial masses and radii, derived via scaling relations as explained in Chapters 2 and 3. 68 of these structures ($>$ 60%) belong to superclusters (see Table 2.3), thus it is possible to study the impact of the large scale structure on galaxy properties. The superclusters considered in this Chapter are: XLSSsC N01, N02, N03, N06, N07, N08, N09, N10, N11, N12, N15, N16, N17, N18, N19.

### 7.1.2 Galaxy catalogue

For this analysis, I use all galaxies in the spectrophotometric catalogue at 0.1≤z≤0.5. Galaxies are grouped into three redshift bins ($0.1 \leq z < 0.2$, $0.2 \leq z < 0.3$, $0.3 \leq z \leq 0.5$), and in the following environments.

- G&C virial members are galaxies whose spectroscopic redshift lies within $3\sigma$ from the mean redshift of their host G&C, where $\sigma$ is the velocity dispersion of their G&C and whose projected distance from the G&C centre is $< 1\, r_{200}$.
- G&C outer members are galaxies whose spectroscopic redshift lies within $3\sigma$ from the mean redshift of their host G&C, and whose projected distance from the G&C centre is between 1 and 3 $r_{200}$.
- Galaxies in the field are all galaxies that do not belong to any G&C.

Note that all galaxies belonging to a structure are always included in the same redshift bin. For example, if a G&C is located at the edge of a redshift bin and its member galaxies spill over another bin, these are all included in the redshift bin of their host G&C, regardless of their actual redshift.
Virial and outer members are also characterised on the basis of either the X-ray luminosity of the G&C they belong to, its virial mass or its belonging to a supercluster.
The stellar population properties of galaxies are derived using both the SED fitting code LePhare and the full spectral fitting code SINOPSIS, as detailed in Chapter 3. Depending on the galaxy properties investigated, I use one of these two codes, and the samples of galaxies where the used code gives reliable outputs, with the aim of maximising the number of galaxies analysed.[1] Specifically, I make use the outputs from LePhare for studying galaxy colours, those from SINOPSIS for studying the star formation properties of galaxies and their ages.
Tables 7.1 and 7.2 report the number of galaxies in different environments and redshift bins in the two samples with either LePhare or SINOPSIS outputs. Within each table, galaxies are divided into G&C virial and outer members, classified as belonging or not to superclusters, and the field; for all of these subsamples, numbers are given for the magnitude limited and mass limited samples. I recall that the magnitude limited sample corresponds to an observed magnitude of $r \leq 20.0$ at all redshifts from 0.1 up to 0.5, and that the stellar mass limit is varying with redshift as derived in Chapter 3. I consider the following values in the redshift bins:

- $0.1 \leq z < 0.2$: $\log(M/M_\odot) > 9.47$
- $0.2 \leq z < 0.3$: $\log(M/M_\odot) > 10.34$
- $0.3 \leq z \leq 0.5$: $\log(M/M_\odot) > 10.78$

[1] I remind the reader that SINOPSIS ran on the spectra coming from the GAMA and SDSS dr10 surveys, and therefore the SINOPSIS sample does not contain all the galaxies in the spectrophotometric catalogue that were given as input to LePhare.

Table 7.1: Final sample used in the analysis with LePhare outputs. Numbers are given according to the three redshift bins given in Col. 1. In both the tables, Col. 2 indicates the total number of G&C which do not belong to any supercluster and Col. 3 those which are located in a supercluster. Top Table: Columns 4-5 indicate the number of galaxies above the magnitude/stellar mass limit in G&C classified as virial members of G&C which are not located in superclusters, Col. 6-7 indicate the number of galaxies classified as outer members of the same systems. Middle Table: Col. 4-9 report the same quantities indicated in columns 4-7 of the top Table but for G&C within superclusters. Bottom Table: Col. 4-5 indicate the number of galaxies in the corresponding field sample; In all tables, the quantities in parentheses refer to the number of galaxies weighted for spectroscopic completeness.

| z_bin | $N_{GC}$ | $N_{GC,S}$ | N_memb_GC | | | |
|---|---|---|---|---|---|---|
| | | | Virial | | Outer | |
| | | | $r \leq 20$ | $\log(M_*/M_\odot) \geq M_{lim}$ | $r \leq 20$ | $\log(M_*/M_\odot) \geq M_{lim}$ |
| 0.1-0.2 | 24 | 16 | 71 (139) | 65 (131) | 103 (182) | 102 (181) |
| 0.2-0.3 | 37 | 20 | 147 (199) | 124 (166) | 184 (251) | 119 (167) |
| 0.3-0.5 | 50 | 32 | 66 (84) | 60 (75) | 69 (90) | 52 (64) |
| total | 111 | 68 | 284 (422) | 249 (372) | 356 (523) | 273 (412) |

| z_bin | $N_{GC}$ | $N_{GC,S}$ | N_memb_GC,S | | | |
|---|---|---|---|---|---|---|
| | | | Virial | | Outer | |
| | | | $r \leq 20$ | $\log(M_*/M_\odot) \geq M_{lim}$ | $r \leq 20$ | $\log(M_*/M_\odot) \geq M_{lim}$ |
| 0.1-0.2 | 24 | 16 | 361 (566) | 350 (549) | 456 (729) | 414 (666) |
| 0.2-0.3 | 37 | 20 | 104 (153) | 97 (136) | 124 (171) | 92 (129) |
| 0.3-0.5 | 50 | 32 | 93 (191) | 78 (165) | 119 (218) | 94 (180) |
| total | 111 | 68 | 558 (910) | 525 (850) | 699 (1118) | 600 (975) |

| z_bin | $N_{GC}$ | $N_{GC,S}$ | N_field | |
|---|---|---|---|---|
| | | | $r \leq 20$ | $\log(M_*/M_\odot) \geq M_{lim}$ |
| 0.1-0.2 | 24 | 16 | 5209 (9786) | 4552 (8554) |
| 0.2-0.3 | 37 | 20 | 7028 (10801) | 4675 (7168) |
| 0.3-0.5 | 50 | 32 | 4642 (7433) | 3201 (5172) |
| total | 111 | 68 | 16879 (28020) | 12428 (20894) |

### 7.1.3 Spectroscopic completeness

Here I compute the spectroscopic completeness in the LePhare and SINOPSIS samples in a different way with respect to that presented in Chapter 4. The necessity of adopting a different approach is imposed by the use of a spectrophotometric sample which spans a redshift range. Indeed, the method requires to slice the sample into different redshift bins and then to quantify the number of galaxies that fall into that given redshift bin, based on both spectroscopic and photometric redshifts. Specifically, the "sampling rate" (SR)

Table 7.2: Same as Table 7.1 but for sample with SINOPSIS outputs.

| z_bin | $N_{GC}$ | $N_{GC,S}$ | N_memb_GC | | | |
|---|---|---|---|---|---|---|
| | | | Virial | | Outer | |
| | | | $r \leq 20$ | $\log(M_*/M_\odot) \geq M_{lim}$ | $r \leq 20$ | $\log(M_*/M_\odot) \geq M_{lim}$ |
| 0.1-0.2 | 24 | 16 | 91 (158) | 65 (115) | 118 (180) | 102 (152) |
| 0.2-0.3 | 37 | 20 | 155 (194) | 111 (140) | 203 (262) | 119 (154) |
| 0.3-0.5 | 50 | 32 | 75 (97) | 56 (69) | 71 (91) | 50 (61) |
| total | 111 | 68 | 321 (449) | 232 (324) | 392 (533) | 271 (367) |

| z_bin | $N_{GC}$ | $N_{GC,S}$ | N_memb_GC,S | | | |
|---|---|---|---|---|---|---|
| | | | Virial | | Outer | |
| | | | $r \leq 20$ | $\log(M_*/M_\odot) \geq M_{lim}$ | $r \leq 20$ | $\log(M_*/M_\odot) \geq M_{lim}$ |
| 0.1-0.2 | 24 | 16 | 432 (612) | 348 (464) | 524 (734) | 412 (559) |
| 0.2-0.3 | 37 | 20 | 110 (136) | 89 (113) | 129 (168) | 89 (117) |
| 0.3-0.5 | 50 | 32 | 97 (185) | 67 (136) | 121 (211) | 93 (170) |
| total | 111 | 68 | 639 (933) | 504 (713) | 774 (1113) | 93 (170) |

| z_bin | $N_{GC}$ | $N_{GC,S}$ | N_field | |
|---|---|---|---|---|
| | | | $r \leq 20$ | $\log(M_*/M_\odot) \geq M_{lim}$ |
| 0.1-0.2 | 24 | 16 | 5779 (9640) | 4511 (7278) |
| 0.2-0.3 | 37 | 20 | 7483 (10958) | 4615 (6686) |
| 0.3-0.5 | 50 | 32 | 4836 (7600) | 3125 (4917) |
| total | 111 | 68 | 18098 (28198) | 12251 (18881) |

is defined as the ratio of the number of objects with spectroscopic redshift to the number of possible targets (i.e. the photo-z sample).
The steps taken to compute the completeness can be summarised as follows.
Considering the galaxies in the spectrophotometric sample with reliable measurements of both spectroscopic and photometric redshift, and defined a redshift range of interest, I call:

- N11= the number of objects with spectroscopic redshift in the selected redshift range, and photo-z in the same range.

- N12= the number of objects with spectroscopic redshift in the selected redshift range, but photo-z not in the same range.

- N21= the number of objects with spectroscopic redshift out of the selected redshift range, but photo-z in the range.

- N22= the remaining number of objects with both spectroscopic and photo-z outside the selected redshift range.

These numbers are used to define the two fractions which allow to compute the expected number of objects relative to the entire photo-z sample (which also includes galaxies with no spectroscopic redshift) starting from the spectrophotometric sample:

$$f1 = \frac{N11}{(N11 + N21)} \tag{7.1}$$

is the fraction of all objects with photo-z in the selected redshift range that truly belong to the range (i.e. with spectroscopic redshift in the range). Then,

$$f2 = \frac{N12}{(N12 + N22)} \tag{7.2}$$

is the fraction of all objects with photo-z outside the range that are instead within the considered redshift bin (i.e. with spectroscopic redshift in the range). These objects should be considered in the SR estimate of the given redshift slice even if their photo-z would not include them.
These two fractions are finally used in order to estimate the number of expected photo-z objects in the range, when applied to the whole photo-z sample:

$$N_{exp} = f1 \times N_{photo-z,in} + f2 \times N_{photo-z,out} \tag{7.3}$$

Where the numbers $N_{photo-z,in}$ and $N_{photo-z,out}$ refer respectively to the number of objects with photo-z in and outside the selected redshift range in the total photo-z sample.
The sampling rate is finally defined as:

$$SR = \frac{(N11 + N12)}{N_{exp}} \tag{7.4}$$

where (N11+N12) is the total number of galaxies with spectroscopic redshift in the selected redshift range.
By construction, the sum of the inverse of the SRs, i.e. the spectroscopic weights, at all redshifts and in the magnitude limited sample approximately gives the number of objects in the magnitude limited parent photo-z sample, with small differences that can be due to the different redshift range covered by the spectroscopic and photo-z sample.
In XXL-N, I consider separately the three redshift bins: 0.1≤z<0.2, 0.2≤z<0.3, 0.3≤z≤0.5. In addition, to account for the dependence on the different SR of spectroscopic surveys in different regions in the sky, I proceed as already performed in Chapter 4 and subdivide the field in three stripes of declination, arbitrarily named as in Chapter 3 C-A, C-B and C-C and I further divide each stripe in RA creating a grid of 1.0 deg width. Finally I consider intervals of 0.5 $r$-band observed magnitude in the 22 resulting cells. The resulting grid is reported in figure 4.2.
From these results, I obtain the spectroscopic completeness curves as the SR as a function of magnitude, in all the sky cells and redshift bins in which the sample has been divided. The curves are shown in Figures 7.1 and 7.2, for the output sample from LePhare and SINOPSIS, respectively. The observed magnitude limit is again confirmed to be $r$=20.0 in

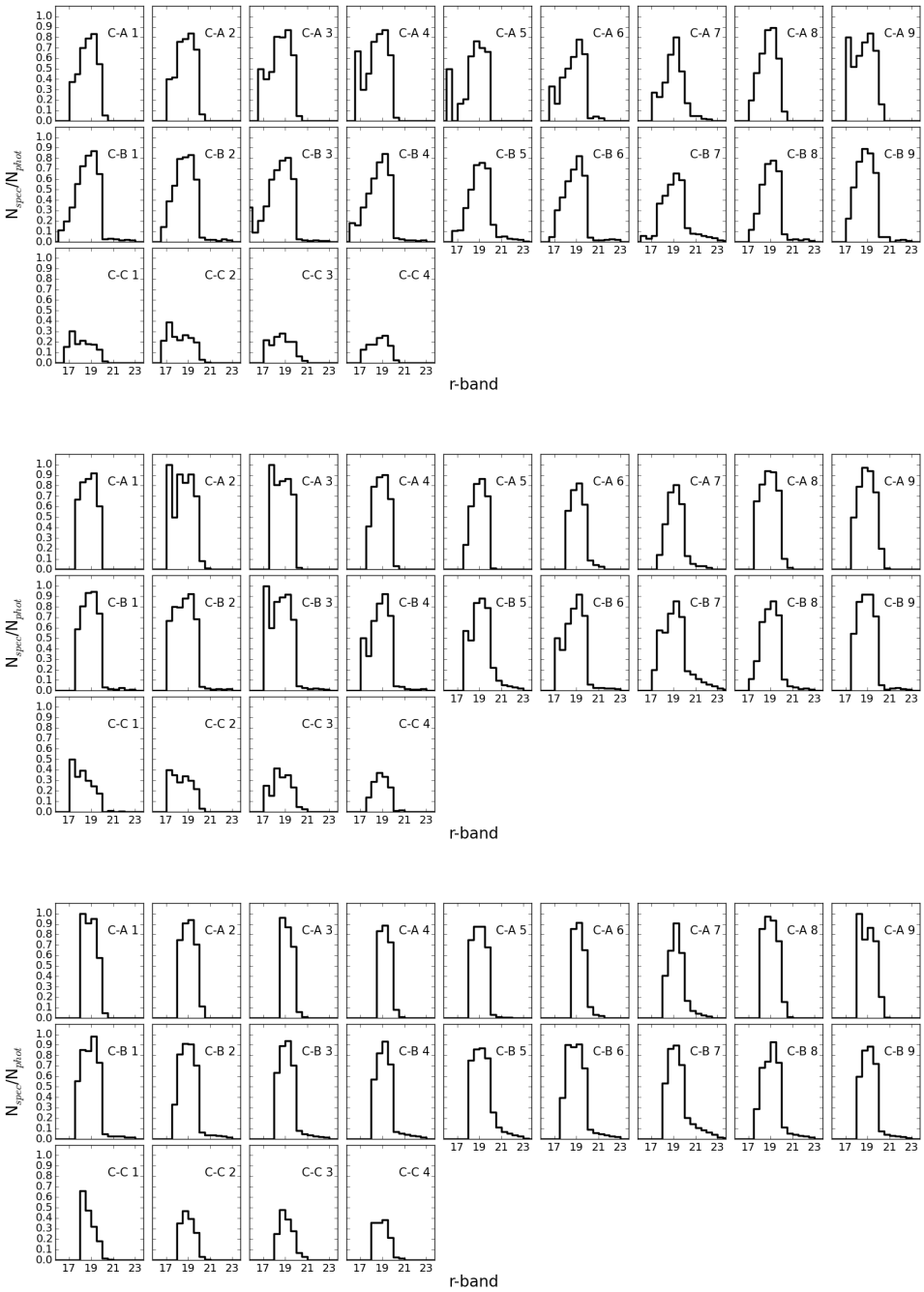


Figure 7.1: Completeness curves computed in three redshift bins and in different RA-DEC cells in the sky, as explained in the main text. From the top to the bottom panel, the represented redshift ranges are respectively $0.1 \leq z < 0.2$, $0.2 \leq z < 0.3$, $0.3 \leq z \leq 0.5$. The spectrophotometric sample used to compute the completeness ratios with respect to the photo-z sample is the one containing the output from LePhare.

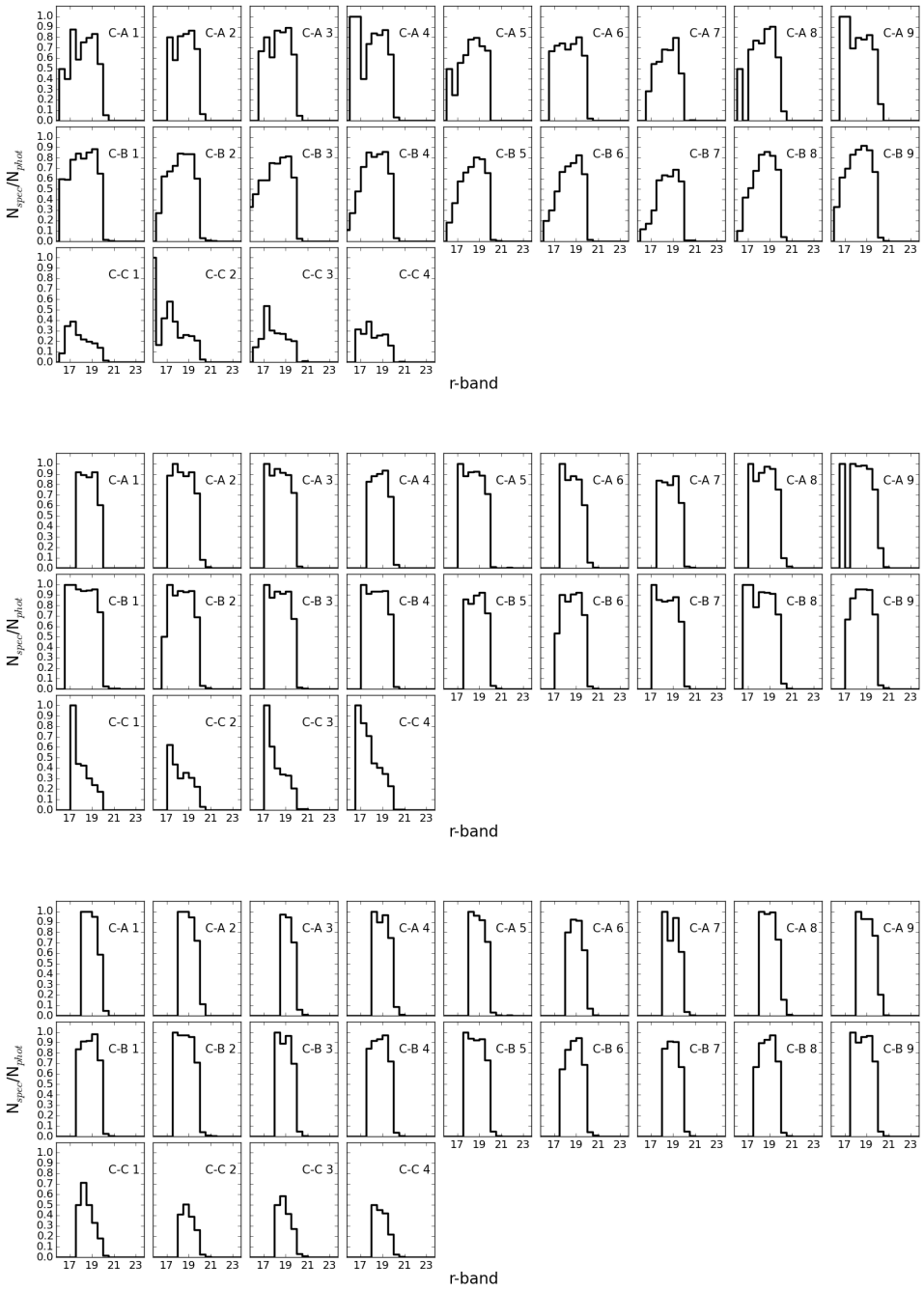


Figure 7.2: Completeness curves computed in three redshift bins and in different RA-DEC cells in the sky, as explained in the main text. From the top to the bottom panel, the represented redshift ranges are respectively $0.1 \leq z < 0.2$, $0.2 \leq z < 0.3$, $0.3 \leq z \leq 0.5$. The spectrophotometric sample used to compute the completeness ratios with respect to the photo-z sample is the one containing the output from SINOPSIS.

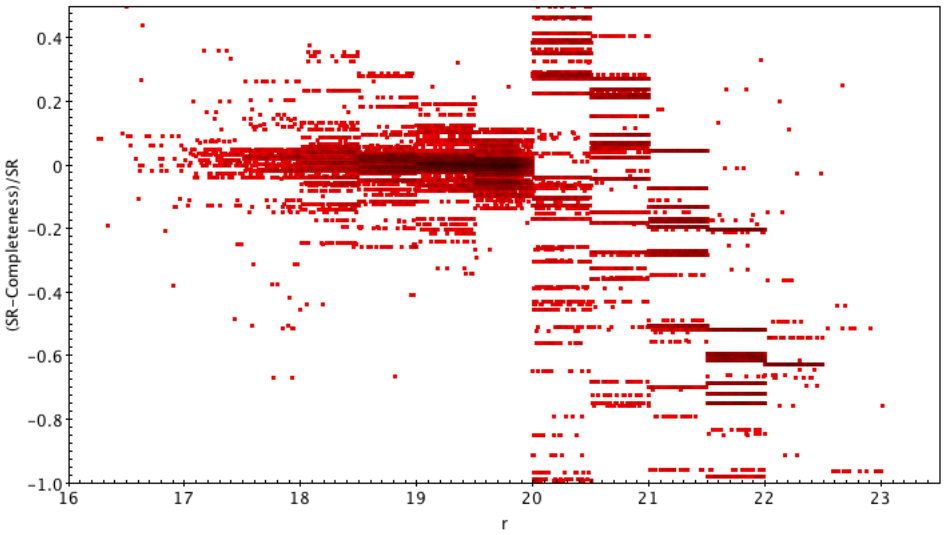


Figure 7.3: Normalized difference between the SR estimated performed in this section and the spectroscopic completeness computed in Chapter 5, as a function of $r$. The figure shows that below the magnitude completeness limit $r$=20.0, differences between the two methods are small.

both the samples and at all redshifts. This allows me to maintain several of the quantities already computed starting from the magnitude limit of the spectrophotometric sample, e.g. the stellar mass completeness limit. Each galaxy is weighted for the inverse of the SR computed here, which accounts for its redshift, position in the sky and observed magnitude.
Finally, I test whether there are important differences between the spectroscopic completeness defined here and that computed in Chapter 4 and used in the scientific analysis presented in both Chapter 5 and 6. Figure 7.3 shows the normalised difference between the two completeness weights as a function of the r-band observed magnitude. In the range of interest (the magnitude limited sample) the two estimates are consistent, being differences $\lesssim 20\%$.

### 7.1.4 Estimate of the LD

The availability of a large spectrophotometric sample of galaxies enables the parametrisation of environment also in terms of local projected density of galaxies. I compute the LD of galaxies in the spectrophotometric sample taking as a reference the photo-z sample used in the spectroscopic completeness computation, and slightly modifying the recipe used in the LD computation of Chapter 6 to properly deal with different redshift bins and with the use of photo-z. The LD around each galaxy is given as the ratio of the number of galaxies in the parent photometric-redshift sample per unit of projected *comoving* area on the sky. The method I adopt proceeds through different phases:

- Computation of the observed magnitude limit used to select galaxies in the sample as a function of redshift. To perform the same sample selection, I apply the same absolute magnitude cut in all the redshift slices. The value is selected in order to balance the error in the photo-z estimate, which increases towards fainter magnitudes, and the propagation of the observed magnitude down to redshift 0.1, and thus to minimise the loss of galaxies occurring with brighter observed magnitude cuts. I consider as observed magnitude limit $r$=23.0 at z=0.5 and I compute the corresponding absolute magnitude through the cosmological formula of the luminosity distance:

$$M_r = r - 5 \cdot (log_{10} D_L - 1) - K_{corr}. \tag{7.5}$$

where $r$ is the observed r-band magnitude, $D_L$ is the luminosity distance in pc, $K_{corr}$ is the K-correction that takes into account that the same photometric filter samples different spectral ranges when applied to the SED of galaxies at different redshifts; K-correction values are taken from the table released in (Poggianti 1997), assuming the typical value of an intermediate type galaxy (Sab) in r-band at the selected redshift. The application of this formula leads to an absolute magnitude of $M_r$ = -19.89, that is then converted into an observed magnitude limit as a function of redshift by means of the inverse formula:

$$r(z) = -19.89 + 5 \cdot (log_{10} D_L(z) - 1) + K_{corr}(z) + P.E.(z) \tag{7.6}$$

where the $D_L$ is computed at the redshift of the considered galaxy, $K_{corr}$ is a function of redshift and P.E.(z) is the passive evolution of galaxies, which become redder with decreasing redshift as a consequence of the aging of their stellar population; the correction for passive evolution is 0.1 mag each $\Delta z$=0.1 (Poggianti et al. 2008).

- Computation of the number of galaxies in the spectrophotometric sample within a *comoving* circle of 1 Mpc radius at the redshift of the galaxy in the centre and within a redshift range of $\pm$0.05 with respect to the redshift of the same galaxy. To account for uncertainties in the photo-z measurements, I estimate the expected number of galaxies in the photo-z sample in the considered redshift range around the selected galaxy with the same method used for the spectroscopic completeness. I define the fractions f1 and f2 given in equations 7.1 and 7.2 in the spectrophotometric sample and use them to weight the photo-z sample and compute $N_{exp}$. This value represents the correct number counts within the *comoving* projected area of 1 Mpc radius around the galaxy. The area of the circle is then computed and the local density is defined as the ratio of the two quantities.

- Correction for edge effects in the field. When a galaxy is located at the edge or in the corner of the field in which the sample of galaxies is located, it is important to correct the circular area for the fraction of area effectively covered by the data points, and therefore remove empty circular sectors. The correction is not simple from a geometrical point of view, thus I adopt a numerical solution based on a Monte-Carlo simulation method. I generate a circular homogeneous distribution of

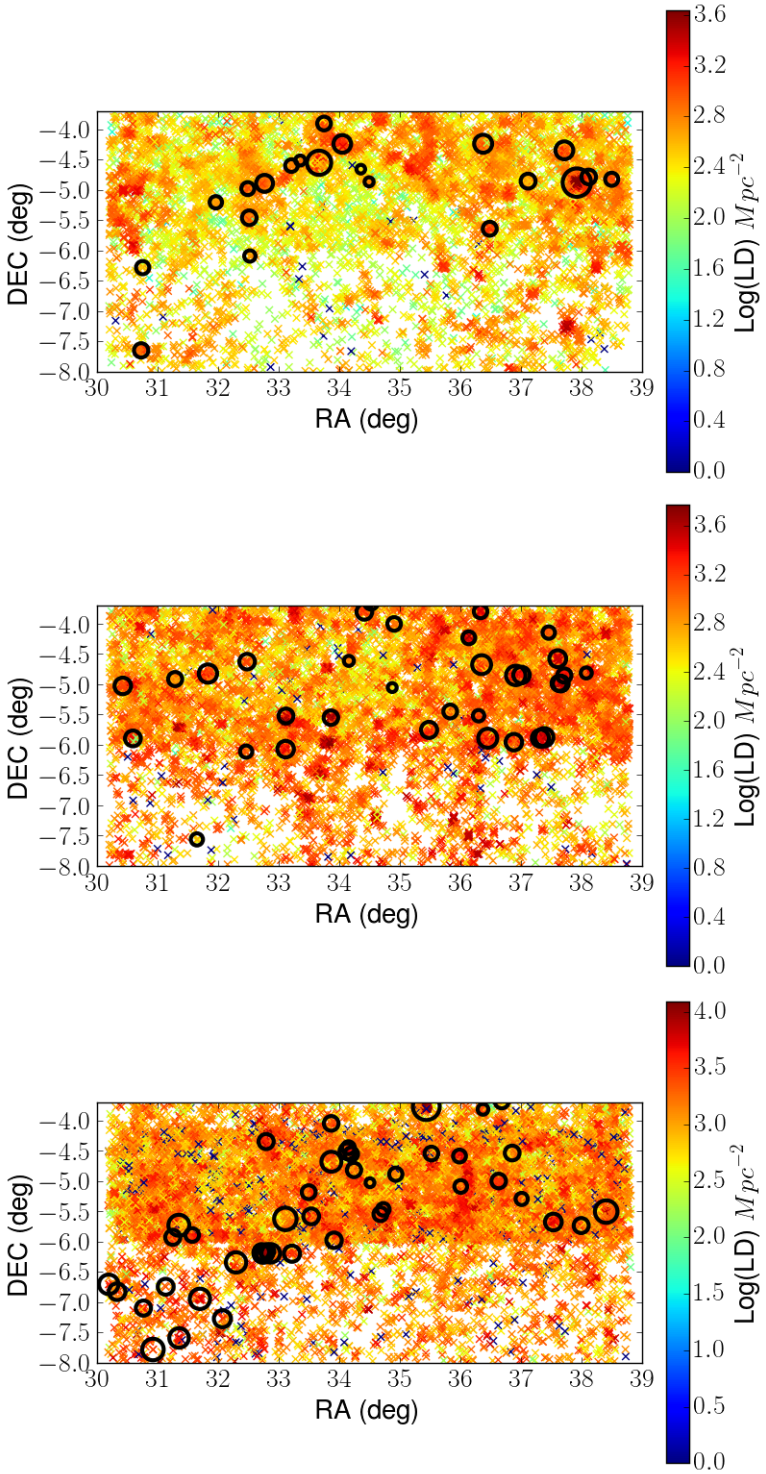


Figure 7.4: Spatial distribution in the sky of the spectrophotometric sample of galaxies used to compute the LD, where the data points are colour-coded according to their log(LD). The logarithmic values of the local density are written in the colour bar next to each panel. From the top to bottom panel the represented redshift bins are respectively $0.1 \leq z < 0.2$, $0.2 \leq z < 0.3$, $0.3 \leq z \leq 0.5$. Each panel contains the $3r_{200}$ extensions of the G&C at the redshift of the bin, represented with black empty circles.

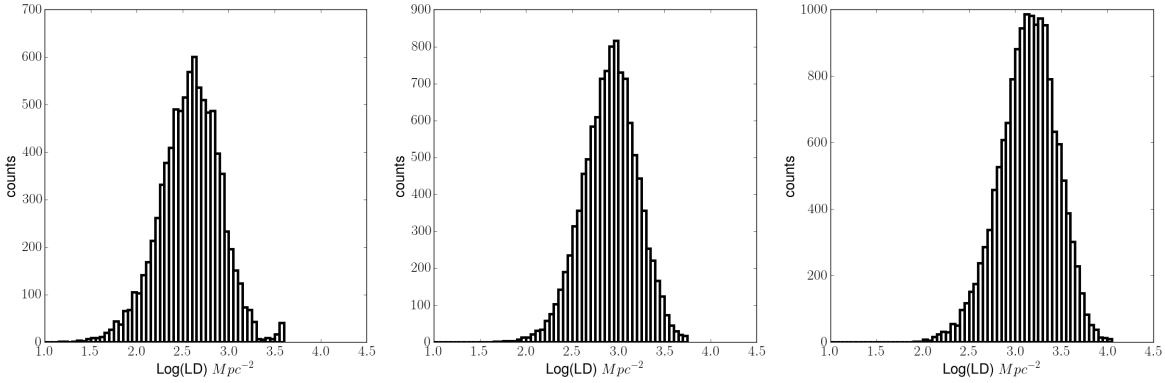


Figure 7.5: Histograms of the logarithm of the LD in the three redshift bins analysed in this chapter. From the top to the bottom panel, the redshift bins represented are respectively $0.1 \leq z < 0.2$, $0.2 \leq z < 0.3$, $0.3 \leq z \leq 0.5$.

data points by populating a circle with a sufficiently high number of points (100000) and I compute the zone of exclusion with respect to the edge conditions of the field as the ratio between the number of points falling outside the edges and the total number of points included in the circle. The area of the circle in physical units that has to be considered in the LD calculation is then the total *comoving* area multiplied by the fraction of area included in the field, $f_{\rm in} = 1 - f_{\rm out}$, where $f_{out}$ is the fraction of area falling outside the galaxy field.

The LD is finally expressed as the logarithm of the quantity computed in the procedure outlined above, with dimension [LD]=Mpc$^{-2}$.
Figure 7.4 reports the spatial distribution in the sky of galaxies within the XXL-N Field divided in the three redshift bins. The data points represent galaxies in the spectrophotometric sample for which the LD has been computed and are colour coded according to their $\log_{10}$(LD) value. Each panel also reports the circle of $3r_{200}$ radius of the G&Cs in the considered redshift bin; as expected, in most of the cases, galaxies within the circles are characterised by high LD values. The LD distributions in the three redshift bins are given in Figure 7.5. As previously found by e.g. Poggianti et al. 2008 the peak of the LD distribution evolves with redshift towards higher values, from ∼2.6 at 0.1≤z<0.2, to ∼3.0 at 0.2≤z<0.3 and up to ∼3.25 at 0.3≤z<0.5.

## 7.2 Galaxy sub-populations

The main observables I focus on in the analysis presented in this section are the SFR at the epoch of observation, the rest-frame colour, the LW-age, the mass assembly history and the SFH.
Following what done in Chapter 6, in order to distinguish the evolutionary phase of galaxies in different environment, two different criteria are adopted to discern between

star forming/younger population and passive/older. Briefly, the first definition is given in terms of the current SFR and stellar mass as measured by SINOPSIS. In particular, I consider as star forming those galaxies with sSFR $> 10^{-12}\mathrm{yr}^{-1}$ and passive the remaining ones. It is important to point out that this threshold in sSFR is the same in the three redshift bins considered from z=0.1 up to z=0.5, and is justified by the scarce evolution in the sSFR-stellar mass plane in this redshift range (see e.g. Whitaker et al. 2012).

The second definition is based on rest frame colours derived from LePhare. To identify the threshold in colour to be assumed in separating the blue and red populations I investigate the relation between sSFR, $(\mathrm{g}-\mathrm{r})_{\mathrm{rest-frame}}$ colour and absolute magnitude $\mathrm{M_r}$, in the three redshift bins separately, for the magnitude limited sample of galaxies with both LePhare and SINOPSIS outputs. Figure 7.6 shows the rest-frame CMD in each redshift bin. Passive galaxies are highlighted in red, the star forming population is colour coded according to its sSFR. The visual inspection of the plots allows to set the most suitable cut in the $(\mathrm{g}-\mathrm{r})_{\mathrm{rest-frame}}$ colour, especially at lower $z$. To corroborate this visual inspection, I consider a 1.0 absolute magnitude bin in the diagrams ([-21:-20] at z<0.3, [-23:-22] at $0.3 \leq \mathrm{z} \leq 0.5$), and compute the $(\mathrm{g}-\mathrm{r})_{\mathrm{rest-frame}}$ histogram of the selected populations; the histograms are shown in the right panels of Figure 7.6 and present a double-peak that corresponds to the blue cloud at lower colours and to the red sequence at higher colours. The $(\mathrm{g}-\mathrm{r})_{\mathrm{rest-frame}}$ colour that separates the two populations, being at the minimum of the colour distribution between the two peaks, can be adopted as the threshold (vertical red dashed line in the figure). This value is unchanged from z=0.1 to z=0.3 and is $(\mathrm{g}-\mathrm{r})_{\mathrm{rest-frame}}$=0.6. At $0.3 \leq \mathrm{z} \leq 0.5$ instead, the passive population spills over bluer colours with respect to $(\mathrm{g}-\mathrm{r})_{\mathrm{rest-frame}}$=0.6, due to the broader redshift bin that is considered here. In this case, I consider a slightly narrower redshift bin around z∼0.4 and draw the histogram in a 1.0 mag bin that is reported in the bottom right panel of Figure 7.6; the value adopted at $0.3 \leq \mathrm{z} \leq 0.5$ on the basis of the histogram is $(\mathrm{g}-\mathrm{r})_{\mathrm{rest-frame}}$=0.65.

Note that, at all redshifts, the star forming population is typically characterised by sSFR$\gtrsim 10^{-9.6}$ $\mathrm{yr}^{-1}$ in the blue portion of the CMD and sSFR$\lesssim 10^{-10}\mathrm{yr}^{-1}$ in the redder part. This further confirms the link between the star formation and colour in galaxies, even though they trace different timescales. I stress that these quantities have been obtained from different observables and using different tools.

## 7.3 Galaxy population properties as a function of the *global* environment

In this section, I study the galaxy fractions and star forming properties of galaxies in different *global* environments, also considering separately G&C belonging to superclusters and of different X-ray luminosity. In the next section, I will consider instead the *local* environment parametrisation.

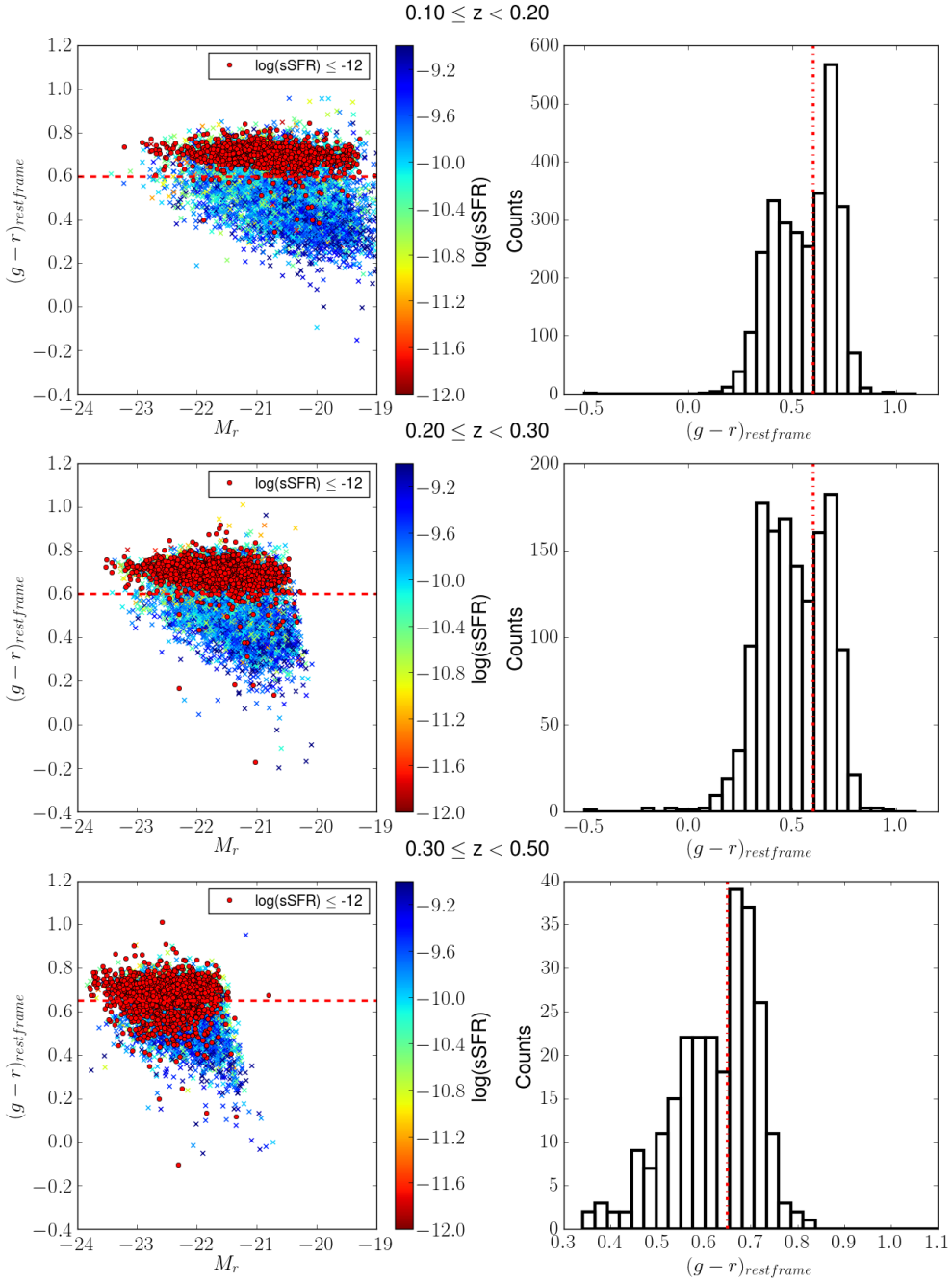


Figure 7.6: Colour-magnitude diagrams in the magnitude limited sample in the three redshift bins analysed, for the subsample of galaxies with LePhare and SINOPSIS outputs. The top panel refers to the $0.1 \leq z < 0.2$ bin, the panel in the middle to the $0.2 \leq z < 0.3$ bin and the bottom panel refers to the $0.3 \leq z \leq 0.5$ redshift bin. Red points indicate passive galaxies, while galaxies with log(sSFR)>-12 are colour coded according to their sSFR. The red dotted line shows the separation between red and blue objects according to the $(g\text{-}r)_{rest-frame}$ colour.

### 7.3.1 Fraction of star forming galaxies

I compute the fraction of blue and star forming galaxies, separately, in the different environments identified in the XXL-N field in Section 7.1.2 and in three redshift bins. The numbers of star forming and blue galaxies are calculated both in the magnitude limited and mass limited sample, following the definitions given in Section 7.1.2.

In addition to the fraction of star forming galaxies, I compute also the Q.E. parameter that is defined on the basis of the fraction of passive/red galaxies in any given environment with respect to the field (see Chapter 6 and Eq. 6.1). The behavior of the Q.E. in any environment can be interpreted as the strength of the environmental quenching mechanism that is responsible for the build up of the passive/red population of the considered environment with respect to the field.

In Figures 7.7, 7.8 and 7.9, G&C virial and outer members are sub-divided in two classes in order to separate G&C belonging to superclusters (S) from the others (NS). Fractions are shown with different colours in different environments, and the x-axis reports the name of the different environments. Error bars are computed using a bootstrap method.

At $0.1 \leq z < 0.2$, in the magnitude limited sample (shown with filled symbols), a clear trend of the star forming fraction with environment emerges (top left panel of Fig. 7.7). Virial members have the lowest fraction of star forming galaxies both in (S)G&C (55±3%) and in (NS)G&C (60±6%), with the former having a slightly lower fraction but still compatible within the errors. The fraction increases when considering outer members: (NS)G&C have 75±5% of galaxies that are still forming stars, which is compatible with the star formation activity in (S)G&C, that is 76±2% of the total population. The percentage of star forming galaxies in the field is the highest, being 84±1%. Turning the attention to colours, shown in the top right panel of the figure, the small differences in the trend of (S) and (NS)G&C members, both in the virial and in the outer membership region, are leveled. Blue galaxies in virial members are $19^{+5}_{-4}$% and 17±2% in (NS)G&C and (S)G&C respectively, $41^{+6}_{-5}$% and $43^{+2}_{-3}$% in the outer members of (NS)G&C and (S)G&C, and 58±1% in the field. The relative incidence of outer and virial blue/star forming members is not constant, with a mean ratio of 1.35 when considering the star forming fraction ((NS) and (S)G&C together) increasing up to 2.33 when blue fractions are considered ((NS) and (S)G&C together). In the mass limited sample, shown with empty symbols and dashed error bars, the general trends are confirmed, with small differences due to the lower statistics of the sample.

The Q.E. parameters are reported in the lower panels of Figure 7.7, below the corresponding star forming/blue fraction panels. The efficiency of the virial regions of both (S) and (NS)G&C in suppressing the star formation of galaxies emerges, with even higher values obtained from colour fractions. Differences between virial members, outer members and the field (which has by definition Q.E.=0) are evident in both panels with virial members (0.29±0.08 (NS), 0.34±0.03 (S) using passive galaxies; 0.67±0.08 (NS), 0.71±0.04 (S) using red galaxies) having Q.E. at least doubling that of outer members (0.10±0.06 (NS), 0.10±0.03 (S) using passive galaxies; 0.28±0.11 (NS), 0.25±0.05 (S) using red galaxies). Q.E. values are compatible within the error bars in virial/outer (S) and (NS)G&C

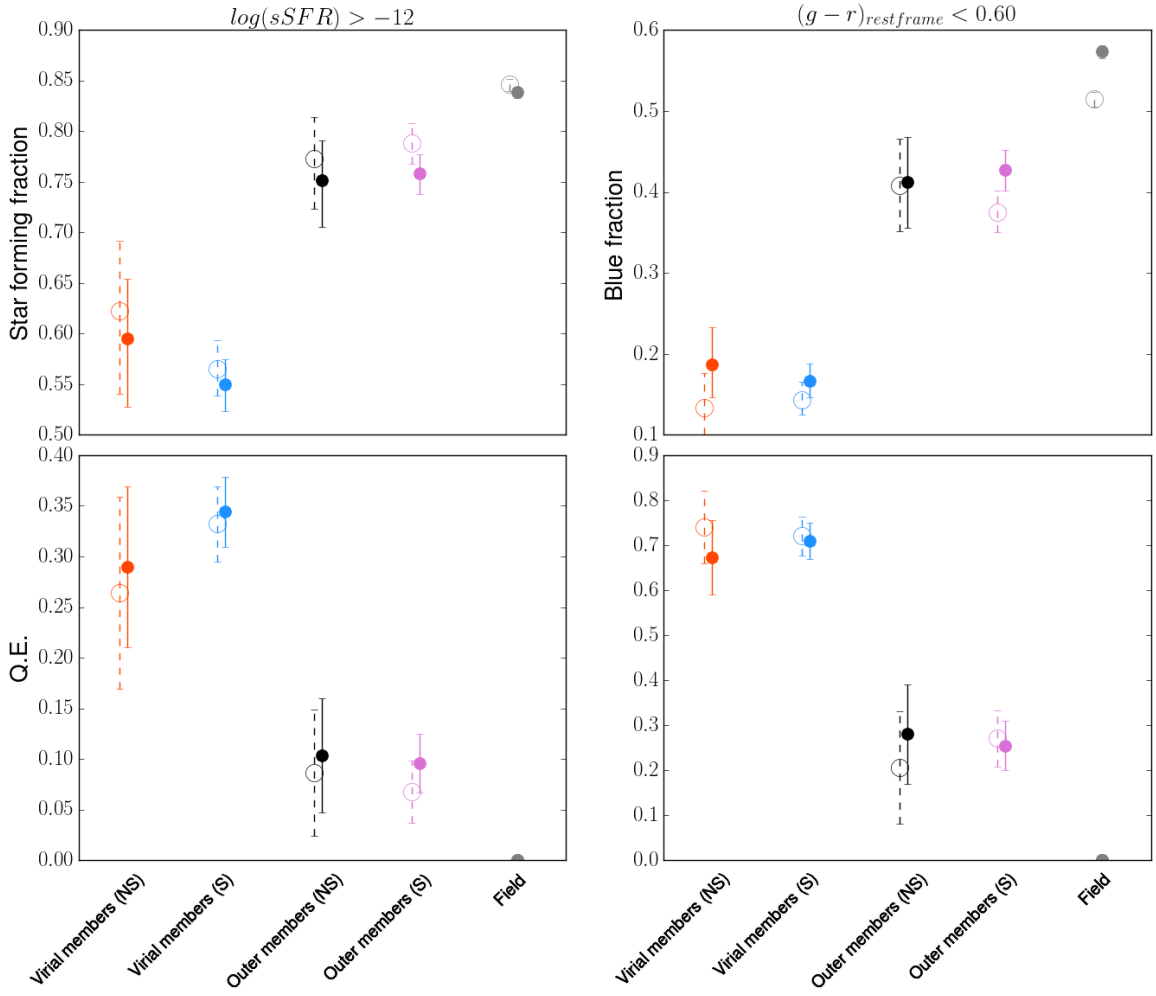


Figure 7.7: Fraction of star forming galaxies in different environments, computed with sSFR (left panel) and rest-frame colour (right panel) in the redshift bin $0.1 \leq z < 0.2$. The different environments represented in the figure are indicated in the x-axis and G&C members are divided into four subsamples: virial members that do not belong to any supercluster, virial members of G&C belonging to a supercluster (S), outer members that do not belong to any supercluster and outer members belonging to a supercluster (S). The fractions obtained using the magnitude limited sample are represented with filled symbols and solid errors, those obtained using the mass limited one are represented by empty symbols and dashed error bars. Errors are derived by means of a bootstrap method. The two lower panels show the Q.E. in different environment, computed with equation 6.1 for both the star forming and blue samples. Errorbars on the Q.E. are derived from the errors in the star forming and blue fractions using the propagation of errors.

members.

Figure 7.8 shows the same analysis performed at 0.2≤z<0.3. According to the fractions

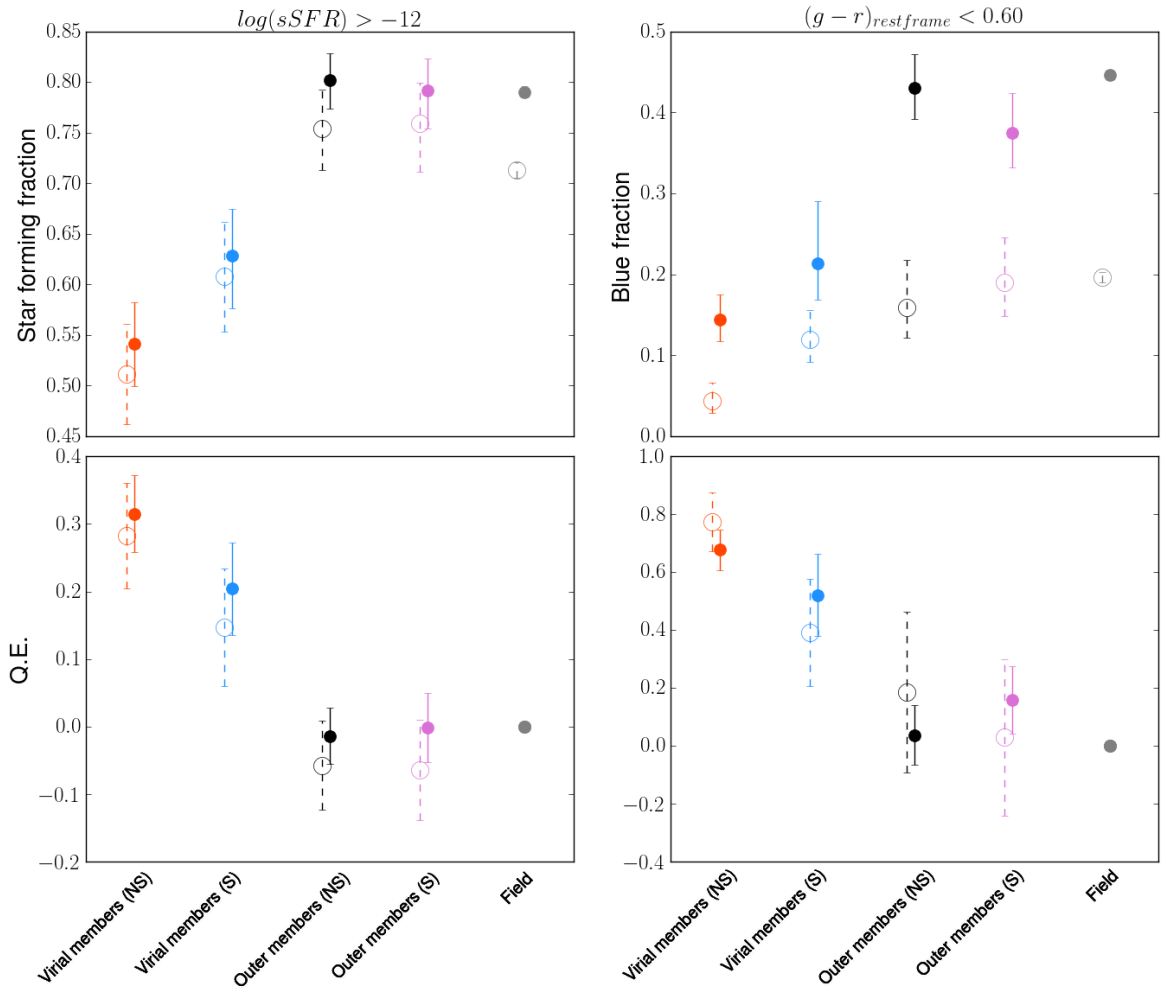


Figure 7.8: Same as Figure 7.7 but for galaxies at $0.2 \leq z < 0.3$.

on the star forming population in the magnitude limited sample (top left panel, filled symbols), virial members as a whole ((NS)+(S)) are found again to have the lowest fraction of star forming galaxies, but with some differences emerging in the two classes: the percentage of star forming galaxies is enhanced in (S)G&C (light blue) with respect to (NS)G&C virial members, being 63±4% in the former and 54±4% in the latter. The most remarkable difference with respect to the trends outlined in the lower redshift bin stands out in outer members, whose fraction of star forming galaxies is still similar in (NS) and (S)G&C but is fully compatible with the values in the field. Indeed, while the Q.E. in virial members is still significant, although decreasing in the (S)G&C population with respect to the (NS) one, outer members have Q.E. close to zero, meaning that the two environments have the same fraction of passive galaxies.

Considering colour fractions, the trends described in the star forming population are confirmed, with a slight enhancement in the (NS)G&C outer members with respect to the

(S)G&C population (43±4% in the former, 38±5% in the latter) which are still compatible within the errors. Some differences with respect to the magnitude limited sample starts to be evident in the mass limited sample, given that higher mass galaxies are selected. This is particularly evident when colour fractions are considered, according to which there is a significant decrease in the contribution of the blue population of outer members and the field with respect to the magnitude limited sample. Differences are still in place when comparing the virial members population, especially in (NS)G&C, whose quenching efficiency is even higher in the mass limited sample than in the magnitude limited one.

It is important to recall that this redshift bin contains the XLSSsC N01 supercluster, which was the subject of the analysis conducted in Chapter 6, and which contributes to the (S)G&C population with 11 out of 20 G&C: within the virial member population of (S)G&C in the bin, ∼67% comes from the XLSSsC N01 supercluster and in the outer member population the contribution is ∼64%. The trends obtained in Chapter 6 are averaged out by the presence of other (S)G&C virial/outer members but the general behavior is maintained.

Finally, Figure 7.9 shows the results at 0.3≤z<0.5. In this interval the lower number of member galaxies results in larger error bars on the plotted quantities. Despite this fact, differences with environment can be identified. In the magnitude limited sample, the fraction of star forming galaxies is lower in virial members as a whole than in all other environments, being ∼47%, while outer members behave analogously with respect to the redshift bin $0.2 \leq z < 0.3$. There is a hint of enhancement in the star formation activity of outer members in (NS)G&C, though the uncertainties prevent me from drawing any conclusion. At these redshifts, a difference between the star forming and blue population emerges. In the magnitude limited sample in fact, outer members belonging to superclusters have a lower percentage of blue galaxies with respect to outer members in (NS)G&C, being 33±5% in the former and 44±6% in the latter, and with (S)G&C showing fractions compatible with virial members in both (S) and (NS)G&C. In addition, the field has the highest fraction of blue galaxies with respect to all other environments.

In the mass limited sample instead, differences among members are not present anymore in the blue population, with only field galaxies remaining slightly higher with respect to all other points. In the star forming population, even though the fractions decrease, small differences with environment among virial members as a whole and all other environments are still present. The flattening of the trend from the magnitude limited to the mass limited sample at $z$ >0.3 is due to the fact that the stellar mass limit is pushed towards high mass galaxies, whose star formation history is expected to be determined by the *downsizing* and therefore quenched via mass quenching rather than environmental quenching.

Note that the differences emerging between virial/outer members in (S) or (NS)G&C in the different redshift bins are not due to a different distribution of X-ray luminosity in these peculiar supercluster environments. Indeed, a KS test on the distributions has not been able to detect any significant difference.

Finally, as previously discussed in Chapter 6, it is important to bear in mind that the two tracers used to characterise the galaxy populations have a different physical meaning.

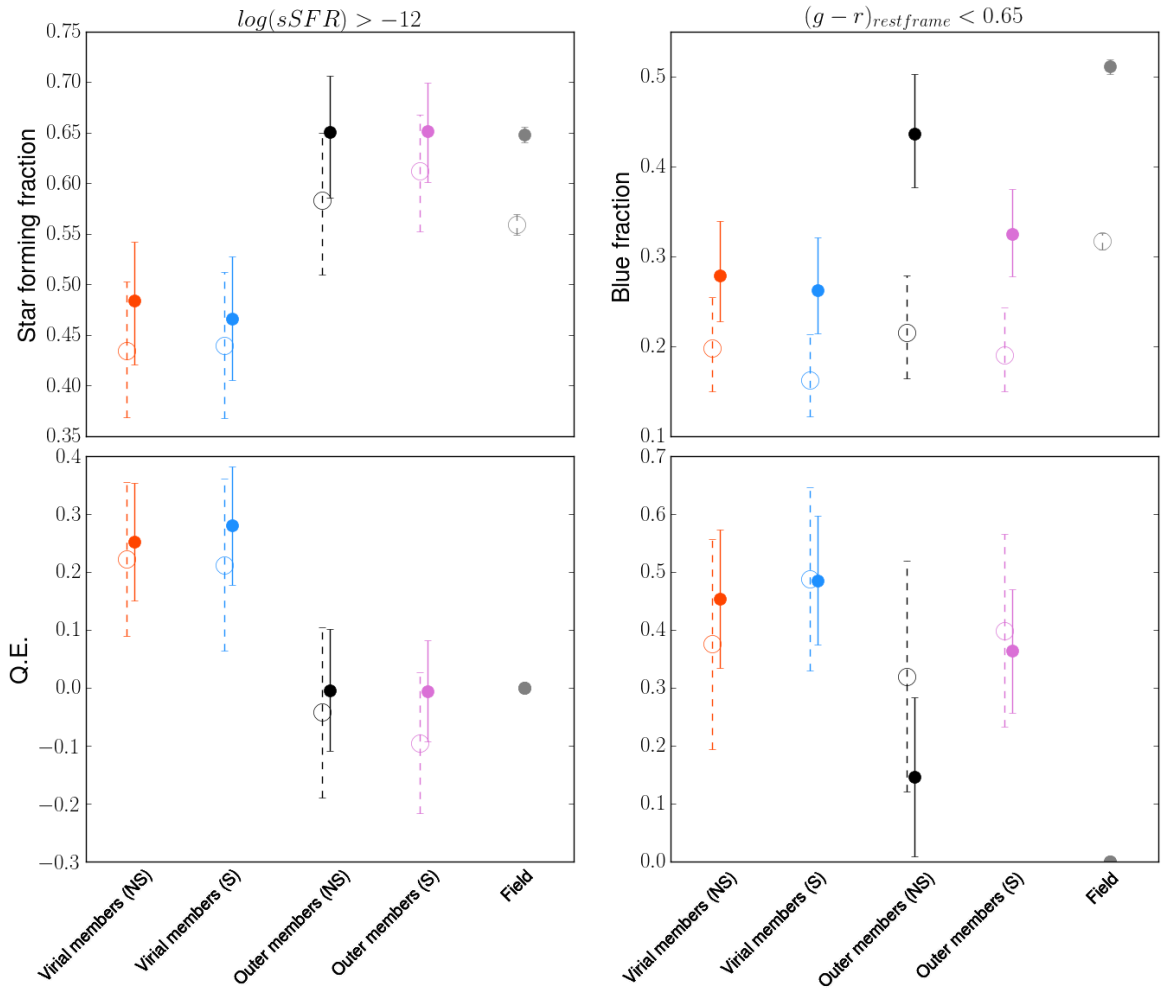


Figure 7.9: Same as Figure 7.7 but for galaxies at $0.3 \leq z \leq 0.5$.

While the SFR is an instantaneous measure of the rate at which a galaxy is forming stars at the epoch it is observed, colours are the result of longer processes tracing the predominant stellar population of a galaxy, whose colour is sensitive to its past history as well as to its current star formation activity. Moreover, colour is also influenced by other characteristics, such as the metallicity and the presence of dust. In addition to this, it is worth recalling that the sSFR and the $(g - r)_{rest-frame}$ are derived following two independents and conceptually different methods: the ongoing SFR is a product of the full spectral fitting analysis performed by SINOPSIS on the spectra, while rest-frame colours are derived by means of SED fitting on the photometry.

Taken together, the results presented in this section reveal that virial members as a whole exhibit a noticeable star formation suppression and a blue fraction deficiency with respect to all other environments at all redshifts. Moreover, fractional differences within and outside of superclusters do not follow a common trend at all redshifts, likely reflecting the

variation of properties of individual supercluster structures at different redshifts. Outer members have enhanced fractions of star forming/blue galaxies compared to virial members at all redshifts, which is also supported by similar results in literature (Bai et al. 2007; Fadda et al. 2008; Santos et al. 2013). In addition, at z≥0.2 outer members behave similarly to field galaxies, while at 0.1< $z$ <0.2 they exhibit a significant suppression of the star forming/blue fractions with respect to the field. Finally, field galaxies maintain higher values of star forming/blue galaxies at all redshifts.

### 7.3.2 Fraction of star forming galaxies in high- and low- X-ray luminosity G&C

Having explored the dependency of the star forming and blue fraction on global environment ranging from superclusters to the field, in this section I focus on virial and outer members of G&C and divide them in two classes of luminosity, assuming a separation value of $L^{XXL}_{500,scal} = 10^{43}$erg/sec, as in Chapter 5. This value approximately corresponds to a threshold in virial mass that separates structures with typical masses of clusters from groups, i.e. $10^{14} M_{\odot}$. The sample statistics does not allow us to separate (S) and (NS)G&C, because the size of the error bars would be too large to infer any result. The fractions of star forming and blue galaxies in the magnitude limited sample and in the three usual redshift bins are shown in Figures 7.10, 7.11 and 7.12. Virial members are shown with dark orange circles, outer members are shown with black circles and the error bars are computed using the bootstrap method.

At 0.1≤z<0.2, a significant difference between virial and outer members in both ranges of X-ray luminosity is visible both for star forming and blue galaxies. Outer members are systematically more star forming/bluer than virial members (75% vs 55%). In no case strong environmental dependences emerge, except for a hint of decreasing fraction of star forming galaxies in virial members at high X-ray luminosities. It is important to notice that, according to the sSFR, at least ∼60% of G&C members are star forming.

At 0.2≤z<0.3, differences between outer and virial members are even more outstanding. The fraction in outer members is maintained around $\sim 0.80$ when the star formation activity is considered and $\gtrsim 0.4$ when colours are considered. In virial members instead, the hint of dependence with X-ray luminosity in the star forming fraction is overturned with respect to the previous redshift bin, and becomes statistically meaningful when the fraction of blue galaxies is considered. Against expectations, this difference reveals an enhancement in the fraction of blue galaxies in high luminosity G&C (0.23) and a simultaneous decrease in the blue fraction of low-luminosity G&C (0.07). When the sSFR is used, the trend of the two populations is the same but with less pronounced difference with luminosity and higher error bars.

At the highest redshift, despite the large uncertainties, some trends still emerge. Considering the star forming population, virial and outer members in low-luminosity G&C have compatible fractions within the error bars, with values in outer members which are higher than in virial ones, but with a reduced fraction compared to other redshifts; in contrast, in high-luminosity G&C, the fraction of star forming galaxies in virial members signif-

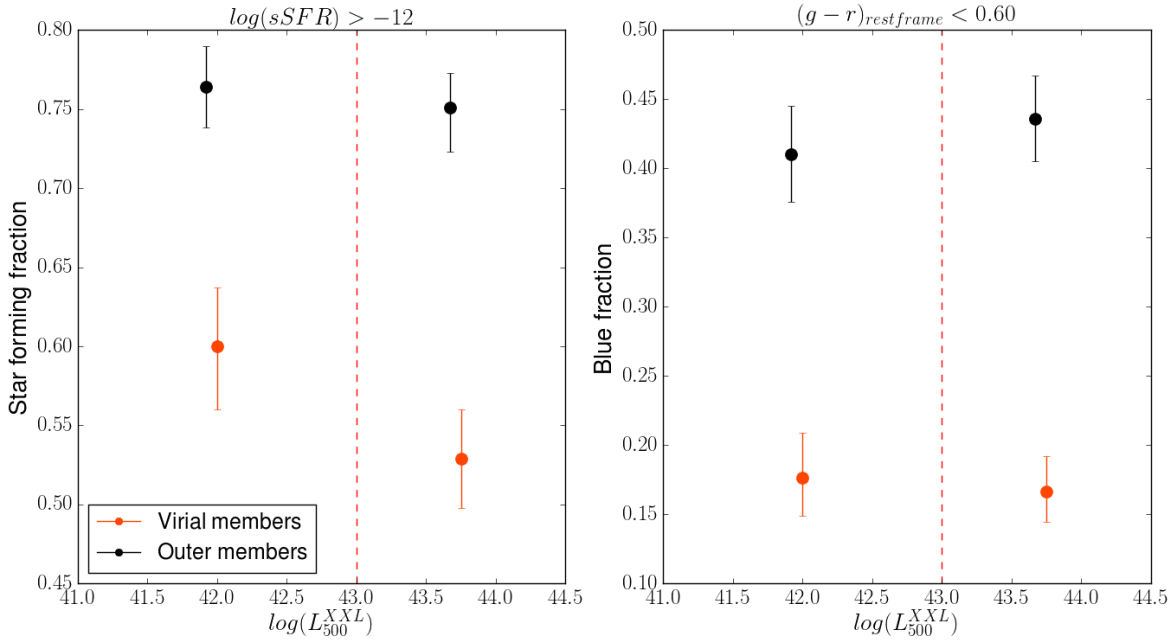


Figure 7.10: Fraction of star forming galaxies in G&C members, divided into two bins of X-ray luminosity (x-axis), computed using the sSFR (left panel) and rest-frame colour (right panel) in the redshift range $0.1 \leq z < 0.2$. G&C members are divided into virial (dark orange) and outer members (black). The fractions are obtained using the magnitude limited sample and errors are derived by means of a bootstrap method.

icantly decreases, with the result that the two populations present different properties. Considering the blue populations, opposite results emerge: in low luminosity systems the population of blue outer members is significantly larger than the population of blue virial members, while in high-luminosity G&C differences are washed out.
To summarise, X-ray luminosity is not found to play a decisive role in the determination of the fraction of star forming and blue galaxies in G&C, neither in the virial nor in the outer member components. A peculiar case is represented by the increase in the number of blue galaxies in high X-ray luminosity G&C at $0.2 \leq z < 0.3$, which are significantly more numerous. At the highest redshifts, the fraction of star forming and blue galaxies in outer members tends to approach the value of virial members, becoming similar within the error bars in the low-luminosity regime for star forming galaxies and in the high luminosity regime in blue galaxies.

### 7.3.3 SFR and sSFR-mass relation

I now proceed the analysis by investigating the correlation between the sSFR and galaxy stellar mass. This allows me to look into another side of the quenching process. Measuring the fraction of star forming galaxies gives a snapshot of the ongoing star formation

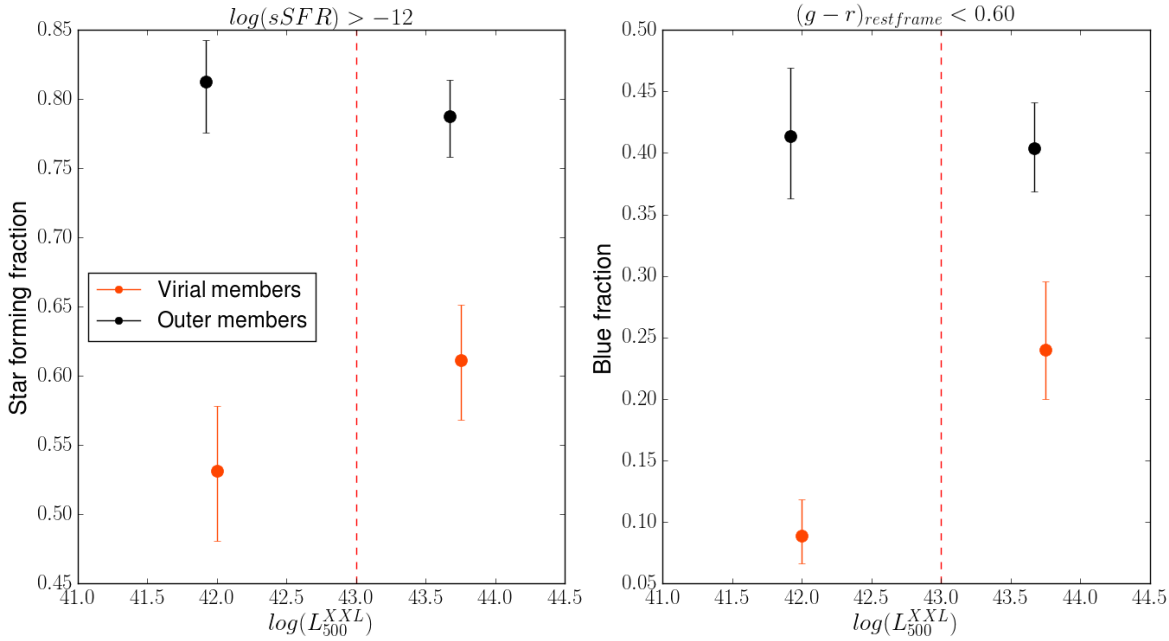


Figure 7.11: Same as Figure 7.10 but for the redshift range $0.2 \leq z \leq 0.3$.

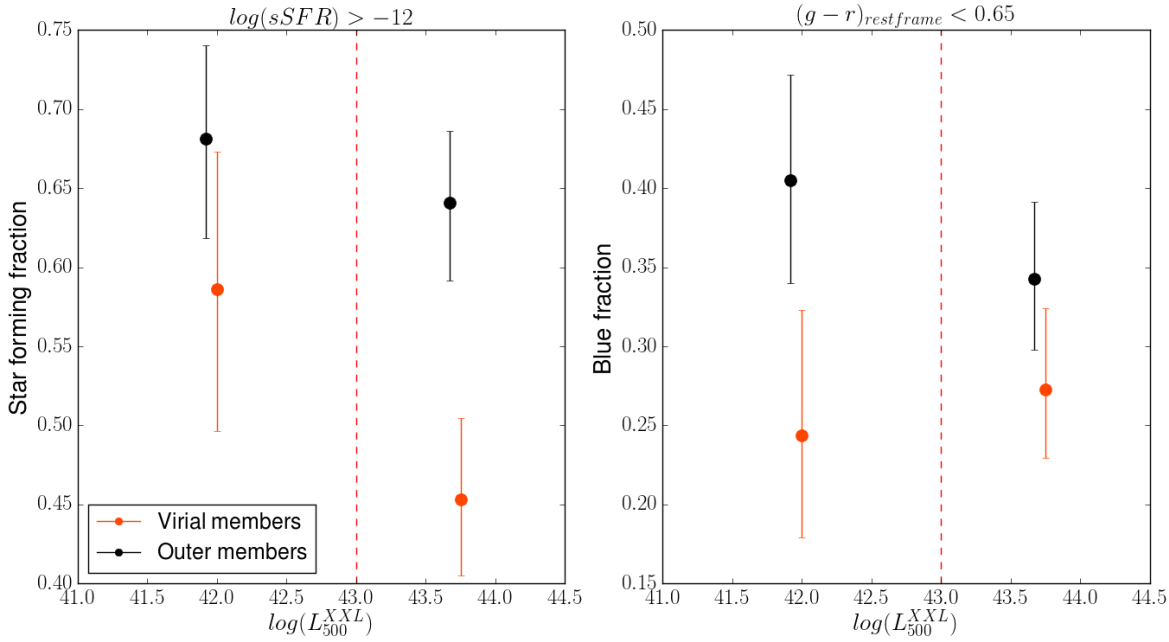


Figure 7.12: Same as Figure 7.10 but for the redshift range $0.3 \leq z \leq 0.5$.

activity in a given environment, without carrying any information about the way the quenching process builds up the quenched population. On the other hand, the sSFR-

mass relation carries important information about the rapidity of the quenching process: a fast quenching channel causes a sudden relocation from the sequence of star forming galaxies to the quenched population with typical values of sSFR below a given threshold; a slow quenching mechanism instead sets the presence of a population of galaxies which are still star forming but whose rates of star formation are reduced with respect to the main star forming population. Throughout the following sections, I will concentrate in defining the population of star forming galaxies and unveiling the presence of a population of galaxies in transition in different global environments, and considering virial members in different X-ray luminosity regimes.

Figure 7.13 compares the distributions of galaxies in different environments at a given redshift in the sSFR-mass plane, in the mass limited sample. I perform a fit to the relation by considering different environments altogether in the mass complete regime and by removing outliers using a sigma-clipping method. The resulting fitting line is shown in blue and the corresponding line equation is written within a small box inside each panel of the figure. Different environments are shown with different colours as detailed in the legend. In the figure, I also report the fitting lines of G&C virial member and field galaxies separately, which reveal some differences: while the sSFR-mass relation of field galaxies is always superposed to the blue global fitting line, the relation of G&C virial members is parallel and lower with respect to the latter in the first two redshift bins, and presents differences also in the slope at the highest considered redshifts. However, in this case, the limited mass range could affect the reliability of the fit. The right hand panels report the histograms, for any given environment, of the differences between the sSFR recovered from the global fitting line ($\Delta$sSFR) with respect to the sSFR of a galaxy with a given stellar mass; on these, I perform a KS test in order to quantify statistically the comparison. Positive values of $\Delta$sSFR correspond to reduced sSFRs with respect to the fitting line. The results point out the presence of differences in the distribution of $\Delta sSFR$ of virial members and field populations, with the former presenting a tail of reduced sSFR values with respect to the latter and with typical p-values derived from the KS test $\leq 10^{-2}$; outer members have statistically different distribution with respect to the field only at $0.3 \leq z \leq 0.5$ (p-value$<$0.02).

A better visualization and quantification of the population of galaxies that produce the tails in the $\Delta$sSFR histograms is obtained when the SFR is contrasted to the stellar mass. The relation is shown in Figure 7.14 for the three redshift bins. Galaxies classified as virial and outer members of G&C and the field sample are represented with different colours as indicated in the legend. I perform a sigma-clipping linear fitting of the SFR-mass relation in the mass complete regime at each redshift, and compute $1\sigma$ confidence intervals which are shown as blue shaded areas around the solid blue fitting line. Following the procedure described in Paccagnella et al. (2016) and already implemented in 6, I compute the fraction of galaxies in transition between the star forming main sequence and the quenched population, defined as those galaxies with $(\mathrm{sSFR/yr^{-1}}) > 10^{-12}$ and SFR below -1$\sigma$ with respect to the SFR-mass fitting line. The fraction is computed as the ratio of this population with respect to the population of galaxies with $\log(\mathrm{sSFR/yr^{-1}}) > -12$, in each environment. It is important to note that, by definition, the percentage of galaxies

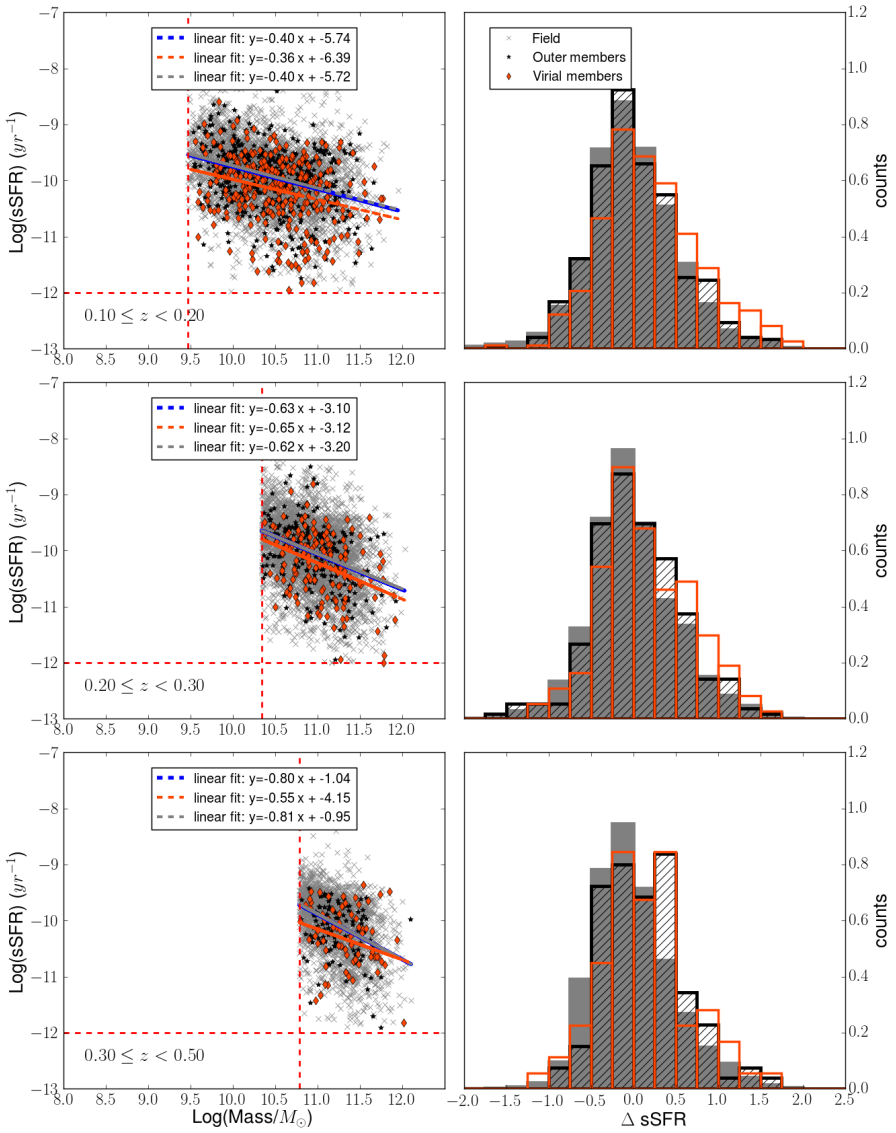


Figure 7.13: Specific star formation rate (sSFR)-mass relation for galaxies in the field and galaxies in G&C virial and outer members (grey crosses, orange diamonds, and black stars in the left panel) in the mass limited sample. The vertical and horizontal lines show the stellar mass limit and our adopted separation between star forming and passive galaxies. The blue line is the fit to the relation of the sample including all the environments, and its equation is written on top of each histogram. The right panel shows the distribution of the differences between the galaxy sSFRs and their expected values according to the fit given their mass.

below a $1\sigma$ cut of the SFR-mass relation should be ∼15-17%, therefore the identification of a population of galaxies in transition is measured as excess of galaxies compared to

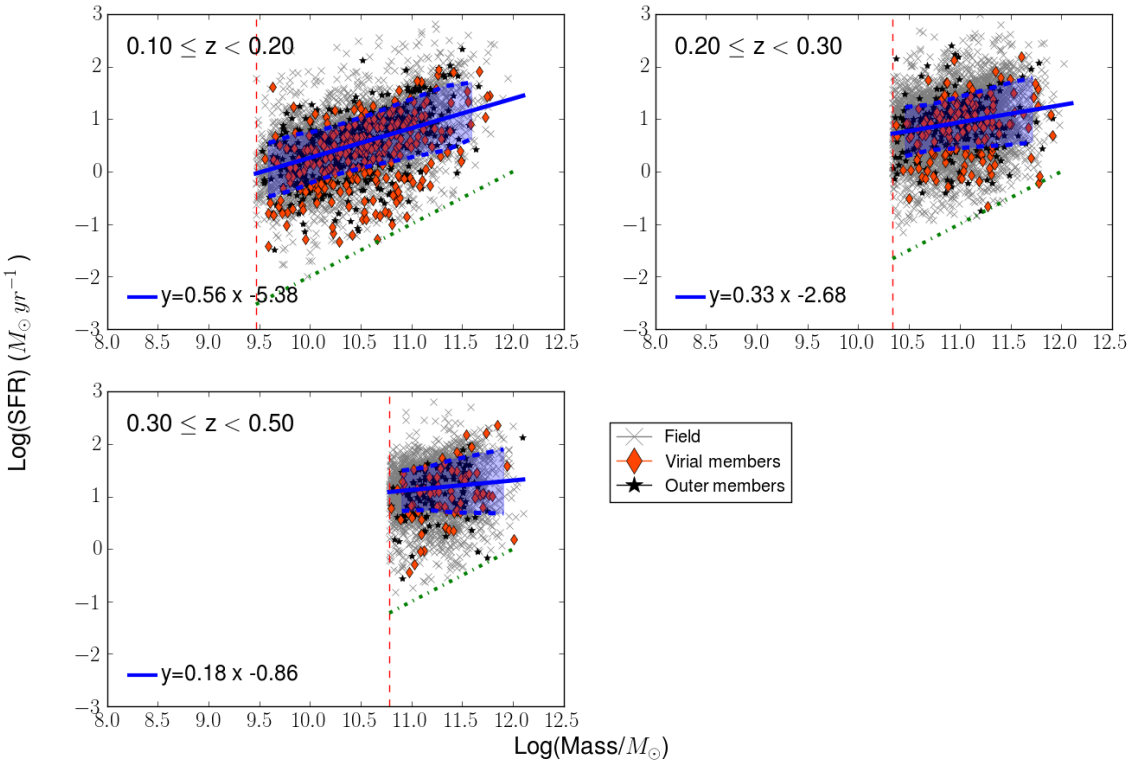


Figure 7.14: SFR-mass relation for galaxies in the field and galaxies in G&C virial and outer members (grey crosses, orange diamonds, and black stars) in the mass limited sample. The three panels refer to different redshift bins, as indicated inside each panel. The vertical line show the stellar mass limit at each redshift. The blue line is the fit to the relation including all the environments at each redshift, and the shaded areas correspond to $1\sigma$ errors on the fitting line. Fitting lines equations are written inside each panel. The fraction of galaxies in transition in each environment is computed as the fraction of galaxies located below the lower $1\sigma$ line and above the green line representing the log(sSFR)=-12 limit with respect to the total number of galaxies in the considered environment above the green line.

this statistical value.

The fractions of galaxies in transition shown in Figure 7.14 are given in Table 7.3. I compute the fraction of galaxies in transition also dividing virial/outer members of G&C residing in superclusters and of G&C of high- and low- X-ray luminosity, and considering galaxies within 0.6 $r_{200}$, to allow fair comparison with Paccagnella et al. 2016, who found a significant population of galaxies in transition within 0.6 $r_{200}$ in a sample of massive clusters at $0.04 \leq z \leq 0.7$. Finally, in order to compare the results obtained at different redshifts, I compute the fractions relative to the highest stellar mass limit, i.e. $\log(M/M_\odot)=11.78$, the stellar mass completeness limit at $0.3 \leq z \leq 0.5$.

A first glance on the statistics reveals that the incidence of a population of galaxies in

Table 7.3: Fraction of galaxies in transition in different environments defined in the main text and in the three usual redshift bins investigated throughout this chapter. Numbers are computed above the stellar mass completeness limit of each redshift bin, and numbers in parenthesis are computed with respect to the highest stellar mass limit, in order to allow the comparison at different redshifts. Error bars are binomials. The last two lines of the table correspond to the values computed in two bins of LD, and will be analysed in Section 7.4.

| | $0.1 \leq z < 0.2$ $\log(M/M_\odot)$ 9.47 | $0.2 \leq z < 0.3$ $\log(M/M_\odot)$ 10.34 | $0.3 \leq z < 0.5$ $\log(M/M_\odot)$ 10.78 |
|---|---|---|---|
| Field | $0.15^{+0.01}_{-0.01}$ $(0.15^{+0.02}_{-0.02})$ | $0.17^{+0.01}_{-0.01}$ $(0.17^{+0.01}_{-0.01})$ | $0.16^{+0.01}_{-0.01}$ |
| G&C virial members | $0.29^{+0.04}_{-0.04}$ $(0.25^{+0.08}_{-0.07})$ | $0.30^{+0.06}_{-0.05}$ $(0.26^{+0.07}_{-0.06})$ | $0.24^{+0.08}_{-0.07}$ |
| G&C outer members | $0.18^{+0.03}_{-0.02}$ $(0.17^{+0.06}_{-0.05})$ | $0.18^{+0.04}_{-0.04}$ $(0.17^{+0.05}_{-0.04})$ | $0.26^{+0.07}_{-0.06}$ |
| G&C virial members (S) | $0.30^{+0.05}_{-0.04}$ $(0.22^{+0.09}_{-0.07})$ | $0.19^{+0.08}_{-0.06}$ $(0.14^{+0.08}_{-0.06})$ | $0.21^{+0.12}_{-0.09}$ |
| G&C virial members (NS) | $0.24^{+0.1}_{-0.08}$ $(0.4^{+0.2}_{-0.2})$ | $0.40^{+0.09}_{-0.08}$ $(0.4^{+0.1}_{-0.1})$ | $0.28^{+0.14}_{-0.11}$ |
| G&C outer members (S) | $0.18^{+0.03}_{-0.03}$ $(0.18^{+0.07}_{-0.06})$ | $0.10^{+0.06}_{-0.04}$ $(0.12^{+0.07}_{-0.05})$ | $0.32^{+0.10}_{-0.09}$ |
| G&C outer members (NS) | $0.14^{+0.07}_{-0.03}$ $(0.13^{+0.14}_{-0.08})$ | $0.23^{+0.06}_{-0.05}$ $(0.22^{+0.08}_{-0.06})$ | $0.16^{+0.10}_{-0.07}$ |
| G&C virial members @$r \leq 0.6r_{200}$ | $0.25^{+0.05}_{-0.05}$ $(0.25^{+0.10}_{-0.08})$ | $0.28^{+0.07}_{-0.06}$ $(0.26^{+0.08}_{-0.07})$ | $0.21^{+0.10}_{-0.08}$ |
| G&C virial members, $L^{XXL}_{500,scal} \geq 10^{43} erg/s$ | $0.27^{+0.05}_{-0.05}$ $(0.23^{+0.11}_{-0.08})$ | $0.26^{+0.07}_{-0.06}$ $(0.19^{+0.08}_{-0.06})$ | $0.22^{+0.10}_{-0.08}$ |
| G&C virial members, $L^{XXL}_{500,scal} < 10^{43} erg/s$ | $0.31^{+0.06}_{-0.06}$ $(0.3^{+0.1}_{-0.1})$ | $0.37^{+0.10}_{-0.09}$ $(0.4^{+0.1}_{-0.1})$ | $0.3^{+0.2}_{-0.2}$ |
| High-LD (85th) | $0.16^{+0.02}_{-0.02}$ $(0.17^{+0.04}_{-0.04})$ | $0.17^{+0.02}_{-0.02}$ $(0.18^{+0.03}_{-0.02})$ | $0.18^{+0.03}_{-0.03}$ |
| Low-LD (15th) | $0.17^{+0.02}_{-0.02}$ $(0.18^{+0.04}_{-0.04})$ | $0.16^{+0.02}_{-0.02}$ $(0.15^{+0.02}_{-0.02})$ | $0.17^{+0.03}_{-0.03}$ |

transition depends on environment, with field galaxies having fewer transition galaxies compared to G&C virial members, at any redshift. Among outer members instead, the presence of transition galaxies varies in the different redshift intervals.

Considering in detail galaxies at 0.1≤z<0.2, transition galaxies in the field are 0.15±0.01 of the total star forming population, and the fraction almost doubles in G&C virial members; in addition, transition galaxies in G&C belonging to superclusters (S) might have a slightly higher incidence than transition galaxies in G&C not belonging to any supercluster ($0.3^{+0.05}_{-0.04}$ vs $0.24^{+0.1}_{-0.08}$), though the two are compatible within the error bars. Fractions are compatible within the errors also when considering the population of G&C of high- and low- X-ray luminosity. Transition galaxies in outer members have a similar incidence as transition galaxies in the field, regardless to the belonging to a supercluster.

Moving on to the intermediate redshift bin, the same trends can be recovered by comparing the field, virial and outer members populations as a whole, with the transition population having the highest fraction in G&C virial members ($0.30^{+0.06}_{-0.05}$), while a lower and similar incidence (∼0.17) is detected in G&C outer members and in the field. At these redshifts, the differential contribution of galaxies in (S) and (NS) systems stands out: in virial members, transition galaxies in (NS)G&C clearly dominate the overall fraction, being $0.4^{+0.09}_{-0.08}$ versus a fraction of only $0.19^{+0.08}_{-0.06}$ in superclusters. Also outer members show the same tendency, with galaxies in (S)G&C having an even lower proportion of transition galaxies ($0.10^{+0.06}_{-0.04}$) compared to the field ($0.17^{+0.01}_{-0.01}$), and with a simultaneous higher

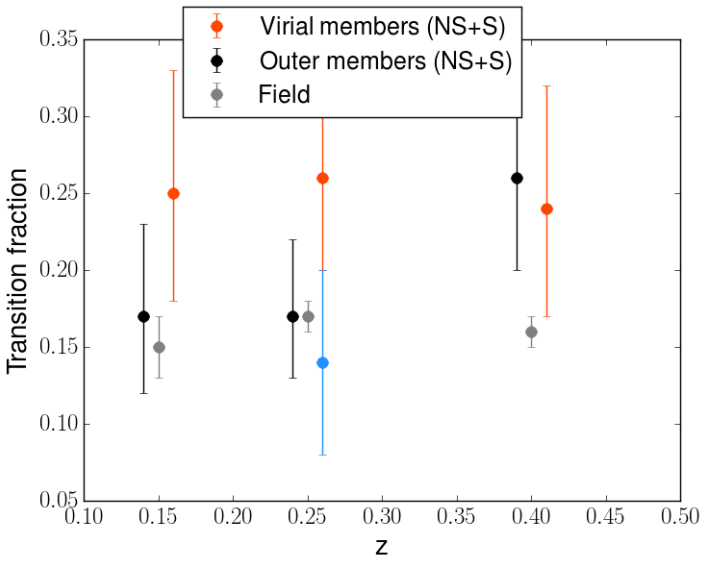


Figure 7.15: Fraction if galaxies in transition from z=0.1 to z=0.5, in different environments as indicated in the legend. Fractions are computed above the same, most conservative, stellar mass completeness limit corresponding to the highest redshift interval in the range ($0.3 \leq z \leq 0.5$). The light blue dot at $z \sim 0.25$ represents the fraction of galaxies in transition in the virial regions of (S) G&C at $0.2 \leq z < 0.3$

incidence of transition galaxies located in (NS)G&C. These results confirms the findings performed in the XLSSsC N01 supercluster in Chapter 6, where I did not report any difference in the sSFR-mass relation of galaxies in different environments ranging from virial members within the supercluster to the field, and I unveiled the presence of a population of recently quenched galaxies instead.

Finally, in the highest redshift bin, the fraction of transition galaxies in the field is lower than among both the virial and the outer members. The latter seems to be driven by galaxies in transition within superclusters, which represent a much higher fraction than in lower redshift bins. No visible differences for virial members in and out of superclusters are present at these redshifts.

Considering only galaxies above the same, most conservative, mass limit at all redshift, I can quantify the evolution of the incidence of galaxies in transition. The fractions corresponding to virial and outer (S)+(NS) G&C members are shown in Figure 7.15. For virial members and for the field, the overall fractions of massive galaxies in transition do not significantly vary with cosmic time around a value of $\sim 25\%$ and $\sim 16\%$, respectively. In contrast, the transition fraction among outer members appears to be higher at z=0.3-0.5 than at lower redshifts (26% vs. 17%), and this effect is dominated by galaxies in the outer regions of superclusters. In the figure, virial members within superclusters in the redshift range $0.2 \leq z < 0.3$ are represented with a light blue point, in order to highlight its deficiency of transition galaxies with respect to the average population of G&C at

the same redshift. It is worth recalling that the (S) at these redshift is dominated by XLSSsC N01, in which the fraction of transition galaxies computed in Chapter 6 was not environmental dependent.

Paccagnella et al. (2016) found that in the local Universe the vast majority of galaxies in transition is confined within 0.6 $r_{200}$. Instead, if I limit the analysis to virial member galaxies within 0.6 $r_{200}$, I still recover a similar fraction of galaxies in transition as in the global population of G&C virial members, at all redshifts. This finding suggests that such segregation is not visible at higher redshift.

### 7.3.4 LW-age mass relation

The results obtained in the previous sections were based on the SFR, which is an indicator of the ongoing star formation activity of a galaxy at the time it is observed, and colour, which depends also on the integrated stellar history. In this section I complement the results acquired so far by inspecting the galaxy LW-age, a parameter that is linked to the last star formation episode occurred within a galaxy.

Figure 7.16 reports the relation between the median LW-age of all galaxies inhabiting a given environment (in the legend) with their stellar mass, in the magnitude limited sample, and with shaded area indicating the percentiles corresponding to the $1\sigma$ confidence level. Galaxies are divided in virial members, outer members and the field. The mass limited sample is also shown with a vertical red dotted line inside each panel representing a given redshift bin.

The LW-age is known to be an increasing function of stellar mass, with galaxies with the highest mass being also the oldest, according to the aforementioned *downsizing* effect, as seen also in Fig. 7.16 for all environments. A weak environmental dependence is visible in this plot, with a slightly higher LW-age for virial members following the edge of the upper $1\sigma$ contour of the other environments up to z=0.3 and, below a mass $M = 10^{11.2} M_{\odot}$, also at higher redshifts. No large differences between environments are found at the highest stellar masses at all redshifts, in that high-mass galaxies in any environment formed at earlier epochs and already completed their star production. The LW age-mass relation of outer members and field galaxies is indistinguishable, except perhaps for masses below $10^{11} M_{\odot}$ in the highest redshift bin.

In order to understand the contribution to this relation coming from the star forming and passive population, I proceed by dividing the star forming from the passive population in all environment and in the three redshift ranges. The result is given in Figure 7.17. The LW-age vs stellar mass relation split into star forming and passive galaxies reveals some environmental trends. Galaxies in G&C virial members present a population of higher LW-age galaxies with respect to other environments in the star forming population up to z=0.3, at masses $\log(M/M_{\odot}) \lesssim 10.5$ at $0.1 \leq z < 0.2$ and $\log(M/M_{\odot}) \lesssim 11.5$ at $0.2 \leq z < 0.3$. At $z > 0.3$, the presence of a recently quenched population among virial members is visible at high masses $M > 10^{11} M_{\odot}$, with an enhanced LW age of star-forming galaxies and a younger LW age of passive galaxies.

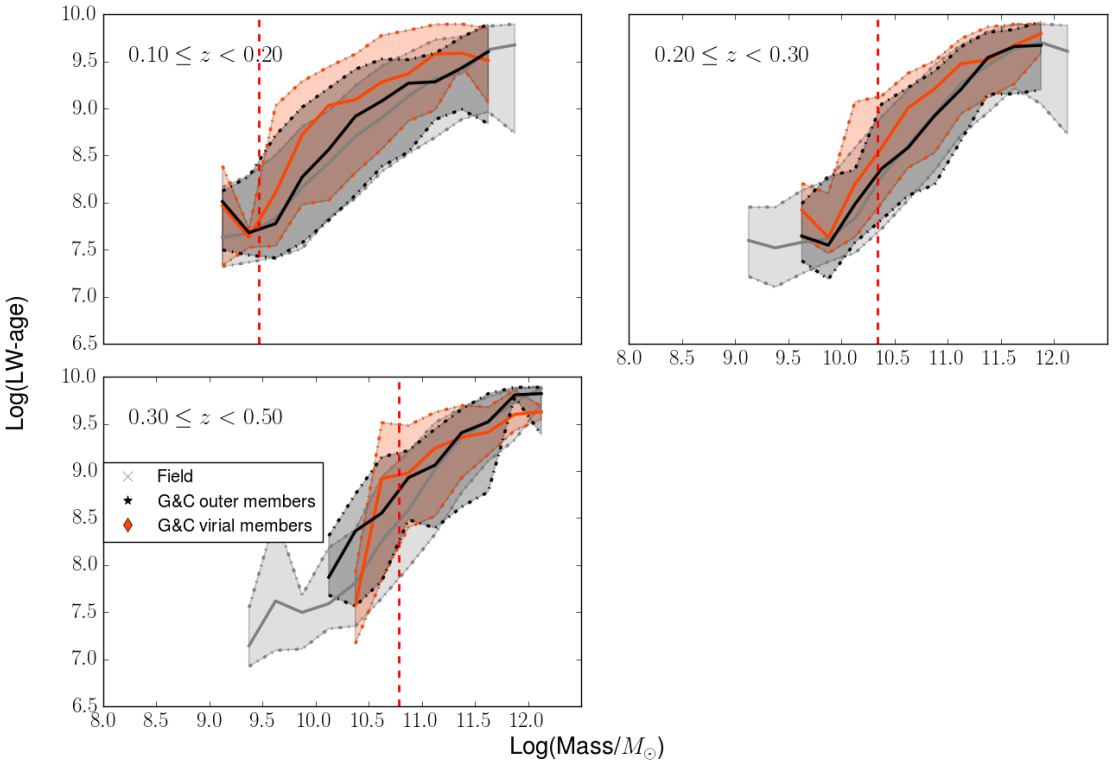


Figure 7.16: Median LW-age-mass relation computed in non-independent stellar mass bins for different environments, as shown in the legend. Each panel refer to a different redshift bin, as indicated inside each panel. The stellar mass limit is shown with a vertical black dashed line. Shaded areas are the 16th and 84th percentiles, corresponding to $1\sigma$ errorbars.

### 7.3.5 Mass-assembly and star formation history

As discussed previously throughout the thesis, the stellar history of galaxies is influenced by its properties, with a concurrent interplay between the physical characteristics of a galaxy and the environmental conditions it experiences. The relative importance of stellar mass, global environment and observed morphology for the star formation history of galaxies in the local Universe was investigated in Guglielmo et al. (2015) (see Appendix), where I found that stellar mass was the main responsible in changing the slope of the decline in the SFR from high- to low- redshift, in all environments. Beside this, also the environment plays an important role at a given fixed stellar mass, with cluster galaxies having the highest rate in star formation at high redshift compared to field galaxies. In this section I investigate how the mass and star formation proceeded in four epochs of look-back time with respect to the epoch of observation of galaxies, by plotting the median of the mass formed and of the SFR in each epoch as a function of stellar mass in order to look for traces of environmental and mass dependence in the assembly history of the

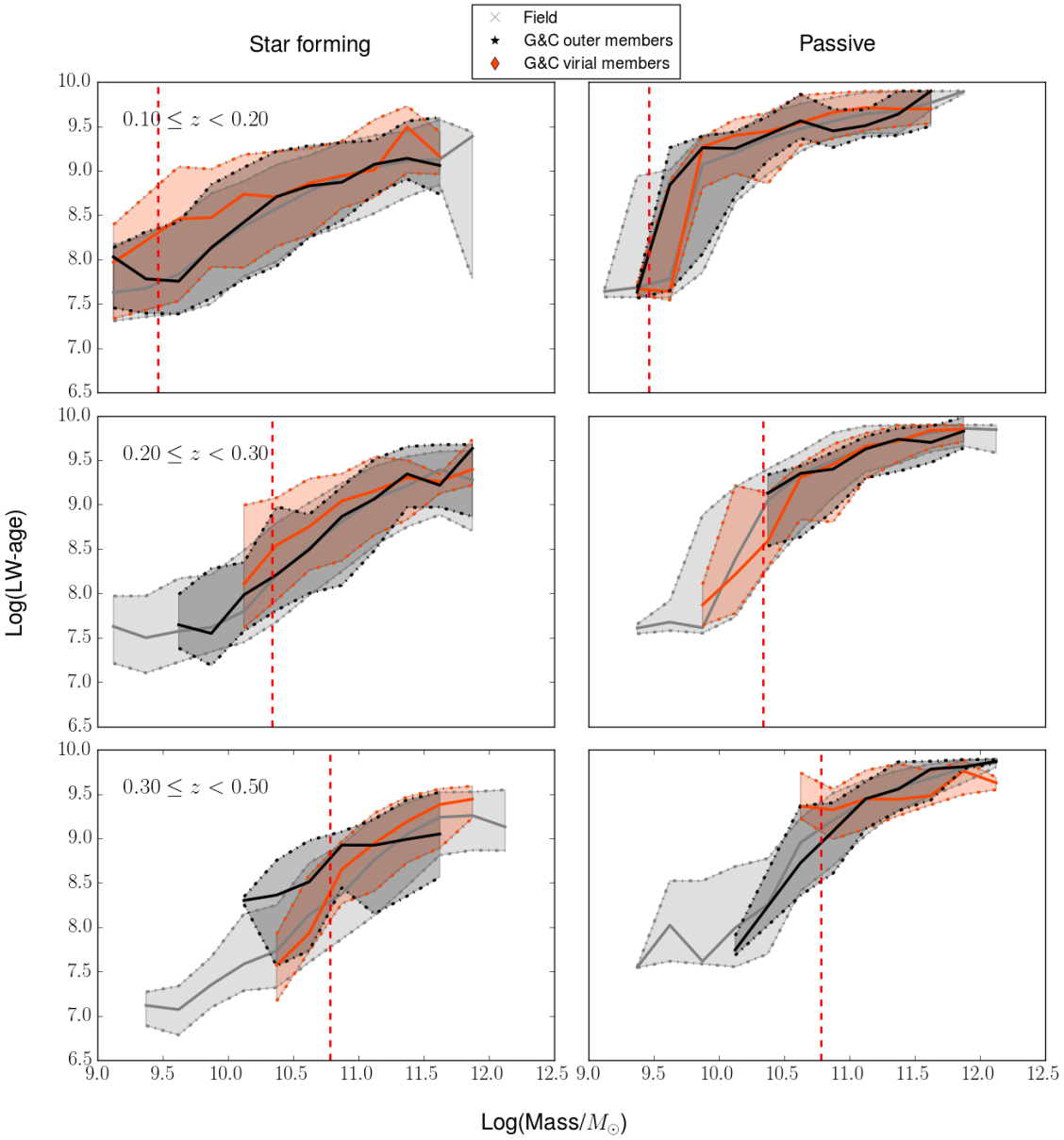


Figure 7.17: Median LW-age-mass relation computed in non-independent stellar mass bins for different environments, as shown in the legend, for star forming and passive galaxies. The stellar mass limit is shown with a vertical black dashed line. Each panel refers to a different redshift bin, as indicated inside each panel. Shaded areas are the 16th and 84th percentiles, corresponding to 1$\sigma$ error bars.

galaxies analysed here. I consider separately the three redshift bins in which galaxies are divided because the look-back time epochs that are explored are not comparable one to each other, since their starting point is the redshift of observation of galaxies.

Starting from the stellar mass assembly of galaxies, shown in the first line panels of Figure 7.18, Figure 7.19, and Figure 7.20, a few conclusions for galaxies above the mass limit are immediately evident:
a) the average fraction of stellar mass formed in each look-back time interval shows only very small variations with environment. Only in the lowest redshift bin, for high mass galaxies, there is a hint of an accelerated mass assembly in group virial members, with respect to field/outer members, in the oldest age bin, and a correspondingly lower fraction formed between about 1 and 6 Gyr ago;
b) the fraction of mass formed at recent times (last 600 Myr, and also at 0.6-5.6 Gyr) decreases with galaxy stellar mass, while the fraction formed more than 6 Gyr ago increases with mass;
c) in all environments, galaxies with $\log(M/M_{\odot}) \gtrsim 10.5$ up to z=0.3 ($\log(M/M_{\odot}) \gtrsim 10.75$ at z=0.3-0.5) formed more than 50% of their stellar mass more than 5.6 Gyr before the epoch of observation.
Similarly to the trends outlined in the stellar mass assembly history, the median star formation rate of galaxies depends on stellar mass in a nearly environmental independent fashion. The highest rates of star formation ($\mathrm{SFR} \leq 20 \mathrm{M}_{\odot}\mathrm{yr}^{-1}$) characterise galaxies with masses $\log(M/M_{\odot}) \gtrsim 11.0$ at the earliest ages of their formation, as expected according to *downsizing*. The average SFR in the oldest age bin steeply and monotonically increases with galaxy mass at the time these galaxies are observed. At intermediate times (0.6-5.6 Gyr before observations) this is not the case anymore, with the most massive galaxies departing from the monotonic trend with lower SFRs than other massive galaxies, and possible environmental trends becoming visible: virial members are forming more stars than galaxies of similar mass in other environments. At recent times (last 600 Myr), the average SFR only weakly depends on galaxy stellar mass. In the last 20 Myr the SFR in virial members is nearly zero while non-negligible amount of stars are still being formed in the field and in outer members.

## 7.4 Analysis on *local* environment

### 7.4.1 Fraction of star forming galaxies

I now consider all the global environments together, and rely only on local galaxy densities in order to establish to what extent the star formation activity is influenced by this parametrisation of environment.
I consider logarithmic bins of 0.2 dex in LD and compute, at any given redshift, the star forming and blue fraction of galaxies in the magnitude and mass limited samples, and derived error bars by bootstrapping. The results are plotted in figures 7.21, 7.22 and 7.23. In the first redshift bin (Fig. 7.21), a general monotonous decrease in the fraction of star forming galaxies is depicted from low- to high- LD, with the star forming fraction in the magnitude limited sample that decreases of a factor $\sim$2.1 in a local density range of 2.0 dex. In the same range, the fraction of blue galaxies decreases ten times more, with values that drop to zero at the highest densities. The mass limited sample at these redshifts

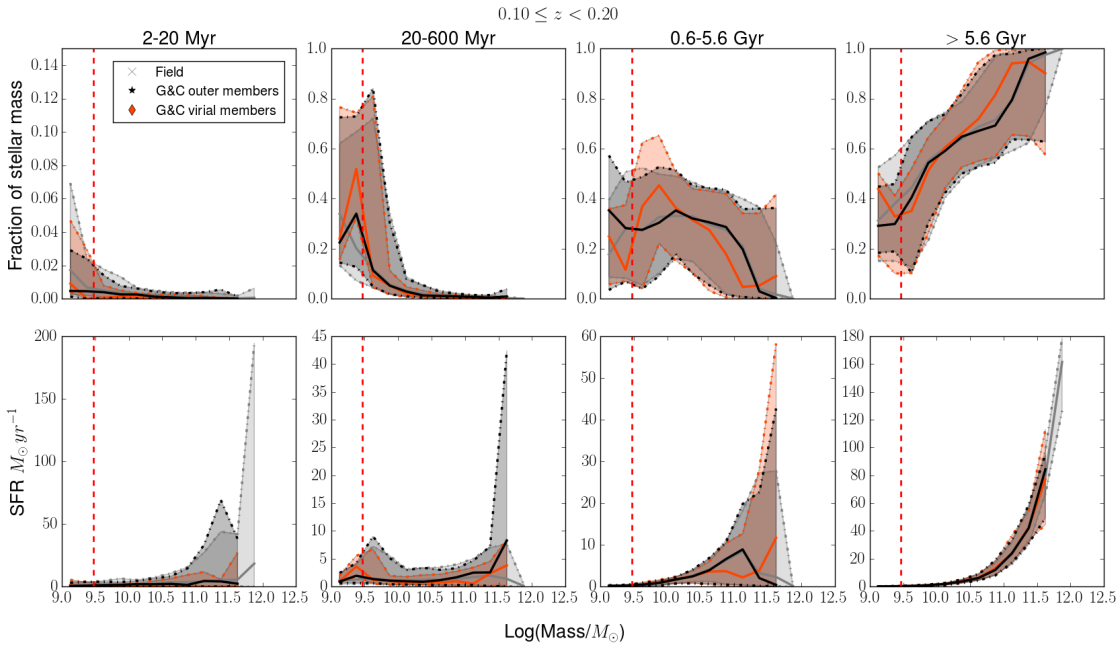


Figure 7.18: Median mass (top panels) and median SFR (bottom panels) formed in four look-back time epochs from the redshift of the galaxy, as a function of the galaxy stellar mass at the time of observations. This figure represents galaxies in the redshift range 0.1≤ z < 0.2. The look-back time from the redshift of the galaxy is written on top of each panel, and increases from left to right. Different environments are represented with different colours as indicated in the legend. Shaded areas are the 16th and 84th percentiles, corresponding to 1$\sigma$ error bars.

closely follows the trends outlined by the magnitude limited sample, as it is expected given that the stellar mass completeness limit is still low.

At redshift $0.2 \leq z < 0.3$, similar trends are found in the magnitude complete sample, even though the fraction of star forming galaxies reaches a sort of plateau at intermediate densities; the decrease in the fraction of blue galaxies is steeper in the magnitude limited sample than the fraction of star forming galaxies: the overall decrease in the fraction of star forming galaxies from low- to high- LD is a factor ∼1.7 and reaches the value of ∼ 3 in the blue fraction in the same range of approximately 2.0 dex in LD. At these redshift, as previously noted in the analysis on the global environment, in the mass limited sample the environment plays a minor role. Galaxies with masses $\log(M/M_\odot) > 10.78$ are on average more passive and red at all LD with respect to the magnitude limited sample, washing out almost any environmental trend.

The behavior in the magnitude limited sample of star forming galaxies is maintained in the last redshift bin, where the fraction of star forming galaxies keeps decreasing with increasing LD. The star forming fraction drops of a factor ∼3 from low- to high- LD in a range of 2.0 dex, while more fluctuations on the underlying smoother decrease are visible

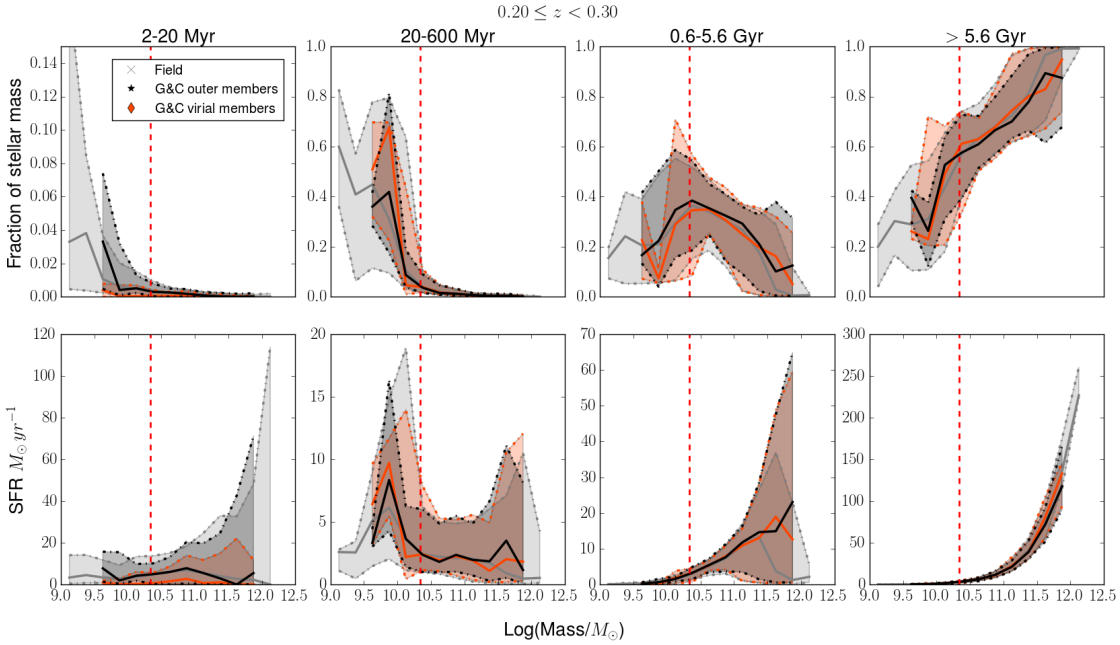


Figure 7.19: Same as Figure 7.18 but for galaxies at $0.2 \leq$ z $< 0.3$.

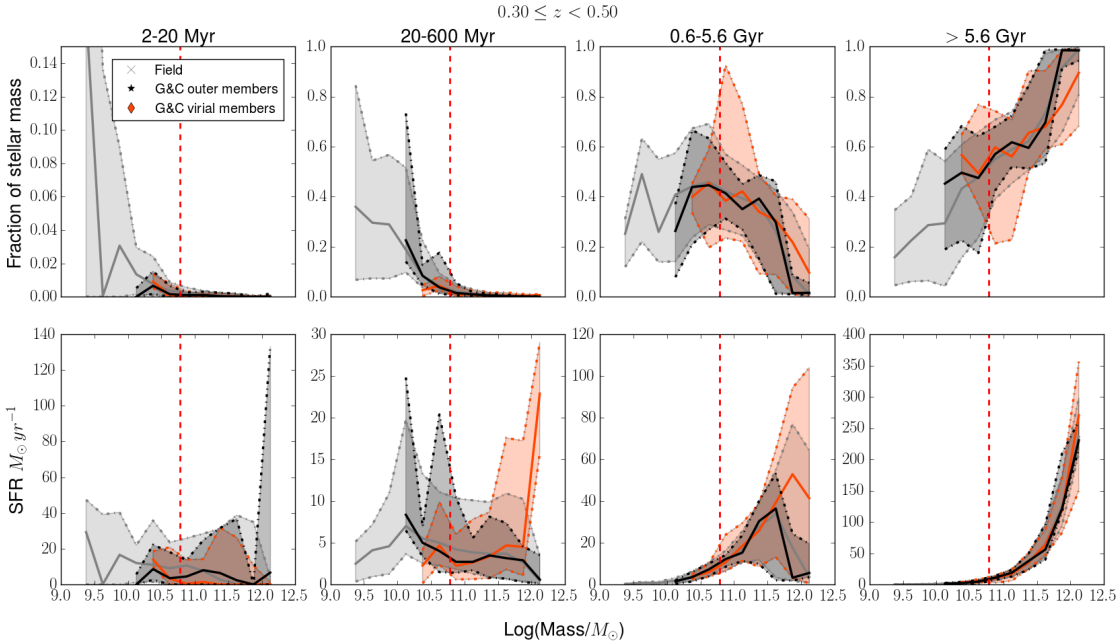


Figure 7.20: Same as Figure 7.18 but for galaxies at $0.3 \leq$ z $\leq 0.5$.

when colours are considered. Once again, the mass limited sample evidences lower star forming and blue components at any LD, and in the star forming population continue to

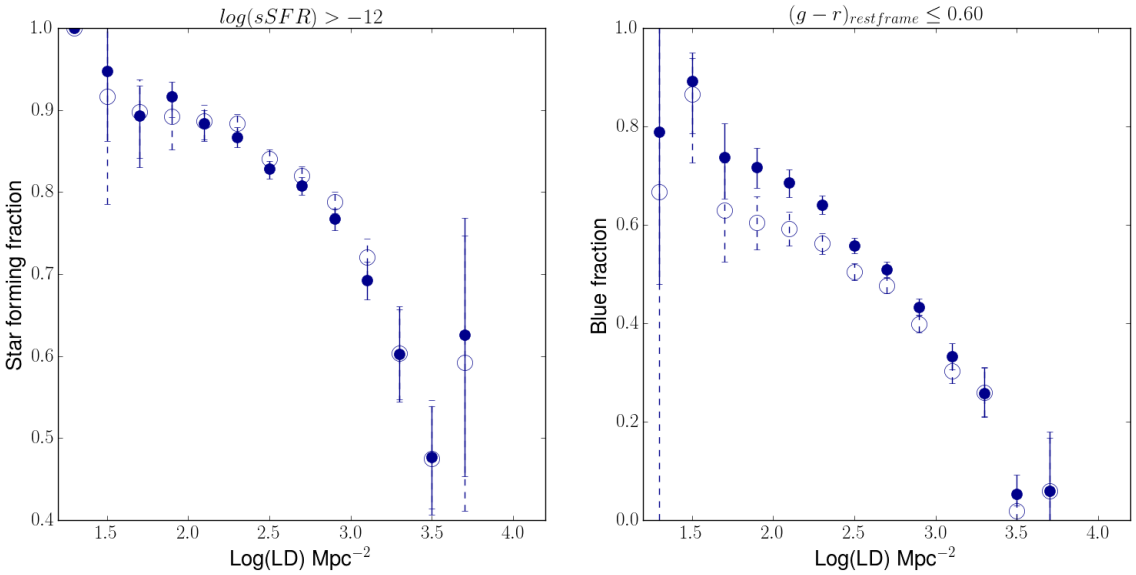


Figure 7.21: Fraction of star forming galaxies in different bins of LD, computed with the sSFR (left panel) and rest-frame colour (right panel) in the redshift bin $0.1 \leq z < 0.2$. The fractions obtained using the magnitude limited sample are represented with filled symbols and solid errors, those obtained using the mass limited one are represented by empty symbols and dashed error bars. Errors are derived by means of a bootstrap method.

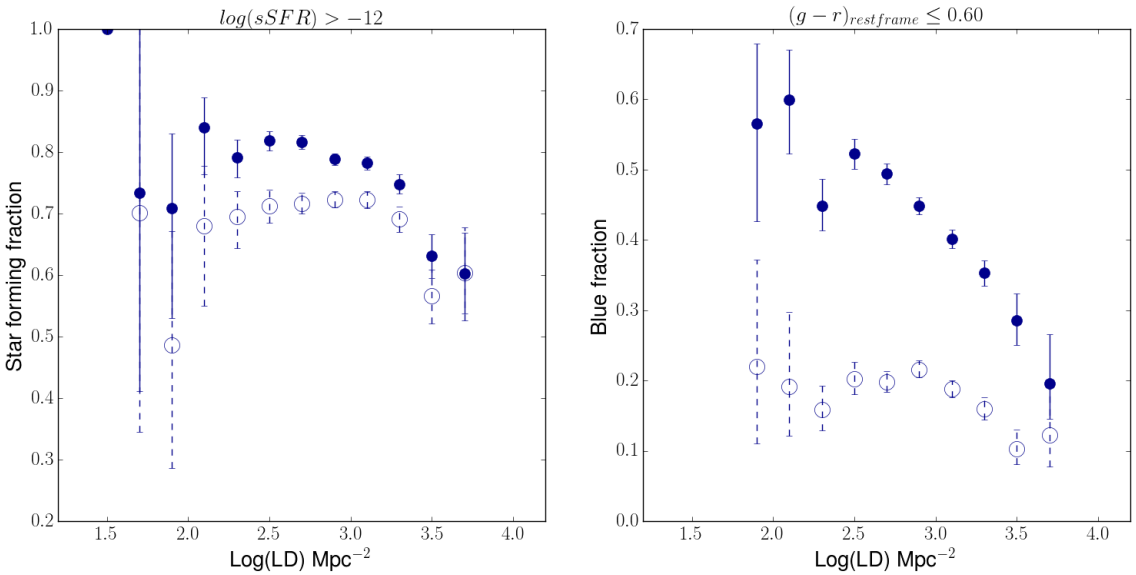


Figure 7.22: Same as Figure 7.21 but for galaxies at $0.2 \leq z \leq 0.3$.

follow the values of the magnitude limited sample.

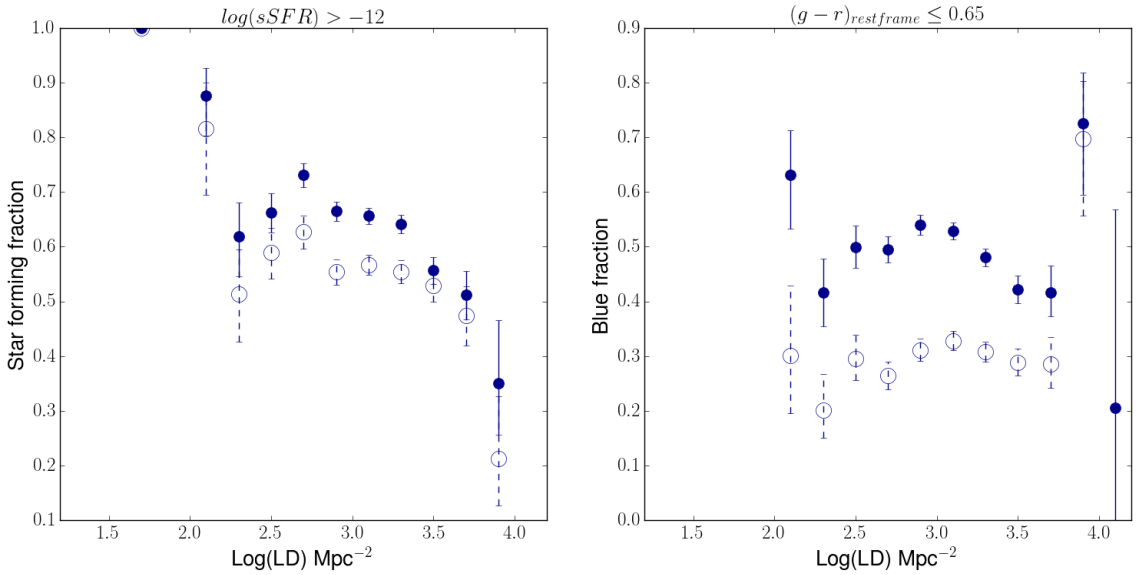


Figure 7.23: Same as Figure 7.21 but for galaxies at $0.3 \leq z \leq 0.5$.

### 7.4.2 SFR-mass relation

With reference to Section 7.3.3, I now study the SFR-mass relation of galaxies in two extreme bins of LD, selected from the histograms shown in Figure 7.5. At each redshift, I consider the median of the distribution and selected galaxies with LD higher than the value at the 85th percentile to define the High-LD bin, and those with LD lower than the value at the 15th percentile to define the Low-LD bin.

In Figure 7.24 I report the SFR-mass relation of galaxies in the low- and high- LD regimes shown with different colours as indicated in the legend. Then, by means of a sigma-clipping method to remove outliers, I perform a linear fit to the data points populating the plane in the two range of LD separately, and plot the $\pm 1\sigma$ contours to the fitting line as shaded areas in the figure. Both the fits and the $1\sigma$ contour levels show little variation with LD. This result is more robust at z<0.3, where the variation in the slope of the fitting line is of the order of the 10%. At higher redshift, galaxies in the low-LD bin might display a flattening of the relation (slope close to zero), but the small mass range probe prevent me from drawing solid conclusions.

Then, in order to compute the fraction of transition galaxies, I perform a linear fit to the data points populating the plane in the whole range of LD and computed the $\pm 1\sigma$ contours to the fitting line. I can now define the regime in which galaxies in transition are located in the two density bins, assuming the same criteria outlined above in Section 7.3.3: I consider as transition galaxies those with $\log(\mathrm{sSFR}/\mathrm{yr}^{-1}) > -12$ and below the $-1\sigma$ with respect to the fitting line and computed their fraction with respect to the population of galaxies with $\log(\mathrm{sSFR}/\mathrm{yr}^{-1}) > -12$.

The fractions are reported in the last two lines of Table 7.3, with the same meaning of

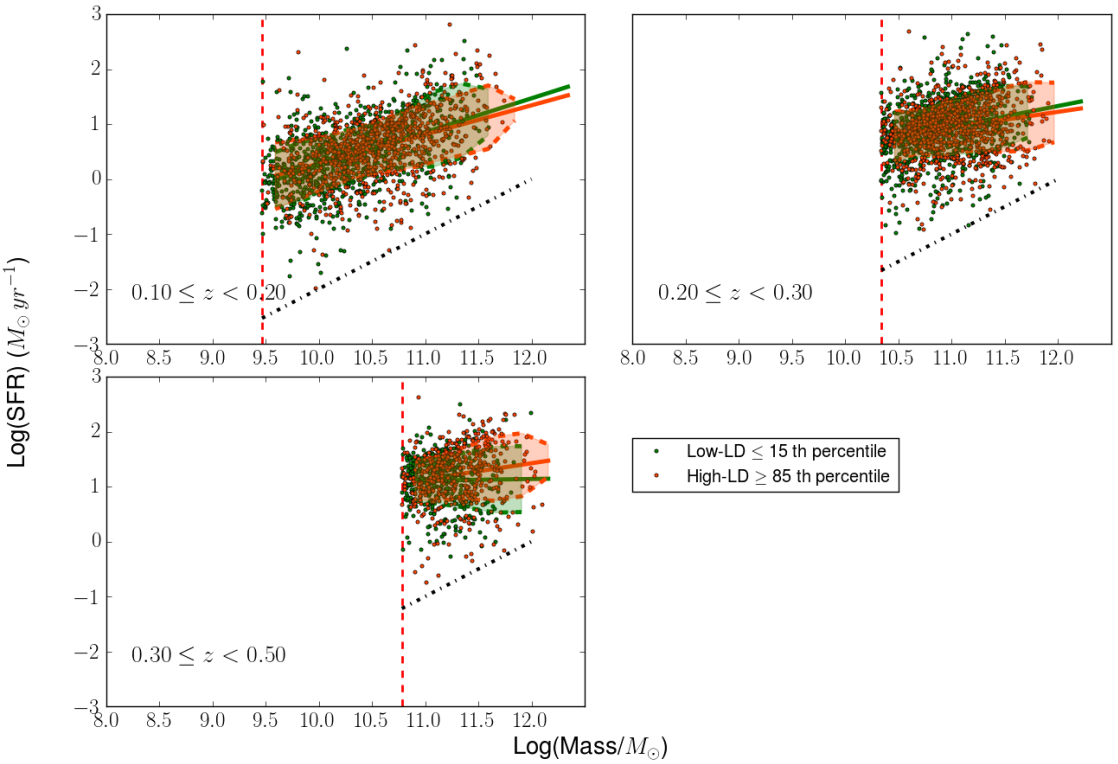


Figure 7.24: SFR-mass relation for galaxies in two bins of LD, corresponding to the wings of the LD histograms shown in figure 7.5. The percentiles used as reference values for separating the two LD subsamples are written in the legend. The three panels refer to different redshift bins, as indicated inside each panel. The vertical line show the stellar mass limit at each redshift. The green and orange lines are the fits to the sSFR-mass relations, and the shaded areas correspond to $1\sigma$ errors on the fitting line. The fraction of galaxies in transition in any of the environments is computed as the fraction of galaxies located below the lower $1\sigma$ line with respect to the total number of galaxies in the considered bin of LD.

the fractions computed in global environment. All the fractions are compatible within the error bars: no dependence with LD is resulting in the fraction of transition galaxies in any of the redshift bins, and no evolution with redshift is present when fixing the LD (according to the number in parenthesis, which refer to the same stellar mass limit).

### 7.4.3 Summary

In this chapter, I have conducted a study on the stellar population and star formation properties of galaxies in the range $0.1 \leq z \leq 0.5$, by making use of two definitions of environment. When considering the *global* environment, I divided galaxies into G&C virial and outer members and the field. I considered also the G&C of different X-ray

luminosity and their belonging to a supercluster. When considering the *local* environment, I characterised galaxy properties as a function of the LD.

The main observables I considered for investigating galaxy properties in different environments are the fraction of star forming/blue galaxies, the correlation between the SFR and the stellar mass, the LW-age, the stellar mass assembly and star formation history as a function of stellar mass.

First, I analysed the fraction of star forming and blue galaxies, defined on the basis of the sSFR and colour, respectively. With respect to the *global* environment, G&C virial members reveal a deficiency of star forming/blue galaxies with respect to all other environments at all redshifts, while field galaxies are the most star forming/blue population at all redshifts. Outer members revealed intermediate fractions at $0.1 \leq z < 0.2$ and rising up to field values at $z > 0.2$. Furthermore, neither the X-ray luminosity of G&C nor their eventual belonging to superclusters are found to drive the suppression of the fractions registered in the virial component or the enhancement in the outer members population.

In the literature, the environmental dependence of the galaxy fractions was previously investigated by e.g. Iovino et al. (2010), who analysed a sample of galaxies in groups and in the field at intermediate redshift in the range $0.25 \leq z \leq 1.0$. They found that the fraction of blue galaxies is systematically higher in the field than in groups in the entire redshift range, and that the fractions decrease with increasing absolute magnitude and stellar mass. At slightly higher redshift in the context of the GCLASS survey ($0.85 \leq z \leq 1.20$), Muzzin et al. (2012) studied the star forming fraction, the SFR and sSFR in clusters and in the field. In the perspective of trying to disentangle the mass and environment effects, they found that the mean SFR, sSFR and star forming fraction are mass dependent keeping fixed the environment, and are always higher in field galaxies compared to clusters. Furthermore, when subdividing the cluster environment according to the cluster centric distance, the number of star forming galaxies is the highest in the field at all stellar masses, and progressively decreases going from the outskirts to the central regions of clusters. In particular, galaxies in the external regions of clusters (located at distances $R > 700$ kpc from the cluster centre) behave similarly to the field, especially in the lowest stellar mass bin ($M < 10^{10} M_{\odot}$) and galaxies in the core of clusters have the lowest fraction of star forming galaxies at the highest stellar masses compared to the other samples, especially at $M \geq 10^{10} M_{\odot}$.

With respect to the *local* environment, I find a monotonically decreasing fraction of star forming/blue galaxies with increasing LD, at all redshift. Overall, the decrement with increasing LD is steeper in the blue population than in the star forming one from $z = 0.1$ up to $z = 0.3$, while more fluctuations in the sample are present at higher redshift. Furthermore, similarly to the *global* environment, when high mass galaxies are considered in the mass limited sample, i.e. at $z > 0.2$, the trends with LD deteriorate.

At $z < 0.2$, many studies show a lower SFR or sSFR in denser regions compared to less dense, field-like environments for all galaxies (see e.g. Balogh et al. 2004; Kauffmann et al. 2004; Baldry et al. 2006), which are in agreement with the results presented in this thesis.

The effect of *local* environment on galaxy properties was also exploited in the COSMOS field up to $z \sim 3$ in Darvish et al. (2016), who found evidences of an environmental de-

pendent SFR and sSFR up to z∼1. The SFR and sSFR are decreasing with the local galaxy overdensity up to redshift one, and is particularly pronounced at the lowest redshifts (0.1≤z<0.5), those of interests for this thesis. Furthermore, the authors suggest that environmental and mass quenching are interconnected and influence each other at z<1: in fact, denser environments more efficiently quench galaxies with higher masses ($\log(M/M_{\odot}) > 10.7$), possibly due to a higher merger rate of massive galaxies in denser environments, and, correspondingly, mass quenching is more efficient in denser regions.

The framing of the environmental-dependent contribution of star forming and blue galaxies raised the question of whether the shutdown of the star formation activity in G&C is a sharp process, leading to the sudden relocation of galaxies from the main sequence of star formation down to the quenched regime. In order to address this aspect, I searched for the presence of galaxies in a transition phase of star formation, i.e. galaxies with reduced star formation activity. The results indicate that G&C virial members hold the highest fraction of galaxies in transition compared to other environments, at all redshifts. Furthermore, at intermediate redshift, only (NS)G&C host a significant number of transition galaxies and in (S)G&C the fraction is less than a half compared to the (NS) population. Again no correlation was found with X-ray luminosity and, interestingly, no increase in the fraction of transition galaxies is found towards the G&C centre (at $r<0.6r_{200}$). Field galaxies show the lowest contribution of galaxies in transition at all redshifts, suggesting that the phenomenon is much more efficient in G&C. Finally, the contribution of the transition population varies with redshift in outer members: at z>0.3, the fractional contribution of transition galaxies to the whole star forming population is comparable to virial members, and is found to be mostly related to high fractions of galaxies in transition within superclusters, while at lower redshifts the fraction drops to values typical of field galaxies.

So far, the results obtained revealed that not only galaxies in the virial regions of G&C have less star forming galaxies compared to galaxies in G&C outskirts and in the field, but also that on average, nearly one third of star forming galaxies among virial members have reduced star formation rates, while the average value in field galaxies is lower than one fifth at all redshifts.

In the *local* density parametrisation of the environment, no differences appear in the population of galaxies in transition within the overall star forming population, computed in two extreme LD regimes and in any of the redshift bins. Furthermore, the fit to the SFR-mass relation is compatible in the different regimes of LD within the error bars. This invariance emerging when the LD is considered should not be confused with the clear evidence that the fraction of galaxies that are star forming depends quite strongly on the same environmental measure. This result is consistent with other results in the literature showing that the LD mostly changes the fraction of passive galaxies but has little effect on the SFR-mass relation (Poggianti et al. 2006; Peng et al. 2010; Wijesinghe et al. 2012, but see Popesso et al. 2011 at high z). Conversely, the concurrence of the dependence of the fraction of star forming galaxies on the global environment together with the presence of a non-negligible amount of galaxies with a reduced star formation activity compared to galaxies of similar mass in the main sequence point in the direction

of slow environmental quenching processes leading to the formation of passive galaxies. Evidently, the two parametrisations are able to probe different physical conditions for galaxies, determining different timescales in the star formation process and quenching timescales.

I proceeded the analysis by inspecting the LW-age of galaxies in the sample, as an indicator of the epoch of the last burst of star formation in galaxies. I found mild differences in the LW-age mass relation of the whole population of galaxies in different environments, with G&C virial members having slightly higher LW-ages at all masses up to z=0.3 and up to $\log(M/M_{\odot})$=11.3 at z>0.3. When isolating star forming and passive galaxies some environmental trends emerge: G&C virial members present a population of higher LW-age galaxies with respect to other environments in the star forming population up to z=0.3, at masses $\log(M/M_{\odot}) \lesssim 10.5$ at $0.1 \leq z < 0.2$ and $\log(M/M_{\odot}) \lesssim 11.5$ at $0.2 \leq z < 0.3$. At $z > 0.3$, the presence of a recently quenched population among virial members is visible at high masses $M > 10^{11} M_{\odot}$, with an enhanced LW-age of star-forming galaxies and a younger LW-age of passive galaxies.

Results on the mass assembly and star formation history of galaxies show instead a weak dependence on environment, at least as far as the formation of the bulk of star is concerned. Indeed, the highest rate of star and thus mass formation occurred more than 6 Gyr before the epoch of observation of the galaxy, and increased with stellar mass. Opposite trends with stellar mass but still weak environmental dependences are found from 0.6 to 5.6 Gyr, and in more recent epochs the dependence with stellar mass also degenerates. Environment comes into play at ages from 0.6-5.6 Gyr, where high mass G&C galaxies have accelerated rates of star formation compared to field galaxies, which in turn have still active SF in the last 20 Myr, where the star formation activity of G&C galaxies becomes negligible.

# 8 Conclusions

Throughout this thesis I aimed at making the most of the potential offered by the XXL Survey of X-ray groups and clusters from low to intermediate redshift to address one of the most puzzling questions in astrophysics: the role of environment in galaxy evolution.

The XXL Survey (Pierre et al. 2016) observed more than 360 extended X-ray sources identified as groups and clusters (G&C), which are spectroscopically confirmed and cover a broad range of halo masses ($1.24 \times 10^{13} \leq M_{500,scal}(M_{\odot}) \leq 6.63 \times 10^{14}$) and X-ray luminosities ($2.27 \times 10^{41} \leq L^{XXL}_{500,scal}(erg\,s^{-1}) \leq 2.15 \times 10^{44}$). The great advantage of XXL is that the XXL-North field is fully covered by photometric observations from the CFHT Legacy Survey (Veillet 2007, CFHTLS) Wide1 (W1) T0007 data release and spectroscopic observations coming from a wide variety of programmes, mainly GAMA, SDSS, VIPERS and XXL dedicated spectroscopic campaigns. Despite the unprecedented combination of multi-wavelength information linking X-ray G&C with the embedded and surrounding galaxy population, spectroscopic and photometric catalogues were still raw and unexplored.

*The first essential task of this work was the creation of a homogeneous spectrophotometric catalogue of galaxies providing all quantities necessary for pursuing many outstanding scientific questions.*

The main stages I went through during this phase are presented in Chapters 3 and 4. The superposition of different spectroscopic surveys in fact led to the presence of multiple observations of the same source. I identified and removed the duplicates by selecting those with the best spectral quality and redshift measurement reliability. I then matched this 'clean' spectroscopic catalogue with photometric and photo-z information coming mainly from the CFHTLS Survey and complemented with other photometric data in order to maximise the number of spectra finally used. The build up of the final spectrophotometric catalogue proceeded with the spectroscopic membership assignment by taking advantage of virial masses, radii and velocity dispersions of X-ray G&C. I computed the spectroscopic completeness of the sample as a function of $r$-band observed magnitude in different position in the sky in order to account for completeness variation arising from the contribution of different surveys. This analysis allowed me to set the observed magnitude

completeness limit of the analysis to $r$=20.0, and compute the corresponding stellar mass completeness limit of the sample as a function of redshift (ranging from $\log(M/M_{\odot})$=9.6 at z=0.1 to $\log(M/M_{\odot})$=11.0 at z=0.6).
The spectrophotometric catalogue was then employed to derive stellar masses and absolute magnitudes through the SED fitting code LePhare (Arnouts et al. 1999; Ilbert et al. 2006). Altogether, the quantities derived enabled to address the scientific questions tackled during in this work.
*The first scientific achievement of this thesis is the systematic study of the dependence of the Galaxy Stellar Mass Function (GSMF) on environment.*
This is one of the first systematic studies of the GSMF in X-ray extended sources ranging from the group to the cluster environment, and the results are published in the second part of Guglielmo et al. (2017). After having validated the method used for computing the GSMF by comparing with literature results, I could establish its dependence on *global* environment, namely field versus X-ray G&C, and among G&C as a function of X-ray luminosity.
I considered galaxies in four redshift bins and compared the shape of the GSMF in different environments by analysing the parameters resulting from Schechter fits. I found weak dependence on the environment, even when high- and low- X-ray luminosity regimes were contrasted. This result is further confirmed by the invariance in the dependence of the mean stellar mass of members galaxies on X-ray luminosity. I also looked into the evolution of the mass assembly in the *general field* (field+G&C) from z=0.6 down to z=0.1, finding that the high mass end is already in place at the oldest epoch and does not evolve and detecting an increase in the low-mass galaxy population with decreasing redshift. These findings led to the conclusion that galaxies with masses above the stellar mass completeness limit already assembled the bulk of their stellar mass before environmental influences became effective.
The aforementioned results motivate the second main aspect considered in this thesis: the role of the environment in shutting off the star formation activity of galaxies and the subsequent transformations in the observed properties of galaxy stellar populations.
*Given the complexity of this topic, it stands to reason to focus the attention on the study of a newly discovered supercluster within XXL at z∼0.3.*
XLSSsC N01 is the richest XXL supercluster, it is located at z∼0.3 and composed of 14 G&C. It is worth mentioning that this is one of the first studies on the properties of stellar populations and star formation activity in a supercluster entirely composed of X-ray groups and cluster at intermediate redshift. I characterised the galaxy population surrounding the supercluster and I assigned galaxies to different environments based on a combination of *global* and *local* environment definitions in order to probe the whole range of environmental conditions a galaxy could experience in the regions. The analysis on the properties of galaxies followed two different channels: star formation properties and galaxy rest-frame colour.
In Chapter 6 I used the full spectral fitting code SINOPSIS (SImulatiNg OPtical Spectra wIth Stellar population models, Fritz et al. 2007, 2011, 2017) to derive the current SFR, the star formation and mass assembly history in four look-back epochs, and the luminosity-

weighted(LW)-age.
The effect of the supercluster environment on galaxies is visible when looking at the fraction of star forming and blue galaxies. Indeed, in the virial regions of G&C the fraction of star forming/blue galaxies is lower than in all other environments. Conversely, galaxies in the outskirts have enhanced star formation activity compared to virial members, leading to a fraction of star forming galaxies which is even higher than filaments and field galaxies. In the stellar mass complete regime, which selects only high mass galaxies ($\log(M/M_{\odot}) > 10.78$), the number of star forming and blue galaxies lowers in all environments, and environmental dependences become hard to detect. This result confirms the *downsizing* scenario for the evolution of massive galaxies. I have also investigated the sSFR-mass relation in the mass complete regime, and computed the number of galaxies in transition between the star formation main sequence and the quenched population, finding no difference among galaxies in the field, filaments, and G&C. The fact that the sSFR-mass relation does not show any dependence on environment while the fraction of star forming galaxies does, points towards the direction of a fast quenching mechanisms acting in this rich supercluster and leading to the formation of a passive population without any evidence of transition. Finally, evidence of a recent episode of environmental quenching of the star formation is found in the stellar ages of passive galaxies in the virialised regions of X-ray structures.
*The final stage and goal of this thesis is to complete the analysis on star formation and observed stellar properties in the whole sample of galaxies in the XXL-N field in three redshift bins from $0.1 \leq z \leq 0.5$.*
This objective is addressed in Chapter 7. The larger sample statistics allowed me to explore the impact of adopting different definitions of environment on the derived environmental trends. In the first part I considered the *global* environment, and further divided the sample of groups and clusters in two classes of X-ray luminosity and according to their membership to superclusters.
The imprint of the *global* environment on galaxies is twofold. First, the fraction of star forming/blue galaxies presents the lowest value in G&C virial members, at all redshifts and with respect to all other environments, while field galaxies are the most star forming/blue population at all redshifts. Outer members revealed intermediate fractions at $0.1 \leq z < 0.2$ and rising up to field values at $z > 0.2$. Neither the X-ray luminosity of G&C nor their eventual belonging to superclusters are found to drive the suppression of the fractions registered in the virial component or the enhancement in the outer members population. Second, the SFR-mass relation is also environment dependent, and in particular the number of galaxies having reduced SFR (galaxies in transition) increases in the virial regions of G&C with respect to the field at all redshifts, and is maintained nearly constant across epochs. Again, outer members show intermediate properties: the fraction of galaxies in transition is similar to the virial population at $z > 0.3$, when it is found to be associated to the supercluster environment, and then reduces to values typical of field galaxies at $0.1 \leq z < 0.3$. Interestingly, the peculiarity of superclusters at $0.2 \leq z < 0.3$, where also XLSSsC N01 supercluster is located, emerges. Indeed, at these redshifts the fraction of transition galaxies in superclusters is the lowest, and is less than a half of the values found

in other groups and clusters in the range both in the virial regions and in the outskirts.
The *local* environment presents substantial differences. The star forming and blue fraction are found to depend on the local density (LD) with a monotonous decrement with increasing LD at all redshifts. In contrast, the fraction of galaxies in transition at low-LD is comparable to that of field galaxies in the global environment definition. No dependence is found with increasing LD.
This dicothomy emerging in the galaxy properties when investigated in either a *global* or a *local* environment framework are intrinsically related to the different physical meaning of the two parametrisations. The potential well of X-ray groups and clusters must enhance physical processes related to the presence of the potential well of the dark matter halo and the hot intra cluster medium on one side, whereas high-LD regions select associations of galaxies which are physically close thus more prone to interactions and encounters with other galaxies.

# Future perspectives

Inserted in the context of XXL, this thesis provides important insights on the connection between the build-up and evolution of galaxy properties and environment in a fundamental epoch for the building of the stellar mass in G&C. However, several aspects should be further analysed in order to acquire a more general understanding of the physical phenomena related to environment.
In the context of GSMF, the complete GAMA data release on the field covered also by the XXL survey (G02) has just been performed in Baldry et al. (2018), and I plan to pursue the collaboration with this team to perform a direct comparison with their results on this topic. Furthermore, I recently started to collaborate for comparing our results on the GSMF with the HSC data (Aihara et al. 2017) in the highest redshift bins sampled in Chapter 5.
A natural follow-up of the analysis presented in this thesis is the full investigation of spectral properties of galaxies as a function of LD, following the footsteps of the *global* environment analysis. Combining together the huge amount of information that can be recovered from galaxy spectra and photometry is fundamental for the determination of the quenching timescales and thus the main physical processes responsible for the process. Detailed analysis on the presence of a population of post-starburst galaxies, i.e. galaxies that have recently turned passive, would also shed light on the preferred channel leading to the build up of the passive population in different environments. Furthermore, the availability of a consistent sample of superclusters would open a window for the systematic study of the incidence of this population in these structures and, more in general, to the investigation of the evolution of galaxies of these large scale systems.
Moreover, the availability of full spectral fitting results enables to explore a complementary approach, by tracing the stellar history of each individual galaxy, and investigate how the star formation history proceeded in X-ray groups and clusters, in the field and in high-/low- local enhancements of the density of galaxies. This technique was already employed

in Guglielmo et al. (2015) in a low-redshift sample of galaxies in clusters and in the field, which would also allow the comparison with the local universe population.
Finally, to complement the scenario, I aim at comparing observations with simulations. This project would open a completely new branch with respect to what has been performed in this thesis, and in this respect we are starting to collaborate with two groups of simulations: the EAGLE project (Schaye et al. 2015, and in particular e.g. Katsianis et al. 2017 on the comparison between observations and predictions on the evolution of the SFR), and the IllustrisTNG simulations (Pillepich et al. 2018).

# Acronyms

**BCG** Brightest Central Galaxy
**CMD** Color-Magnitude Diagram
**EW** Equivalent Width
**FoF** Friend-of-Friend
**G&C** Group and Cluster
**GSMF** Galaxy Stellar Mass Function
**ICM** Intra Cluster Medium
**IMF** Initial Mass Function
**ISM** InterStellar Medium
**KS** Kolmogorov-Smirnov
**LD** Local density
**LW-age** Luminosity-Weighted age
**MDR** Morphology-Density Relation
**ML** Maximum-Likelihood
**MW-age** Mass-Weighted age
**(NS)** G&C Not belonging to a Supercluster
**PDF** Probability Distribution Function
**PSF** Point Spread Function
**Q.E.** Quenching Efficiency
**(S)** G&C belonging to a Supercluster
**SED** Spectral Energy Distribution
**SINOPSIS** SImulatiNg OPtical Spectra wIth Stellar population models
**SFH** Star Formation History
**SFR** Star Formation Rate
**SNR** Signal to Noise Ratio
**SR** Sampling Rate
**SSP** Single Stellar Population
**sSFR** Specific Star Formation Rate

*Commonly used surveys*
**XXL-N** XXL North field
**XXL-S** XXL South field
**GAMA** Galaxy And Mass Assembly (survey)
**CFHTLS** CFHT (Canada-France-Hawaii Telescope) Legacy Survey
**SDSS** Sloan Digital Sky Survey
**VIPERS** VIMOS Public Extragalactic Redshift Survey

# Appendix

Monthly Notices
of the
ROYAL ASTRONOMICAL SOCIETY
MNRAS **450,** 2749–2763 (2015) doi:10.1093/mnras/stv757

# The star formation history of galaxies: the role of galaxy mass, morphology and environment

Valentina Guglielmo,[1,2]★ Bianca M. Poggianti,[1] Alessia Moretti,[1,2] Jacopo Fritz,[3,4] Rosa Calvi,[5] Benedetta Vulcani,[6] Giovanni Fasano[1] and Angela Paccagnella[2]

[1]*INAF-Astronomical Observatory of Padova, I-35122 Padova, Italy*
[2]*Department of Physics and Astronomy, University of Padova, I-35122 Padova, Italy*
[3]*Sterrenkundig Observatorium Vakgroep Fysica en Sterrenkunde Universiteit Gent, B-S9 9000 Gent, Belgium*
[4]*Centro de Radioastronomía y Astrofísica, CRyA, UNAM, Campus Morelia, A.P. 3-72, C.P. 58089, Michoacán, Mexico*
[5]*Instituto de Astrofisica de Canarias, Departamento de Astrofisica, Universidad de La Laguna, E-38200 La Laguna, Spain*
[6]*Kavli Institute for the Physics and Mathematics of the Universe (WPI), The University of Tokyo Institutes for Advanced Study (UTIAS), the University of Tokyo, Kashiwa, 277-8582, Japan*

Accepted 2015 April 2. Received 2015 March 20; in original form 2015 January 8



**ABSTRACT**

We analyse the star formation history (SFH) of galaxies as a function of present-day environment, galaxy stellar mass and morphology. The SFH is derived by means of a non-parametric spectrophotometric model applied to individual galaxies at $z \sim 0.04$–$0.1$ in the WIde-field Nearby Galaxy-cluster Survey (WINGS) clusters and the Padova Millennium Galaxy and Group Catalogue (PM2GC) field. The field reconstructed evolution of the star formation rate density (SFRD) follows the values observed at each redshift, except at $z > 2$, where our estimate is $\sim$1.7 $\times$ higher than the high-$z$ observed value. The slope of the SFRD decline with time gets progressively steeper going from low-mass to high-mass haloes. The decrease of the SFRD since $z = 2$ is due to (1) quenching – 50 per cent of the SFRD in the field and 75 per cent in clusters at $z > 2$ originated in galaxies that are passive today – and (2) the fact that the average SFR of today's star-forming galaxies has decreased with time. We quantify the contribution to the SFRD($z$) of galaxies of today's different masses and morphologies. The current morphology correlates with the current star formation activity but is irrelevant for the past stellar history. The average SFH depends on galaxy mass, but galaxies of a given mass have different histories depending on their environment. We conclude that the variation of the SFRD($z$) with environment is not driven by different distributions of galaxy masses and morphologies in clusters and field, and must be due to an accelerated formation in high-mass haloes compared to low-mass ones even for galaxies that will end up having the same galaxy mass today.

**Key words:** galaxies: clusters: general – galaxies: evolution – galaxies: formation – galaxies: star formation.

## 1 INTRODUCTION

In the quest to understand when galaxies formed their stars and assembled their mass, two complementary observational techniques can be employed: direct observations of galaxies at different redshifts, and reconstruction of the previous galaxy history from fossil records at a given epoch. The main advantage of the first method is that measuring the current star formation is less uncertain than estimating the past history, especially in galaxies in which the light of young stars outshines the older population, in particular at high redshift (Papovich, Dickinson & Ferguson 2001; Zibetti, Charlot & Rix 2009; Conroy 2013). On the other hand, the second method has the benefit of tracing the evolution of each individual galaxy, without having to infer histories in a statistical sense with the problems involved in the identification of progenitors and descendants. Both methods heavily rely on spectrophotometric modelling, to calibrate the star formation rate (SFR) indicators and derive the star formation histories (SFHs), and are affected by the choice of the initial mass function (IMF).

On a cosmic scale, the collection of the star formation rate density (SFRD) measurements at different cosmic times (from $z = 8$ to 0) give us an indication on the summa of the SFH of the Universe (Madau et al. 1996; Lilly et al. 1996; Hopkins & Beacom 2006;

★ E-mail: valentina.guglielmo@oapd.inaf.it

Karim et al. 2011, (radio); Burgarella et al. 2013, (FIR+UV); Sobral et al. 2013, (H-alpha); Bouwens et al. 2014, (UV); Madau & Dickinson 2014, MD14).

It has emerged that the SFRD of the cosmos peaks at $z \sim 2$, following a rise after the big bang and before falling by a factor about 10 to the current value. This picture is now well established, though large uncertainties still exist at high redshifts. The SFRD($z$) has important implications for the reionization of the Universe, the cosmic chemical evolution, the transformation of gas into stars and the build-up of stellar mass.

Ideally, however, one would want to go beyond the description of cosmic global history, and trace galaxy evolution on a galaxy-by-galaxy basis to understand the physical processes driving it. In this respect, great progress has been made by surveys at different redshifts that have established the existence of a strong dependence of galaxy histories on galaxy stellar mass. On average, more massive galaxies have formed their stars and completed their star formation activity at higher $z$ than less massive galaxies (the so-called downsizing effect, Cowie et al. 1996; Gavazzi et al. 2006; De Lucia et al. 2007; Sánchez-Blázquez et al. 2009). The existence of relations between SFR and galaxy stellar mass (SFR–Mass) and specific star formation rate and mass (sSFR = SFR/Mass) have been established from $z = 0$ out to $z > 2$ (Brinchmann et al. 2004; Daddi et al. 2007; Noeske et al. 2007; Salim et al. 2007; Rodighiero et al. 2011; Whitaker et al. 2012; Sobral et al. 2014; Speagle et al. 2014), and many other galaxy properties have been found to be correlated with galaxy mass. Furthermore, a number of works have pointed out that galaxy properties are even more strongly correlated with a combination of galaxy mass and galaxy 'size', arguing for velocity dispersion (Bernardi et al. 2003; Franx et al. 2008; Smith, Lucey & Hudson 2009; Wake, van Dokkum & Franx 2012) or galaxy surface mass density (Brinchmann et al. 2004; Kauffmann et al. 2006) as principal drivers. The exact origin of these trends is still unknown, but evidence has accumulated for a dependence of galaxy stellar population ages on galaxy sizes at fixed mass (van der Wel et al. 2009; Cappellari et al. 2012; Poggianti et al. 2013), suggesting that also galaxy structure, and not just stellar mass, is relevant. In a recent paper, Omand, Balogh & Poggianti (2014) argue that the observed correlation of the quenched fraction with $M/R^{1.5}$ is related to the dominance of the bulge component with respect to the disc, suggesting it might ultimately be linked with galaxy morphology (see also Driver et al. 2013). Even the sSFR–Mass relation might be due to the increase of the bulge mass fractions with galaxy stellar mass, as the ratio of SFR and stellar mass of the galaxy disc is virtually independent of total stellar mass (Abramson et al. 2014).

On the other hand, galaxy stellar population properties have been known to vary strongly with galaxy environment (Spitzer & Baade 1951; Oemler 1974; Davis & Geller 1976; Dressler 1980). Galaxy clusters have seen an evolution in their blue galaxy fractions that is even stronger than in the field, and the evolution from blue star-forming to red passive takes place sooner in dense environments and massive haloes (Wilman et al. 2005; Cooper et al. 2006; Cucciati et al. 2006; Poggianti et al. 2006; Iovino et al. 2010). Whether this environmental dependence is simply due to different galaxy mass distributions and/or morphological distributions with environment, or it reflects a stellar history that differs with environment at a given mass, is still a matter of debate (Thomas et al. 2005, 2010; Baldry et al. 2006; Peng et al. 2010, 2012; Poggianti et al. 2013). On a global scale, the evolution of the SFRD in different environments at low redshift is not yet known, though the evolution of the blue galaxy fractions suggests a steeper decline in clusters than in the field (Kodama & Bower 2001). The contribution of haloes of different masses to the SFRD($z$) has been recently quantified by Popesso et al. (2014a,b), who argue that the process of structure formation, and the associated quenching processes, play an important role in the drop of the SFRD($z$) since $z = 1$. Overall, several lines of evidence suggest that both galaxy mass and environment play a role, with environment being more relevant for lower mass galaxies, at least as far as quenching is concerned (Haines et al. 2007; Cooper et al. 2010; Pasquali et al. 2010; Peng et al. 2010, 2012; McGee et al. 2011; Sobral et al. 2011; Muzzin et al. 2012; Smith et al. 2012; Wetzel, Tinker & Conroy 2012; La Barbera et al. 2014; Lin et al. 2014; Vulcani et al. 2015). However, while it is well established that the relative incidence of star-forming and passive galaxies changes with environment, it is still debated whether environment matters for the whole galaxy stellar history, or it only causes it to end leading to quenching at some point.

Turning to the reconstruction of galaxy SFHs from fossil records, this reaches high levels of precision in galaxies with resolved stellar populations, such as our Milky Way and the Local Group. Going to more distant galaxies, it has to rely on the interpretation of the galaxy integrated spectrum, and is limited by our capability to discriminate between stars of different ages from the spectrum they emit. Spectrophotometric models capable of extracting SFHs from integrated spectra have been built by a number of groups: Heavens, Jimenez & Lahav (2000; MOPED), Cid-Fernandes et al. (2004; STARLIGHT), Ocvirk et al. (2006a,b; STECMAP), Fritz et al. (2007; now called SINOPSIS), MacArthur, González & Courteau 2009, Koleva et al. (2009; ULyss), Tojeiro et al. (2007; VESPA) and others (see sedfitting.org/SED08). They have been applied to reconstruct the SFH of galaxies in large surveys (e.g. Panter et al. 2007 and Tojeiro et al. 2009 on Sloan Digital Sky Survey (SDSS); Fritz et al. 2011 on WINGS), and to study these histories for galaxy subsets of special interest (e.g. Tojeiro et al. 2013; Vulcani et al. 2015). Two studies in particular (Heavens et al. 2004; Panter et al. 2007) derived the cosmic SFH from SDSS spectra, and were successful in reproducing the SFRD($z$) and the downsizing effect.

In this work, we make use of a non-parametric spectrophotometric model to derive the past history of star formation in five broad bins of age from integrated spectra of galaxies in clusters and the field and, within the field, in groups and lower mass haloes. Searching for the origin of the overall decline observed in the SFRD($z$) since $z = 2$, we also consider present-day star-forming galaxies separately from the rest, and quantify the relative role of their decline in star formation and that of galaxies that have been quenched. Our goal is to shed light on the history of galaxies of different masses and morphologies, and isolate any residual environmental trend. We stress that we look for SFH trends with galaxy parameters *today*, that is as a function of the mass, morphology and environment that galaxies have at low redshift, when the spectra we use to derive their past stellar history are taken.

The outline of the paper is as follows: in Section 2, we describe the data sets used, and in Section 3 the methods for assigning galaxy morphology and the spectrophotometric model used for galaxy stellar masses and SFHs. Section 4 presents our results: in 4.1, the SFRD of the field sample is compared with recent observational measurements at different redshifts; in 4.2, we study the SFRD in different environments; in 4.3, we analyse the SFH of star-forming galaxies both in the field and in clusters; in 4.4, the contribution of galaxies of different mass and morphological type to the total SFRD; and in 4.5, we present a global picture which considers the mean SFH of galaxies in different environments, with the same stellar mass but different morphology. Finally, we summarize our findings in Section 5.

The IMF adopted is a Salpeter one in the mass range 0.1–100 $M_\odot$ (Salpeter 1955), and the cosmological constants assumed are $\Omega_m = 0.3$, $\Omega_\Lambda = 0.7$, $H_0 = 70\,km\,s^{-1}\,Mpc^{-1}$.

## 2 DATASET

### 2.1 PM2GC

The *Padova Millennium Galaxy and Group Catalogue* (Calvi, Poggianti & Vulcani 2011) is a data base built on the basis of the Millennium Galaxy Catalogue (MGC), a deep and wide B-imaging survey along an equatorial strip of ∼38 deg$^2$ obtained with the Isaac Newton Telescope (INT). The final catalogue is restricted to galaxies brighter than $M_B = -18.7$ with a spectroscopic redshift in the range $0.03 \leq z \leq 0.11$, taken from the MGCz catalogue, the spectroscopic extension of the MGC, that has a 96 per cent spectroscopic completeness at these magnitudes (Driver et al. 2005). Most of the MGCz spectra of our sample come from the SDSS (Abazajian et al. 2003, ∼2.5 Å resolution) and the remaining ones from the 2dF Galaxy Redshift Survey (2dFGRS) (Colless et al. 2001) and the 2dF follow-up obtained by the MGC team (Driver et al. 2005), with a 2dF resolution of 9 Å full width at half-maximum (FWHM). The fibre diameters are 3 arcsec for the SDSS and 2.16 arcsec for the 2dF setup, corresponding to the inner 1.3 to 6 kpc of the galaxies. The PM2GC galaxy stellar mass completeness limit was computed as the mass of the reddest $M_B = -18.7$ galaxy ($B - V = 0.9$) at our redshift upper limit ($z = 0.1$), and it is equal to $\mathrm{Log}M_\star/M_\odot = 10.44$. The comoving volume of the PM2GC survey is 361 424 $h^{-3}$ Mpc$^3$.

The image quality and the spectroscopic completeness of the PM2GC are superior to SDSS, and these qualities result in more robust morphological classifications and better sampling of dense regions. In particular, the MGC is based on INT data (2.5 m telescope) obtained with a median seeing of 1.3 arcsec and at least 750 s of exposure, with a pixel scale of 0.333 arcsec pixel$^{-1}$, while the SDSS (again, 2.5 m telescope) has a median seeing of 1.5 arcsec in g (the closest band to the PM2GC), an exposure time of 54.1 s and 0.396 arcsec pixel$^{-1}$. As for spectroscopic completeneness, 14 per cent of all PM2GC galaxies do not have an SDSS spectrum, and the SDSS incompleteness is particularly severe in dense regions such as groups. Moreover, the PM2GC data are very comparable in quality to our cluster sample (WINGS) and the two samples have been analysed in a homogenous way with the same tools.

The characterization of the environment of the galaxies was conducted by means of a friends-of-friends (FoF) algorithm. The methods and the presentation of the catalogues are described in Calvi et al. (2011). Briefly, a catalogue of 176 groups of galaxies with at least three members was built in the redshift range $0.04 \leq z \leq 0.1$, containing 43 per cent of the total general field population at these redshifts. The mean redshift and velocity dispersion $\sigma$ of the groups are, respectively, 0.0823 and 192 km s$^{-1}$. 88 per cent of the selected groups are composed by less than 10 members, and 63 per cent by less than 5 members. Galaxies were assigned to a group if they were within $3\sigma$ from the group redshift and 1.5 $R_{200}$ from the group geometrical centre. We define as $R_{200}$ the radius of the sphere inside which the mean density is a factor 200× the critical density of the Universe at that redshift. This parameter gives an approximation of the virial radius of a cluster or group and for our structures it is computed from the velocity dispersions using the formula (Finn et al. 2005):

$$R_{200} = 1.73 \frac{\sigma}{1000\ (\mathrm{km\,s^{-1}})} \frac{1}{\sqrt{\Omega_\Lambda + \Omega_0 (1+z)^3}}\ h^{-1}\ (\mathrm{Mpc}) \qquad (1)$$

with $\sigma$ the group velocity dispersion and $z$ its mean redshift.

**Table 1.** List of the number of galaxies in different environments in the PM2GC sample.

| Environment | Number of galaxies |
|---|---|
| Groups | 1033 |
| Single | 1123 |
| Binary | 486 |
| Mixed sample | 517 |
| General field | 3159 |

Galaxies that do not satisfy the group membership criteria have been placed either in the catalogue of single field galaxies, that comprises the isolated galaxies, or in the catalogue of binary field galaxies, which comprises the systems with two galaxies within 1500 km s$^{-1}$ and 0.5 $h^{-1}$ Mpc. Finally, galaxies that were part of the trial groups in the FoF procedure but did not fulfil the final group membership criteria are treated separately as 'Mixed sample'.

All galaxies in the environments described above are collected in the 'general field' sample PM2GC.

The number of galaxies in each sub-environment and in the general field sample are shown in Table 1.

In addition to the identification of PM2GC sub-environments, the masses of the dark matter haloes hosting PM2GC galaxies were estimated by Paccagnella et al. (in preparation) exploiting a mock galaxy catalogue from semianalytic models (De Lucia & Blaizot 2007) run on the Millennium Simulation (Springel et al. 2005), and making use of the already-mentioned FoF algorithm (Calvi et al. 2011), as described in Vulcani et al. (2014). The mass of a dark matter halo associated with a *group* (where in this definition of *group* also singles and binaries are included) is tightly correlated with the total stellar mass of all member galaxies (see e.g. Yang et al. 2007; Yang, Mo & van den Bosch 2008). Applying this method to the PM2GC magnitude limited sample, Paccagnella et al. (in preparation) derived halo masses for 1141 single galaxies, 245 binary systems and 92 groups. In this case not all PM2GC groups are considered but only 92 of the 176 in the complete catalogue, those in which the fraction of interlopers (i.e. the galaxies which are associated with a groups by the FoF algorithm due to projection effects but do not belong physically to them) is less than 30 per cent.

### 2.2 WINGS

The WIde-field Nearby Galaxy-cluster Survey (WINGS; Fasano et al. 2006) is a multiwavelength survey of clusters at $0.04 < z < 0.07$ in the local Universe.

The complete sample contains 76 clusters selected from three X-ray flux limited samples compiled from *ROSAT* All-Sky Survey data (Ebeling et al. 1996, 1998, 2000), covering a wide range in velocity dispersion, $500\,km\,s^{-1} \leqslant \sigma_{cl} \leqslant 1100\,km\,s^{-1}$ and X-ray luminosity, typically 0.2-5 × $10^{44}$ erg s$^{-1}$. The survey is mainly based on optical imaging in $B$ and $V$ bands for all the 76 clusters taken with the Wide Field Camera mounted at the corrected f/3.9 prime focus of the INT-2.5 m in La Palma and from the Wide Field Imager at the 2.2 m MPG/European Southern Observatory telescope in La Silla (Varela et al. 2009). The imaging survey covers a 34 arcmin × 34 arcmin field, and this area corresponds to at least $0.6R_{200}$ for all clusters.[1] In the following analysis, all the cluster members are used regardless of clustercentric distance since the fraction of galaxies that do not satisfy the $0.6R_{200}$ criterion is tiny

[1] $R_{200}$ was computed from the cluster velocity dispersion $\sigma_{cl}$ (in km s$^{-1}$) using equation (1) (Cava et al. 2009).

compared to the entire distribution and does not affect significantly the sample.

The optical imaging was complemented by a spectroscopic survey of a subsample of about 6000 galaxies in 48 of the 76 clusters (Cava et al. 2009). The spectra were taken from August 2002 to October 2004 at the 4.2 m William Herschel Telescope (WHT) using the AF2/WYFFOS multifibre spectrograph (∼6 Å FWHM) and from January 2003 to March 2004 at the 3.9 m Anglo Australian Telescope (AAT) using the 2dF multifibre spectrograph (∼9 Å FWHM) (see Cava et al. 2009 for details). The fibre diameters were 1.6 arcsec and 2.16 arcsec for WHT and AAT, respectively, therefore the spectra cover the central 1.3 to 2.8 kpc of our galaxies depending on the cluster redshift. The spectroscopic selection criteria were only based on $V$ magnitude and $(B-V)$ colour, so to maximize the probability of observing galaxies at the cluster redshift and avoiding the introduction of biases in the sample (Cava et al. 2009). A galaxy is considered a member of the cluster if its spectroscopic redshift lies within $\pm 3\sigma_{\rm cl}$ from the cluster mean redshift.

The WINGS spectroscopic sample is affected by incompleteness. The completeness parameter, that is the ratio of the number of spectra yielding a redshift to the total number of galaxies in the parent photometric catalogue, was computed using the $V$-band magnitude and turned out to be essentially independent from the distance to the centre of the cluster (Cava et al. 2009). In the following, SFRs and stellar mass estimates in WINGS galaxies have always been corrected for incompleteness.

From the $\sigma_{\rm cl}$, by means of the virial theorem, the mass of the dark matter halo in which the cluster resides was calculated as follows (Poggianti et al. 2006)[2]:

$$M_{\rm halo} = 1.2 \times 10^{15} \left( \frac{\sigma}{1000\ ({\rm km\,s^{-1}})} \right)^3 \times \frac{1}{\sqrt{\Omega_\Lambda + \Omega_0 (1+z)^3}}\, h^{-1}\ ({\rm M}_\odot) \quad (2)$$

The latter equation was applied to all WINGS clusters using the velocity dispersions given in Cava et al. (2009) for 32 of the 48 clusters, and for the remaining 16 clusters the most recent data from the OMEGAWINGS spectroscopic catalogue (Moretti et al. in preparation).

To compare different environments, we apply to the WINGS sample the same magnitude cut of the PM2GC. Therefore, in the following, for both WINGS and PM2GC, we use only galaxies brighter than $M_{\rm B} = -18.7$. In WINGS, this leaves 1249 galaxies (∼2608 when corrected for spectroscopic incompleteness). Equally, when considering galaxy mass bins, we will always compare WINGS and PM2GC above the same mass limit ${\rm Log}M_\star/{\rm M}_\odot = 10.44$ (corresponding to $M_{\rm B} = -18.7$). Only for WINGS, with no comparison in PM2GC, we will display results for an additional mass bin, down to the completeness mass limit of WINGS which is ${\rm Log}M_\star/{\rm M}_\odot = 10.0$.

To compute the WINGS volume, for each cluster we have considered the effective area on the sky covered by our data, derived the radius corresponding to this area, converted this radius in Mpc and computed the volume of the corresponding sphere, assuming spherical symmetry. The total volume is the sum of the volumes of all clusters and is approximately 288 $h^{-3}$ Mpc$^3$. In order to convert this volume into the comoving value, it is multiplied for a factor $(1+z)^3 = 1.17$, where $z$ is the median redshift of the survey, $z = 0.055$.

[2] This relation yields reliable mass measurements for clusters, but not for groups where the $\sigma$ is computed from a few redshifts, therefore for the groups we adopted the mass estimate method described in Section 2.1.

## 3 METHODS

### 3.1 Morphologies

All galaxies in both the PM2GC and WINGS samples have been morphologically classified using MORPHOT, an automatic non-parametric tool designed to obtain morphological type estimates of large galaxy samples (Fasano et al. 2007), which has been shown to be able to distinguish between ellipticals and S0 galaxies with unprecedented accuracy. It combines a set of 11 diagnostics, directly and easily computable from the galaxy image and sensitive to some particular morphological characteristic and/or feature of the galaxies. It provides two independent estimates of the morphological type based on: (i) a maximum likelihood technique; (ii) a neural network machine. The final morphological estimator combines the two techniques. The comparison with visual classifications provides an average difference in Hubble type $\Delta T$ ($\leq$0.04) and a scatter ($\leq$1.7) comparable to those among visual classifications of different experienced classifiers.

The classification process has been performed using $B$-band images for PM2GC galaxies and $V$-band images for WINGS (Fasano et al. 2012), after testing that no significant systematic shift in broad morphological classification (ellipticals E, lenticulars S0 or late-types LT) exists between the $V$ and $B$ WINGS images (see Calvi et al., 2012 for more details). The morphological types we will consider are ellipticals, S0s (lenticulars) and late types (any type later than S0s).

### 3.2 SFHs and masses

The SFHs and stellar masses of galaxies in the PM2GC and WINGS samples are derived using a model which is an improved and extended version of the spectrophotometric code developed by Poggianti, Bressan & Franceschini (2001) to derive the SFHs from a galaxy integrated spectrum.

The model and its application to WINGS are fully described in Fritz et al. (2007, 2011, 2014). It is based on a stellar population synthesis technique that reproduces the observed optical galaxy spectra.

The code reproduces the main features of an observed spectrum: the equivalent widths of several lines – both in absorption and in emission – and the fluxes emitted in given bands of the continuum. This model assumes that an observed galactic spectrum is a combination of simple stellar population spectra, and therefore a galaxy model spectrum is computed by adding the synthetic spectra of single stellar populations (SSPs) of different ages.

The model makes use of the Padova evolutionary tracks (Bertelli et al. 1994) with asymptotic giant branch treatment as in Bressan, Granato & Silva (1998), and two different sets of observed stellar libraries: for ages younger than $10^9$ yr Jacoby, Hunter & Christian (1984) was used, while for older SSPs spectra were taken from the MILES library (Sánchez-Blázquez et al. 2006). Both sets were degraded in spectral resolution, in order to match that of the observed spectra. SSP spectra were then extended to the ultraviolet and infrared using theoretical libraries from Kurucz (private communication), and gas emission was included by means of the photoionization code CLOUDY (Ferland 1996).

The initial set of SSPs was composed of 108 theoretical spectra referring to age intervals from $10^5$ to $20 \times 10^9$ yr, that were binned into a final set of 12 SSPs used in the fitting.

To treat dust extinction, the Galactic extinction curve ($R_v = 3.1$, Cardelli, Clayton & Mathis 1989) is adopted, but the value of the colour excess, $E(B-V)$ is let free to vary as a function of SSP age: dust extinction will be higher for younger stellar populations.

A single metallicity value is adopted and the model is run for three metallicities: $Z = 0.05$, $Z = 0.02$, $Z = 0.004$, choosing as best-fitting model the one with the smallest $\chi^2$. Fitting an observed spectrum with a single value of the metallicity is equivalent to assuming that this value belongs to the stellar population that is dominating its light. A check on the reliability of the mass and SFHs derived using this method has been performed analysing synthetic spectra of different SFHs with metallicity that varies as a function of stellar ages, so to simulate the chemical evolution of the galaxy, and it turns out that the way metallicity is treated does not introduce any significant bias in the recovered stellar mass or SFH (Fritz et al. 2007).

The SFH and mass estimates obtained from the fibre spectrum are scaled from the fibre magnitude to the total magnitude to recover galaxy-wide integrated properties assuming a constant M/L. The differences in colour between the fibre and the total magnitudes are however small for our cluster sample, as shown in Fritz et al. (2011), therefore the assumption of a constant M/L ratio should not introduce large uncertainties. It is worthwhile citing that the application of full spectral fitting techniques to integral field spectroscopy data yields much more detailed information about the SFH per pixel (ATLAS3D: Cappellari et al. 2012, CALIFA: Sánchez et al. 2012; Cid-Fernandes et al. 2013; Gonzalez-Delgado et al. 2014, SAMI: Allen et al. 2015, MaNGA: Bundy et al. 2015, CANDELS: Wuyts et al. 2012), however current Integral Field Unit (IFU) surveys are not suited for a complete census of magnitude limited samples in different environments.

### 3.2.1 *Fitting Algorithm, model outputs and uncertainties*

During the fitting, each one of the 12 SSP spectra is multiplied by a value of SFR in that age interval. The fitting algorithm searches the combination of SFR values that best matches the observed spectrum, calculating the differences between the observed and model spectra, and evaluating them by means of a standard $\chi^2$ function. The 12 SFR values are let free to vary completely independently from one another, without any a priori assumption on the form of the SFH. The observed features that are used to compare the likelihood between the model and the observed spectra are chosen from the most significant emission and absorption lines and continuum flux intervals, after the line equivalent widths are automatically measured (see Fritz et al. 2007, 2014). The observed errors on the flux are computed by taking into account the local spectral signal-to-noise ratio, while uncertainties on the equivalent widths are derived mainly from the measurements method. An adaptive simulated annealing algorithm randomly explores the parameters space, searching for the absolute minimum of the $\chi^2$ function.

The search of the combination of parameters that minimizes the differences between the observed and model spectrum is a non-linear problem and it is also underdetermined, which means that the number of constraints is lower than the number of parameters. The solution given with this method is non-unique, due to the limited wavelength range under analysis, together with the age–metallicity degeneracy and the already-mentioned non-linearity and underdetermination. To account for this, error bars are associated with mass, extinction and age values, computed as follows. The path performed by the minimization algorithm towards the best-fitting model (the minimum $\chi^2$) depends on the starting point, so, in general, starting from different initial positions can lead to different minimum points: 11 optimizations are performed, each time starting from a different point in the space parameter, obtaining 11 best-fitting models which are representative of the space of the solutions. Among these, the model with the median value for the mass is considered, and error bars are computed as the average difference between the values of the model with the highest and lowest total stellar mass formed in that age bin. In this way, we are confident that the expected values are contained within the error bars we calculate. The values for the stellar masses have been thoroughly compared both against other methods (Vulcani et al. 2011) and other data sets (e.g. SDSS) having objects in common with WINGS, showing an excellent agreement (Fritz et al. 2011).

The application of the spectrophotometric synthesis model allows us to derive the characteristics of the stellar populations whose light constitutes the integrated spectrum: the total stellar mass, the mass of stars formed as a function of age – i.e. the SFR within each time interval in the galaxy life – the extinction and the single 'luminosity-weighted' metallicity value. It is important to keep in mind that the model outputs describe the global history of all stars that at low redshift are in the galaxy: the assembly of such stars in a single galaxy, i.e. the galaxy merger history, is totally unconstrained with this method.

All the galaxy stellar masses used in this paper are masses locked into stars, including both those that are still in the nuclear-burning phase, and remnants such as white dwarfs, neutron stars and stellar black holes.

The current SFR values are derived by fitting the flux of emission lines, whose luminosities are entirely attributed to the star formation process, neglecting all other mechanisms that can produce ionizing flux. In this way, for LINERS and active galactic nuclei (AGNs), the SFR values can in principle be severely overestimated. The AGN identification for PM2GC galaxies was done using the latest AGN catalogue from SDSS[3]. The selection of AGNs in WINGS was performed with a very similar method (Marziani et al. 2013, in preparation). We calculate that the AGN contribution to the total SFR of the PM2GC sample is $<3$ per cent. Similarly, the contribution of AGNs in WINGS is only $\sim$1.6 per cent. These estimates allow us to neglect the contribution of AGNs as a source of contamination in the SFRD analysed in this work (see also Section 4.4).

### 3.2.2 *Model reliability*

The reliability of the spectrophotometric technique was tested in two ways (Fritz et al. 2007, 2011). First, template spectra – which resemble the characteristics and the quality of the observed ones – spanning a wide range of SFHs were built, to assess the capability of the model to recover the input SFH. This test was done both on low and high S/N spectra, in order to verify whether there was a dependence of the quality of results from the spectral noise. This showed that the error bars provided by our method for the physical parameters reasonably account for the uncertainties that are dominated by the similarity of old SSP spectra and by the limited spectral range at disposal for our analysis (Fritz et al. 2007).

The second test-phase was done on WINGS spectra in common with the SDSS project, to verify the reliability of the model in

[3] https://www.sdss3.org/dr10/spectro/spectro_access.php

**Table 2.** Age and redshift intervals adopted. With the cosmological parameters adopted, $t_{\rm Universe} = 13.462$ Gyr. $z_{\rm mean}$ is the mean redshift of the intervals, whose starting and ending values are given in $z_{\rm lower}$ and $z_{\rm upper}$ columns, respectively. $\delta_t$ is the corresponding time duration of the redshift bin, $t_{\rm mean}$, $t_{\rm lower}$ and $t_{\rm upper}$ are the age values corresponding to $z_{\rm mean}$, $z_{\rm lower}$ and $z_{\rm upper}$, respectively.

| Model time and redshift intervals adopted | | | | | | |
|---|---|---|---|---|---|---|
| $z_{\rm mean}$ | $z_{\rm lower}$ | $z_{\rm upper}$ | $\delta_t$ Gyr | $t_{\rm mean}$ Time from big bang (Gyr) | $t_{\rm lower}$ | $t_{\rm upper}$ |
| 0.06 | 0.04 | 0.09 | 0.6 | 12.7 | 12.9 | 12.3 |
| 0.10 | 0.09 | 0.12 | 0.4 | 11.9 | 12.3 | 11.9 |
| 0.40 | 0.12 | 0.67 | 4.6 | 9.6 | 11.9 | 7.3 |
| 1.44 | 0.67 | 2.21 | 4.4 | 5.4 | 7.3 | 2.9 |
| 6.49 | 2.21 | 10.71 | 2.5 | 1.4 | 2.9 | 0.4 |

absolute terms, and the agreement with the results on galaxy stellar masses obtained by other works was very satisfactory (Fritz et al. 2007, 2011).

There is an intrinsic degeneracy in the typical features of spectra of similar age, and this degeneracy increases for older stellar population spectra. There is, hence, an intrinsic limit to the precision of this method in determining the age of the stellar populations that compose a spectrum. The choice of the time interval in which SFRs estimates can be considered reliable accounts for this aspect, and the initial 12 ages of the set of SSP spectra, i.e. the time intervals over which the SFR is assumed to be constant, were further binned into five intervals. These are the age intervals that are used throughout this paper. Time and corresponding redshift intervals are listed in Table 2.

To visually illustrate the reason for using a few age intervals, we plot in the lower panel of Fig. 1 the spectra of stellar populations with ages reflecting the five age intervals adopted. The oldest spectrum, corresponding to a mean elapsed time from the big bang of ∼1.4 Gyr, is plotted in red in order to be distinguished from the second oldest one, which is very similar: the ratio of the fluxes of the two spectra is plotted in the upper panel of the figure, and shows 20 per cent level differences noticeable only in the short wavelength domain. The plot shows that the average spectra in each time interval are significantly different one from another, and this is how their contribution to the integrated spectrum can be distinguished by the model. The only exception is the similarity between the spectra of the two oldest populations. For this reason, in the following, results at $z \geq 1$ should be taken with great caution, considering the possible 'spilling' between the SFR reconstruction of the two oldest populations.

### 3.2.3 *Error bars on the SFR and sSFR*

When comparing model and observational SFR estimates, there are two sources of error: that associated with the SFR estimates from the spectrophotometric model and the typical error for SFR estimates from observations.

The first type of errors, computed as described in Section 3.2.1, are considered symmetric with respect to the central SFR value in the spectrophotometric fit. The observational errors are taken to be equal to the typical observational error (0.225 dex), defined as the mean deviation of star formation estimates obtained using different observables (i.e. UV, IR, H$\alpha$, etc.) (Hao et al. 2011). In the following, when plotting SFR estimates for WINGS and PM2GC, these two estimates are combined in quadrature. For errors on the sSFR, we calculate the propagation of errors assuming a typical uncertainty on the stellar mass of 0.2 dex. The value obtained is then combined in quadrature with the observational error for the SFR, normalized with the same procedure according to the mass.

These estimates can be considered intrinsic errors and do not take into account eventual systematic errors arising from systematic uncertainties in the spectrophotometric modelling, for example in the SSP spectra due to isochrones and/or stellar libraries inaccuracy. Therefore, it is important to keep in mind that the errors shown are lower limits.

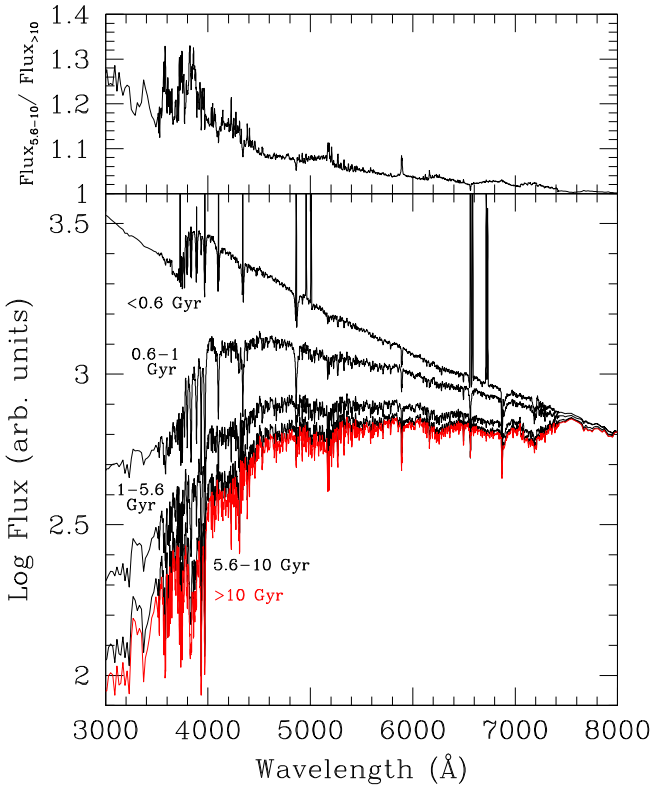


**Figure 1.** Bottom: comparison between spectra of stellar populations of the five age intervals corresponding to each of the five redshift intervals in Table 2. The age of the populations (and the redshift) is decreasing from the bottom to the top of the panel. The oldest spectrum is plotted in red. Spectra are in arbitrary units and are normalized at 8000 Å. Top: ratio between the spectra of the two oldest populations.

## 4 RESULTS

In this section, we present the methods and most significant results of the SFH analysis conducted with our spectrophotometric model on the PM2GC and WINGS.

The reconstruction of the SFH of galaxies has been performed as follows: the 12 model SFRs are binned into the five final age intervals as described in Section 3.2.2 computing the mean constant value of SFR for the entire length of the corresponding redshift bin. These values are then divided by the comoving volume of the survey the galaxies belong to, to obtain the SFRDs.

In all the plots, five values of star formation are presented, with horizontal bars indicating the redshift interval they refer to, and vertical error bars indicating the uncertainty computed as already described.

The sub-division of galaxies according to their morphology and environments has been described in Sections 2 and 3. Below, we will consider the following galaxy stellar mass bins:

(i) $10 \leq \log M_{\rm star}(\mathrm{M}_\odot) < 10.44$ – this bin is used only for WINGS galaxies, whose mass completeness limit is lower than in the PM2GC

(ii) M1: $10.44 \leq \log M_{\rm star}(\mathrm{M}_\odot) < 10.7$

(iii) M2: $10.7 \leq \log M_{\rm star}(\mathrm{M}_\odot) < 11.2$

(iv) M3: $\log M_{\rm star}(\mathrm{M}_\odot) \geq 11.2$. The most massive galaxy in the PM2GC has $\log M_{\rm star}(\mathrm{M}_\odot) = 12.6$, and in WINGS $\log M_{\rm star}(\mathrm{M}_\odot) = 12.5$.

In the following, it is important to keep in mind that there is a degeneracy between the results in the two highest redshift bins. However, the total stellar mass formed at these high redshifts is well constrained, since it is strictly linked to the observed spectrum and the stellar mass formed at lower redshifts.

### 4.1 The cosmic SFH

In Fig. 2, we compare the SFRD of the PM2GC general field sample and the cosmic SFH derived from the most recent data at all redshifts (MD14). These latter data are taken from galaxy surveys that provide SFR measurements from rest-frame far-UV (1500 Å) and mid- and far-infrared, and span the redshift range $z = 0$–8. All the surveys considered provide best-fitting LF parameters, therefore SFRD values can be obtained integrating the luminosity functions down to the same limiting luminosity in units of the characteristic luminosity $L*$, $L_{\rm min} = 0.03L*$. A Salpeter$_{0.1-100}$ IMF was assumed in MD14. Together with the data we also plot the best-fitting function given by MD14, expressed by the analytical form:

$$SFRD(z) = 0.015 \frac{(1+z)^{2.7}}{1+[(1+z)/2.9]^{5.6}}\ \mathrm{M}_\odot\ \mathrm{yr}^{-1}\ \mathrm{Mpc}^{-3}. \quad (3)$$

The PM2GC values are shown as black circles. We note that the Madau and PM2GC values refer to galaxy samples selected with different criteria: the $L_{\rm min} = 0.03L*$ limit at each redshift in MD14, as opposed to $M_B < -18.7$ in the PM2GC at low-$z$. The PM2GC SFRD trend follows quite well the SFRD estimates at different redshifts, suggesting that the histories traced by galaxies selected according to the PM2GC criterion account quite well for the cosmic evolution derived adopting the MD14 selection.[4] The most noticeable discrepancy is in the highest redshift bin ($z > 2$), where the PM2GC value is a factor ∼1.66 higher than the mean SFRD obtained by integrating the MD14 best-fitting function at the same epoch. This behaviour can have several reasons: (a) the uncertainty in the two highest redshift bins of the SFRD computed by our spectrophotometric model already discussed in Section 3.2; (b) an underestimation of the observed SFRD due to incompleteness of high-redshift data from current surveys; (c) the differences in the MD14 versus PM2GC selection criteria mentioned above.

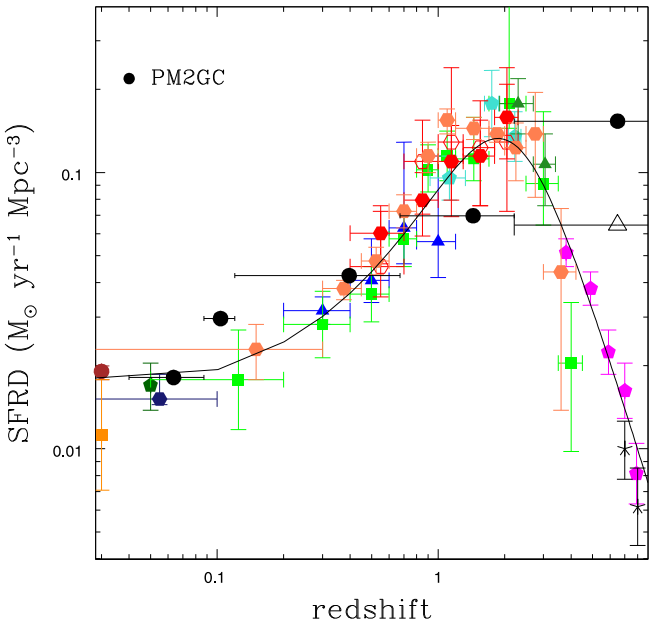


**Figure 2.** Comparison between the PM2GC cosmic SFH and observational data from the literature (table 1 in MD14). The black circles refer to the PM2GC field data set. Error bars in ordinate are smaller than the symbols, while the horizontal error bars show the redshift intervals each circle is referring to. The solid curve is the best-fitting SFRD shown in equation (3), as calculated by MD14. The black empty triangle is the integral of the MD14 curve between 10 Gyr and 13 Gyr, corresponding to the last redshift bin in PM2GC. The data points refer to FUV+UV and mid- and far-IR rest-frame measurements and are taken from table 1 in MD14. Wyder et al. (2005), midnight blue hexagon. Schiminovich et al. (2005), blue triangles. Robotham & Driver (2011), dark green pentagon. Cucciati et al. (2012), green squares. Dahlen et al. (2007), turquoise pentagons. Reddy & Steidel (2009), forest green triangles. Bouwens et al. (2012a,b), magenta pentagons. Schenker et al. (2013), black crosses. Sanders et al. (2003), brown circle. Takeuchi, Yoshikawa & Ishii (2003), dark orange square. Magnelli et al. (2011), red open hexagons. Magnelli et al. (2013), red filled hexagons. Gruppioni et al. (2013), coral hexagons.

### 4.2 The SFH in different environments

In Fig. 3, we compare the PM2GC field SFRD (black circles) with that of the WINGS cluster sample (red empty triangles). The PM2GC sample has also been divided into single galaxies (blue squares), binaries (cyan diamonds) and groups (green full triangles), according to the criteria described in Section 2.

The SFRD is systematically higher in clusters than in the field, of a factor >100 at any redshift. This simply reflects the difference in density (number of galaxies per unit volume) between the two environments, being clusters much denser environments than the field. Single galaxies contribute to the total field SFRD by a factor 1.4 higher than groups in the lowest redshift bin, while at $z > 0.1$ the relation is inverted in favour of groups by about the same factor.

To better compare the slope of the SFRD in the different environments, in the lower panel all the values have been normalized so to coincide with the SFRD of PM2GC at $z = 0$. It is evident that in all environments the star formation process was more active in the past than at the present age, which makes the SFRDs decrease with decreasing redshift. However, the slope is much steeper for cluster than for field galaxies. Clusters have formed the majority of their stars at high $z$: 2/3 of all stars ever formed in clusters were born at $z \geq 2$, while more than half of all stars in field galaxies formed at $z < 2$. The decreasing factor defined as the ratio of SFRD in the highest and the lowest redshift bin is roughly 40 for WINGS, while is ∼ 7 for PM2GC. Considering the field finer environments, in groups the decreasing factor is 10.5, while it is 5 and 5.5 for binary and single galaxies, respectively.

[4] To assess the effect of the different selection criteria on the total SFRD estimate at low redshift, we compare the integral of the PM2GC SFR distribution function for the $M_B = -18.7$ limited sample with that of the SFR function measured by Bothwell et al. (2011) for galaxies at $z = 0.005$–0.1 integrated down to $0.03L^\star$. We find that the $M_B = -18.7$ cut yields a total SFR value that is 9 per cent higher than the $0.03L^\star$ cut, thus we conclude that the different criteria can lead to a ∼10 per cent difference.

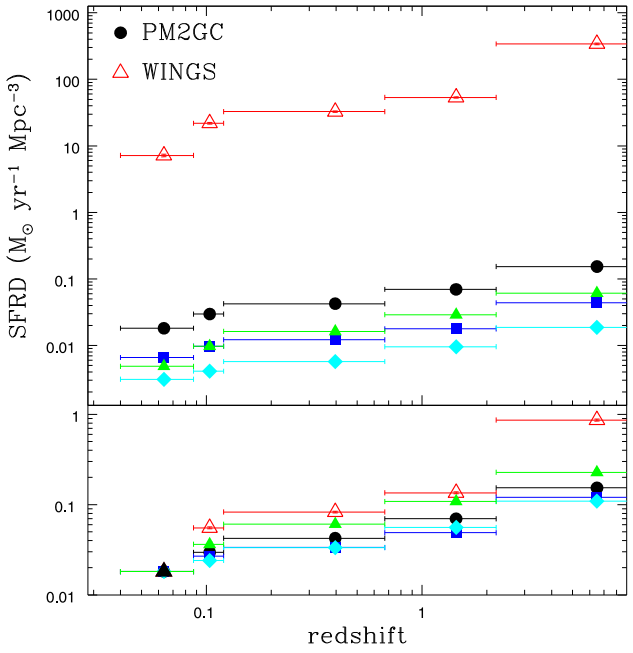


**Figure 3.** Comparison between the field (PM2GC, black circles) and clusters (WINGS, red empty triangles) SFRD. The field sample has also been divided into groups (green triangles), binary (cyan diamonds) and single (blue squares) galaxies. Horizontal bars show the extension of time the circles are referring to. In the top panel SFRD is given in $M_\odot\,yr^{-1}\,Mpc^{-3}$, in the bottom panel all samples are normalized to the PM2GC low-$z$ value, indicated by the black solid triangle.

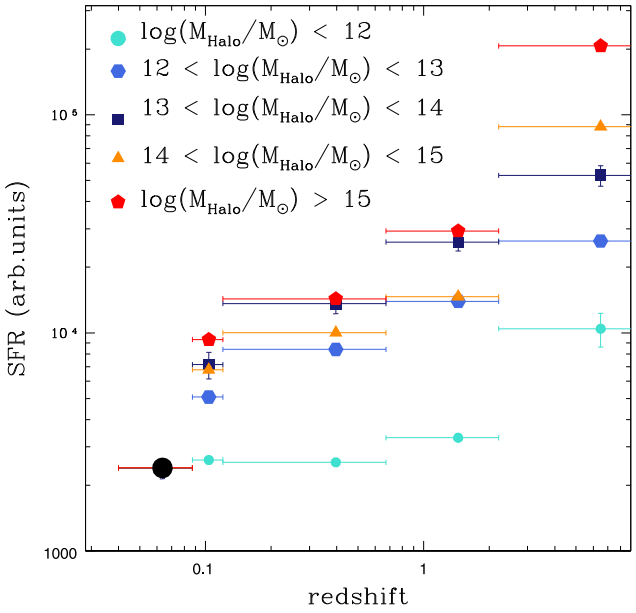


**Figure 4.** The SFH of galaxies divided according to the mass of their host halo. Galaxies are from the PM2GC sample until halo masses of $\log(M_{Halo})/M_\odot = 14$ and from the WINGS cluster sample for more massive haloes. The SFRs are normalized so to coincide in the lowest redshift bin, as indicated by the large black filled circle. The halo mass ranges considered are shown in the legend.

Calvi et al. (2013) found that the galaxy stellar mass function is similar in the field and in clusters at these magnitudes/masses; therefore, the different slope of the decline of the SFRD with redshift in the clusters and in the field is not due to the presence in clusters of more massive galaxies whose star formation occurred at earlier epochs compared to lower mass galaxies. We will return to this point in more detail in the next sections.

In Fig. 4, the SFH of PM2GC and WINGS galaxies is plotted according to the mass of their parent dark matter halo. In the PM2GC, only galaxies in systems with halo masses $<10^{14}\,M_\odot$ are considered, while in WINGS only galaxies in more massive systems are taken into account. The number of galaxies in each halo mass interval is listed in Table 3. The SFRs on the $y$-axis are normalized so to be equal to that of galaxies in the lowest mass haloes in the lowest redshift bin. As a consequence, only the redshift dependence of the SFHs of galaxies hosted in different haloes is compared, while absolute values of SFR are not.

Globally, the decline in SFH gets progressively steeper going from lower to higher mass haloes. The exact shape of such decline seems to vary with the halo mass. In fact, the SFR ranking order at the highest redshift respects the halo mass ranking, while at $z \sim 0.1$–2 the ranking of $10^{13}$–$10^{14}\,M_\odot$ groups and $10^{14}$–$10^{15}\,M_\odot$ clusters is not respected. Galaxies in haloes of mass $< 10^{12}\,M_\odot$ show a very flat and well separated SFH compared to all other masses. Yet, they still display an SFR at $z > 2$ significantly higher than at any other redshift, a feature common to haloes of all masses.

To conclude, the slope of the decline of the SFRD strongly changes with environment. This is clearly visible with both of our definitions of environment. In Section 4.5, we will analyse in detail the origin of this effect.

**Table 3.** List of the number of galaxies with different halo mass estimates both in the PM2GC and WINGS samples.

| Data sample | Halo mass | Number of galaxies |
|---|---|---|
| PM2GC | $M_{halo} < 10^{12}\,M_\odot$ | 1137 |
| PM2GC | $10^{12}\,M_\odot < M_{halo} < 10^{13}\,M_\odot$ | 708 |
| PM2GC | $10^{13}\,M_\odot < M_{halo} < 10^{14}\,M_\odot$ | 261 |
| WINGS | $10^{14}\,M_\odot < M_{halo} < 10^{15}\,M_\odot$ | 771 |
| WINGS | $M_{halo} > 10^{15}\,M_\odot$ | 478 |

### 4.3 The SFH of star-forming galaxies

The SFH throughout the cosmic time in a given environment includes a large number of galaxies and at each epoch is the result of star formation processes taking place in galaxies that are still actively forming stars. The decline of the SFRD from the past to the present age is in principle the cumulative result of declining star formation in galaxies that are still star-forming today (i.e. at the redshift they are observed in the PM2GC or WINGS) together with the increase in the number of galaxies that at some point have stopped forming stars, i.e. have been quenched. The study of the SFH of today's star-forming galaxies aims to disentangle these two effects.

In the following, we consider as currently star-forming those galaxies whose sSFR at the time they are observed (i.e. $z = 0.03$–0.11) is above a fixed threshold. For computing the sSFR, the current SFR is taken to be the average during the last 20 Myr as obtained from the model.

In Fig. 5, we report the sSFR–Mass relation from low-redshift measurements of SFR and galaxy stellar masses. The black dots in the figure are the PM2GC field galaxy sample values ($z = 0.03$–0.11), the green dotted line is the fit from the star-forming sequence from Salim et al. (2007) ($z \simeq 0.1$), the blue solid line is

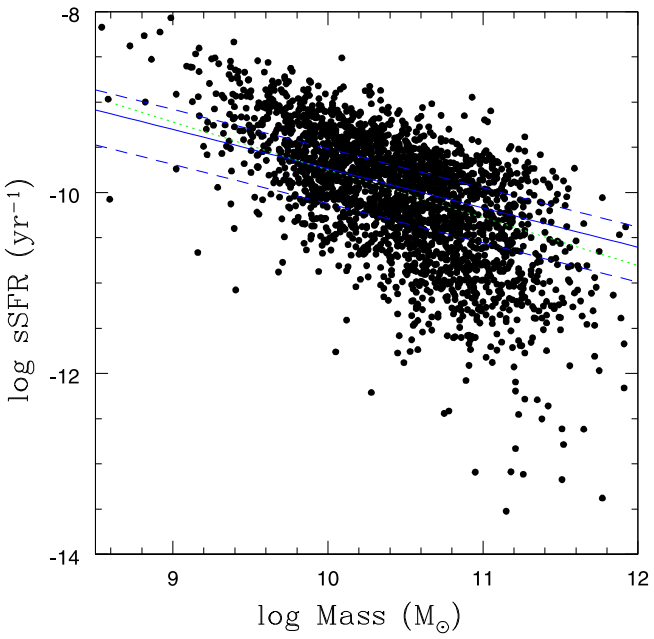


**Figure 5.** The sSFR–Mass relation. Black dots refer to the PM2GC galaxy sample. The main sequence of star-forming galaxies from Salim et al. (2007) is plotted with the green dotted line and from Lara-López et al. (2013) with the blue solid line. The two blue dashed lines are located at one sigma with respect to the blue solid one.

the same quantity as given in Lara-López et al. (2013) ($z$ up to $\simeq$ 0.36) and the blue dashed lines are located at one sigma with respect to the blue solid one. The threshold separating star-forming from passive galaxies is chosen on the basis of this sSFR–mass relation and is taken to be equal to sSFR $=10^{-12}$yr$^{-1}$ (see Fig. 5). This criterion selects 2094 star-forming galaxies in the field and 612 in clusters.

Fig. 6 shows the mean SFH per star-forming galaxy in different galaxy mass bins, obtained dividing the sum of all SFRs by the number of galaxies. The global decline in the cosmic star formation is not only due to an increasing fraction of galaxies becoming quenched at lower redshifts, but also to the decrease with time of the average SFR of today's star-forming galaxies.

The trend depends on galaxy mass, as shown in Fig. 6: it is steeper in high-mass galaxies than in low-mass ones, both in the field and in clusters. In clusters, the SFR drop between the oldest and the second oldest time intervals is much more pronounced than in the field for all galaxy masses, in agreement with the fact that star formation in cluster galaxies occurred very early on.

Fig. 7 shows the redshift dependence of the ratio between the total SFR of all galaxies at any given redshift and the total SFR at the same redshift of galaxies that are still forming stars today, for PM2GC (full circles) and WINGS (empty triangles) separately. The fractional contribution to the total SFR at any redshift of galaxies that are now quenched is equal to (1–1/$y$), with $y$ being the $Y$-axis value in Fig. 7. There is one extra redshift bin in this figure, because the first time interval of 600 Myr was splitted into 20 Myr and 580 Myr, to isolate the present-day value according to our definition of star-forming galaxies. The first point plotted in the figure represents the ratio between the SFR of today's star-forming galaxies and the current measured SFR, and by definition it has a value equal to 1.

The resulting values have been interpolated using a least-squares method and the resulting interpolation lines are as follows:

$$\text{PM2GC} : y = (0.46 \pm 0.04) \times \log(z) + (1.7 \pm 0.04) \quad \text{rms} = 0.061 \tag{4}$$

$$\text{WINGS} : y = (1.31 \pm 0.39) \times \log(z) + (3.61 \pm 0.36) \quad \text{rms} = 0.61 \tag{5}$$

where $y$ is the $Y$-axis value in Fig. 7.

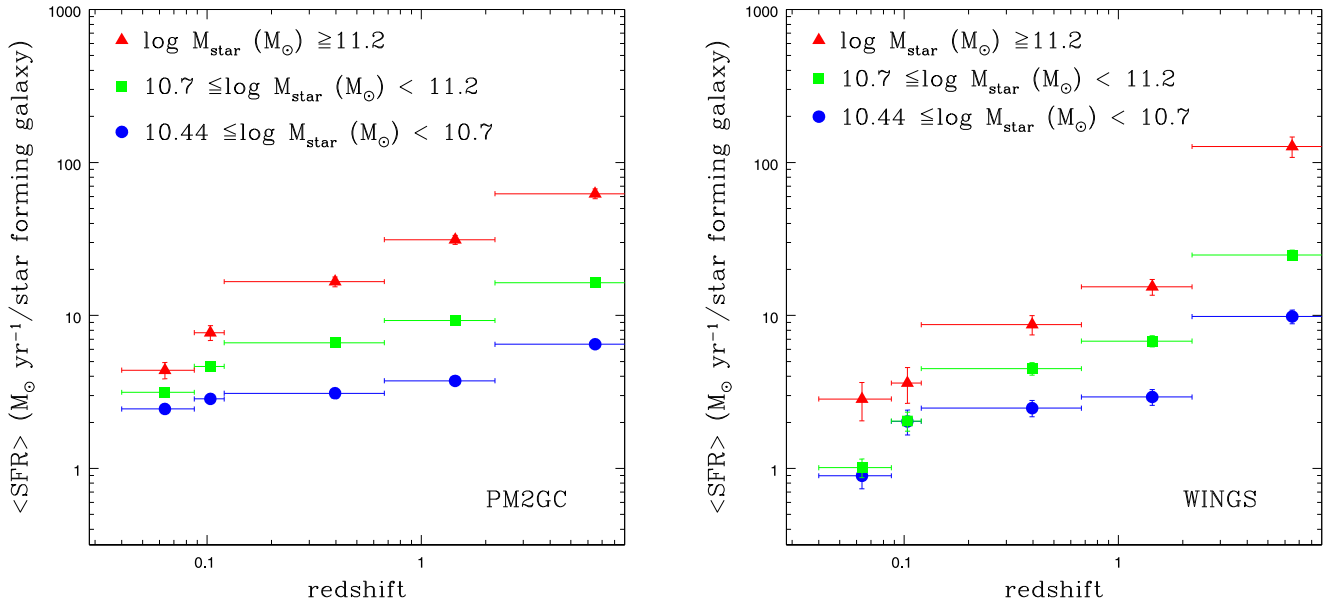


**Figure 6.** The PM2GC (left) and WINGS (right) mean SFR of today's star-forming galaxies. Galaxies are considered as star-forming if they have an sSFR higher than $10^{-12}$ in the last 20 Myr. The selected galaxies are divided into three mass bins, plotted with different colours and shapes as shown in the legend. Horizontal bars refer to the time interval over which the mean SFR is computed, while vertical ones are associated with errors in the SFR determination.

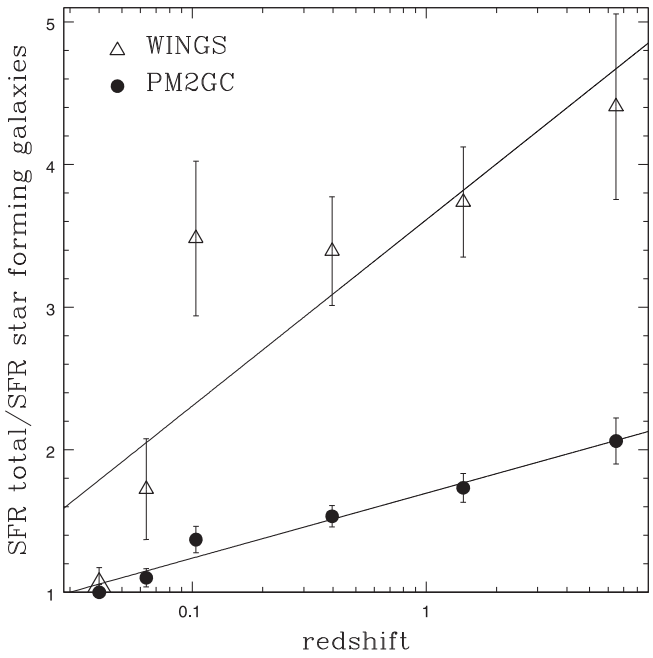


**Figure 7.** Ratio between the SFR from the complete sample and the SFR of currently star-forming galaxies for PM2GC (full circles) and WINGS (empty triangles). The solid lines are the linear interpolation computed using an ordinary least-square method and whose equations are given in equation (5). Error bars have been computed from the errors relative to SFRs in both the complete and star-forming samples using error propagation.

A good correlation for PM2GC galaxies is found, with the interpolation line reproducing well within the error bars the temporal behaviour of the ratio. For WINGS not all the points follow a linear correlation within the error bars, even if the general trend is decreasing as in the field.

This figure illustrates that the star formation process at high $z$ was mainly due to galaxies which today are not active anymore. In fact, ∼50 per cent of the SFR in the field and ∼75 per cent in clusters at $z > 2$ originated in galaxies that are not forming stars today. At $z \sim 1.5$, these factors are 42 per cent in the field and 73 per cent in clusters.

Moreover, in clusters the interpolation line is almost three times steeper than in the field, meaning that the contribution of quenching to the SFRD(z) decline is much more significant in clusters than in the field.

### 4.4 The contribution to the SFRD($z$) of galaxies of different morphologies and masses

In this section, we focus on the comparison between clusters and field taking into consideration the contribution to the SFRD($z$) of galaxies of different mass and morphology. Recall that stellar masses and morphologies refer to galaxies as they appear at low redshift, when we observe them. Their morphological type at higher $z$, at the moment they possessed the SFRs we infer, might have been different, due to the well-known morphological evolution taking place both in clusters and in the field (e.g. Dressler et al. 1997; Oesch et al. 2010; Vulcani et al. 2011).

Fig. 8 shows that the contribution to the SFRD($z$) depends on the morphological type and, considering a given type, on the environment.[5]

The main contribution to the SFRD in the field sample (left-hand panel in the figure) is given by today's late-type galaxies (marked with blue circles), which dominate at all redshifts. Compared to the total values estimated for the PM2GC, the SFRD of late-types is ∼70 per cent of the total at the present epoch and ∼40 per cent at the highest $z$. The relative contribution of different morphological types to the total star formation varies with time: (today's) early-type galaxies, which are composed mainly of old and red stars, gave a larger contribution to the SFRD at earlier epochs, while today they contribute only for 30 per cent of the total SFRD. S0s and ellipticals have quite similar values at every epoch, with ellipticals slightly dominating at all redshifts except the lowest bin.

In principle, the analysis just performed depends on both the stellar history of each type and the morphological distribution of galaxies within each environment, i.e. the number of galaxies populating each type. In our field sample, 59 per cent of all galaxies are late types, 21 per cent are S0s and 19 per cent are ellipticals. At $z = 0$, on average the star formation activity in a late-type galaxy is 1.5 times higher than in an elliptical and 1.6 times than in an S0, which is expected given that early-type galaxies today are on average more passive than late types.

In contrast with the field, early-type galaxies dominate the total SFRD in clusters at all epochs, except in the lowest redshift bin. The difference in the fractional contribution of late- and early-types, however, is much smaller than in the field: in clusters, 40 per cent of the total today SFRD is due to late types, only slightly higher than the 32 per cent and 28 per cent of S0s and ellipticals, respectively. This picture reverses going back in time: within the range $0.1 \lesssim z \lesssim 1$, today's lenticular galaxies produce the majority of stars, and finally at the highest $z$ ellipticals dominate. The scenario just described is influenced by the significantly different distribution of morphologies in cluster galaxies compared with that in the field: in clusters, 28 per cent of all galaxies are ellipticals, 44 per cent are S0s and 27 per cent are late type.

Overall, the trends in clusters and in the field are clearly very different as far as the relative roles of each type are concerned.

We now divide galaxies into mass bins, according to the completeness limits of the two surveys: $M \geq 10^{10.44}\,\mathrm{M}_{\odot}$ for PM2GC and $M \geq 10^{10}\,\mathrm{M}_{\odot}$ for WINGS. In Fig. 9, the field and the cluster SFRDs are divided into, respectively, three and four mass bins. Qualitatively, the global SFRD in both environments is dominated by galaxies with $M > 10^{10.7}\,\mathrm{M}_{\odot}$. Going into more details, in the field, galaxies with masses $M \geq 10^{11.2}\,\mathrm{M}_{\odot}$ give the main contribution to the total SFRD for $z \gtrsim 0.35$, while in the two lowest redshift intervals galaxies with masses $10^{10.7}\,\mathrm{M}_{\odot} \leq M < 10^{11.2}\,\mathrm{M}_{\odot}$ prevail. Low-mass galaxies (blue circles) have lower SFRD than the intermediate mass galaxies, but still higher than the most massive galaxies for $z \lesssim 0.1$. The trends plotted in the left-hand panel of Fig. 9 are influenced again by both the size of the subsamples and the average SFRs of galaxies of different masses.

[5] We note that the results for early-type galaxies (ellipticals and S0s) should be considered as upper limits, since the presence of AGN could produce an overestimation of the SFR, therefore of the SFRD. Nonetheless, in our sample the total contribution from AGN is negligible, as discussed in Section 3.2.1. AGNs classified as early type in the PM2GC sample are 28 and their contribution to the $z = 0$ early-type SFRD is ∼5.4 per cent. The number of early-type AGNs contaminating WINGS galaxies is only 3: in the present epoch they contribute to the early-type SFRD only for ∼1.36 per cent.

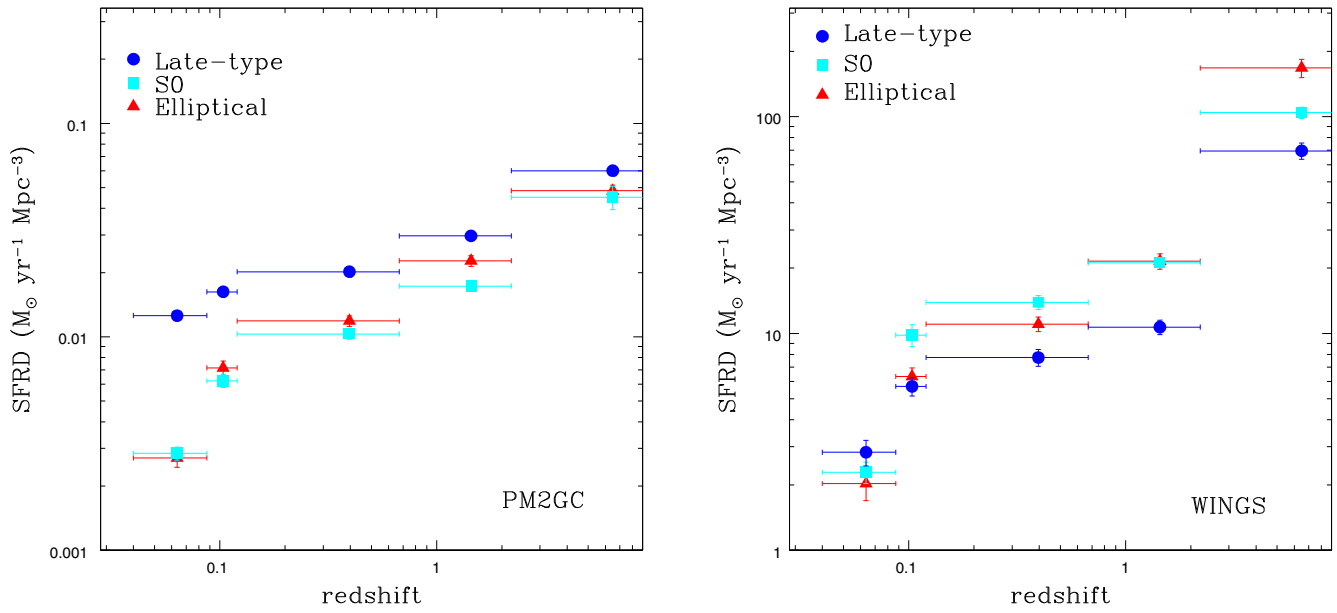


**Figure 8.** The SFH of PM2GC (in the left-hand panel) and WINGS (in the right-hand panel) whose galaxies have been divided according to their morphological type. Red triangles stand for ellipticals, cyan squares for lenticulars (S0) and blue circles for late-types. All SFRDs refer to the same time intervals, here represented with horizontal bars. Vertical bars are associated with indetermination in SFRD values.

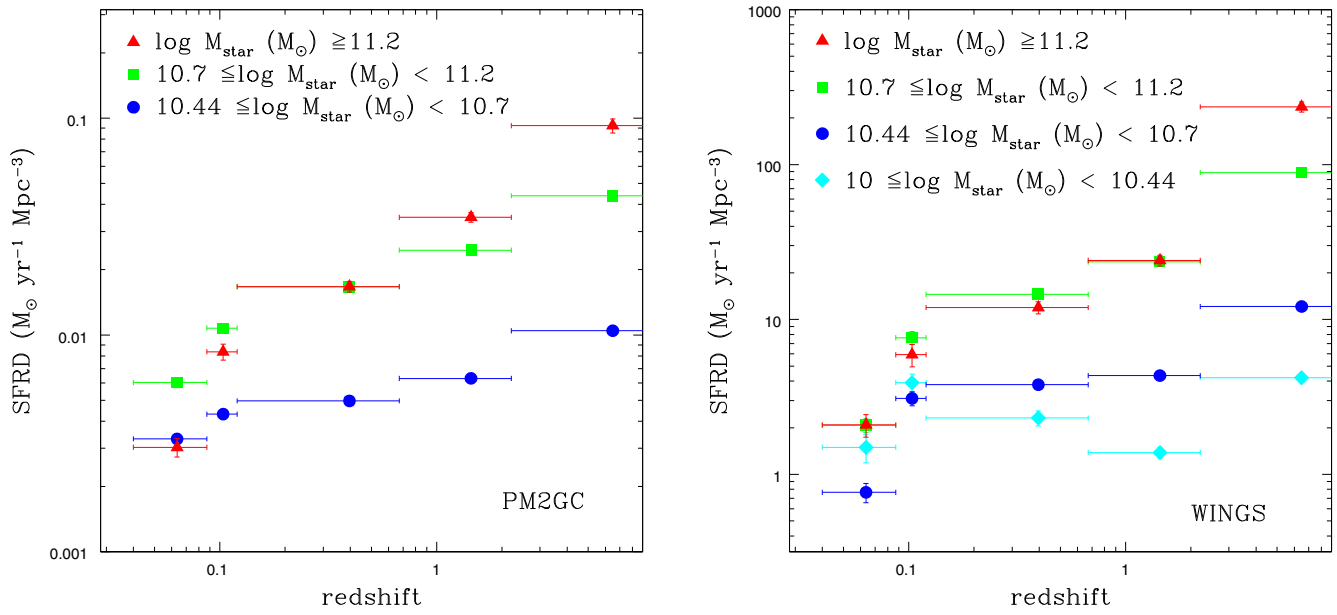


**Figure 9.** The PM2GC (on the left) and WINGS (on the right) SFH for galaxies divided in mass bins, as shown in the legend. Mass values here reported are calculated according to a Salpeter (0.1–100) IMF. All SFRDs are supposed to be constant in the same time intervals, here represented with horizontal bars. Vertical bars are associated with indetermination in SFRD values.

To compare the average SFR of a typical galaxy of a certain mass, it is useful to divide the SFR by the number of galaxies populating the considered mass bin. Today, on average, galaxies in different mass bins (including passive ones) form roughly the same amount of stars, and intermediate-mass galaxies dominate the global SFRD in the field just because they are more numerous. On the contrary, at higher $z$, the hierarchy established in the total SFRD is very pronounced: the SFR per unit galaxy of $M \geq 10^{11.2}$ $M_{\odot}$ galaxies on average is $\backsim$5 times higher than that of intermediate-mass galaxies and about 13 times the one of the low-mass systems.

The right-hand panel of Fig. 9 refers to WINGS cluster galaxies. Galaxies with the lowest mass always give the smallest contribution to the total SFRD at any redshift, while the intermediate and high-mass galaxies have similar SFRD values until $z$ $\backsim$2, and at higher $z$ the most massive ones prevail. Analysing again the mean SFRD per galaxy within a certain range in mass it turns out that today the SFRD of the average low-mass galaxy becomes roughly equal to that of intermediate-mass ones, while high-mass galaxies have values higher of a factor of $\backsim$2.3. Going to higher redshifts, the ratio of the average SFRD of high-mass and intermediate-mass

(low-mass) galaxies becomes greater, reaching a value of ∽6 (16) at the highest redshift.

An important phenomenon strictly connected with masses is downsizing: galaxies with higher masses are characterized by shorter and earlier star formation on average, while lower mass galaxies have longer star formation time-scales. The variation of the SFH of galaxies according to their stellar mass is evident comparing the slopes of the hypothetical curve connecting points of the same colour and shape (red, green and blue) in Fig. 9. In particular, as an estimate of the process, we can calculate the ratio between the value of SFR in the first and in the last redshift intervals and analyse its variation as a function of mass. This ratio is ∽3 for low-mass galaxies, ∽6 for intermediate-mass ones and ∽26 for high-mass galaxies in the field. The same ratios in WINGS galaxies are the following: ∽13 for low masses, ∽36 for intermediate ones and ∽94 for the highest masses. The numbers listed above demonstrate that the downsizing phenomenon acts in the field as well as in clusters, but in the latter it is stronger. Even galaxies of the same mass are characterized by different time-scales and SFHs depending on their environment. The average decline of the star formation process in galaxies of a given mass is less steep in the field than in clusters. Cluster galaxies form the bulk of their stars at earlier epochs with average high-$z$ SFRD values per galaxy systematically higher than those of the field at any given galaxy stellar mass today, as we will see in more details in the next section.

### 4.5 Masses, morphologies and environment: a global picture

The last sequence of plots in Fig. 10 aims to answer the following questions: on average, do galaxies of different morphological types but same masses have different histories? Do galaxies of the same mass and morphological type have different histories depending on the environment?

We divide galaxies according to their morphological type, mass bin and environment. To avoid any possible residual mass dependence in each mass bin, we first verified whether galaxies in each given mass bin and given morphological type had the same mass distribution in both environments, performing a Kolmogorov–Smirnov test (KS). The KS test found significantly different mass distributions only in three cases (elliptical galaxies in the lowest mass bin and lenticular galaxies both in the lowest and in the highest mass bins, plots not shown). For these, we constructed ad hoc samples of randomly selected WINGS galaxies that matched the PM2GC mass distribution. Moreover, for this plot, we limit the M3 bin to $<7 \times 10^{11}\,M_{\odot}$, to have a similar upper mass limit for spirals, ellipticals and S0s in each environment.

Fig. 10 presents the SFH of galaxies in each mass bin, matched in mass when necessary, for different environments and morphologies. The total SFR is divided by the number of galaxies of each subsample, in order to derive the mean history of a galaxy of a given type, mass and environment. Environments are plotted in figures with different symbols (full circles, squares and triangles for field galaxies and empty circles, squares and triangles for cluster galaxies) and colours follow the same legend of the morphological analysis in Fig. 8.

Fig. 10 highlights that, perhaps surprisingly, in a given environment, galaxies of the same mass but different morphologies share the same history of star formation, except for the lowest redshift bin. In fact, the average SFR of late-type, S0 and elliptical galaxies of a given mass is similar within the errors at all redshifts, except at $z < 0.1$ when late-type galaxies have a systematically higher value than early-type galaxies. There is, instead, a different SFH in clusters and field for galaxies of a given mass and morphological type: all types in clusters have a higher SFR at $z > 2$ and a lower SFR at lower redshifts, than field galaxies.

Comparing now the different mass bins, the downsizing in star formation is again visible (the slope of the SFH gets steeper at higher masses). The range of SFR at the lowest redshift is similar for galaxies of all masses, while it varies greatly at the highest $z$ (see Section 4.4).

From the analysis of these plots, it is possible to establish a general hierarchy in the properties of galaxies which mostly influence the star formation process.

Galaxy mass is clearly an important factor in determining the SFR slope with time, in all environments. However, it is not the only factor, as cluster galaxies of a given mass have a steeper decline of SF with time. For each mass, the highest average SFR at $z > 2$ is found for cluster galaxies, and does not depend on morphology.

Morphology, in contrast, has little influence on the SFH. The only morphological dependence is at the present epoch when, on average, a late-type galaxy forms more stars than an early-type galaxy of the same mass.

These results seem to suggest that the stellar history of a galaxy depends mainly on its mass *and* environment, and is almost independent of its present-day morphology.

Finally, computing from Fig. 10 the ratio of the average SFR in the highest and lowest redshift bins for galaxies of the same mass and morphology and comparing it for different environments, we obtain cluster-to-field ratios typically ranging from 4 to 7, with an average of 5. Thus, the much steeper SFRD decline in clusters compared to the field (ratio = 40/7 = 5.7) discussed in 4.2 can be explained by the steeper history of cluster galaxies compared to the field, at fixed galaxy mass and morphology. We conclude that the different slope in the SFRD($z$) of clusters and field is not driven by variations of the galaxy mass or morphological distributions with environment, but by the fact that galaxy stellar histories vary with galaxy location at each given mass and morphology.

## 5 SUMMARY

Having derived the SFH of galaxies in clusters (WINGS) and the field (PM2GC), we have investigated the SFRD evolution with redshift as a function of environment, the histories of galaxies that are still forming stars at the time they are observed, and the role of galaxy masses, morphologies and environment in driving the differences of the SFRD($z$) with environment. We have found the following.

(i) The PM2GC cumulative SFRD agrees quite well with the SFRD observed at different redshifts (Fig. 2). The only discrepancy is seen at the highest $z$ ($z > 2$), where the PM2GC SFRD is a factor ∼1.7 lower than the integral of the MD14 best-fitting function over the same redshift interval.

(ii) The SFRD changes with environment (Fig. 3) and in particular two effects contribute simultaneously to the cluster-field differences in the SFRD: the different density of the two environments, which changes the normalization of the SFRDs at all epochs, and the intrinsic differences of the histories within the environments, which change the slope of the SFRD. The cluster SFRD decline is much steeper than in the field, and there is a progressive steepening going from single to binaries to groups and clusters, as well as going from lower mass to higher mass haloes.

(iii) The decline of the SFRD($z$) is due to two factors: the decline of the SFH of star-forming galaxies and the quenching rate of

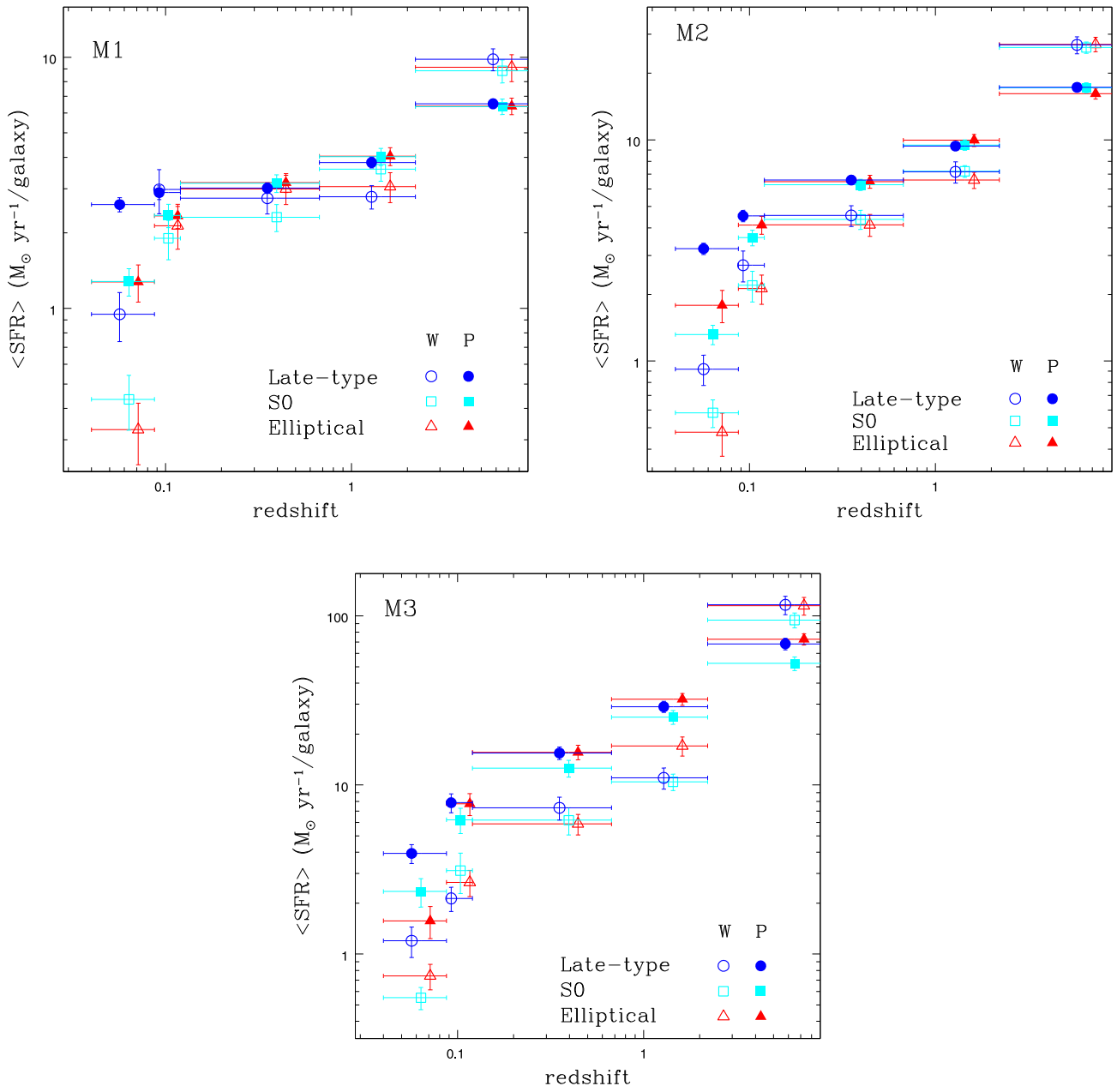


**Figure 10.** The SFH of galaxies with different morphological type and mass: in the first plot galaxies have $10^{10.44}\,M_\odot \leq M1 < 10^{10.7}M_\odot$, in the second galaxies have $10^{10.7}\,M_\odot \leq M2 < 10^{11.2}M_\odot$ and in the third galaxies have masses $M3 \geq 10^{11.2}M_\odot$. Data reported with full circles, squares and triangles refer to the field sample PM2GC and empty ones refer to the cluster sample WINGS, with different colours meaning different morphological types, as shown in the legend. The average SFRs are assumed to be constant in the same temporal extension, here represented with horizontal bars. Vertical bars are associated with indetermination in SFR values. Symbols are horizontally shifted by small arbitrary amounts within their redshift bin in order to avoid superpositions.

galaxies as a function of redshift (Fig. 6). We have quantified the relative importance of the two processes (Fig. 7): the star formation process at high $z$ was mainly due to galaxies which today are not active anymore, and this is true in particular for clusters. More than 50 per cent of the SFR in the field and more than 75 per cent in clusters at $z > 2$ originated in galaxies that are not currently forming stars. At $z \sim 1$, these factors are 42 per cent in the field and 73 per cent in clusters.

(iv) Galaxies of different morphological types but same mass and environment have on average remarkably similar SFRs at all epochs except at the lowest redshift, suggesting that the current morphological type is linked with the current morphology but is largely non-influent for the past SFH.

(v) The average SFH of a galaxy depends on galaxy stellar mass and, at fixed mass, on galaxy environment. The different slope of the decline in the SFRD($z$) in clusters and field is due to the fact that galaxies of given mass and morphology form their stars sooner in clusters than in the field.

These results point to an accelerated formation in high-mass haloes compared to low-mass ones even for galaxies that will end up having the same galaxy mass today.

## ACKNOWLEDGEMENTS

We acknowledge the anonymous referee for her/his careful report, important suggestions and comments which helped us improving our work. We thank Joe Liske, Simon Driver and the whole MGC team for making easily accessible a great data set. We are grateful to the rest of the WINGS team for help and useful discussions. VG and BMP acknowledge financial support from the Istituto Nazionale di Astrofisica through a PhD Cycle 30th grant. BV was supported by the World Premier International Research Center Initiative (WPI), MEXT, Japan and by the Kakenhi Grant-in-Aid for Young Scientists (B)(26870140) from the Japan Society for the Promotion of Science (JSPS).

We gratefully acknowledge Prof. Giuseppe Tormen for inspiring discussions, precious suggestions and support as internal supervisor during all the work.

## REFERENCES

Abazajian K. et al., 2003, AJ, 126, 2081
Abramson L. E., Gladders M. D., Dressler A., Oemler A., Poggianti B., Vulcani B., 2014, ApJ, 801, L12
Allen J. T. et al., 2015, MNRAS, 446, 1567
Baldry I. K., Balogh M. L., Bower R. G., Glazebrook K., Nichol R. C., Bamford S. P., Budavari T., 2006, MNRAS, 373, 469
Bernardi M. et al., 2003, AJ, 125, 1849
Bertelli G., Bressan A., Chiosi C., Fagotto F., Nasi E., 1994, A&AS, 106, 275
Bothwell M. S. et al., 2011, MNRAS, 415, 1815
Bouwens R. J. et al., 2012a, ApJ, 752, L5
Bouwens R. J. et al., 2012b, ApJ, 754, 83
Bouwens R. J. et al., 2014, ApJ, 795, 126
Bressan A., Granato G. L., Silva L., 1998, A&A, 332, 135
Brinchmann J., Charlot S., White S. D. M., Tremonti C., Kauffmann G., Heckman T., Brinkmann J., 2004, MNRAS, 351, 1151
Bundy K. et al., 2015, ApJ, 798, 7
Burgarella D. et al., 2013, A&A, 554, AA70
Calvi R., Poggianti B. M., Vulcani B., 2011, MNRAS, 416, 727
Calvi R., Poggianti B. M., Fasano G., Vulcani B., 2012, MNRAS, 419, L14
Calvi R., Poggianti B. M., Vulcani B., Fasano G., 2013, MNRAS, 432, 3141
Cappellari M. et al., 2012, Nature, 484, 485
Cardelli J. A., Clayton G. C., Mathis J. S., 1989, ApJ, 345, 245
Cava A. et al., 2009, A&A, 495, 707
Cid-Fernandes R., Gu Q., Melnick J., Terlevich E., Terlevich R., Kunth D., Rodrigues Lacerda R., Joguet B., 2004, MNRAS, 355, 273
Cid Fernandes R. et al., 2013, A&A, 557, A86
Colless M. et al., 2001, MNRAS, 328, 1039
Conroy C., 2013, ARA&A, 51, 393
Cooper M. C. et al., 2006, MNRAS, 370, 198
Cooper M. C. et al., 2010, MNRAS, 409, 337
Cowie L. L., Songaila A., Hu E. M., Cohen J. G., 1996, AJ, 112, 839
Cucciati O. et al., 2006, A&A, 458, 39
Cucciati O. et al., 2012, A&A, 539, AA31
Daddi E. et al., 2007, ApJ, 670, 156
Dahlen T., Mobasher B., Dickinson M., Ferguson H. C., Giavalisco M., Kretchmer C., Ravindranath S., 2007, ApJ, 654, 172
Davis M., Geller M. J., 1976, ApJ, 208, 13
De Lucia G., Blaizot J., 2007, MNRAS, 375, 214
De Lucia G. et al., 2007, MNRAS, 374, 809
Dressler A., 1980, ApJ, 236, 351
Dressler A. et al., 1997, ApJ, 490, 577
Driver S. P., Liske J., Cross N. J. G., De Propris R., Allen P. D., 2005, MNRAS, 360, 81
Driver S. P., Robotham A. S. G., Bland-Hawthorn J., Brown M., Hopkins A., Liske J., Phillipps S., Wilkins S., 2013, MNRAS, 430, 2622
Ebeling H., Voges W., Bohringer H., Edge A. C., Huchra J. P., Briel U. G., 1996, MNRAS, 281, 799
Ebeling H., Edge A. C., Bohringer H., Allen S. W., Crawford C. S., Fabian A. C., Voges W., Huchra J. P., 1998, MNRAS, 301, 881
Ebeling H., Edge A. C., Allen S. W., Crawford C. S., Fabian A. C., Huchra J. P., 2000, MNRAS, 318, 333
Fasano G., Vanzella E., Wings Team, , 2007, in Vallenari A., Tantalo R., Portinari L., Moretti A., eds, Vol. 374, From Stars to Galaxies: Building the Pieces to Build Up the Universe. Astron. Soc. Pac., San Francisco, p. 495
Fasano G. et al., 2006, A&A, 445, 805
Fasano G. et al., 2012, MNRAS, 420, 926
Ferland G. J., 1996, Hazy, a Brief Introduction to Cloudy. Univ. Kentucky Phys. Dep. Int. Rep., Lexington
Finn R. A. et al., 2005, ApJ, 630, 206
Franx M., van Dokkum P. G., Schreiber N. M. F., Wuyts S., Labbé I., Toft S., 2008, ApJ, 688, 770
Fritz J. et al., 2007, A&A, 470, 137
Fritz J. et al., 2011, A&A, 526, AA45
Fritz J. et al., 2014, A&A, 566, AA32
Gavazzi G., Boselli A., Cortese L., Arosio I., Gallazzi A., Pedotti P., Carrasco L., 2006, A&A, 446, 839
González Delgado R. M. et al., 2014, A&A, 562, A47
Gruppioni C. et al., 2013, MNRAS, 432, 23
Haines C. P., Gargiulo A., La Barbera F., Mercurio A., Merluzzi P., Busarello G., 2007, MNRAS, 381, 7
Hao C.-N., Kennicutt R. C., Johnson B. D., Calzetti D., Dale D. A., Moustakas J., 2011, ApJ, 741, 124
Heavens A. F., Jimenez R., Lahav O., 2000, MNRAS, 317, 965
Heavens A., Panter B., Jimenez R., Dunlop J., 2004, Nature, 428, 625
Hopkins A. M., Beacom J. F., 2006, ApJ, 651, 142
Iovino A. et al., 2010, A&A, 509, AA40
Jacoby G. H., Hunter D. A., Christian C. A., 1984, ApJS, 56, 257
Karim A. et al., 2011, ApJ, 730, 61
Kauffmann G., Heckman T. M., De Lucia G., Brinchmann J., Charlot S., Tremonti C., White S. D. M., Brinkmann J., 2006, MNRAS, 367, 1394
Kodama T., Bower R. G., 2001, MNRAS, 321, 18
Koleva M., Prugniel P., Bouchard A., Wu Y., 2009, A&A, 501, 1269
La Barbera F., Pasquali A., Ferreras I., Gallazzi A., de Carvalho R. R., de la Rosa I. G., 2014, MNRAS, 445, 1977
Lara-López M. A. et al., 2013, MNRAS, 434, 451
Lilly S. J., Le Fevre O., Hammer F., Crampton D., 1996, ApJ, 460, L1
Lin L. et al., 2014, ApJ, 782, 33
MacArthur L. A., González J. J., Courteau S., 2009, MNRAS, 395, 28
Madau P., Dickinson M., 2014, ARA&A, 52, 415 ( MD14)
Madau P., Ferguson H. C., Dickinson M. E., Giavalisco M., Steidel C. C., Fruchter A., 1996, MNRAS, 283, 1388
Magnelli B., Elbaz D., Chary R. R., Dickinson M., Le Borgne D., Frayer D. T., Willmer C. N. A., 2011, A&A, 528, A35
Magnelli B. et al., 2013, A&A, 553, A132
Marziani P., D'Onofrio M., Bettoni D., Fasano G., Fritz J., Poggianti B. M., Cava A., 2013, AN, 334, 412
McGee S. L., Balogh M. L., Wilman D. J., Bower R. G., Mulchaey J. S., Parker L. C., Oemler A., 2011, MNRAS, 413, 996
Muzzin A. et al., 2012, ApJ, 746, 188
Noeske K. G. et al., 2007, ApJ, 660, L43
Ocvirk P., Pichon C., Lançon A., Thiébaut E., 2006a, MNRAS, 365, 46
Ocvirk P., Pichon C., Lançon A., Thiébaut E., 2006b, MNRAS, 365, 74
Oemler A., Jr, 1974, ApJ, 194, 1
Oesch P. A. et al., 2010, ApJ, 714, L47
Omand C. M. B., Balogh M. L., Poggianti B. M., 2014, MNRAS, 440, 843
Panter B., Jimenez R., Heavens A. F., Charlot S., 2007, MNRAS, 378, 1550
Papovich C., Dickinson M., Ferguson H. C., 2001, ApJ, 559, 620
Pasquali A., Gallazzi A., Fontanot F., van den Bosch F. C., De Lucia G., Mo H. J., Yang X., 2010, MNRAS, 407, 937
Peng Y.-j. et al., 2010, ApJ, 721, 193
Peng Y.-j., Lilly S. J., Renzini A., Carollo M., 2012, ApJ, 757, 4
Poggianti B. M., Bressan A., Franceschini A., 2001, ApJ, 550, 195

Poggianti B. M. et al., 2006, ApJ, 642, 188
Poggianti B. M. et al., 2013, ApJ, 762, 77
Popesso P. et al., 2014a, A&A, 574, A105
Popesso P. et al., 2014b, preprint (arXiv:1407.8231)
Reddy N. A., Steidel C. C., 2009, ApJ, 692, 778
Robotham A. S. G., Driver S. P., 2011, MNRAS, 413, 2570
Rodighiero G. et al., 2011, ApJ, 739, L40
Salim S. et al., 2007, ApJS, 173, 267
Salpeter E. E., 1955, ApJ, 121, 161
Sánchez-Blázquez P. et al., 2006, MNRAS, 371, 703
Sánchez-Blázquez P. et al., 2009, A&A, 499, 47
Sánchez S. F. et al., 2012, A&A, 538, A8
Sanders D. B., Mazzarella J. M., Kim D.-C., Surace J. A., Soifer B. T., 2003, AJ, 126, 1607
Schenker A. et al., 2013, ApJ, 768, 196
Schiminovich D. et al., 2005, ApJ, 619, L47
Smith R. J., Lucey J. R., Hudson M. J., 2009, MNRAS, 400, 1690
Smith R. J., Lucey J. R., Price J., Hudson M. J., Phillipps S., 2012, MNRAS, 419, 3167
Sobral D., Best P. N., Smail I., Geach J. E., Cirasuolo M., Garn T., Dalton G. B., 2011, MNRAS, 411, 675
Sobral D., Smail I., Best P. N., Geach J. E., Matsuda Y., Stott J. P., Cirasuolo M., Kurk J., 2013, MNRAS, 428, 1128
Sobral D., Best P. N., Smail I., Mobasher B., Stott J., Nisbet D., 2014, MNRAS, 437, 3516
Speagle J. S., Steinhardt C. L., Capak P. L., Silverman J. D., 2014, ApJS, 214, 15
Spitzer L., Jr, Baade W., 1951, ApJ, 113, 413
Springel V. et al., 2005, Nature, 435, 629
Takeuchi T. T., Yoshikawa K., Ishii T. T., 2003, ApJ, 587, L89
Thomas D., Maraston C., Bender R., Mendes de Oliveira C., 2005, ApJ, 621, 673
Thomas D., Maraston C., Schawinski K., Sarzi M., Silk J., 2010, MNRAS, 404, 1775
Tojeiro R., Heavens A. F., Jimenez R., Panter B., 2007, MNRAS, 381, 1252
Tojeiro R., Wilkins S., Heavens A. F., Panter B., Jimenez R., 2009, ApJS, 185, 1
Tojeiro R. et al., 2013, MNRAS, 432, 359
van der Wel A., Bell E. F., van den Bosch F. C., Gallazzi A., Rix H.-W., 2009, ApJ, 698, 1232
Varela J. et al., 2009, A&A, 497, 667
Vulcani B. et al., 2011, MNRAS, 413, 921
Vulcani B., De Lucia G., Poggianti B. M., Bundy K., More S., Calvi R., 2014, ApJ, 788, 57
Vulcani B., Poggianti B. M., Fritz J., Fasano G., Moretti A., Calvi R., Paccagnella A., 2015, ApJ, 798, 52
Wake D. A., van Dokkum P. G., Franx M., 2012, ApJ, 751, L44
Wetzel A. R., Tinker J. L., Conroy C., 2012, MNRAS, 424, 232
Whitaker K. E., van Dokkum P. G., Brammer G., Franx M., 2012, ApJ, 754, L29
Wilman D. J. et al., 2005, MNRAS, 358, 88
Wuyts S. et al., 2012, ApJ, 753, 114
Wyder T. K. et al., 2005, ApJ, 619, L15
Yang X., Mo H. J., van den Bosch F. C., Pasquali A., Li C., Barden M., 2007, ApJ, 671, 153
Yang X., Mo H. J., van den Bosch F. C., 2008, ApJ, 676, 248
Zibetti S., Charlot S., Rix H.-W., 2009, MNRAS, 400, 1181

This paper has been typeset from a TEX/LATEX file prepared by the author.

# Bibliography


Adami, C., Giles, P., Koulouridis, E., & al. 2018, A&A, accepted arXiv:

Adami, C., Mazure, A., Pierre, M., et al. 2011, A&A, 526, A18

Ahn, C. P., Alexandroff, R., Allende Prieto, C., et al. 2014, ApJS, 211, 17

Aihara, H., Armstrong, R., Bickerton, S., et al. 2017, ArXiv e-prints arXiv:1702.08449

Akiyama, M., Ueda, Y., Watson, M. G., et al. 2015, PASJ, 67, 82

Araya-Melo, P. A., Reisenegger, A., Meza, A., et al. 2009, MNRAS, 399, 97

Arnouts, S., Cristiani, S., Moscardini, L., et al. 1999, MNRAS, 310, 540

Arnouts, S., Moscardini, L., Vanzella, E., et al. 2002, MNRAS, 329, 355

Avila-Reese, V., Colín, P., Gottlöber, S., Firmani, C., & Maulbetsch, C. 2005, ApJ, 634, 51

Bahcall, N. A. & Soneira, R. M. 1984, ApJ, 277, 27

Bai, L., Marcillac, D., Rieke, G. H., et al. 2007, ApJ, 664, 181

Bai, L., Rieke, G. H., Rieke, M. J., Christlein, D., & Zabludoff, A. I. 2009, ApJ, 693, 1840

Baldry, I. K., Balogh, M. L., Bower, R. G., et al. 2006, MNRAS, 373, 469

Baldry, I. K., Glazebrook, K., & Driver, S. P. 2008, MNRAS, 388, 945

Baldry, I. K., Liske, J., Brown, M. J. I., et al. 2018, MNRAS, 474, 3875

Balogh, M., Eke, V., Miller, C., et al. 2004, MNRAS, 348, 1355

Balogh, M. L., Babul, A., Voit, G. M., et al. 2006, MNRAS, 366, 624

Balogh, M. L., Christlein, D., Zabludoff, A. I., & Zaritsky, D. 2001, ApJ, 557, 117

Balogh, M. L., Navarro, J. F., & Morris, S. L. 2000, ApJ, 540, 113

Bardelli, S., Zucca, E., Zamorani, G., Moscardini, L., & Scaramella, R. 2000, MNRAS, 312, 540

Bell, E. F. & de Jong, R. S. 2001, ApJ, 550, 212

Belsole, E., Pratt, G. W., Sauvageot, J.-L., & Bourdin, H. 2004, A&A, 415, 821

Berlind, A. A., Frieman, J., Weinberg, D. H., et al. 2006, ApJS, 167, 1

Bertin, E. & Arnouts, S. 1996, **??**jnlA&AS, 117, 393

Bertin, E. & Tissier, G. 2007, in Astronomical Society of the Pacific Conference Series, Vol. 376, Astronomical Data Analysis Software and Systems XVI, ed. R. A. Shaw, F. Hill, & D. J. Bell, 507

Biviano, A., Moretti, A., Paccagnella, A., et al. 2017, A&A, 607, A81

Blanton, M. R., Eisenstein, D., Hogg, D. W., Schlegel, D. J., & Brinkmann, J. 2005, ApJ, 629, 143

Blitz, L. 1993, in Protostars and Planets III, ed. E. H. Levy & J. I. Lunine, 125–161

Bohlin, R. C., Colina, L., & Finley, D. S. 1995, AJ, 110, 1316

Bolzonella, M., Kovač, K., Pozzetti, L., et al. 2010, A&A, 524, A76

Bond, N. A., Strauss, M. A., & Cen, R. 2010, MNRAS, 409, 156

Boselli, A. & Gavazzi, G. 2006, PASP, 118, 517

Boselli, A., Roehlly, Y., Fossati, M., et al. 2016, A&A, 596, A11

Bower, R. G., Benson, A. J., Malbon, R., et al. 2006, MNRAS, 370, 645

Bressan, A., Marigo, P., Girardi, L., et al. 2012, MNRAS, 427, 127

Brinchmann, J., Charlot, S., White, S. D. M., et al. 2004, MNRAS, 351, 1151

Bruzual, G. & Charlot, S. 2003, MNRAS, 344, 1000

Bundy, K., Ellis, R. S., Conselice, C. J., et al. 2006, ApJ, 651, 120

Calvi, R., Poggianti, B. M., & Vulcani, B. 2011, MNRAS, 416, 727

Calvi, R., Poggianti, B. M., Vulcani, B., & Fasano, G. 2013, MNRAS, 432, 3141

Calzetti, D., Armus, L., Bohlin, R. C., et al. 2000, ApJ, 533, 682

Calzetti, D., Kinney, A. L., & Storchi-Bergmann, T. 1994, ApJ, 429, 582

Cardelli, J. A., Clayton, G. C., & Mathis, J. S. 1989, ApJ, 345, 245

Carlberg, R. G., Yee, H. K. C., Morris, S. L., et al. 2001, ApJ, 552, 427

Chabrier, G. 2003, PASP, 115, 763

Chabrier, G., Baraffe, I., Allard, F., & Hauschildt, P. 2000, ApJ, 542, 464

Charlot, S. & Longhetti, M. 2001, MNRAS, 323, 887

Chon, G., Böhringer, H., & Nowak, N. 2013, MNRAS, 429, 3272

Chow-Martínez, M., Andernach, H., Caretta, C. A., & Trejo-Alonso, J. J. 2014, MNRAS, 445, 4073

Cid Fernandes, R., Mateus, A., Sodré, L., Stasińska, G., & Gomes, J. M. 2005, MNRAS, 358, 363

Clerc, N., Pierre, M., Pacaud, F., & Sadibekova, T. 2012, MNRAS, 423, 3545

Cohen, S. A., Hickox, R. C., Wegner, G. A., Einasto, M., & Vennik, J. 2017, ApJ, 835, 56

Coil, A. L., Newman, J. A., Croton, D., et al. 2008, ApJ, 672, 153

Cole, S., Lacey, C. G., Baugh, C. M., & Frenk, C. S. 2000, MNRAS, 319, 168

Cooper, M. C., Coil, A. L., Gerke, B. F., et al. 2010, MNRAS, 409, 337

Cooper, M. C., Newman, J. A., Croton, D. J., et al. 2006, MNRAS, 370, 198

Costa-Duarte, M. V., Sodré, L., & Durret, F. 2013, MNRAS, 428, 906

Cowie, L. L., Barger, A. J., Bautz, M. W., Brandt, W. N., & Garmire, G. P. 2003, ApJ, 584, L57

Cowie, L. L. & Songaila, A. 1977, Nature, 266, 501

Cowie, L. L., Songaila, A., Hu, E. M., & Cohen, J. G. 1996, AJ, 112, 839

Coziol, R., Andernach, H., Caretta, C. A., Alamo-Martínez, K. A., & Tago, E. 2009, AJ, 137, 4795

Cucciati, O., Davidzon, I., Bolzonella, M., et al. 2017, A&A, 602, A15

Cucciati, O., Iovino, A., Marinoni, C., et al. 2006, A&A, 458, 39

Cucciati, O., Marinoni, C., Iovino, A., et al. 2010, A&A, 520, A42

Daddi, E., Dickinson, M., Morrison, G., et al. 2007, ApJ, 670, 156

Darvish, B., Mobasher, B., Sobral, D., et al. 2016, ApJ, 825, 113

Darvish, B., Mobasher, B., Sobral, D., Scoville, N., & Aragon-Calvo, M. 2015, ApJ, 805, 121

Davidzon, I., Cucciati, O., Bolzonella, M., et al. 2016, A&A, 586, A23

De Lucia, G. 2007, in Astronomical Society of the Pacific Conference Series, Vol. 379, Cosmic Frontiers, ed. N. Metcalfe & T. Shanks, 257

De Lucia, G., Boylan-Kolchin, M., Benson, A. J., Fontanot, F., & Monaco, P. 2010, MNRAS, 406, 1533

De Lucia, G., Poggianti, B. M., Aragón-Salamanca, A., et al. 2007, MNRAS, 374, 809

De Lucia, G., Springel, V., White, S. D. M., Croton, D., & Kauffmann, G. 2006, MNRAS, 366, 499

De Lucia, G., Weinmann, S., Poggianti, B. M., Aragón-Salamanca, A., & Zaritsky, D. 2012, MNRAS, 423, 1277

Dolag, K., Bartelmann, M., Perrotta, F., et al. 2004, A&A, 416, 853

Dressler, A. 1980, ApJ, 236, 351

Dressler, A., Oemler, A., Gladders, M. G., et al. 2009, ApJ, 699, L130

Dressler, A., Oemler, Jr., A., Couch, W. J., et al. 1997, ApJ, 490, 577

Ebeling, H., Stephenson, L. N., & Edge, A. C. 2014, ApJ, 781, L40

Eckert, D., Ettori, S., Coupon, J., et al. 2016, A&A, 592, A12

Eckert, D., Molendi, S., Owers, M., et al. 2014, A&A, 570, A119

Eckert, D., Molendi, S., & Paltani, S. 2011, A&A, 526, A79

Eggen, O. J., Lynden-Bell, D., & Sandage, A. R. 1962, ApJ, 136, 748

Einasto, M., Einasto, J., Tago, E., Müller, V., & Andernach, H. 2001, AJ, 122, 2222

Einasto, M., Liivamägi, L. J., Saar, E., et al. 2011, A&A, 535, A36

Einasto, M., Saar, E., Liivamägi, L. J., et al. 2007, A&A, 476, 697

Einasto, M., Tago, E., Saar, E., et al. 2010, A&A, 522, A92

Eke, V. R., Baugh, C. M., Cole, S., et al. 2004a, MNRAS, 348, 866

Eke, V. R., Frenk, C. S., Baugh, C. M., et al. 2004b, MNRAS, 355, 769

Elbaz, D., Daddi, E., Le Borgne, D., et al. 2007, A&A, 468, 33

Elbaz, D., Dickinson, M., Hwang, H. S., et al. 2011, A&A, 533, A119

Etherington, J., Thomas, D., Maraston, C., et al. 2016, Monthly Notices of the Royal Astronomical Society, 466, 228

Ettori, S. & Balestra, I. 2009, A&A, 496, 343

Fadda, D., Biviano, A., Marleau, F. R., Storrie-Lombardi, L. J., & Durret, F. 2008, ApJ, 672, L9

Farouki, R. & Shapiro, S. L. 1981, ApJ, 243, 32

Fasano, G., Marmo, C., Varela, J., et al. 2006, A&A, 445, 805

Fasano, G., Poggianti, B. M., Bettoni, D., et al. 2015, MNRAS, 449, 3927

Fasano, G., Poggianti, B. M., Couch, W. J., et al. 2000, ApJ, 542, 673

Ferland, G. J. 1993, Hazy, A Brief Introduction to Cloudy 84

Ferland, G. J., Korista, K. T., Verner, D. A., et al. 1998, PASP, 110, 761

Ferland, G. J., Porter, R. L., van Hoof, P. A. M., et al. 2013, RMxAA, 49, 137

Fernandes, R. C., Leão, J. R. S., & Lacerda, R. R. 2003, MNRAS, 340, 29

Finn, R. A., Zaritsky, D., McCarthy, Jr., D. W., et al. 2005, ApJ, 630, 206

Fitzpatrick, E. L. 1986, AJ, 92, 1068

Fleenor, M. C., Rose, J. A., Christiansen, W. A., et al. 2005, AJ, 130, 957

Fontana, A., Pozzetti, L., Donnarumma, I., et al. 2004, A&A, 424, 23

Fossati, M., Wilman, D. J., Fontanot, F., et al. 2015, MNRAS, 446, 2582

Fotopoulou, S., Pacaud, F., Paltani, S., et al. 2016, A&A, 592, A5

Franzetti, P., Scodeggio, M., Garilli, B., Fumana, M., & Paioro, L. 2008, in Astronomical Society of the Pacific Conference Series, Vol. 394, Astronomical Data Analysis Software and Systems XVII, ed. R. W. Argyle, P. S. Bunclark, & J. R. Lewis, 642

Fritz, J., Moretti, A., Poggianti, B., et al. 2017, ArXiv e-prints arXiv:1704.05088

Fritz, J., Poggianti, B. M., Bettoni, D., et al. 2007, A&A, 470, 137

Fritz, J., Poggianti, B. M., Cava, A., et al. 2014, A&A, 566, A32

Fritz, J., Poggianti, B. M., Cava, A., et al. 2011, A&A, 526, A45

Fujita, Y. 1998, ApJ, 509, 587

Fumagalli, M., Fossati, M., Hau, G. K. T., et al. 2014, MNRAS, 445, 4335

Gal, R. R. & Lubin, L. M. 2004, ApJ, 607, L1

Gao, L., Springel, V., & White, S. D. M. 2005, MNRAS, 363, L66

Gavazzi, G., Boselli, A., Cortese, L., et al. 2006, A&A, 446, 839

Geach, J. E., Ellis, R. S., Smail, I., Rawle, T. D., & Moran, S. M. 2011, MNRAS, 413, 177

Gehrels, N. 1986, ApJ, 303, 336

Geller, M. J. & Huchra, J. P. 1983, ApJS, 52, 61

George, M. R., Ma, C.-P., Bundy, K., et al. 2013, ApJ, 770, 113

Gilbank, D. G., Yee, H. K. C., Ellingson, E., et al. 2008, ApJ, 677, L89

Giles, P. A., Maughan, B. J., Pacaud, F., et al. 2016, A&A, 592, A3

Giodini, S., Finoguenov, A., Pierini, D., et al. 2012, A&A, 538, A104

González, V., Labbé, I., Bouwens, R. J., et al. 2010, ApJ, 713, 115

Gott, III, J. R., Jurić, M., Schlegel, D., et al. 2005, ApJ, 624, 463

Gott, III, J. R. & Thuan, T. X. 1976, ApJ, 204, 649

Guglielmo, V., Poggianti, B. M., Moretti, A., et al. 2015, MNRAS, 450, 2749

Guglielmo, V., Poggianti, B. M., Vulcani, B., et al. 2017, ArXiv e-prints arXiv:1710.04667

Gunn, J. E. & Gott, III, J. R. 1972, ApJ, 176, 1

Gutkin, J., Charlot, S., & Bruzual, G. 2016, MNRAS, 462, 1757

Guzzo, L., Cassata, P., Finoguenov, A., et al. 2007, ApJS, 172, 254

Gwyn, S. D. J. 2008, PASP, 120, 212

Haines, C. P., Gargiulo, A., La Barbera, F., et al. 2007, MNRAS, 381, 7

Haines, C. P., Pereira, M. J., Smith, G. P., et al. 2013, ApJ, 775, 126

Hashimoto, Y., Oemler, Jr., A., Lin, H., & Tucker, D. L. 1998, ApJ, 499, 589

Helsdon, S. F. & Ponman, T. J. 2003, MNRAS, 339, L29

Henriksen, M. & Byrd, G. 1996, ApJ, 459, 82

Henry, J. P., Gioia, I. M., Huchra, J. P., et al. 1995, ApJ, 449, 422

Hickson, P., Kindl, E., & Auman, J. R. 1989, ApJS, 70, 687

Hickson, P., Kindl, E., & Huchra, J. P. 1988, ApJ, 331, 64

Hoffman, Y., Lahav, O., Yepes, G., & Dover, Y. 2007, JCAP, 10, 016

Hogg, D. W., Blanton, M. R., Eisenstein, D. J., et al. 2003, ApJ, 585, L5

Hopkins, P. F., Bundy, K., Croton, D., et al. 2010, ApJ, 715, 202

Hubble, E. P. 1926, ApJ, 64

Huchra, J. P. & Geller, M. J. 1982, ApJ, 257, 423

Icke, V. & van de Weygaert, R. 1987, A&A, 184, 16

Ilbert, O., Arnouts, S., McCracken, H. J., et al. 2006, A&A, 457, 841

Ilbert, O., McCracken, H. J., Le Fèvre, O., et al. 2013, A&A, 556, A55

Iovino, A., Cucciati, O., Scodeggio, M., et al. 2010, A&A, 509, A40

Jeltema, T. E., Mulchaey, J. S., Lubin, L. M., & Fassnacht, C. D. 2007, ApJ, 658, 865

Jian, H.-Y., Lin, L., Oguri, M., et al. 2017, ArXiv e-prints arXiv:1704.06219

Kartaltepe, J. S., Ebeling, H., Ma, C. J., & Donovan, D. 2008, MNRAS, 389, 1240

Katsianis, A., Blanc, G., Lagos, C. P., et al. 2017, MNRAS, 472, 919

Kauffmann, G., Heckman, T. M., White, S. D. M., et al. 2003, MNRAS, 341, 33

Kauffmann, G., White, S. D. M., Heckman, T. M., et al. 2004, MNRAS, 353, 713

Kawata, D. & Mulchaey, J. S. 2008, ApJ, 672, L103

Kim, S., Rey, S.-C., Bureau, M., et al. 2016, ApJ, 833, 207

Knobel, C., Lilly, S. J., Iovino, A., et al. 2009, ApJ, 697, 1842

Kofman, L. A., Einasto, J., & Linde, A. D. 1987, Nature, 326, 48

Koleva, M., Prugniel, P., Bouchard, A., & Wu, Y. 2009, A&A, 501, 1269

Koulouridis, E., Poggianti, B., Altieri, B., et al. 2016, A&A, 592, A11

Kovač, K., Lilly, S. J., Cucciati, O., et al. 2010, ApJ, 708, 505

Koyama, Y., Smail, I., Kurk, J., et al. 2013, MNRAS, 434, 423

La Barbera, F., Pasquali, A., Ferreras, I., et al. 2014, MNRAS, 445, 1977

Lamastra, A., Menci, N., Fiore, F., & Santini, P. 2013, A&A, 552, A44

Larson, R. B. 1974, MNRAS, 166, 585

Larson, R. B. 1975, MNRAS, 173, 671

Larson, R. B., Tinsley, B. M., & Caldwell, C. N. 1980, ApJ, 237, 692

Le Fèvre, O., Tasca, L. A. M., Cassata, P., et al. 2015, A&A, 576, A79

Le Fèvre, O., Vettolani, G., Garilli, B., et al. 2005, A&A, 439, 845

Leauthaud, A., Finoguenov, A., Kneib, J.-P., et al. 2010, ApJ, 709, 97

Leauthaud, A., George, M. R., Behroozi, P. S., et al. 2012, ApJ, 746, 95

Lemson, G. & Kauffmann, G. 1999, MNRAS, 302, 111

Lidman, C., Ardila, F., Owers, M., et al. 2016, PASA, 33, e001

Lietzen, H., Tempel, E., Heinämäki, P., et al. 2012, A&A, 545, A104

Lieu, M., Smith, G. P., Giles, P. A., et al. 2016, A&A, 592, A4

Lin, L., Cooper, M. C., Jian, H.-Y., et al. 2010, ApJ, 718, 1158

Lin, L., Jian, H.-Y., Foucaud, S., et al. 2014, ApJ, 782, 33

Liu, G., Calzetti, D., Hong, S., et al. 2013, ApJ, 778, L41

Longhetti, M. & Saracco, P. 2009, MNRAS, 394, 774

Lubin, L. M., Gal, R. R., Lemaux, B. C., Kocevski, D. D., & Squires, G. K. 2009, AJ, 137, 4867

Luparello, H. E., Lares, M., Yaryura, C. Y., et al. 2013, MNRAS, 432, 1367

MacArthur, L. A., González, J. J., & Courteau, S. 2009, MNRAS, 395, 28

Madau, P., Ferguson, H. C., Dickinson, M. E., et al. 1996, MNRAS, 283, 1388

Mamon, G. A. 1986, ApJ, 307, 426

Mantz, A., Allen, S. W., Rapetti, D., & Ebeling, H. 2010, MNRAS, 406, 1759

Marchesini, D., van Dokkum, P. G., Förster Schreiber, N. M., et al. 2009, ApJ, 701, 1765

Martínez, H. J., Zandivarez, A., Merchán, M. E., & Domínguez, M. J. L. 2002, MNRAS, 337, 1441

Maulbetsch, C., Avila-Reese, V., Colín, P., et al. 2007, ApJ, 654, 53

McGee, S. L., Balogh, M. L., Bower, R. G., Font, A. S., & McCarthy, I. G. 2009, MNRAS, 400, 937

McGee, S. L., Balogh, M. L., Wilman, D. J., et al. 2011, MNRAS, 413, 996

Mihos, J. C. 2004, in IAU Symposium, Vol. 217, Recycling Intergalactic and Interstellar Matter, ed. P.-A. Duc, J. Braine, & E. Brinks, 390

Miniati, F., Finoguenov, A., Silverman, J. D., et al. 2016, ApJ, 819, 26

Mobasher, B., Dickinson, M., Ferguson, H. C., et al. 2005, ApJ, 635, 832

Moore, B., Frenk, C. S., & White, S. D. M. 1993, MNRAS, 261, 827

Moore, B., Katz, N., Lake, G., Dressler, A., & Oemler, A. 1996, Nature, 379, 613

Moore, B., Lake, G., & Katz, N. 1998, ApJ, 495, 139

Moran, S. M., Ellis, R. S., Treu, T., et al. 2007, ApJ, 671, 1503

Moretti, A., Gullieuszik, M., Poggianti, B., et al. 2017, A&A, 599, A81

Moster, B. P., Somerville, R. S., Maulbetsch, C., et al. 2010, ApJ, 710, 903

Moustakas, J., Coil, A. L., Aird, J., et al. 2013, ApJ, 767, 50

Mulchaey, J. S., Davis, D. S., Mushotzky, R. F., & Burstein, D. 2003, ApJS, 145, 39

Muldrew, S. I., Croton, D. J., Skibba, R. A., et al. 2012, MNRAS, 419, 2670

Muzzin, A., Marchesini, D., Stefanon, M., et al. 2013, ApJ, 777, 18

Muzzin, A., Wilson, G., Yee, H. K. C., et al. 2012, ApJ, 746, 188

Nantais, J. B., Muzzin, A., van der Burg, R. F. J., et al. 2017, MNRAS, 465, L104

Nantais, J. B., van der Burg, R. F. J., Lidman, C., et al. 2016, A&A, 592, A161

Newman, A. B., Ellis, R. S., Bundy, K., & Treu, T. 2012, ApJ, 746, 162

Nichol, R. C., Sheth, R. K., Suto, Y., et al. 2006, MNRAS, 368, 1507

Nipoti, C., Treu, T., Leauthaud, A., et al. 2012, MNRAS, 422, 1714

Noeske, K. G., Weiner, B. J., Faber, S. M., et al. 2007, ApJ, 660, L43

Nordon, R., Lutz, D., Genzel, R., et al. 2012, ApJ, 745, 182

Ocvirk, P., Pichon, C., Lançon, A., & Thiébaut, E. 2006, MNRAS, 365, 46

Oemler, Jr., A., Dressler, A., Gladders, M. G., et al. 2013a, ApJ, 770, 63

Oemler, Jr., A., Dressler, A., Gladders, M. G., et al. 2013b, ApJ, 770, 61

Olive, K. A., Schramm, D. N., Steigman, G., & Walker, T. P. 1990, Physics Letters B, 236, 454

Ouchi, M., Shimasaku, K., Akiyama, M., et al. 2005, ApJ, 620, L1

Pacaud, F., Clerc, N., Giles, P. A., et al. 2016, A&A, 592, A2

Pacaud, F., Pierre, M., Adami, C., et al. 2007, MNRAS, 382, 1289

Pacaud, F., Pierre, M., Refregier, A., et al. 2006, MNRAS, 372, 578

Paccagnella, A., Vulcani, B., Poggianti, B. M., et al. 2017, ApJ, 838, 148

Paccagnella, A., Vulcani, B., Poggianti, B. M., et al. 2016, ApJ, 816, L25

Pagel, B. E. J. 1988, GEMINI Newsletter Royal Greenwich Observatory, 18, 1

Pagel, B. E. J. & Simonson, E. A. 1989, RMxAA, 18, 153

Pascut, A. & Ponman, T. J. 2015, MNRAS, 447, 3723

Pasquali, A., Gallazzi, A., Fontanot, F., et al. 2010, MNRAS, 407, 937

Patel, S. G., Holden, B. P., Kelson, D. D., Illingworth, G. D., & Franx, M. 2009, ApJ, 705, L67

Peng, Y.-j., Lilly, S. J., Kovač, K., et al. 2010, ApJ, 721, 193

Peng, Y.-j., Lilly, S. J., Renzini, A., & Carollo, M. 2012, ApJ, 757, 4

Percival, W. J., Scott, D., Peacock, J. A., & Dunlop, J. S. 2003, MNRAS, 338, L31

Pickles, A. J. 1998, PASP, 110, 863

Pierre, M., Pacaud, F., Adami, C., et al. 2016, A&A, 592, A1

Pierre, M., Valtchanov, I., Altieri, B., et al. 2004, JCAP, 9, 011

Pillepich, A., Springel, V., Nelson, D., et al. 2018, MNRAS, 473, 4077

Planck Collaboration, Ade, P. A. R., Aghanim, N., et al. 2014, A&A, 571, A16

Poggianti, B. M. 1997, **??**jnlA&AS, 122, 399

Poggianti, B. M., Bressan, A., & Franceschini, A. 2001, ApJ, 550, 195

Poggianti, B. M., Desai, V., Finn, R., et al. 2008, ApJ, 684, 888

Poggianti, B. M., Fasano, G., Omizzolo, A., et al. 2016, AJ, 151, 78

Poggianti, B. M., Moretti, A., Gullieuszik, M., et al. 2017, ApJ, 844, 48

Poggianti, B. M., Smail, I., Dressler, A., et al. 1999, ApJ, 518, 576

Poggianti, B. M., von der Linden, A., De Lucia, G., et al. 2006, ApJ, 642, 188

Poggianti, B. M. & Wu, H. 2000, ApJ, 529, 157

Pompei, E., Adami, C., Eckert, D., et al. 2016, A&A, 592, A6

Popesso, P., Böhringer, H., Brinkmann, J., Voges, W., & York, D. G. 2004, A&A, 423, 449

Popesso, P., Rodighiero, G., Saintonge, A., et al. 2011, A&A, 532, A145

Postman, M., Franx, M., Cross, N. J. G., et al. 2005, ApJ, 623, 721

Postman, M. & Geller, M. J. 1984, ApJ, 281, 95

Pozzetti, L., Bolzonella, M., Lamareille, F., et al. 2007, A&A, 474, 443

Pozzetti, L., Bolzonella, M., Zucca, E., et al. 2010, A&A, 523, A13

Presotto, V., Iovino, A., Scodeggio, M., et al. 2012, A&A, 539, A55

Ramella, M., Geller, M. J., & Huchra, J. P. 1989, ApJ, 344, 57

Ramella, M., Pisani, A., & Geller, M. J. 1997, AJ, 113, 483

Ramella, M., Zamorani, G., Zucca, E., et al. 1999, A&A, 342, 1

Renzini, A. 2006, ARA&A, 44, 141

Rodighiero, G., Daddi, E., Baronchelli, I., et al. 2011, ApJ, 739, L40

Rose, J. A., Gaba, A. E., Christiansen, W. A., et al. 2002, AJ, 123, 1216

Salim, S., Rich, R. M., Charlot, S., et al. 2007, ApJS, 173, 267

Sánchez, S. F., Pérez, E., Sánchez-Blázquez, P., et al. 2016, RMxAA, 52, 21

Sánchez-Blázquez, P., Jablonka, P., Noll, S., et al. 2009, A&A, 499, 47

Santos, J. S., Altieri, B., Popesso, P., et al. 2013, MNRAS, 433, 1287

Sargent, M. T., Béthermin, M., Daddi, E., & Elbaz, D. 2012, ApJ, 747, L31

Schaye, J., Crain, R. A., Bower, R. G., et al. 2015, MNRAS, 446, 521

Schechter, P. 1976, ApJ, 203, 297

Schirmer, M., Hildebrandt, H., Kuijken, K., & Erben, T. 2011, A&A, 532, A57

Schlegel, D. J., Finkbeiner, D. P., & Davis, M. 1998, ApJ, 500, 525

Schneider, P. 2006, Extragalactic Astronomy and Cosmology (Springer)

Scodeggio, M., Guzzo, L., Garilli, B., et al. 2016, ArXiv e-prints arXiv:1611.07048

Scodeggio, M., Vergani, D., Cucciati, O., et al. 2009, A&A, 501, 21

Scoville, N., Aussel, H., Brusa, M., et al. 2007, ApJS, 172, 1

Scoville, N., Lee, N., Vanden Bout, P., et al. 2017, ApJ, 837, 150

Severgnini, P. & Saracco, P. 2001, Ap&SS, 276, 749

Shankar, F., Lapi, A., Salucci, P., De Zotti, G., & Danese, L. 2006, ApJ, 643, 14

Shen, S., Madau, P., Guedes, J., et al. 2013, ApJ, 765, 89

Simpson, C., Rawlings, S., Ivison, R., et al. 2012, MNRAS, 421, 3060

Smith, R. J., Lucey, J. R., Price, J., Hudson, M. J., & Phillipps, S. 2012, MNRAS, 419, 3167

Smith, R. K., Brickhouse, N. S., Liedahl, D. A., & Raymond, J. C. 2001, ApJ, 556, L91

Sobral, D., Best, P. N., Smail, I., et al. 2011, MNRAS, 411, 675

Sobral, D., Best, P. N., Smail, I., et al. 2014, MNRAS, 437, 3516

Söchting, I. K., Coldwell, G. V., Clowes, R. G., Campusano, L. E., & Graham, M. J. 2012, MNRAS, 423, 2436

Speagle, J. S., Steinhardt, C. L., Capak, P. L., & Silverman, J. D. 2014, ApJS, 214, 15

Spitzer, Jr., L. & Baade, W. 1951, ApJ, 113, 413

Stalin, C. S., Petitjean, P., Srianand, R., et al. 2010, MNRAS, 401, 294

Stanger, J. 2009, Galaxy Formation and Evolution

Swinbank, A. M., Edge, A. C., Smail, I., et al. 2007, MNRAS, 379, 1343

Tanaka, M., Goto, T., Okamura, S., Shimasaku, K., & Brinkmann, J. 2004, AJ, 128, 2677

Tanaka, M., Hoshi, T., Kodama, T., & Kashikawa, N. 2007, MNRAS, 379, 1546

Tasca, L. A. M., Kneib, J.-P., Iovino, A., et al. 2009, A&A, 503, 379

Tojeiro, R., Heavens, A. F., Jimenez, R., & Panter, B. 2007, MNRAS, 381, 1252

Toomre, A. & Toomre, J. 1972, ApJ, 178, 623

Tran, K.-V. H., Saintonge, A., Moustakas, J., et al. 2009, ApJ, 705, 809

Treu, T., Ellis, R. S., Kneib, J.-P., et al. 2003, ApJ, 591, 53

Tucker, D. L., Oemler, Jr., A., Hashimoto, Y., et al. 2000, ApJS, 130, 237

Tully, R. B. 1987, ApJ, 321, 280

Ueda, Y., Watson, M. G., Stewart, I. M., et al. 2008, ApJS, 179, 124

Valluri, M. 1993, ApJ, 408, 57

van den Bosch, F. C., Aquino, D., Yang, X., et al. 2008, MNRAS, 387, 79

van der Burg, R. F. J., Hoekstra, H., Muzzin, A., et al. 2015, A&A, 577, A19

Veillet, C. 2007, in Bulletin of the American Astronomical Society, Vol. 39, American Astronomical Society Meeting Abstracts #210, 170

Venemans, B. P., Röttgering, H. J. A., Overzier, R. A., et al. 2004, A&A, 424, L17

Verdugo, M., Lerchster, M., Böhringer, H., et al. 2012, MNRAS, 421, 1949

Vogeley, M. S., Hoyle, F., Rojas, R. R., & Goldberg, D. 2004, in Bulletin of the American Astronomical Society, Vol. 36, American Astronomical Society Meeting Abstracts, 1496

von der Linden, A., Wild, V., Kauffmann, G., White, S. D. M., & Weinmann, S. 2010, MNRAS, 404, 1231

Vulcani, B., Bundy, K., Lackner, C., et al. 2014a, ApJ, 797, 62

Vulcani, B., De Lucia, G., Poggianti, B. M., et al. 2014b, ApJ, 788, 57

Vulcani, B., Poggianti, B. M., Aragón-Salamanca, A., et al. 2011, MNRAS, 412, 246

Vulcani, B., Poggianti, B. M., Fasano, G., et al. 2012, MNRAS, 420, 1481

Vulcani, B., Poggianti, B. M., Finn, R. A., et al. 2010, ApJ, 710, L1

Vulcani, B., Poggianti, B. M., Fritz, J., et al. 2015, ApJ, 798, 52

Vulcani, B., Poggianti, B. M., Oemler, A., et al. 2013, A&A, 550, A58

Wang, L., Li, C., Kauffmann, G., & De Lucia, G. 2006, MNRAS, 371, 537

Wetzel, A. R., Tinker, J. L., & Conroy, C. 2012, MNRAS, 424, 232

Whiley, I. M., Aragón-Salamanca, A., De Lucia, G., et al. 2008, MNRAS, 387, 1253

Whitaker, K. E., van Dokkum, P. G., Brammer, G., & Franx, M. 2012, ApJ, 754, L29

White, S. D. M., Clowe, D. I., Simard, L., et al. 2005, A&A, 444, 365

Wijesinghe, D. B., Hopkins, A. M., Brough, S., et al. 2012, MNRAS, 423, 3679

Wilkinson, D. M., Maraston, C., Thomas, D., et al. 2015, MNRAS, 449, 328

Williams, J. P., Blitz, L., & McKee, C. F. 2000, Protostars and Planets IV, 97

Wilman, D. J., Balogh, M. L., Bower, R. G., et al. 2005a, MNRAS, 358, 88

Wilman, D. J., Balogh, M. L., Bower, R. G., et al. 2005b, MNRAS, 358, 71

Wilman, D. J., Oemler, Jr., A., Mulchaey, J. S., et al. 2009, ApJ, 692, 298

Woo, J., Dekel, A., Faber, S. M., et al. 2013, MNRAS, 428, 3306

Wuyts, S., Förster Schreiber, N. M., van der Wel, A., et al. 2011, ApJ, 742, 96

Yang, Y., Zabludoff, A. I., Zaritsky, D., & Mihos, J. C. 2009, ApJ, 702, 1683

York, D. G., Adelman, J., Anderson, Jr., J. E., et al. 2000, AJ, 120, 1579

Zabludoff, A. I. & Mulchaey, J. S. 1998, ApJ, 496, 39

Zibetti, S., Charlot, S., & Rix, H.-W. 2009, MNRAS, 400, 1181

# List of Figures

# List of Tables